# Anisotropic translational diffusion in passive and active colloidal suspensions : Rheology and complex flows

Hamza Issa

## To cite this version:

Hamza Issa. Anisotropic translational diffusion in passive and active colloidal suspensions : Rheology and complex flows. Fluids mechanics [physics.class-ph]. Université de Bretagne Sud, 2023. English. NNT : 2023LORIS683 . tel-04885923

HAL Id: tel-04885923
https://theses.hal.science/tel-04885923v1
Submitted on 14 Jan 2025

DOCTORAT
BRETAGNE SCIENCES
LOIRE POUR L'INGENIEUR

Université
Bretagne Sud

# THÈSE DE DOCTORAT DE

L'UNIVERSITÉ DE BRETAGNE SUD

ÉCOLE DOCTORALE N° 602
*Sciences pour l'Ingénieur*
Spécialité : *génie mécanique*

Par
**Hamza ISSA**

# Anisotropic Translational Diffusion in Passive and Active Colloidal Suspensions: Rheology and complex flows.

**Thèse présentée et soutenue à Lorient, le 14 December 2023**
**Unité de recherche : IRDL UMR CNRS 6027**
**Thèse N° : 683**

**Rapporteurs avant soutenance :**

| | |
|---|---|
| Luisa SILVA | Professeure à l'Ecole Centrale, Nantes |
| David DEAN | Professeur des Universités, Université de Bordeaux |

**Composition du Jury :**

| | | |
|---|---|---|
| Président : | Eric CLIMENT | Professeur des Universités, Université Toulouse III - Paul Sabatier |
| Examinateurs : | | |
| Dir. de thèse : | Julien FEREC | Professeur des Universités, Université Bretagne Sud |
| Co-directeur : | Giovaniantonio NATALE | Professeur, University of Calgary |
| Co-directeur : | Gilles AUSIAS | Professeur des Universités, Université Bretagne Sud |

# ACKNOWLEDMENT

This thesis manuscript is the culmination of more than three years of dedicated work conducted at the Dupuy de Lôme Research Institute (IRDL) of Bretagne Sud University in Lorient, France, and the University of Calgary in Calgary, Canada. I extend my sincere gratitude to the Brittany Region, Isblue, and the Natural Sciences and Engineering Research Council of Canada (NSERC) for their unwavering trust and generous financial support, which created the optimal conditions for the successful completion of my thesis.

I am deeply indebted to Julien Férec, Giovaniantonio Natale, and Gilles Ausias, my thesis directors, for entrusting me with this captivating research journey. Thank you for not only providing me with the opportunity but also for sharing your wealth of knowledge, offering invaluable advice, and providing relevant comments that propelled me forward.

To the esteemed members of the jury who evaluated my thesis work, I express my gratitude. Special thanks to Mr. Eric Clement for the honor of chairing the jury, and to Ms. Luisa Silva and Mr. David Dean for their dedication in reviewing my work. Your critical feedback, probing questions, and genuine interest in my research are deeply appreciated.

While the essence of a thesis is undoubtedly scientific, its richness extends beyond into the personal realm. I had the privilege of spending several years in Brittany and Alberta, particularly in the vibrant cities of Lorient and Calgary. To all those who shared in the adventures of Lorient and Calgary with me, contributing to a tapestry of unforgettable moments marked by kindness and shared experiences, I extend my heartfelt thanks.

A profound appreciation goes out to my lab colleagues, with whom I collaborated daily and shared doctoral evenings. Together, we created memories that are not only professionally enriching but also personally fulfilling.

I am grateful to my office colleagues for their unwavering support during moments of stress over these three years. Thank you for the beautiful moments, the endless debates, and the meaningful discussions that shaped not just my academic journey but also my personal growth. Thanks for Ajinkya Pawar and Malik Spahics.

I reserve a special place in my heart for my most beautiful encounters in Lorient—Asmahan Zaafouri, Cynthia Tayeh, and Abbas Ramadan. Your presence in my life has been a beacon of joy and support from the very beginning.

In the tapestry of my time in Lorient and Calgary, certain threads shine brighter. To my second family in Lorient—Machour El Asaad, Joseph Jabour, Jad Hussein, Patrick El Helou, and Maria Bitar—your warmth and hospitality have transformed Lorient into a home away from

home. Your support has been a source of strength throughout this journey.

Gratitude extends to all my friends in Lorient—Kassem Saied, Abbas Assi, Hasan Harb, and Hussein Saad. Your camaraderie has added depth to my experiences, and I am thankful for the shared moments of joy and encouragement.

In Calgary, I extend a special thanks to Elias El Deek, Nathir Haimoun, Ibrahim Hozain, Mohammad Khaled Afshin, Hamed saadat and all my friends who have been part of my Canadian journey. Your friendship has been a comforting presence, making Calgary feel like a second home.

This thesis is not just a testament to academic endeavors; it is a reflection of the friendships that have colored my world with joy, support, and shared memories. Each of you holds a special place in my heart, and I am grateful for the richness you've brought to my life.

I reserve heartfelt thanks for Sarah Kheireddine, a pillar of support and friendship transcending any distance. Your unwavering presence has been a source of strength throughout this journey, and I am grateful for the enduring bond we share.

I extend my heartfelt gratitude to my best friends, Khouloud Koteich and Hassan Itawi, for their unwavering support regardless of the distance. Your friendship has been a source of strength, and I am grateful for the enduring bond that transcends miles.

A heartfelt thank you to my best friends, Ahmad Karnib, Ibrahim Harb, and Ali Moallem, for the continuous support and the countless beautiful moments we've shared since we met. Your friendship has added immeasurable joy to my life.

A great thanks to my friends Hasan Kolkas, Bilal Fakih, Andre Mrad, Ibrahim Hatoum, Zahraa Zeidan, Jihan Saad, Mouhanad Alchaar, Youssef Hussein, Karim Mousa, Hassan Zein Eddine, Mohammad Akil, Hussein El Dor and Mahmoud Gharib .

A special note of gratitude goes to my cousin, whose support has been a constant presence since my arrival in France. From the very beginning until now, your encouragement has been a guiding light, and I am deeply appreciative of the enduring support you've provided.

A profound and special thanks to my family, the unwavering pillars of support throughout my entire life. My deepest gratitude goes to my mother, father, brothers, and sisters—your constant standing by me has been the cornerstone of who I am today. No words can capture the magnitude of your hard work and sacrifices. You hold the first and most significant credit for every achievement and success.

In reflection, this thesis stands as more than a mere document of research; it is a testament to the collaborative efforts and shared experiences that have woven the fabric of both my academic and personal journey.

Undoubtedly, there are individuals whose names I may have unintentionally omitted, but rest assured that your support has not gone unnoticed. To all those who have been part of this journey, your presence and encouragement are etched in my heart. Thank you for being an integral part of this chapter in my life.

With sincere gratitude,

# CONTENTS

# LIST OF FIGURES

---

# LIST OF TABLES

# NOMENCLATURE

| | |
|---|---|
| $a_r$ | Particle aspect ratio |
| $c$ | Particles concentration |
| $C_I$ | Interaction coefficient |
| $d$ | Particle width |
| $D_r$ | Rotary diffusion |
| $F_d$ | Drag force |
| $F_p$ | Particle's force |
| $k_B$ | Boltzman constant |
| $L$ | Particle length |
| $n$ | Number of particles per unit volume |
| $Pe$ | Peclet number |
| $t$ | Time |
| $V_s$ | Particle's velocity |
| $\lambda$ | Shape factor |
| $\theta$ | Polar angle |
| $\phi$ | Azimuthal angle |
| $\phi_f$ | Particle's volume fraction |
| $\gamma$ | Strain |
| $\dot{\gamma}$ | Deformation rate |
| $\eta_0$ | Newtonian viscosity |
| $\psi$ | Orientation probability distribution function |
| $\Psi$ | Orientation and position probability distribution function |
| $\mathbf{p}$ | Orientation vector |
| $\dot{\mathbf{p}}$ | Orientation velocity |

| | |
|---|---|
| $\mathbf{r_c}$ | Position vector |
| $\dot{\mathbf{r}}_\mathbf{c}$ | Translational velocity |
| $\mathbf{u}$ | Flow velocity vectors |
| $\boldsymbol{a}_2$ | Second-order orientation tensor |
| $\boldsymbol{a}_4$ | Fourth-order orientation tensor |
| $\mathbf{D}_t$ | Translational diffusion tensor |
| $\boldsymbol{\omega}$ | Vorticity tensor |
| $\dot{\boldsymbol{\gamma}}$ | Deformation rate tensor |
| $\boldsymbol{\delta}$ | Identity tensor |
| $\boldsymbol{\Sigma}$ | Stress tensor |
| $log$ | Logarithmic function |
| $\frac{D}{Dt}$ | Material derivative |
| $\frac{\partial}{\partial t}$ | Partial derivative |
| $\Delta_\mathbf{p}$ | Orientational gradient operator |
| $\Delta_\mathbf{x}$ | Spatial gradient operator |
| $\Delta^2_\mathbf{p}$ | Orientational Laplacian operator |
| $\Delta^2_\mathbf{x}$ | Spatial Laplacian operator |
| $FVM$ | Finite volume method |
| $DFC$ | Distribution function calculation |
| $FP$ | Fokker-Planck |
| $FEM$ | Finite element method |

# GENERAL INTRODUCTION

## Context

## 0.1 Introduction

### 0.1.1 General informations

Suspended particles come in diverse sizes and shapes. Moreover, they can be categorized as either passive or active particles in nature. Passive particles lack the ability to self-propel within a fluid. They simply move with the flow of the fluid that they are suspended in. Examples of passive particles include many common materials such as fibers and dust in addition to other materials used in nanotechnology, such as gold, silver, titanium dioxide nanoparticles and crystalline nanocarbons. In contrast, active particles have the ability to move or propel themselves through a fluid, typically by converting chemical or other forms of energy into motion. This motion can be self-propelled, meaning that the particle moves independently, or it can be directed by an external force. Examples of active nanoparticles include bacteria, which propel themselves using flagella, and synthetic nanoparticles designed to move through fluids for medical or environmental applications.

Active particles, such as bacteria, microalgae, and zooplankton, play an important role in biofouling in marine engineering. Biofouling is the accumulation of microorganisms, plants, and animals on submerged surfaces, such as ship hulls, buoys, and offshore structures [1]. Biofouling can have negative impacts on the performance and efficiency of these structures, and can also lead to increase maintenance and cleaning costs [2]. Active particles can contribute to biofouling in several ways. For example, bacteria and microalgae can attach to surfaces and produce extracellular polymeric substances (EPS) [3], which can form a matrix that adheres to the surface and provides a substrate for other microorganisms to attach to (see Fig. 1 a). These microorganisms can also produce enzymes and chemicals that can degrade the surface and make it more susceptible to biofouling [4]. Zooplankton, such as barnacles (see Fig. 1 b) and mussels, can also attach to submerged surfaces and form complex communities. These organisms use a range of mechanisms to attach to surfaces, including adhesion, cementation, and secretion of byssal threads. Once attached, they can also produce EPS and other substances that can promote biofilm formation and create a complex and durable fouling community. The study of active particles in biofouling is an active area of research in marine engineering. Scientists are developing new methods to prevent and control biofouling, such as antifouling coatings, surface

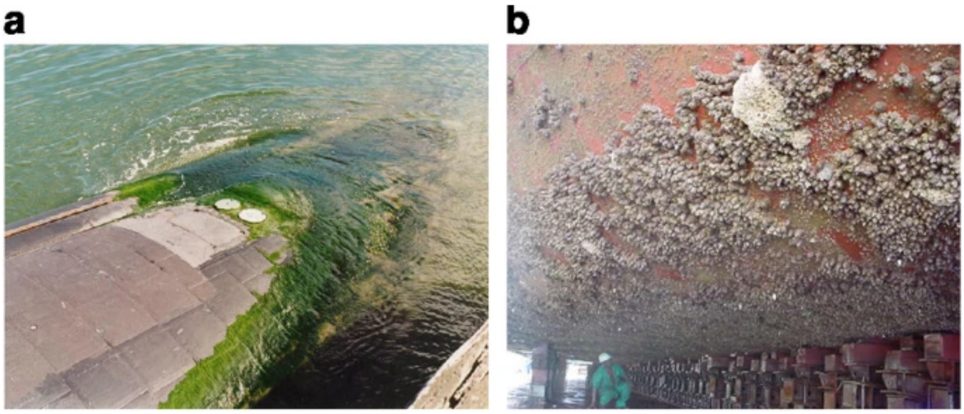

Figure 1 – Images show (a) fouling by the green algae (seaweed) Ulva and (b) barnacles [1].

modifications, and biological control agents that target specific microorganisms. Understanding the role of active particles in biofouling is essential for developing effective strategies to prevent and manage biofouling in marine environments.

Particles with an anisometric structure are even more intriguing, because they can control not only their shape but also their functionality. It has seen an almost unbelievable revolution in science, especially in the study of nano- or micro-sized anisometric particles. The self-assembly of particles has become an increasingly important area of research in recent years, as it offers a powerful approach for designing and controlling the properties of materials at the nanoscale. Anisometric particles are those that have a non-spherical shape, such as rods, plates, or stars, and they can exhibit a wide range of unique properties, such as tunable plasmonic resonances, enhanced magnetic or optical properties, and improved catalytic activity. By carefully controlling the synthesis and assembly of these particles, researchers can create materials with tailored properties and functionalities, such as a high surface area for catalysis, strong plasmonic coupling for sensing or imaging, or tunable optical properties for energy applications.

The study of anisometric particles has opened up new avenues for research in areas such as nanophotonics, nanoelectronics, and nanomedicine, among others. This broad term consists of various of biological and physical systems, including suspensions of self-propelled microorganisms such as motile bacteria and microscopic algae [5–7], swarming of self-propelled polar granular rods [8] and vibrated polar disks [9]. Because of their importance in ecology, medicine, biofouling in marine structures and a variety of technological applications, there is a growing influence in studying their behavior in biophysics, colloidal science, fluid mechanics, and statistical physics [10–16]. The study of the mechanical properties of such substances requires rheological measurements. A rheological measurement perturbs (slightly or significantly) the substance out of equilibrium and measures the stress responses. Thus, the study of the dynamics of the non-equilibrium state of materials is crucial to understanding the rheology of these materials.

When an active particle swims through a fluid, it generates a propulsive force, $F_p$, that is balanced by a resistive drag, $F_d$, from the surrounding fluid. The magnitude of the propulsive force depends on the specific swimming mechanism and the properties of the fluid, while the magnitude of the drag force depends on the size and shape of the particle, as well as the properties of the fluid. In general, the balance between the propulsive and drag forces determines the velocity and direction of the particle's motion.

When an active particle swims through a fluid, it generates a flow field in the surrounding fluid that is characterized by a force dipole. The magnitude and sign of the force dipole depend on the swimming mechanism of the particle. For pusher-type particles, such as E. coli and B. subtilis, the force is generated near the tail of the particle, which pushes the fluid backward, resulting in a negative force dipole [17]. This means that the flow field generated by a pusher-type particle is such that the fluid is being pulled towards the particle's head, and pushed away from its tail [18]. On the other hand, for puller-type particles, such as Chlamydomonas Reinhardtii, the force is generated near the head of the particle, which pulls the fluid forward, resulting in a positive force dipole [17]. This means that the flow field generated by a puller-type particle is such that the fluid is being pulled towards the particle's tail, and pushed away from its head [19].

The magnitude of the force dipole, depends on the details of the swimming mechanism and the properties of the particle and fluid. However, to leading order, the force dipole is proportional to the propulsive force generated by the particle, and it provides a useful way to characterize the particle's swimming behavior and its interaction with the surrounding fluid [17].

### 0.1.2 Thesis presentation

Surprisingly, despite the different ways they move, the mathematics describing how passive Brownian particles behave shows striking similarities to the equations that explain the actions of active particles. This thesis presents a comprehensive exploration of both suspended Brownian rods and active Brownian particles within fluid flow systems. It starts with investigating the intricate behaviors of suspended Brownian rod-like particles within fluid flow systems. A kinetic macro-model based on the Fokker-Planck equation is developed to unravel the coupling between rod concentration and orientation. This model serves as a foundational framework for understanding the complex dynamics of the system. Subsequently, the investigation is extended to encompass active Brownian particles, where the developed kinetic macro-model is adapted to address the distinctive characteristics of these self-propelled entities. The research commences by elucidating the coupling between rod concentration and orientation within the context of fluid flows. Numerical simulations across diverse flow configurations uncover the profound impact of rod presence on flow characteristics, resulting in concentration gradients and altered migration patterns. Furthermore, the role of translational diffusion is established as pivotal in influencing migration behavior and alignment with flow direction. Building upon this foundation, the investigation transitions to active Brownian particles is inspired by natural motile systems. The kinetic macro-model is extended and adapted to encapsulate the unique dynamics of these active particles. The resulting insights shed light on the distinctive behaviors arising from self-propulsion, offering a deeper understanding of the interplay between activity, orientation, and fluid flow. Through the development and extension of this model, the study unveils the complexities underlying these systems.

### 0.1.3 Organisation of the report

This manuscript is built according to several chapters, the bibliographic study and the numerical models. Chapter 1 is a state of art for the suspension of passive and active particles. It describes the types of anisometric particles and their dynamics. Then the mathematical models of the suspension and the rheology of anisometric particles with numerical solutions are presented. After that, it shows the experimental studies on the rheology and cross-stream migrations. A summary of the numerical work is presented in Chapter 2 to allow a better structuring of the scientific work produced around the numerical modeling of Brownian rod suspensions. This chapter is a published article in the Journal of Physical Review Fluids [20]. It derivates a new kinetic macro-model based on the moments of the probability distribution function to study the flow of rodlike Brownian particle suspensions. This model is verified by comparing the results with the solution of the associated Fokker-Planck equation. In Chapter 3, this model is used to study the rheological behavior of Brownian rod suspensions in flow systems. This chapter is an article that will be submitted to the Journal of Physical Review Rheology. Chapter 4 explores the dynamics of active particles in complex flow systems, focusing on the active particles accumulation induced by anisotropic translational diffusion. The study is done by solving the Fokker-Planck equation for the active particles. Chapter 5 discusses the effect of active particles on the rheology of the flow systems. Finally, the thesis is finished with a general conclusion and some perspectives for future work.

CHAPTER 1

# STATE OF ART

## 1.1 Brief historical overview

The study of non-Brownian particle suspensions also has a long history, dating back to the early 20th century. One of the earliest studies was carried out by Hagen and Poiseuille in 1837, they developed the law that describes laminar flow of Newtonian fluids through a cylindrical pipe. Einstein, building on the work of Reynolds, developed a theoretical framework for the study of small particle suspensions, known as the Einstein equation [21]. This equation relates the diffusion coefficient of the particles to the size and volume fraction of the particles and the viscosity of the fluid. When particles are suspended, the properties of non-spherical, axisymmetric particles such as ellipsoids or rods become more difficult to study. Jeffery developed an equation for the viscosity of infinitely dilute suspensions using Einstein's hydrodynamic method [22]. This equation provides an analytical solution for the orientation dynamics of these particles in shear flows. The Jeffery's equation takes into account the effects of both rotational and translational motions of the particles, as well as the effects of deformation rate and particle geometry. Mason and co-workers [23, 24] conducted pioneering work in studying the behavior of single particles in dilute suspensions. Their studies were aimed at validating Jeffery's equation, which describes the orientation dynamics of non-spherical particles in shear flows. They analyzed the motion of single particles in diluted suspensions in detail, using a combination of experimental techniques and theoretical models. They were able to show that the motion of the particles in shear flow was consistent with Jeffery's equation, thereby validating the equation for use in predicting the behavior of suspensions of non-spherical particles. A particle sample can cause interaction between these particles and affect the motion. Several studies have explored the orientation and behavior of particle suspensions in different flow conditions and geometries. For example, Batchelor and Green [25] studied the orientation of particles in simple shear flow. Dinh and Armstrong [26] investigated the rheology of suspensions of rigid particles, in semi-concentrated regimes. They derived a constitutive equation for the total stress in the suspension as a function of the particle concentration, aspect ratio, and orientation distribution function. They also showed that the effect of particle-particle interactions becomes significant as the concentration of particles increases, and that the constitutive equation is sensitive to the form of the interaction potential. Folgar and Tucker [27] investigated the behavior of particle suspensions in semi-dilute and concentrated regimes. They demonstrated that the critical volume fraction, above which the particles begin to interact and align with each other, decreases as the aspect ratio of the particles increases. To deal with a particle population instead of a single particle, the orientation distribution function is introduced and it is calculated by solving the Fokker-Planck equation. Advani and Tucker [28] introduced the concept of orientation tensors to describe the average particle orientation. The orientation tensors are mathematical quantities that capture information about the orientation of a population of particles in a suspension. These tensors can be used to calculate various rheological properties, such as viscosity and elasticity, and are also used in computational models to predict the behavior of particle suspensions under different conditions. The orientation tensors provide a way to describe the complex orientation of particles in a suspension, which can be difficult to visualize and understand using other methods.

## 1.2 Single particle

The analysis of the dynamics of suspending particles includes looking at factors like shape and size that have an impact on the orientation and distribution of their centers of mass within the fluid medium. Particle can be considered as a rigid and symmetric in Cartesian coordinates $(x_1, x_2, x_3)$, described as shown in Fig.1.1. A single particle's orientation can be characterized by a unit vector $\mathbf{p}$ oriented along its primary axis, or by the spherical coordinates $\theta$ and $\phi$. The relation between the Cartesian and the spherical components of the particle is

$$p_1 = sin\theta cos\phi, \qquad p_2 = sin\theta sin\phi, \qquad p_3 = cos\theta, \tag{1.1}$$

where $(p_1, p_2, p_3)$ are the Cartesian components of $\mathbf{p}$. It is noted that the particles are symmetric, so the "head" of the particle is identical to its "tail", this gives

$$\mathbf{p} \rightarrow -\mathbf{p}, \tag{1.2}$$

or equivalent to

$$\theta \rightarrow \pi - \theta \quad \text{and} \quad \phi \rightarrow \phi + \pi. \tag{1.3}$$

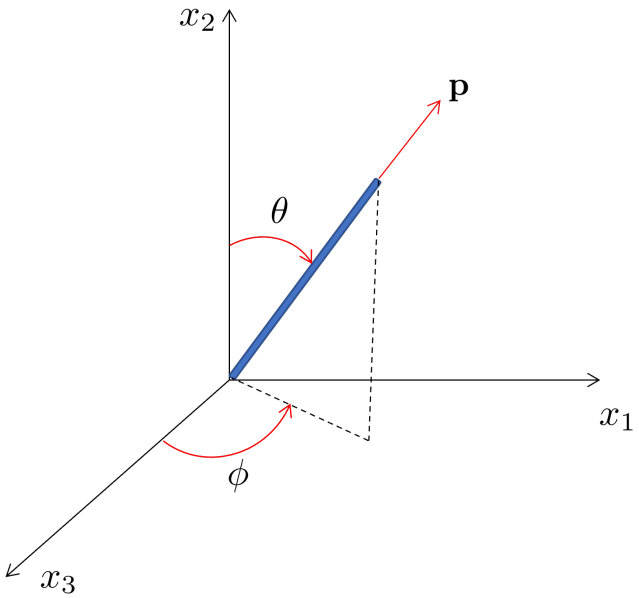

Figure 1.1 – Orientation of a single axisymmetric slender particle which is described by the two angles $\theta$ and $\phi$, or by a unit vector $\mathbf{p}$.

Particle is generally characterised with the shape factor $\lambda$, which is a scalar parameter related to the particle aspect ratio $a_r = L/d$, where $L$ is the particle's length and $d$ is the particle's diameter, such as

$$\lambda = \frac{a_r^2 - 1}{a_r^2 + 1}. \tag{1.4}$$

For spherical particles, $\lambda = 0$, while for slender particles $\lambda \to 1$, and for ellipsoidal particles $0 < \lambda < 1$.

Particle position in space is determined by a vector $\mathbf{r}_c$ where this vector defines the position of center of mass of the particle with respect to the center of the coordinates system (see Fig. 1.2), and translational velocity vector $\dot{\mathbf{r}}_c$ in the Cartesian system.

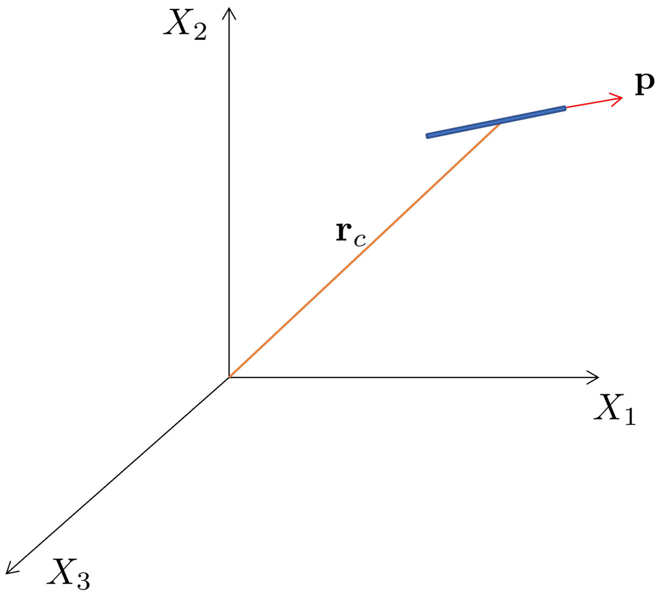

Figure 1.2 – Position presentation of single particle and particle orientation in a Cartesian system $(X_1, X_2, X_3)$.

## 1.3 Particle Sample

### 1.3.1 Particle Sample: Concentration regimes

The rheological behavior of a particle in a suspension depends on the amount of particles in the solution. This particle concentration can be represented by

- the volume fraction of the particles $\phi_f$ which is the ratio between the volume occupied by the particles and the volume of the suspension,
- or $n$ is the number of particles per unit volume.

For example, for cylindrical particles of length $L$ and diameter $d$, $\phi_f$ is written

$$\phi_f = n\pi\frac{Ld^2}{4}. \tag{1.5}$$

Particle concentration regimes are classified according to the volume fraction of solid particles in the fluid. Consider a sample of particles suspending in a flow. Depending on the particle volume fraction, suspension is called a dilute regime when the distance between the particles is significant so the particle can suspend freely without encountering other particles. This regime is defined by

$$\phi_f << 1/a_r^2 \text{ or } n << \frac{1}{L^3}. \tag{1.6}$$

When the distance between the particles is reduced, the semi-dilute regime is defined, for this case, $\phi_f$ and $n$ are written

$$1/a_r^2 << \phi_f << 1/a_r \text{ or } \frac{1}{L^3} << n << \frac{1}{L^2 d}. \tag{1.7}$$

Particle interactions take place, these interactions affect the orientation of each particle in the sample.

Finally, if the distance between two particles becomes of the order of $d$, the particles can no longer move without interacting with each other, which leads to intersections of particles between them [29]. In this case, the suspension is in the concentrated regime,

$$\phi_f >> 1/a_r \text{ or } n >> \frac{1}{L^2 d}. \tag{1.8}$$

Figure 1.3 illustrates the concentration regimes in the function of concentration $\phi_f$ and aspect ratio $a_r$. This graph makes it possible to locate the concentration regime of a suspension by knowing $\phi_f$ and $a_r$. For example, taking $a_r = 20$, the volume fraction must be less than 0.004 for a solution to be dilute and greater than 0.067 for it to be concentrated.

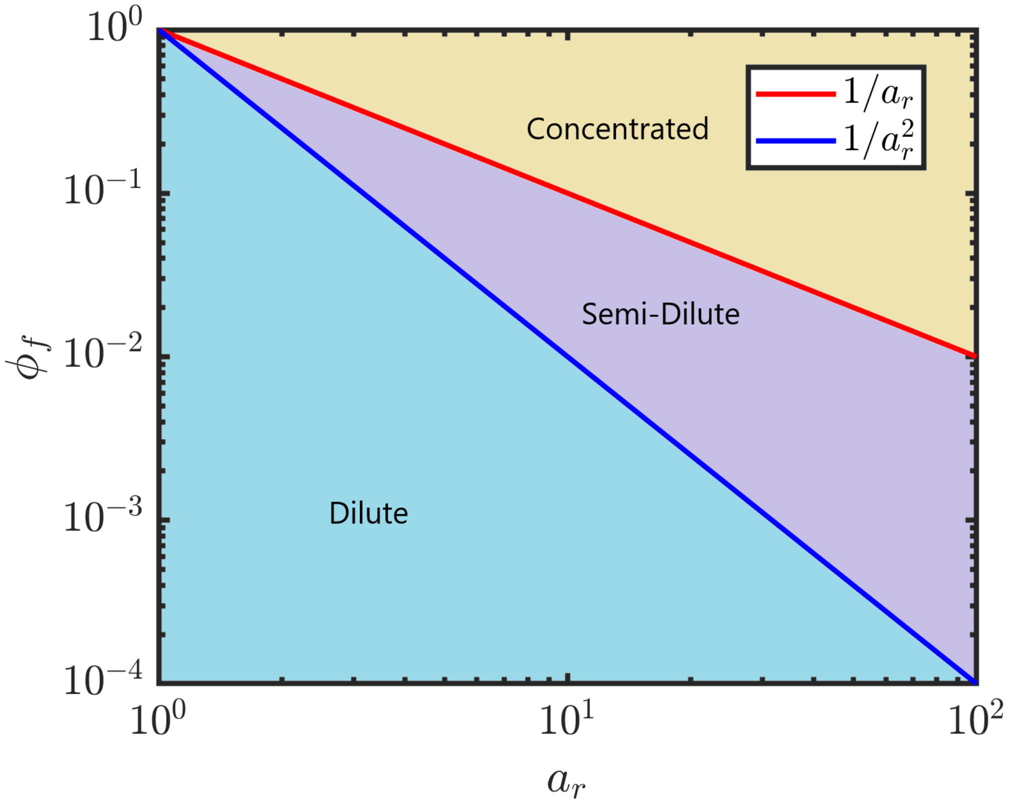

Figure 1.3 – Concentration regimes of volume fraction and aspect ratio [30].

### 1.3.2 Particle Sample: Distiribution function

In reality, the particles in a suspension will have different orientations and positions, and their distribution may not be homogeneous. Therefore, to study the behavior of a particle sample, it is necessary to consider the orientation and position of each particle in the suspension.

To describe the orientation state and specific location of monodispersed particles in the suspension, a probability distribution function is used, denoted by $\Psi(\mathbf{r}_c, \mathbf{p}, t)$. This function provides a broad description of the distribution of particles with a specific length and diameter in terms of their orientation and location. It is defined such that the number of particles with a center of mass vector $\mathbf{r}_c$ and orientation vectors $\mathbf{p}$, at time $t$ is equal to

$$\Psi(\mathbf{r}_c, \mathbf{p}, t) d\mathbf{r}_c d\mathbf{p}. \tag{1.9}$$

In homogeneous flows, where the flow properties do not vary with position, the distribution function $\Psi(\mathbf{r}_c, \mathbf{p}, t)$ can be factored as the product of two separate functions [26]

$$\Psi(\mathbf{r}_c, \mathbf{p}, t) = c(\mathbf{r}_c, t)\psi(\mathbf{p}, t), \tag{1.10}$$

where $c(\mathbf{r}_c, t)$ is the particle concentration function and represents the probability of finding a particle at a particular position at a given time [17]

$$c(\mathbf{r}_c, t) = \int_{\mathbf{p}} \Psi(\mathbf{r}_c, \mathbf{p}, t) d\mathbf{p}, \tag{1.11}$$

and $\psi(\mathbf{p})$ or $\psi(\theta, \phi)$, describes the orientation state of a set of particles. The probability of finding a particle lying in the range between $\theta_1$ and $\theta_1 + d\theta_1$, and between $\phi_1$ and $\phi_1 + d\phi_1$ is

$$P(\theta_1 \leq \theta \leq \theta_1 + d\theta_1,\ \ \phi_1 \leq \phi \leq \phi_1 + d\phi_1) = \psi(\theta_1, \phi_1) sin\theta_1 d\theta d\phi. \tag{1.12}$$

Due to normalization conditions, the integral of this function over oriented space must equal unity

$$\int_{\phi=0}^{2\pi} \int_{\theta=0}^{\pi} \psi(\theta, \phi) sin\theta d\theta d\phi = \int_{\mathbf{p}} \psi(\mathbf{p}) d\mathbf{p} = 1. \tag{1.13}$$

For symmetric particles, $\psi(\mathbf{p}, t)$ must be periodic or, in other words, it must satisfy the following relation

$$\psi(\mathbf{p}) = \psi(-\mathbf{p}). \tag{1.14}$$

and

$$\psi(\theta, \phi) = \psi(\pi - \theta, \phi + \pi). \tag{1.15}$$

When particles are isotropic in 3D, $\psi = 1/(4\pi)$, when particles are planar $\psi = 1/(2\pi)$ over all the domain (see Fig. 1.4a), while when particles are aligned in the flow direction, $\Psi/c$ is a Dirac function (see Fig. 1.4b).

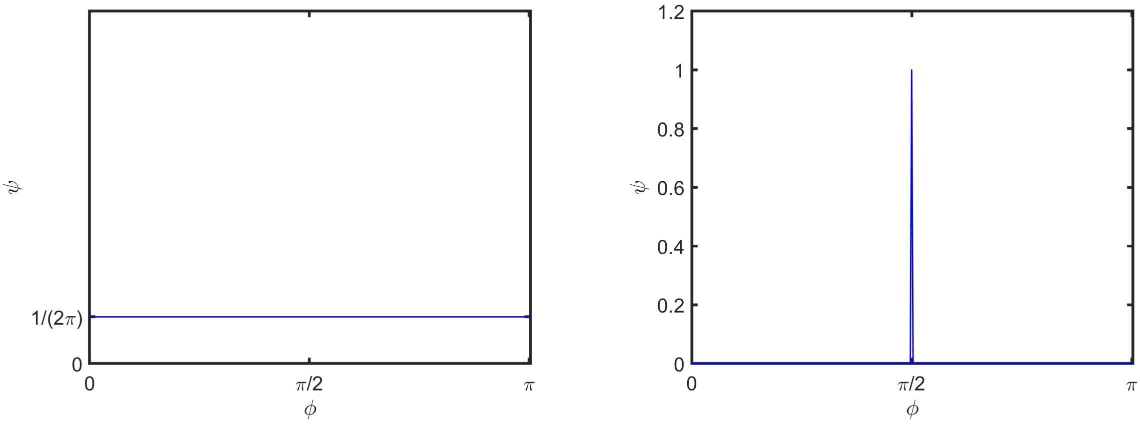

(a)

(b)

Figure 1.4 – Representation of $\psi$ with respect to $\phi$ for (a) random planar, (b) aligned particles in 2D orientation.

### 1.3.3 Particle Sample: Orientation tensors

Orientation tensors are used to represent the orientation state of particles in a more compact and convenient manner. They are mathematical objects that describe the statistical distribution of particle orientations within a given volume or region of space.

The definition of an orientation tensor depends on the order of the tensor. For example, the second-order tensor is often used to represent the orientation of particles in a suspension. It is defined as

$$\boldsymbol{a}_2 = \int_{\mathbf{p}} \mathbf{pp} d\mathbf{p} \psi(\mathbf{p}) = \int_{\phi=0}^{2\pi} \int_{\theta=0}^{\pi} \mathbf{pp} \psi(\theta, \phi) sin\theta d\theta d\phi \tag{1.16}$$

Similarly, the fourth-order orientation tensor can be defined as

$$\boldsymbol{a}_4 = \int_{\mathbf{p}} \mathbf{pppp} d\mathbf{p} \psi(\mathbf{p}) = \int_{\phi=0}^{2\pi} \int_{\theta=0}^{\pi} \mathbf{pppp} \psi(\theta, \phi) sin\theta d\theta d\phi \tag{1.17}$$

If the distribution function $\psi$ is even for axisymmetric particles (i.e., $\mathbf{p} = -\mathbf{p}$ ), then all odd-order tensors will be zero. This is because odd-order tensors describe asymmetry in the distribution of particles, which is not present in an axisymmetric distribution. Symmetric properties are expressed as

$$a_{ij} = a_{ji}, \tag{1.18}$$

$$a_{ijkl} = a_{jikl} = a_{kijl} = a_{lijk} \cdots \tag{1.19}$$

Normalization properties are expressed as

$$\sum a_{ii} = 1, \tag{1.20}$$

$$\sum a_{ijkk} = a_{ij}. \tag{1.21}$$

Due to symmetry and normalization conditions (Eqs. 1.18-1.21), the second-order orientation tensor has only 5 independent components, while the fourth-order orientation tensor has 15 independent components.

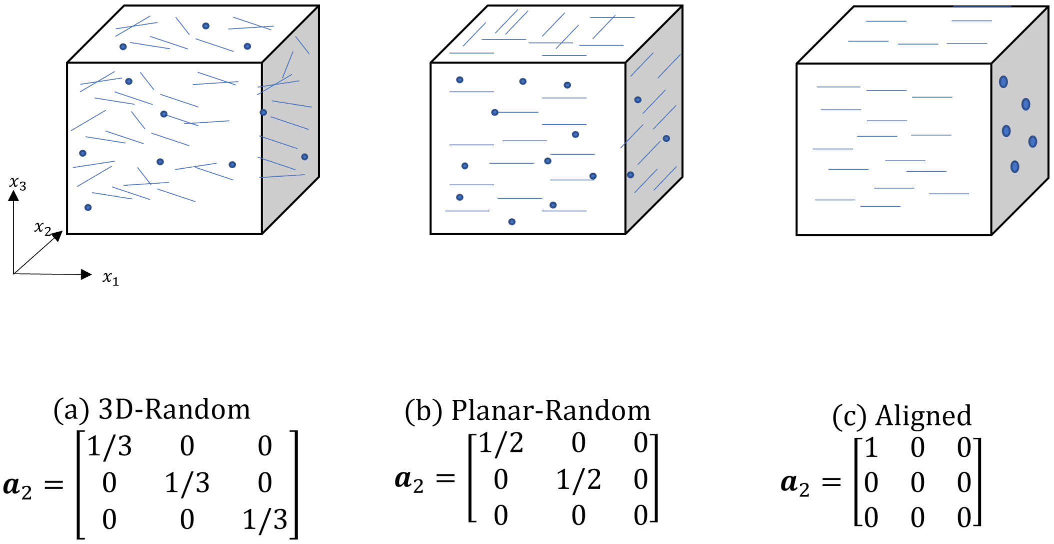

(a) 3D-Random

$$\boldsymbol{a}_2 = \begin{bmatrix} 1/3 & 0 & 0 \\ 0 & 1/3 & 0 \\ 0 & 0 & 1/3 \end{bmatrix}$$

(b) Planar-Random

$$\boldsymbol{a}_2 = \begin{bmatrix} 1/2 & 0 & 0 \\ 0 & 1/2 & 0 \\ 0 & 0 & 0 \end{bmatrix}$$

(c) Aligned

$$\boldsymbol{a}_2 = \begin{bmatrix} 1 & 0 & 0 \\ 0 & 0 & 0 \\ 0 & 0 & 0 \end{bmatrix}$$

Figure 1.5 – Representation of the particle orientation with the related orientation tensor $\boldsymbol{a}_2$ in a representative elementary volume [31].

The components of the orientation tensor ($a_{ij}$) have a physical explanation. The diagonal terms $a_{ii}$ represents the degree of alignment of particles along the $x_i$ direction, the larger the value of $a_{ii}$, the more aligned the particles are in the corresponding direction. The off-diagonal components $a_{ij}$ ($i \neq j$) represent the correlation between the orientation of particles along different principal axes. Fig. 1.5a shows an isotropic orientation distribution, with $\boldsymbol{a}_2$ a diagonal matrix of $a_{ii} = \frac{1}{3}$. If all particles lie in the $x_1x_2$ plane (Fig. 1.5b), then $\boldsymbol{a}_2$ is a diagonal of $a_{11} = a_{22} = \frac{1}{2}$ related to Fig. 1.4a while $a_{33} = 0$. If the particles are perfectly aligned in the direction of $x_1$ (Fig. 1.5c) related to Fig. 1.4b, then $a_{11} = 1$ and $a_{22} = a_{33} = 0$.

## 1.4 Suspension of anisometric particles

### 1.4.1 Single particle

The translation motion is due to the fluid forces acting on the particle, which can be described by the drag force. In a fluid flow, the drag force acting on the particle will cause it to move with the fluid. The orientation motion of the particle is due to the torque resulting from the velocity gradient of the flow. The velocity gradient induces a difference in the fluid flow on different parts of the particle, resulting in a net torque that tends to align the particle with the flow direction. The value of this torque is dependent to the particle's aspect ratio and the orientation of the particle, it will change with time as the particle rotates and aligns with the flow. Both translation and orientation motion are important in understanding the behavior of particle suspensions in fluid flows. The translation motion establishes the overall motion and transport of the particles, while the orientation motion determines the alignment and structure of the particles in the flow.

For a motion of particle in a moving fluid given by the velocity vector $\mathbf{u}$, the classical analysis by Jeffery [22] treats a single, rigid particle in an infinite body of Newtonian fluid. The unperturbed fluid velocity is assumed to be a linear function of position, inertia and body forces are assumed to be negligible. The solution from Jeffery indicates that at that point, the centroid of the particle translates with the unperturbed fluid velocity. His solution for the time derivation of centroid position vector $\mathbf{r}_c$ is

$$\dot{\mathbf{r}}_c = \mathbf{u}, \tag{1.22}$$

while the rotational motion of the particle, written as an expression for the time derivative of the orientation vector $\mathbf{p}$ is

$$\dot{\mathbf{p}}_j = -\frac{1}{2}\boldsymbol{\omega} \cdot \mathbf{p} + \frac{1}{2}\lambda(\dot{\boldsymbol{\gamma}} \cdot \mathbf{p} - \dot{\boldsymbol{\gamma}} : \mathbf{ppp}), \tag{1.23}$$

where $\boldsymbol{\omega}$ and $\dot{\boldsymbol{\gamma}}$ are the vorticity and the deformation rate tensors, respectively.

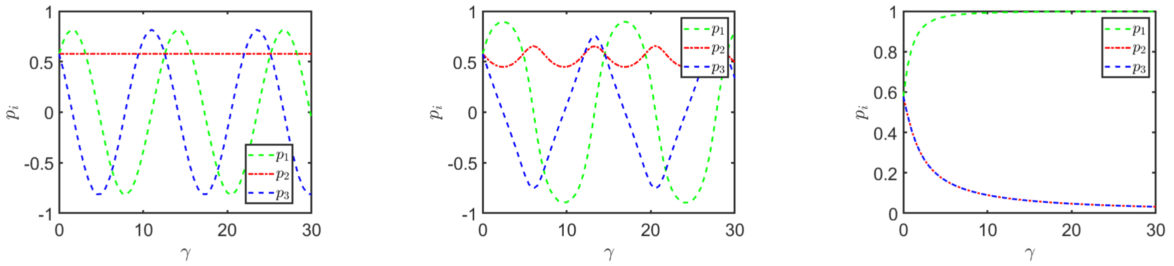

(a) Sphere particle $\lambda = 0$.

(b) Ellipsoidal particle $\lambda = 0.5$.

(c) Slender particle $\lambda = 1$.

Figure 1.6 – Particle orientation as a function of strain using Jeffery's equation for different values of $\lambda$ (a) $\lambda = 0$, (b) $\lambda = 0.5$ and (c) $\lambda = 1$ of initial value $\vec{p}_0 = (\frac{1}{\sqrt{3}}, \frac{1}{\sqrt{3}}, \frac{1}{\sqrt{3}})$. The particles are initially isotropic and subjected to a simple shear flow with $\dot{\gamma} = 1s^{-1}$.

Solving the equation of particle orientation as a function of the deformation $\gamma = \dot{\gamma}t$ in a simple shear flow with a flow direction parallel to $x_1$, and velocity gradient parallel to $x_3$ for different values of $\lambda$ gives the results in Fig. 1.6, which shows that for a spherical particle (see Fig. 1.6a) the values of $p_1$ and $p_3$ is changing periodically with deformation while $p_2$ is constant. The spherical particle goes constant rotation around $x_3$ axis. Ellipsoidal particle (see Fig. 1.6b) undergoes a periodic rotation in the $x_3$ direction but different amplitudes, $p_3$ has the lowest amplitude, while $p_1$ has the highest amplitude and, $p_1$ and $p_2$ has approximately the same period. For a slender particle (see Fig. 1.6c) $p_1$ increased to 1 and, $p_2$ and $p_3$ decreased to 0 meaning that the particle aligns in the direction of $x_1$, the direction of the flow.

Fig. 1.7 provides an explanation for these results in 2D. For slender particle when the particle is aligned vertical the torque "$T_{11}$"(see Fig.1.7) will cause the particle to rotate rapidly, and as time passes and the particle rotates, the torque magnitude will decrease due to the cross-section affected by the fluid flow is becoming smaller "$T_{11} > T_{12} > T_{13} > T_{14}$", when the particle aligns with the flow, the torque $T_{14}$ is negligible because the width of the slender particle $d$ is negligible, as a result the particle will stop rotating. For the ellipsoidal particle, the same concept "$T_{21} > T_{22} > T_{23} > T_{24}$" but the torque acting on a horizontally aligned particle will not be zero "$T_{24} \neq 0$" because the ellipsoidal width $d$ is not negligible, this gives continuous rotation of the particle with different rotating velocity. For spherical particle, $L = d$ this will keep the torque rotating the particle constant independent on the orientation of the particle "$T_{31} = T_{32} = T_{33} = T_{34}$", which will cause constant rotation in both directions $x_1$ and $x_2$.

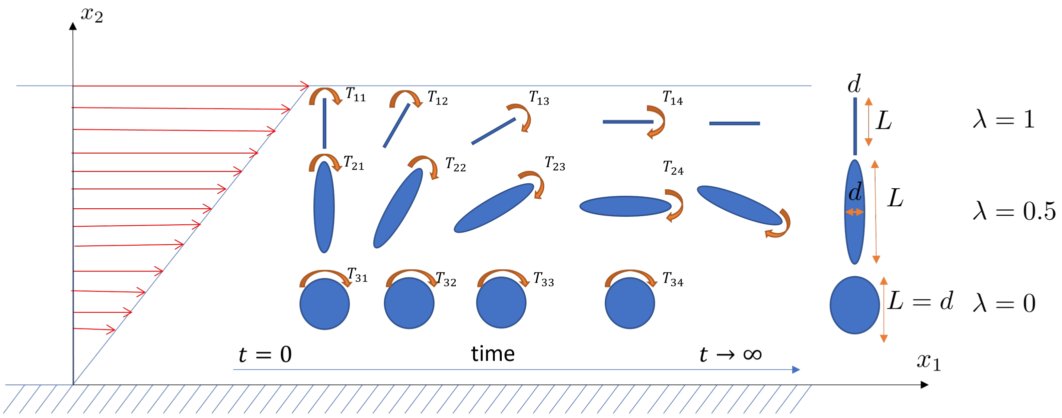

Figure 1.7 – Schemes representing how particle orients in a simple shear flow for different values of $\lambda$.

### 1.4.2 Particle interactions

Folgar and Tucker [27] represented a general version of the particle orientation equation for three dimensional flow fields, based on Jeffery's equation, which describes the complete orientation of the particles in a semi-concentrated regime, where particle-particle interaction occurs. The rotary diffusion $D_r = C_I\dot{\gamma}$ is introduced, where $C_I$ is the interaction coefficient, $\dot{\gamma}$ is the generalized shear rate defined as $\dot{\gamma} = \sqrt{\frac{1}{2}\dot{\boldsymbol{\gamma}} : \dot{\boldsymbol{\gamma}}}$.

$$\dot{\mathbf{p}} = -\frac{1}{2}\boldsymbol{\omega}\cdot\mathbf{p} + \frac{1}{2}\lambda(\dot{\boldsymbol{\gamma}}\cdot\mathbf{p} - \dot{\boldsymbol{\gamma}} : \mathbf{ppp}) + C_I\dot{\gamma}\nabla_{\mathbf{p}}log(\Psi) \tag{1.24}$$

Depending on the particle concentration, there are many models of $C_I$. Bay [32] conducted significant experimental work and proposed the following fitting curve for $C_I$ as a function of $\phi_f L/D$:

$$C_I = 0.0184exp(-0.7148\frac{\phi_f L}{d}) \tag{1.25}$$

This research demonstrates the particle interaction's screening impact in concentrated suspensions. Ranganathan and Advani [33] presented the following theoretical model based on Doi-Edwards theory:

$$C_I = \frac{K}{a_c/L} \tag{1.26}$$

where $K$ is a proportionality constant and $a_c$ is the average interparticle spacing.The particle interaction in this model is influenced by the orientation states via $a_c$. Particularly, for particle suspension in a viscoelastic media, Ramazani et al. [34] modified the work of Ranganathan and Advani as follows:

$$C_I = \frac{K}{a_c/L}\frac{1}{(\boldsymbol{a} : \mathbf{c})^n} \tag{1.27}$$

where $n$ is a constant and $\mathbf{c}$ is the polymer conformation tensor. According to this theory, the particle interaction decreases as the polymers are stretched in the direction of the particle orientation. The work of Ramazani et al. [34] was also used by Park and Kwon [35] in developing a rheological model for a particle suspension in a viscoelastic media, and the coupling effect between particle and polymer in $C_I$ was found to be dominant only at the high shear rate regime.

Also there had been several anisotropic diffusivity models developed in the literature [36–38]. The anisotropic diffusivity model could fit the experimental data better than the isotropic model particularly for a long particle composite [38].

### 1.4.3 Fokker-Planck equation

A mathematical model known as the Fokker-Planck equation is used to explain how the probability distribution of particles in a system varies over time, offering important insights into their collective behavior. The time evolution of the probability distribution function $\psi(p)$ (Fokker-Planck Equation) is

$$\frac{\partial \psi}{\partial t} = -\nabla_{\mathbf{p}} \cdot (\psi \dot{\mathbf{p}}_j) + C_I \dot{\gamma} \nabla^2_{\mathbf{p}} \psi. \tag{1.28}$$

The particle orientation distribution function $\psi$ is a convected quantity because it moves with the bulk motion of the fluid due to the advection of the particles. However, the evolution of $\psi$ is also affected by the particle-particle interactions and the fluid flow field, which can cause changes in the particle orientation distribution. The convective term in the transport equation for $\psi$ represents the advection of $\psi$ due to the fluid flow (the first term of the right-hand side of Eq. 1.28), while the diffusive term represents the rotary diffusion of the particles and their interactions with neighboring particles in the suspension (the second term of the right-hand side of Eq. 1.28). The balance between advection and diffusion of particles in the suspension determines the evolution of the orientation distribution function.$\nabla^2_{\mathbf{p}}$ represents the Laplacian operator in the configurational space.

Distribution function calculation (DFC) is the process of solving the orientation states using the probability distribution function $\psi$. Although numerical approaches may be used to calculate DFC necessitates high computing effort. Thus one needs a more compact and efficient description of the orientation state to be used. For this case, orientation tensors were derived.

The Fokker-Planck equation of evolution of $\psi(\mathbf{r}_c, \mathbf{p}, t)$ is

$$\frac{\partial \psi}{\partial t} + \mathbf{u} \cdot \nabla_{\mathbf{x}}(\psi) = -\nabla_{\mathbf{p}} \cdot (\psi \dot{\mathbf{p}}_j) + C_I \dot{\gamma} \nabla_{\mathbf{p}} log(\psi). \tag{1.29}$$

Fig. 1.8 shows the influence of the parameter $C_I$ on the orientation distribution function calculated from Eq. 1.28, in the stationary case. It is observed that

- as long as the interaction coefficient is non-zero, the particles are not perfectly aligned in the direction of flow,
- an exacerbation of the value of the interaction coefficient has the effect of flaring the probability distribution function $\psi$. In other words, an increase in the $C_I$ coefficient has the effect of increasing the average misalignment of the particles.

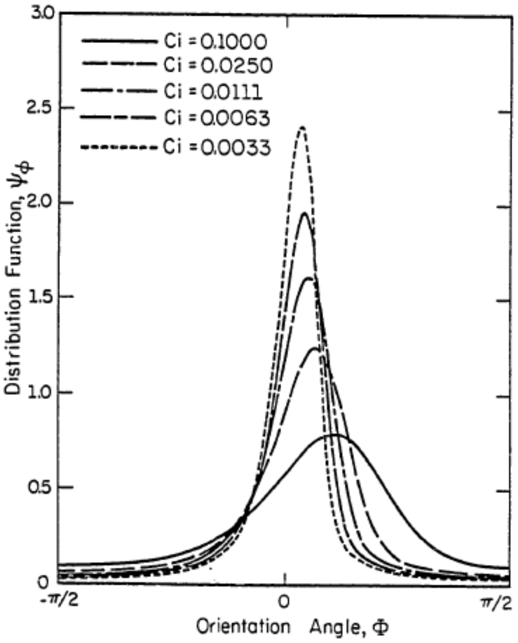

Figure 1.8 – Influence of $C_I$ parameter on the distribution function of orientation ($\psi$) or ($\psi_\phi$), as a function of the orientation angle $\phi$ in a shear flow ($\dot{\gamma} = 1/s$) [27].

To conclude, the flow tends to orient the particles in a certain direction, while the diffusion via $C_I$ tends to bring the particles back to an isotropic distribution. The orientation distribution reaches a steady-state resulting from these two conflicting influences. Moreover, the addition of a coefficient of diffusion makes it possible to account for the irreversible character of the orientation in shear flow for example, in agreement with experimental observations.

### 1.4.4 Orientation tensor: Closure approximations

The second-order tensor evolution is determined from the single particle evolution equation described by Jeffery [22], which is correct only for dilute regimes. In a filled system, the particles will interact with each other during a flow and thus modify the evolution of the orientation tensor.

$$\frac{D\boldsymbol{a}_2}{Dt} + \frac{1}{2}(\boldsymbol{\omega} \cdot \boldsymbol{a}_2 - \boldsymbol{a}_2 \cdot \boldsymbol{\omega}) = \frac{1}{2}\lambda(\dot{\boldsymbol{\gamma}} \cdot \boldsymbol{a}_2 + \boldsymbol{a}_2 \cdot \dot{\boldsymbol{\gamma}} - 2\dot{\boldsymbol{\gamma}} : \boldsymbol{a}_4) + 2D_r(\boldsymbol{\delta} - 3\boldsymbol{a}_2). \tag{1.30}$$

Eq. 1.30 for the evolution of tensor of order 2 involves the orientation tensor of order 4. Generally speaking, the resolution of the evolution equation of order $2k$ requires knowledge of the tensor of order $2k+2$. To get a solution, we focus on finding a relation between $\boldsymbol{a}_2$ and $\boldsymbol{a}_4$. To get around this difficulty, a closure approximation is introduced to allow for example to calculate the tensor of order four as a function of the tensor of order two.

— Linear closure

Hand [39] is one of the pioneers to propose a so-called linear closure equation. This closure approximation is exact for a population of randomly oriented particles. However, for other types of flow, it can sometimes provide non-physical results. The linear closure approximation suggested by Hand [39] is a linear combination of the tensor of order two and identity tensor. It is written

$$a_{ijkl} = c_1(\delta_{ij}\delta_{kl}+\delta_{ik}\delta_{jl}+\delta_{il}\delta_{jk})+c_2(a_{ij}\delta_{kl}+a_{ik}\delta_{jl}+a_{il}\delta_{jk}+a_{kl}\delta_{ij}+a_{jl}\delta_{ik}+a_{jk}\delta_{il}). \tag{1.31}$$

$c_1$ and $c_2$ are in case of 3D

$$c_1 = \frac{-1}{35} \qquad \text{and} \qquad c_2 = \frac{1}{7}, \tag{1.32}$$

while in case of 2D

$$c_1 = \frac{-1}{24} \qquad \text{and} \qquad c_2 = \frac{1}{6}. \tag{1.33}$$

— Quadratic closure

For flows that orient particles in one direction, the use of the quadratic closure approximation is correct [40]. The latter is simple and is written as follows

$$a_{ijkl} = a_{ij}a_{kl}. \tag{1.34}$$

The quadratic closure approximation is widely used, but it does not respect all the symmetry conditions of the order tensor 4. Indeed, writing $a_{1122} = a_{11}a_{22}$ or $a_{1212} = a_{12}a_{12}$ gives very different results [41].

— Hybrid closure

To set up a closing equation with a wider range of validity, Hinch and Leal [42] sought an approximation for the doubly contracted product $\dot{\boldsymbol{\gamma}} : \boldsymbol{a}_4$, in the case of an isotropic distribution and a perfectly aligned orientation of the particles. Then, Advani and Tucker [28] developed a new so-called hybrid closure approximation, based on the idea of a simple mixing law. This approximation is used in many numerical simulations. Writing this approximation combines two approximations described above (linear and quadratic closures) which results in 3D

$$a_{ijkl} = f(a_{ij}a_{kl}) + (1-f)[-\frac{1}{35}(\delta_{ij}\delta_{kl} + \delta_{ik}\delta_{jl} + \delta_{il}\delta_{jk}) \\ + \frac{1}{7}(a_{ij}\delta_{kl} + a_{ik}\delta_{jl} + a_{il}\delta_{jk} + \delta_{ij}a_{kl} + \delta_{ik}a_{jl} + \delta_{il}a_{jk})], \quad (1.35)$$

where

$$f = 1 - 27det(\boldsymbol{a}_2). \quad (1.36)$$

The hybrid closure performance is good in the equations of change for planar orientation, while in the three-dimensional version it is poor.

— IBOF closure

Other more advanced closure approximations exist, for example, the natural approximation (NAT) suggested by Verleye and Dupret [43] and the orthotropic closure approximations proposed by Cintra and Tucker [44]. Both seek a precise approximation by fitting particular solutions for the distribution function $\Psi$. The natural exhibits good transient behavior, but slightly overestimates the equilibrium state of orientation concerning the exact solution of the probability of orientation distribution. However, peculiarities exist when applying the native approximation [45]. To circumvent these difficulties, Chung and Kwon [46] developed a closure approximation based on the adjustment of the invariants of the 2-order orientation tensor, called Invariant-Based Optimal Fitting (IBOF). This approximation improves the precision of the natural approximation by addressing the singularity problems. The IBOF approximation is written as follows

$$\begin{aligned} a_{ijkl} =& \beta_1 S(\delta_{ij}\delta_{ij}) + \beta_2 S(\delta_{ij}a_{kl}) + \beta_3 S(a_{ij}a_{kl}) + \\ & \beta_4 S(\delta_{ij}a_{km}a_{ml}) + \beta_5 S(a_{ij}a_{km}a_{ml}) + \beta_6 S(a_{im}a_{mj}a_{kn}a_{nl}). \end{aligned} \quad (1.37)$$

$S$ is an operator which transforms a tensor of order four into a symmetric tensor satisfying the complete conditions of symmetry. The six coefficients, $\beta_i$, are represented by polynomial expansions as a function of the second and third invariants of the two-order orientation tensor, similar to the natural closure approximation. The unknown parameters in the polynomial expansions are determined by following the method introduced by the orthotropic closure approximation, which is a least squares-optimized adjustment technique of various flow data generated from solutions of the probability of the distribution function.

Figure 1.9 shows a comparison between the quadratic, linear, hybrid and IBOF closures with the distribution function calculation (DFC) solution of $\psi$ for $D_r = 0.01/s$ in a simple shear flow ($\dot{\gamma} = 1/s$).

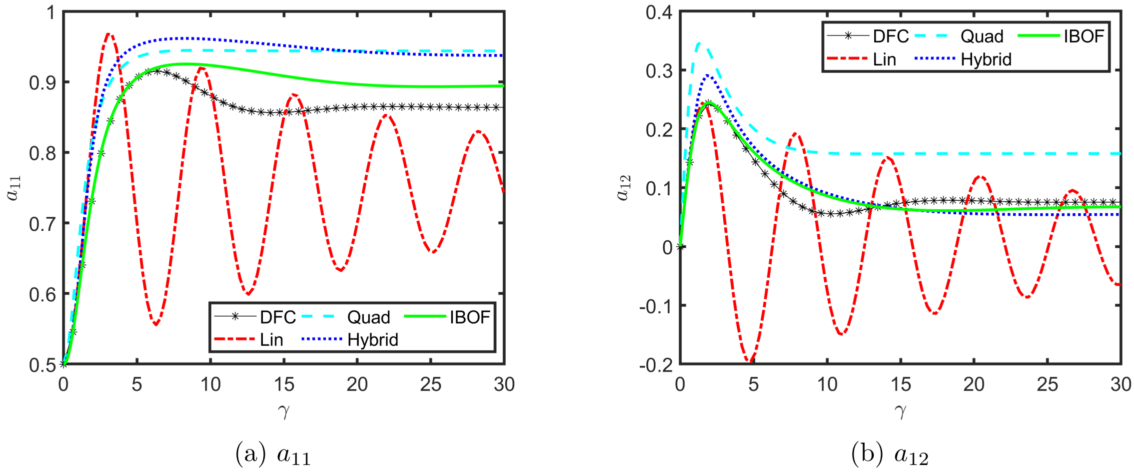

(a) $a_{11}$ (b) $a_{12}$

Figure 1.9 – Comparing orientation tensor components for different closures with the DFC solution for $D_r = 0.01$ for initially random planar particles ($\dot{\gamma} = 1/s$).

## 1.5 Brownian motion

Brownian particles are small particles suspended in a fluid medium, these particles are often on the nanoscale or microscale and can consist of various materials, such as colloids, nanoparticles or biological molecules. Due to the random collisions between the particles and the fluid molecules, these particles exhibit continuous, erratic motion known as Brownian motion. Brownian motion is a physical phenomenon discovered by the Scottish botanist Robert Brown in 1827 [47]. Brown observed that small particles suspended in a fluid undergo a random motion, which he attributed to the motion of the fluid molecules. The random motion observed in Brownian motion is a consequence of the diffusion phenomenon [48]. However, it was not until the work of Einstein in 1905 that the theory of Brownian motion was fully explained [21]. Einstein's theoretical work showed that the motion of the particles was a result of the random collisions with the fluid molecules. He derived an expression for the mean squared displacement of a Brownian particle, which is now known as the Einstein-Smoluchowski equation. This equation relates the diffusion coefficient of the particle to its size, shape, and viscosity of the fluid.

The study of Brownian motion has since become a fundamental topic in statistical physics and has led to important insights into the behavior of materials at the nanoscale.

The mathematical description of Brownian motion is based on the theory of stochastic processes. In particular, Brownian motion is modeled as a continuous-time random walk, where the position of the particle at any given time is a random variable. The statistical properties of Brownian motion can be described by the Wiener process, which is a continuous-time stochastic process that has independent and identically distributed Gaussian increments. The Wiener process is a mathematical model for the random walk of a particle undergoing Brownian motion, and is named after Norbert Wiener, who first introduced the process in his paper "Differential Space" [49].

Brownian motion can be mathematically described using stochastic differential equations known as Langevin equations. The Langevin equation for a particle in one dimension is given by

$$m\frac{d^2x}{dt^2} = -\gamma_f \frac{dx}{dt} + F(t), \tag{1.38}$$

where $m$ is the mass of the particle, $\gamma_f$ is the friction coefficient, $F(t)$ is the random force due to collisions with the surrounding fluid molecules, and $x$ is the position of the particle.

The random force $F(t)$ is modeled as a Gaussian white noise process, which has the properties

$$\langle F(t) \rangle = 0, \tag{1.39}$$

$$\langle F(t)F(t') \rangle = 2D\delta(t - t'). \tag{1.40}$$

$\langle \cdot \rangle$ denotes the ensemble average, $D$ is the diffusion coefficient, and $\delta(t)$ is the Dirac delta function.

### 1.5.1 Suspension of Brownian particles

Particles fluctuate because of a large number of collisions with fluid molecules [50]. Hydrodynamic forces compete with thermal and interparticle interactions to set the structure and dictate attributes when an external driving force, such as shear, is applied. Brownian motion plays a role in determining particle orientation, and one would expect that as the suspension becomes more dilute, this effect will become more important than particle-particle interactions. The case of strong Brownian motion acting on axisymmetric particles has been treated in detail by Burgers [51]. Leal et al. [52] derived an expression for the equilibrium distribution of orbit constants when the effect of Brownian motion is everywhere suitably small, but dominant over inertial and particle-particle interaction effects. A rheological theory for a dilute suspension of Brownian, non-spherical, axisymmetric particles, such as rods and disks, was proposed by Brenner [53]. Based on this research, it was shown that non-spherical particles had anisotropic macroscopic transport characteristics due to their sensitivity to particle orientation. Gallily and Cohen [54] investigated the dynamic interaction of non-spherical particles' translation and Brownian rotation, demonstrating a strong connection between the translational and rotational movements for particles with large aspect ratios. Gentry et al. [55] determined the diffusion coefficients of chrysotile fibers by comparing the fractional penetration and size distribution of the test fibers before and after a diffusion battery.

The Brownian rotary diffusion is $D_r = \frac{k_B T}{R_w}$ [56], where $k_B$ is Boltzman constant, $T$ is the temperature, the resistance coefficient $R_w = \frac{\pi \eta L^3}{log(L/2d)}$, and $\eta$ is the viscosity. Brownian diffusion

also plays an important role in the particle translation velocity [57], where the translational diffusivity is $\mathbf{D}_t = D_{||}\mathbf{pp} + D_{\perp}(\boldsymbol{\delta} - \mathbf{pp})$. $D_{||}$ and $D_{\perp}$ are the translation diffusion coefficients parallel and perpendicular to the particle orientation, respectively. They are equal to $D_{||} = \frac{k_B T}{\zeta_{||}}$ and $D_{\perp} = \frac{k_B T}{\zeta_{\perp}}$, $\zeta_{||}$ is the friction coefficient in the parallel to the particle direction, $\zeta_{||} = \frac{2\pi\eta L}{log(L/d)}$ , while $\zeta_{\perp}$ is the friction coefficient in the perpendicular to the particle direction.
Therefore, the equation of translation of Brownian particles is [40]

$$\dot{\mathbf{r}}_c = \mathbf{u} - \mathbf{D}_t \cdot \nabla_{\mathbf{x}} log(\Psi), \tag{1.41}$$

while the equation of orientation is

$$\dot{\mathbf{p}} = -\frac{1}{2}\boldsymbol{\omega} \cdot \mathbf{p} + \frac{1}{2}\lambda(\dot{\gamma} \cdot \mathbf{p} - \dot{\boldsymbol{\gamma}} : \boldsymbol{ppp}) - D_r \nabla_{\mathbf{p}} log(\Psi), \tag{1.42}$$

where $\nabla_{\mathbf{x}}$ and $\nabla_{\mathbf{p}}$ are the gradient operators in the spatial and configurational spaces, respectively.

### 1.5.2 Fokker-Planck of Brownian particles

By accounting for both the hydrodynamic forces, and the stochastic effects of Brownian motion, the Fokker-Planck equation offers insights into the particles diffusion behavior. Knowing that the particle-particle interactions are negligable in the case of Brownian particles and based on the equations of motion of the Brownian particles (Eqs. 1.41 and 1.42), the FP equation for Brownian particles is

$$\frac{\partial \Psi}{\partial t} + \mathbf{u} \cdot \nabla_{\mathbf{x}}(\Psi) = \nabla_{\mathbf{x}} \cdot (\mathbf{D}_t \cdot \nabla_{\mathbf{x}}\Psi) - \nabla_{\mathbf{p}} \cdot (\Psi\dot{\mathbf{p}}_j) + D_r \nabla^2_{\mathbf{p}}(\Psi). \tag{1.43}$$

The term translational diffusion term $\nabla_{\mathbf{x}} \cdot (\mathbf{D}_t \cdot \nabla_{\mathbf{x}}\Psi)$ appears in the Fokker-Planck equation for Brownian particles.

### 1.5.3 Effect of Brownian rotary diffusion

To study the effect of Brownian motion on particle orientation, a simple test is done, on initially 2D planar oriented particles, initially oriented particles of $a_{11} = 0.6$ and $a_{12} = 0$, and initially perfectly aligned particles in the flow direction. Solving the equation of evolution of $\mathbf{a}_2$, using quadratic closure, for 50 seconds, where we have a simple shear flow for the first 25 seconds, and then we stop the flow for the next 25 seconds (in other words $\dot{\gamma} = 1/s$ for $0s \leq t \leq 25s$ then $\dot{\gamma} = 0/s$ for $25s \leq t \leq 50s$ ) for $C_I = 0.1$ for non-Brownian particles and $D_r = 0.1/s$ for Brownian particles. Then the behavior of the particles rotation is compared for both Brownian particles (Figs. 1.10a,1.11a, and 1.12a) and a non-Brownian particles (Figs. 1.10b, 1.12b, and 1.12b). We found that after stopping the flow, non-Brownain particles remain at their final orientation while Brownian particles returns to be 2D planar independent of the initial orientation. This gives evidence that Brownian diffusion plays an important role in particles orientation, even in the absence of the flow, in taking particles to the isotropic situation.

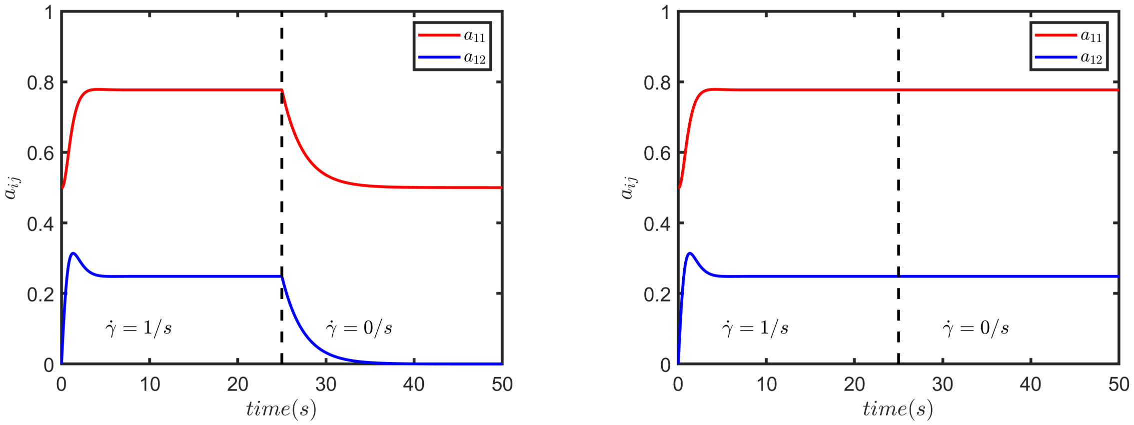

(a) Brownian particles. (b) Non-Brownian particles.

Figure 1.10 – Evolution of second-order orientation tensor components $a_{11}$ and $a_{12}$ as a function of time, for a particles initially 2D planar, in a simple shear flow ($\dot{\gamma} = 1/s$) and then stopping the flow ($\dot{\gamma} = 0/s$).

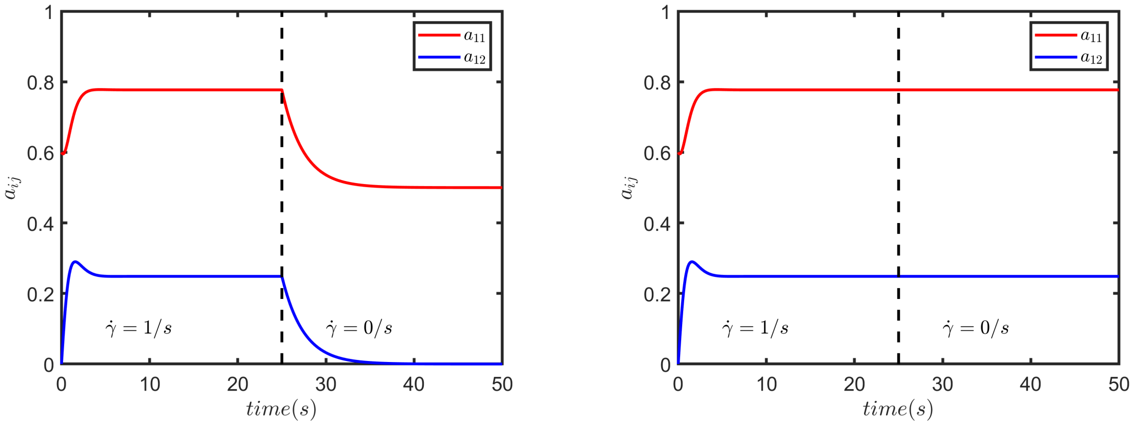

(a) Brownian particles. (b) Non-Brownian particles.

Figure 1.11 – Evolution of second-order orientation tensor components $a_{11}$ and $a_{12}$ as a function of time, for a particles initially oriented particles of $a_{11} = 0.6$ and $a_{12} = 0$, in a simple shear flow ($\dot{\gamma} = 1/s$) and then stopping the flow ($\dot{\gamma} = 0/s$).

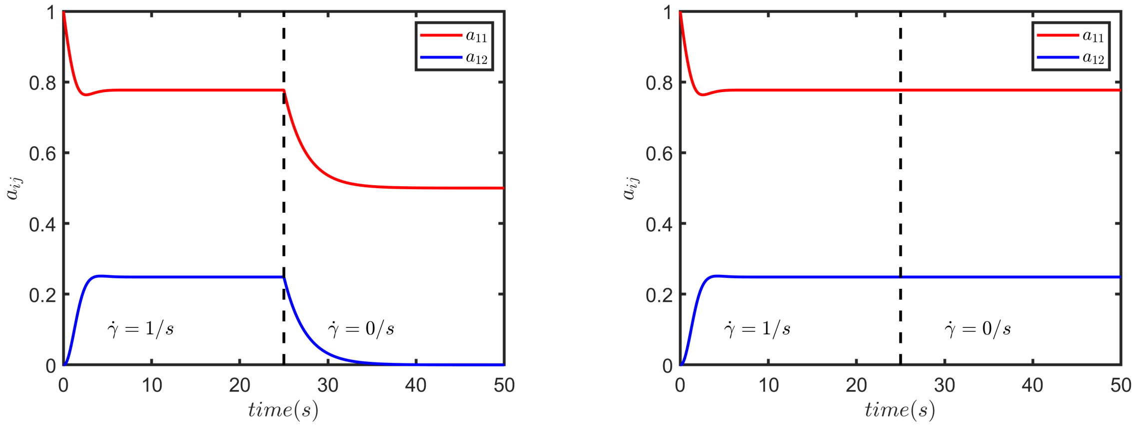

(a) Brownian particles.

(b) Non-Brownian particles.

Figure 1.12 – Evolution of second-order orientation tensor components $a_{11}$ and $a_{12}$ as a function of time, for a particles initially perfectly aligned in the flow direction, in a simple shear flow ($\dot{\gamma} = 1/s$) and then stopping the flow ($\dot{\gamma} = 0/s$).

## 1.6 Active particles

### 1.6.1 Single particle

Active particles are microscopic particles that possess self-propulsion mechanisms, allowing them to move autonomously within a fluid medium, with a particle swimming velocity $V_s$. Their motion is driven by internal energy sources, differentiating them from traditional Brownian particles that rely solely on thermal fluctuations. They generate a propulsive force, $F_p$ that is balanced by the drag force, $F_d$, from the surrounding fluid [17]. These particles are not fully symmetric in shape, the "head" of the particle can be differentiated form the "tail", so $\mathbf{p} \neq -\mathbf{p}$. This fundamental asymmetry, coupled with variations in propulsion mechanisms, categorizes active particles into "pushers" and "pullers" (see Fig. 1.13). Pusher particle exerts a thrust with its tail (such as B.subtilis and E. coli), while puller particle is a head-actuated particle (such as C. reinhardtii).

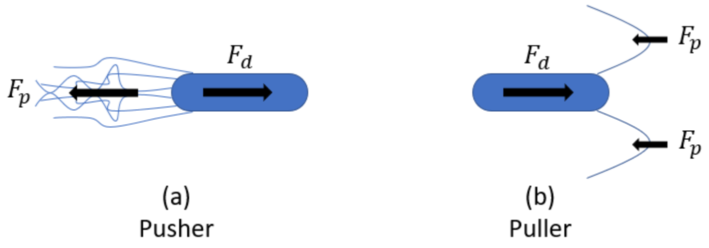

Figure 1.13 – Schematic diagrams of pusher and puller particles, of which E. coli and C. reinhardtii are paradigmatic examples [17].

### 1.6.2 Suspension of active particles

Several models have been proposed to describe the behavior of suspensions of active particles. One of the earliest and most widely used models is the Vicsek model (VM [58–63]) , introduced by Vicsek et al. in 1995 [64]. This model accounts for perturbations by adding a random angle to the average direction, which are thought to be a natural result of the numerous stochastic and deterministic factors influencing the motion of the flocking organisms. The units move with a fixed absolute velocity $V_s$ and take on the average direction of others within a specified distance in this self-propelled particle approach that resembles a cellular automaton. The equations of motion for the velocity ($\mathbf{v}_i$) and position ($\mathbf{x}_i$) of particle $i$ having neighbors labelled with $j$ are

$$\mathbf{v}_i(t+1) = V_s \frac{\langle \mathbf{v}_j(t) \rangle}{|\langle \mathbf{v}_j(t) \rangle|} + \text{ perturbation}, \tag{1.44}$$

$$\mathbf{x}_i(t+1) = \mathbf{x}_i(t) + \mathbf{v}_i(t+1). \tag{1.45}$$

It should be noted that the processes that such an alignment rule can account for can have very different origins (stickiness, hydrodynamics, pre-programmed, information processing, etc.). There are numerous ways to account for perturbations. The way they are represented in the standard version is by adding a random angle to the angle corresponding to the average direction of motion in the neighborhood of particle $i$. The angle of the direction of motion $\vartheta_i(t+1)$ at time $t+1$, is obtained from $\vartheta_i(t) = \arctan\left[\frac{\langle v_{j,x} \rangle}{\langle v_{j,y} \rangle}\right]$, as

$$\vartheta_i(t+1) = \vartheta_i(t) + \Delta_i(t), \tag{1.46}$$

where $v_{j,x}$ and $v_{j,y}$ are the $x$ and $y$ coordinates of the velocity of the $j$th particle in the neighborhood of particle $i$, and the perturbations are represented by $\Delta_i(t)$, which is a random number taken from a uniform distribution in the interval (i.e., the final direction of particle $i$ is obtained after rotating the average direction of the neighbors with a random angle). The normalized

average velocity is , $\varphi \equiv \frac{1}{Nv_0}\left|\sum_{i=1}^{N}\mathbf{v}_i\right|$, where $N$ is the number of particles.
A generic model of a self-propelled spherical particle with dynamics is described by the overdamped Langevin equations [65, 66]. Hydrodynamic models have also been developed previously [67–69].
The most general model is developed by Saintillan [70], which is based on Fokker-Planck equation and similar to the passive particles models. It can be shown that the translational equation of the active particles is

$$\dot{\mathbf{r}}_c = \mathbf{u} - \mathbf{D}_t \cdot \nabla_{\mathbf{x}}(log\Psi) + V_s\mathbf{p}, \tag{1.47}$$

while the orientation equation is

$$\dot{\mathbf{p}} = -\frac{1}{2}\omega \cdot \mathbf{p} + \frac{1}{2}\lambda(\dot{\gamma} \cdot \mathbf{p} - \dot{\boldsymbol{\gamma}} : \boldsymbol{ppp}) - D_r\nabla_{\mathbf{p}}log(\Psi). \tag{1.48}$$

In Eq. 1.47, the velocity of the particle's center of mass is expressed as the sum of its swimming velocity $V_s\mathbf{p}$, the local fluid velocity $\mathbf{u}$ induced on the particles in the suspension and the translational diffusion term. Eq. 1.48 shows that the swimming velocity does not have a direct effect on the evolution of particle orientation.

### 1.6.3 Fokker-Planck equation of active particles

Taking into consideration the particle velocity ($V_s$) and based on Eqs. 1.47 and 1.48 and the work of Saintillan [70], the FP equation of the active particles is

$$\frac{\partial\Psi}{\partial t} + \mathbf{u} \cdot \nabla_{\mathbf{x}}(\Psi) = -\nabla_{\mathbf{x}} \cdot (V_s\mathbf{p}\Psi) + \nabla_{\mathbf{x}} \cdot (\mathbf{D}_t \cdot \nabla_{\mathbf{x}}\Psi) - \nabla_{\mathbf{p}} \cdot (\Psi\dot{\mathbf{p}}_j) + D_r\nabla^2_{\mathbf{p}}(\Psi). \tag{1.49}$$

In the case of active particles, the particle velocity term $\nabla_{\mathbf{x}}\cdot(V_s\mathbf{p}\Psi)$ appears in the Fokker-Planck equation.

### 1.6.4 Issues for active systems

The mentioned closure approximations are based on certain assumptions that does not work with non-symmetric particles. When dealing with these particles, it is important to consider more advanced closure approximations or numerical techniques that can handle the complexities introduced by the active particles. Recently, closures have been used for computational models applied to active fluids [71–73]. Theillard and Saintillan [74] introduced a novel framework designed for the efficient simulation of active fluid dynamics within intricate two- and three-dimensional microfluidic geometries. They employ a continuum mean-field model that integrates partial differential equations. These equations govern the evolution of concentration, polarization, and nematic tensor fields. They implemented a level-set method coupled with an adaptive mesh refinement scheme utilizing Quad-/Octree grids. This combination enables the accurate representation of complex domain shapes while efficiently refining solutions near boundaries or areas of sharp gradients. The Bingham closure, introduced by Chaubal and Leal in the context of liquid crystal polymers [75], has been found to agree well with the underlying kinetic theory; yet the closure is non-trivial to compute, requiring the solution of an often nearly-singular nonlinear equation at every spatial discretization point at every timestep. Weady et al. [76] presented a robust, accurate, and efficient numerical scheme for evaluating the Bingham closure, with a controllable error/efficiency tradeoff. Conducting simulations at high resolution, Weady et al. [76] explored a coarse-grained continuum model applied to an active particle suspension within parameter regimes that lie beyond the reach of conventional kinetic theories. Examination of these simulations brought to light a notable insight: inaccuracies in closure computation can significantly constrain the achievable spatial resolution within the coarse-grained fields.

## 1.7 Stress tensor and flow problem

As a result of the particles motion, it is necessary to express the stress field.

### 1.7.1 Stress contribution: Non-Brownian particles

It is interesting to have the general constitutive equation, which represents the behavior of the material for different flows (shear, elongation or combination of both) and particular regimes (stationary, transient). The total stress generic form is

$$\boldsymbol{\Sigma} = -p\boldsymbol{\delta} + \boldsymbol{\Sigma}_m + \boldsymbol{\Sigma}_f, \tag{1.50}$$

where $-p\boldsymbol{\delta}$ is the hydrostatic part. $\boldsymbol{\Sigma}_m$ and $\boldsymbol{\Sigma}_f$ are the contribution of the fluid and the particles, respectively.

Batchelor [77] proposed a rheological constitutive law for rigid particles of ellipsoid shapes in a Newtonian fluid. He calculated the contribution of particles with the same orientation in the case of a dilute solution. Then Eq. 1.50 becomes

$$\boldsymbol{\Sigma} = -p\boldsymbol{\delta} + 2\eta\dot{\boldsymbol{\gamma}} + 2\eta N_p \boldsymbol{a}_4 : \dot{\boldsymbol{\gamma}}, \tag{1.51}$$

where $\eta$ is the viscosity and $N_p$ is the coupling coefficient which depends on the volume function of the particles $\phi_f$ and their aspect ratio $a_r$ such as

$$N_p = \frac{8\phi_f a_r^2}{3log(a_r)}. \tag{1.52}$$

Batchelor [78] extended his work from the case of a diluted regime to a case of a semi-diluted one. He models the stresses in elongational flow with particles aligned in the direction of fluid flow. The proposed relation for $N_p$ is

$$N_p = \frac{\phi_f a_r^2}{9[log(2a_r) - log(1 + 2a_r\sqrt{\phi_f/\pi}) - 1.5]}. \tag{1.53}$$

Dinh and Armstrong [26] took into account the hydrodynamic interactions by calculating the stress field at the surface of a particle of negligible diameter compared to its length. Their value of $N_p$ is

$$N_p = \frac{\phi_f a_r^2}{3log(2h_r/d)}, \tag{1.54}$$

where $h_r$ represents the characteristic distance between two neighboring particles. This distance then depends on the orientation of the particles and takes the value

- $h_r = d\sqrt{\pi/\phi_f}/2$ for aligned particles
- $h_r = \pi d/(2\phi_f a_r)/2$ for isotropic oriented particles

This value of $N_p$ has given rise to several approaches to have a better prediction of the flow of a suspension [79–81]. However, experimental works have been carried out to determine this parameter [80, 82, 83].

### 1.7.2 Stress contribution: Brownian particles

The contribution of Brownian motion to the stress in a fluid can be modelled by considering the momentum transfer between the Brownian particles and the fluid. The fluid experiences a force due to the random motion of the Brownian particles, which contributes to the stress in the fluid.

The total stress tensor $\Sigma_{ij}$ can be expressed as the sum of the Newtonian stress tensor $\Sigma_{ij}^N$ and the Brownian stress tensor $\Sigma_{ij}^B$ is

$$\Sigma = \Sigma_{ij}^N + \Sigma_{ij}^B. \tag{1.55}$$

The Newtonian stress tensor is given by [84]

$$\Sigma_{ij}^N = -p\delta_{ij} + \mu\left(\frac{\partial u_i}{\partial x_j} + \frac{\partial u_j}{\partial x_i}\right). \tag{1.56}$$

The Brownian stress tensor $\Sigma_{ij}^B$ can be written as

$$\Sigma_{ij}^B = \frac{1}{V}\sum_k^N F_k^i x_k^j. \tag{1.57}$$

where $N$ is the number of Brownian particles, $V$ is the volume of the fluid, $F_k^i$ is the $i$-component of the force on the $k$-th Brownian particle, and $x_k^j$ is the $j$-component of the position of the $k$-th Brownian particle.

According to Brenner [53], the stress generated by a group of Brownian particles depends on their orientation.

$$\mathbf{\Sigma}_f = 2\mu_0\dot{\boldsymbol{\gamma}} + \mu_1(\dot{\boldsymbol{\gamma}} : \boldsymbol{a}_2) + \mu_2\dot{\boldsymbol{\gamma}} : \boldsymbol{a}_4 + 2\mu_3(\boldsymbol{a}_2 \cdot \dot{\boldsymbol{\gamma}} + \dot{\boldsymbol{\gamma}} \cdot \boldsymbol{a}_2) + 2\mu_4 D_r(3\boldsymbol{a}_2 - \boldsymbol{\delta}), \tag{1.58}$$

where $\mu_i$ are five material coefficients that rely on the aspect ratio of the particles $a_r$ and their volume fraction. This equation allows for a more detailed description of the stress generated by Brownian particles, taking into account their orientation distribution.

Concentrated suspensions, according to Phan-Thien [85, 86] are made up of doublets of nearby particles. Their theoretical development results in a constitutive equation for particle stress is

$$\mathbf{\Sigma}_p = \eta(\phi)\left[(1-\xi)\dot{\gamma} : \boldsymbol{a}_4 + \dot{\gamma}\left(\mathbf{K}\cdot\boldsymbol{a}_2 + \boldsymbol{a}_2\cdot\mathbf{K} + \mathrm{tr}(\mathbf{K})\boldsymbol{a}_2 - 2\mathbf{K} : \boldsymbol{a}_4\right)\right]. \tag{1.59}$$

$\xi$ is a scalar value that depends on the separation distance of the sphere pairs. The authors left part of the definition of $\mathbf{K}$, a dimensionless tensor that represents a measure of anisotropy in particle self-diffusion, open. Phan-Thien et al. [37] propose a model for $\mathbf{K}$ is

$$\mathbf{K} = K_3\delta + (K_1 - K_3)\,\frac{2\boldsymbol{a}^{(1)}\cdot\boldsymbol{a}^{(1)}}{\mathrm{tr}\left(\boldsymbol{a}^{(1)}\cdot\boldsymbol{a}^{(1)}\right)} + (K_2 - K_1)\,\frac{\boldsymbol{a}^{(2)}\cdot\boldsymbol{a}^{(2)}}{\mathrm{tr}\left(\boldsymbol{a}^{(2)}\cdot\boldsymbol{a}^{(2)}\right)}, \tag{1.60}$$

where $\boldsymbol{a}^{(1)} = 2\dot{\boldsymbol{\gamma}}$ and $\boldsymbol{a}^{(2)} = \frac{\mathrm{D}}{\mathrm{D}t}\boldsymbol{a}^{(1)} + \nabla\mathbf{v}\cdot\boldsymbol{a}^{(1)} + \boldsymbol{a}^{(1)}\cdot(\nabla\mathbf{v})^T$ are the first two Rivlin-Ericksen tensors. $K_i, (i = 1, 2, 3)$, are constants that have certain restrictions for $\mathbf{K}$ to be positive semidefinite. Even so, different sets of $K_i$ greatly influence the computed normal stress differences, including their sign. The model has proven quite good, at least qualitatively ([37, 87]).

Mason and Weitz [88] used video microscopy to measure the orientation distribution function of Brownian particles in sheared suspensions. They discovered that the Brownian stress makes a significant contribution to the total stress, especially at low shear rates and high particle concentrations. Crocker and Grier [89] used dynamic light scattering to measure the diffusion coefficient of Brownian particles in sheared suspensions. It is shown that the diffusion coefficient is affected by the shear rate and the particle concentration, and they used their results to estimate the Brownian stress contribution to the suspension viscosity. Dhont and Briels [90] used computer simulations to investigate the Brownian stress in sheared suspensions of hard spheres. They found that the Brownian stress is sensitive to the particle size and the interparticle potential, and they showed that the stress can be decomposed into contributions from different length scales.

### 1.7.3 Stress contribution: Active particles

A microswimmer's form can be complicated, with flagella connected to a rigid body similar to bacteria. The drag force created by the rotating flagella is compensated by the drag force at the rigid body's surface, according to the motion's force-free and torque-free features. Then, depending on the orientation of the force dipoles concerning the swimming direction, a microswimmer at low Reynolds number can be considered as a dipole of forces in the far-field limit and dubbed a pusher or a puller [14] (see Fig. 1.14). A pusher generates a force dipole that points away from its swimming direction, while a puller generates a force dipole that points towards its swimming direction. Pusher particles move fluid towards their sides as they swim by creating a flow field away from their body along the swimming axis. However, pullers repel fluid along their sides while drawing it in along their swimming axis.

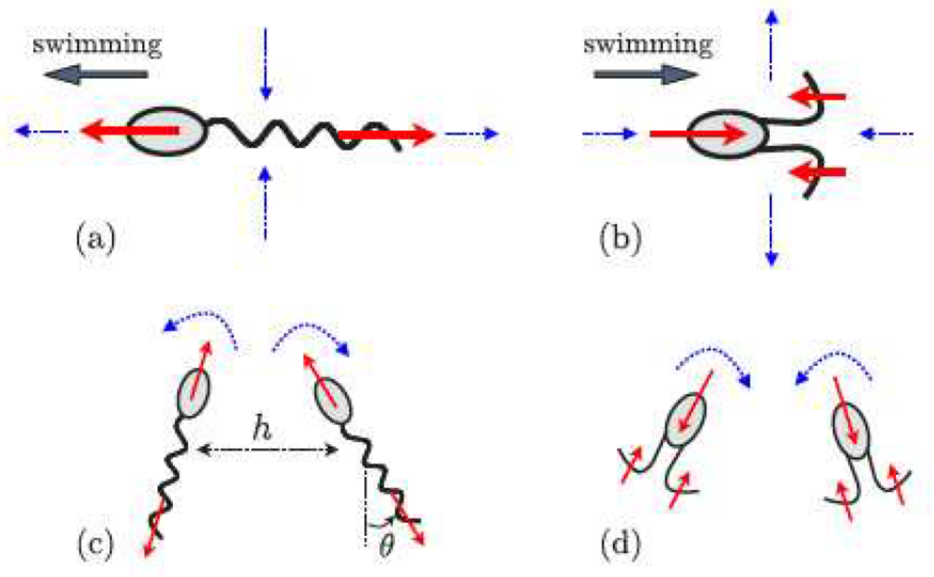

Figure 1.14 – The flow fields produced by pusher and puller particles are as follows: (a) pusher particles produce a flow field that is directed away from the cell along their swimming axis and towards the cell along their side; (b) puller particles produce a flow field that is the opposite of that of pusher particles, i.e., a flow field that is directed towards the cell along their swimming axis and away from the cell along their sides; (c) two pusher particles have a tendency to align with the local forcing of the cell on the surrounding fluid is shown by the red solid arrows, and the induced flow direction is shown by the blue dotted arrows (d) two pullers on a diverging course reorient each other, tending toward a configuration in which the cells are antiparallel, swimming away from each other. [91].

By taking into account the dynamics of two swimmers, it is possible to gain a deeper knowledge of these numerous body systems. Assume that cell A and cell B are two swimming organisms.

In general, cell A's flow field will result in two different passive hydrodynamic interactions with its neighbour (cell B). The disturbance velocity field that cell A has produced will first be felt by cell B, which will then be carried along by this flow. Additionally, cell B's orientation is prone to change due to the gradients of the cell A-created induced disturbance velocity field, which could impact how it swims in the future. Different rotational behaviors are therefore anticipated, depending on the type of induced velocity, such as in suspensions of pusher and puller particles. Two pullers tend to swim away from each other as they approach each other while two pushers tend to align and swim side by side, as shown in Fig. 1.14.

Some micro-swimmers, to propel themselves, do not move or deform their bodies. They are subjected to tangential stresses across their entire surface, as are purely spherical swimmers like droplets propelled by Marangoni stresses [92]. Microswimmers are known as squirmers in this situation.

A stresslet is a mathematical description of the flow created by a dipole of hydrodynamic forces and is presented as [91]

$$\mathbf{v}(\mathbf{r}) = \frac{\sigma_0}{8\pi\eta r^3}\left[3\cos^2\phi - 1\right]\mathbf{r}, \tag{1.61}$$

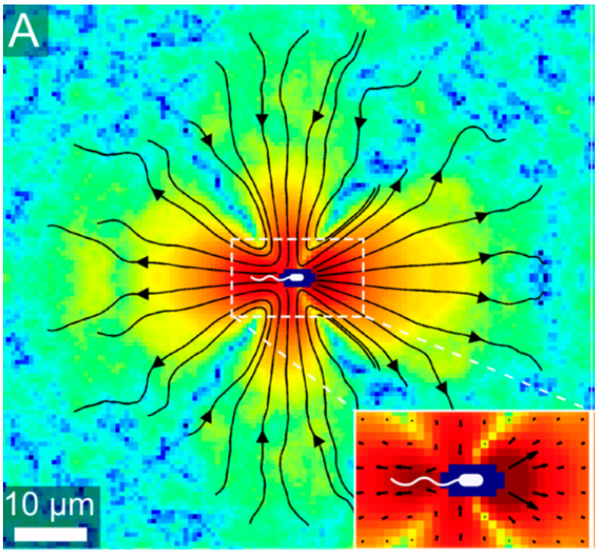

Figure 1.15 – Force dipole structure of the flagellated bacterium E. coli, measured experimentally in the bulk [18]

where $\mathbf{r}$ is the position with respect to the hydrodynamic dipole's center and $\sigma_0$ is the magnitude of the force dipole. $\sigma_0$ is the energy expended by the swimmer to propel himself.

As a result, local stress is created $\sigma_a(\mathbf{r}, t)$. Let us donate by $\mathbf{r}_\alpha(t)$ the position of the centers of the force dipoles. The forces are then applied at positions $\mathbf{r}_\alpha \pm \ell\mathbf{p}_\alpha$ where $\ell$ is the half-distance between the two points where the forces are applied and $\mathbf{p}_\alpha$ is the normalized orientation of the force dipole. The stress $\sigma_a(\mathbf{r}, t)$ created locally by the swimmer's assembly is defined as

$$-\nabla \cdot \sigma_a \equiv \mathbf{f}(\mathbf{r}, t), \tag{1.62}$$

where $\mathbf{f}(\mathbf{r}, t)$ is the local results of the force exerted by the swimmers on the fluid, which reads

$$\mathbf{f}(\mathbf{r}, t) = f \sum_{\alpha=1}^{N} \mathbf{p}_\alpha \left[\delta\left(\mathbf{r} - \mathbf{r}_\alpha(t) - \ell \mathbf{p}_\alpha(t)\right) - \delta\left(\mathbf{r} - \mathbf{r}_\alpha(t) + \ell \mathbf{p}_\alpha(t)\right)\right]. \tag{1.63}$$

$f$ is the magnitude of the force involved in the force dipoles and $\delta$ is the Dirac function. By expanding the Dirac function $\delta\left(\mathbf{r} - \mathbf{r}_\alpha(t) \pm \ell \mathbf{p}_\alpha(t)\right)$ about $\mathbf{r}_\alpha(t)$, it is possible to show that the expression of the shear stress, to the leading order neglecting gradients, is [93]

$$\left(\sigma_a\right)_{i,j}(\mathbf{r}, t) = \ell f n(\mathbf{r}, t)\left(p_i p_j - \frac{1}{3}\delta_{ij}\right). \tag{1.64}$$

This expression is a coarse-grained version of the shear stress, considering a local density of swimmers $n(\mathbf{r}, t)$ with the same orientations. The active shear stress is crucial in rheology and has been used to build the first predictive theory for the rheology of active particles [94].

According to Saintillan et al. [70], the total stress of active particles is decomposed as the sum of the Newtonian stress and a particle extra stress,

$$\mathbf{\Sigma} = -p\mathbf{I} + 2\eta\dot{\boldsymbol{\gamma}} + \mathbf{\Sigma}_p. \tag{1.65}$$

The particle extra stress $\mathbf{\Sigma}_p$ is calculated in the dilute regime as a configurational average of a particle's force dipole $\mathbf{S}(p)$ on the fluid.

$$\mathbf{\Sigma}_p(\mathbf{x}, t) = \int_\Omega \mathbf{S}(\mathbf{p})\Psi(\mathbf{x}, \mathbf{p}, t)\mathrm{d}\mathbf{p}. \tag{1.66}$$

The dipole $\mathbf{S}(\mathbf{p})$ is the result of several contributions, including resistance to stretching of the external flow, Brownian torques, and the permanent dipole due to self-propulsion [42, 79, 95], $\mathbf{S}_f(p), \mathbf{S}_b(p), \mathbf{S}_s(p)$ respectively. It is equal to

$$\mathbf{S}(\mathbf{p}) = \mathbf{S}_f + \mathbf{S}_b + \mathbf{S}_s. \tag{1.67}$$

The hydrodynamic stress can be expressed as

$$\mathbf{S}_f(\mathbf{p}) = A(\mathbf{pp} : \dot{\boldsymbol{\gamma}})\left[\mathbf{pp} - \frac{\boldsymbol{\delta}}{3}\right]. \tag{1.68}$$

where $A$ is a constant depending on the particle shape. For a slender particle, it can be obtained from slender-body theory as $A = \frac{\pi \mu L^3}{6log(2/a_r)}$ [42, 77]. The contribution arises from Brownian motions can be expressed as

$$\mathbf{S}_b(\mathbf{p}) = 3k_B T \left[\mathbf{pp} - \frac{\boldsymbol{\delta}}{3}\right]. \tag{1.69}$$

Finally, the permenant dipole arises from self propulsion is expressed as

$$\mathbf{S}_s(\mathbf{p}) = \sigma_0 \left[\mathbf{pp} - \frac{\boldsymbol{\delta}}{3}\right], \tag{1.70}$$

where the dipole or stresslet strength $\sigma_0$ is a constant that can be regarded as a measure of activity depending on the method used to swim (as mentioned before).

## 1.8 Numerical solutions of particle suspensions

In light of recent developments and research, this section explores the use of computational approaches to solve.

### 1.8.1 Finite volume method and Finite element method for the distribution function

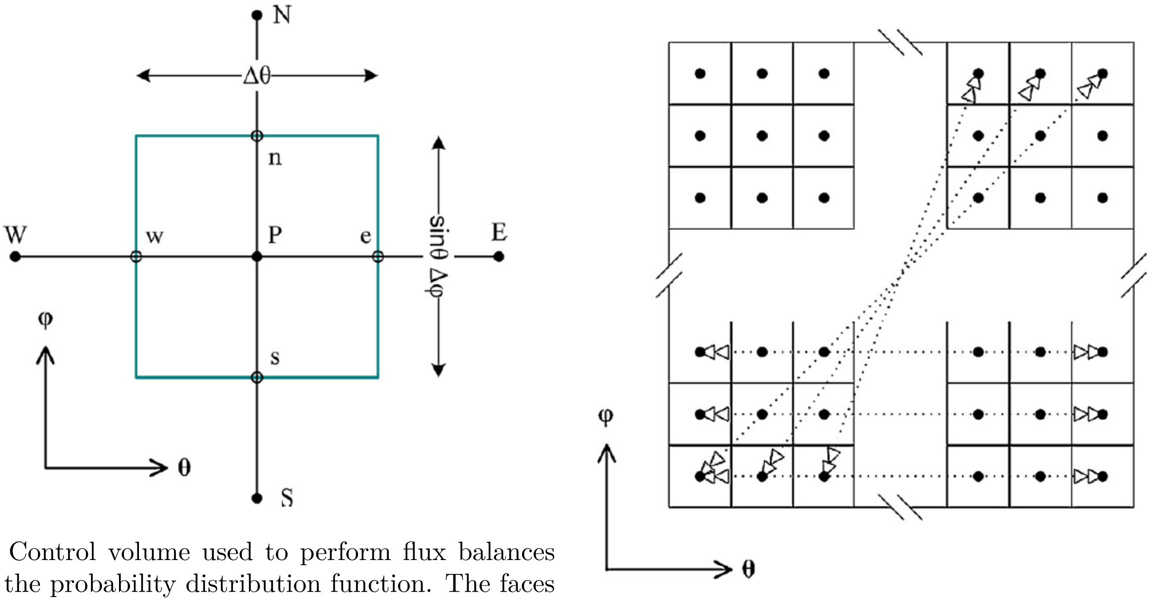

(a) Control volume used to perform flux balances for the probability distribution function. The faces of the control volume labelled as $e$, $w$, $n$ and $s$ refers to east, west, north and south directions.

(b) Schematic representation of the periodic boundary conditions on the total meshed domain.

Figure 1.16 – Representation of the schematic model used by Férec et al. [96] to solve the Fokker Planck equation using FVM.

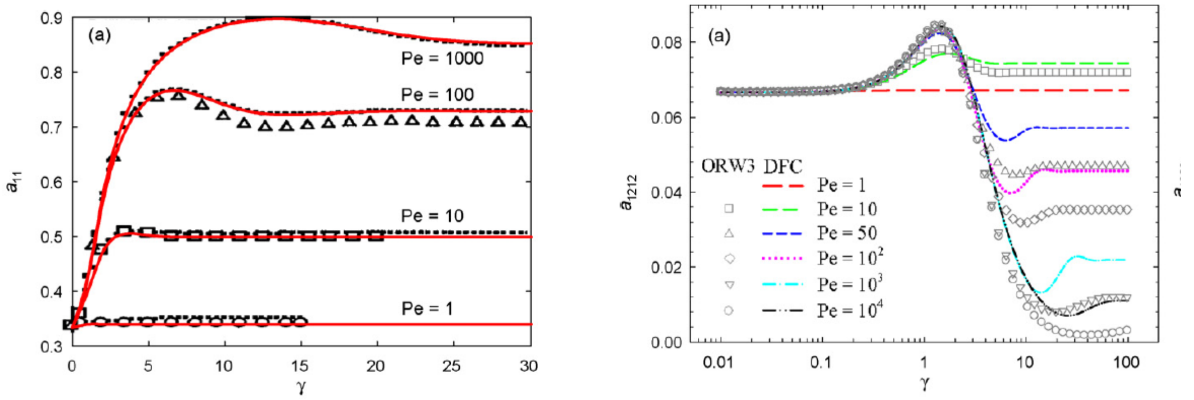

(a) Evolution of $a_{11}$ with respect to strain for $Pe_r = 1, 10, 100$ and $1000$.

(b) Evolution of $a_{1212}$ with respect to strain for $Pe_r = 1, 10, 100, 1000$ and $10000$.

Figure 1.17 – Comparison of $a_{11}$ and $a_{1212}$ components obtained by solving orientation distribution function in simple shear flow by Férec et al. [96] and previous work from literature.

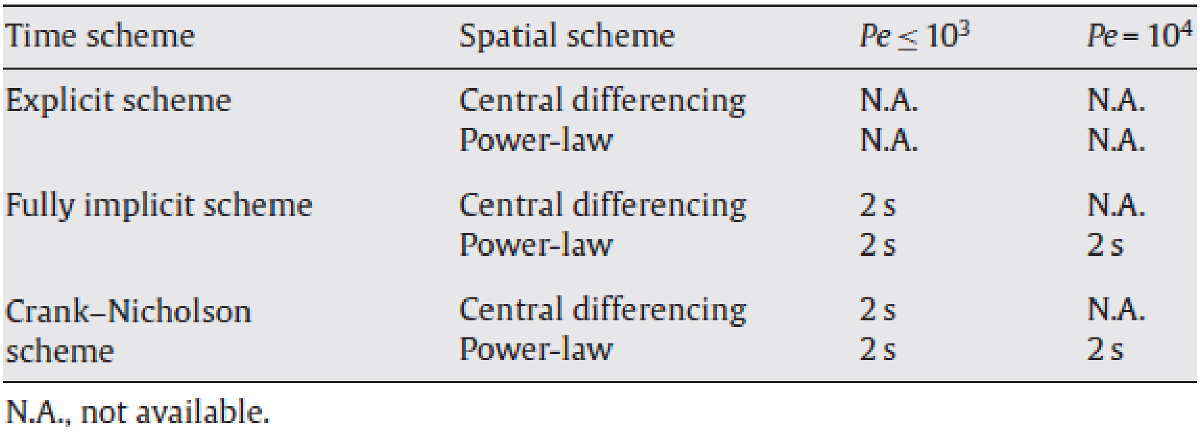

| Time scheme | Spatial scheme | $Pe \leq 10^3$ | $Pe = 10^4$ |
|---|---|---|---|
| Explicit scheme | Central differencing | N.A. | N.A. |
| | Power-law | N.A. | N.A. |
| Fully implicit scheme | Central differencing | 2 s | N.A. |
| | Power-law | 2 s | 2 s |
| Crank–Nicholson scheme | Central differencing | 2 s | N.A. |
| | Power-law | 2 s | 2 s |

N.A., not available.

Figure 1.18 – Calculation CPU time for different spatial schemes, time schemes and Peclet numbers [96].

Férec et al. [96] solved the Fokker-Planck equation using finite volume method (FVM) for non-brownian particles. They tested different time and spatial schemes to reduce considerably the computational time and to cover a wide range of the rotary Peclet ($Pe = \frac{\dot{\gamma}}{D_r}$) number. They compared the results for $Pe \leq 10^3$ with the data available in the literature and for $Pe \geq 10^3$. Excellent agreement was observed and the method allowed them to describe the evolution of the fourth-order orientation tensor components of particles in transient simple shear (forward and reverse) flows, and they compare with the predictions of an orthotropic closure approximation. Fig. 1.16a depicts the control volume used to perform the flux balance and Fig. 1.16b shows the periodic boundary conditions applied to calculate the distribution function. Fig. 1.17a shows the comparison between the results obtained from solving the FVM by Férec et al. [96] and the work of Advani [97] and Bay [32]. The components in Fig. 1.17b are determined by the computation of the probability distribution function for reverse simple shear flows (a negative constant shear rate was considered). For these, the initial orientation is set by the final orientation reached during the previous forward flow. The results are reported for different values of the Peclet number and as functions of strain. Fig. 1.18 shows the required CPU times for various combinations for a total flow time for different schemes.

Following the work of Férec et al. [96], the numerical approach has been updated by Mezi et al. [98] to deal with a two-dimensional representation of particle orientation state (i.e., planar orientation state) (see Fig. 1.19a ), solved using COMSOL Multiphysics. These results where verified with a previous work (see Fig. 1.19b ). A numerical study is presented for particle suspension flows through a parallel plate channel and a planar 4:1 contraction. The suggested method addresses the macroscopic scale by describing the particle orientation state with the probability distribution function (PDF), as opposed to using orientation tensors for the macroscopic constitutive modeling. As the numerical scheme solves the PDF in both the spatial and configurational spaces, it enables them to eliminate the error caused by the closure approximation when using orientation tensor description. This makes it possible to apply expressions for the particle extra stress correctly.

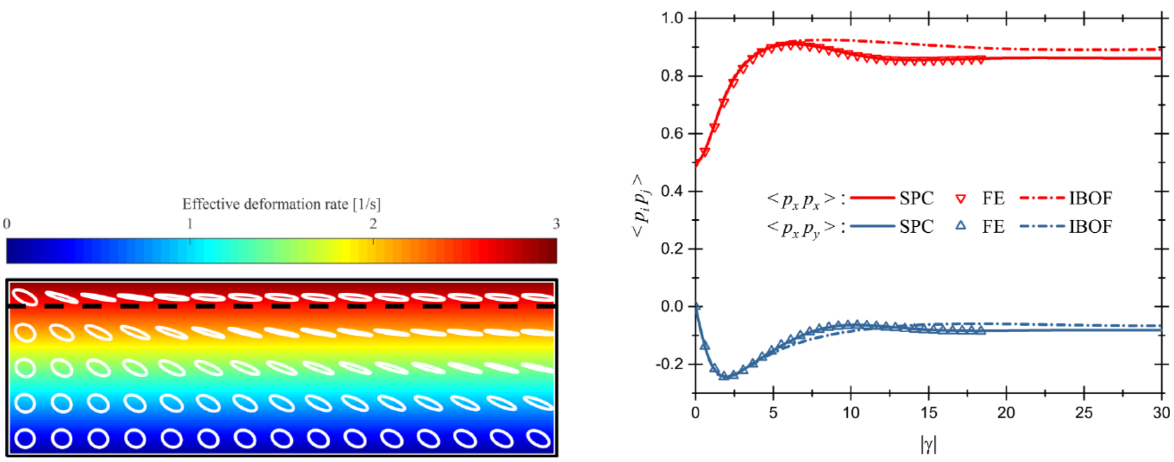

(a) Generalized shear rate distribution of fluid domain in the $xy$-plane for a Newtonian fluid. Ellipsoids represent the average particle orientation and eigenvalues are scaled with 1/10 for better visualization.

(b) Comparison of the FE to single-point calculations (SPC) of the orientation components in parallel plate channel for the streamlines along the line $y/H = 0.85$. Predictions obtained with the IBOF closure approximation are also shown.

Figure 1.19 – Representation of the results obtained by the work of Mezi et al. [98].

Assaad et al. [99] developed numerical model to analyze the dynamic behavior of particles. The foundation of this model lies in a direct solver approach for the Fokker-Planck equation for a 2D probability density function. The implementation of this numerical model takes place within a finite element framework. They conducted a study to assess the impact of mesh refinement, time scheme, and time stepping on the computational modeling of PDF evolution. The objective of this investigation is to strike a balance between model accuracy and computational efficiency. Fig. 1.20a shows the effect of change of time step $\Delta t$ on the evolution of $a_{11}$, while Fig. 1.20b illustrates the effect of mesh on the numerical solutions.

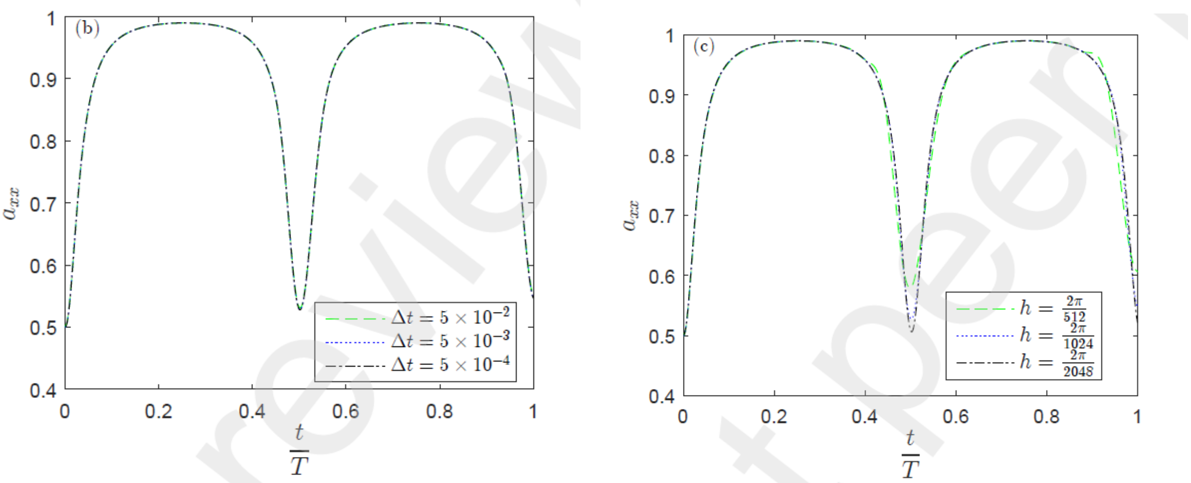

(a) Effect of decreasing time step $\Delta t$ with constant mesh size.

(b) Effect of mesh refinment with a constant time step.

Figure 1.20 – Convergence study: Effect of (a) decreasing time step $\Delta t$ with constant mesh size (b) mesh refinment with a constant time step on the numerical solution of the orientation component $a_{xx}$ [99].

Wegener et al. [100] used an efficient numerical solution of the Fokker-Planck equation for the orientation probability density of particle suspensions using physics-conforming FEM. They utilized the continuous Galerkin method to obtain a numerical solution. This solution is represented in terms of Lagrange basis functions associated with nodes in a computational mesh in 3D physical space, as well as nodes on the surface of a unit sphere representing the configuration space. Fig. 1.21a shows the geometry and the mesh used to solve the problem , they used coarse mesh in 3D. Fig. 1.21b shows the values of the maximum eigen values of $\boldsymbol{a}_2$ ($a_{11}$). These results are in good agreement with those obtained by Lohmann [101] using a physics compatible FE discretization of the Folgar-Tucker equation.

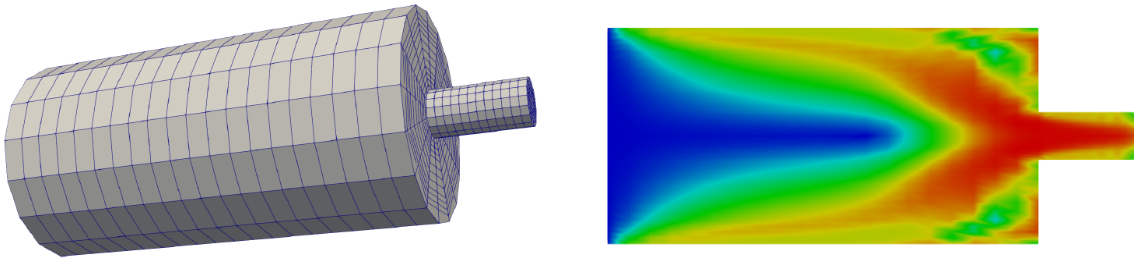

(a) Axisymmetric contraction geometry in 3D, coarse mesh for the spatial domain [100].

(b) Axisymmetric contraction, orientation component $a_{11}$ [100].

Figure 1.21 – Representation of (a) mesh of the axisymmetric contraction geometry (b) orientation component $a_{11}$ by the work of Wegener et al. [100].

## 1.9 Experiments on anisometric particles

### 1.9.1 Rheological features for different concentration regimes

Mangesana et al. [102] studied the effect of high solids concentration and coarse particle sizes of different average diameters ($d_{50} = 90\mu m, 180\mu m$ and $300\mu m$) on the viscosity of a suspension of water and silica sand. They found that the apparent viscosity and yield stress increased with solids concentration and particle size at the different pseudo shear rates. Fig. 1.22 shows how the apparent viscosity of the three size fractions varies with shear rate and different solids concentrations. As can be seen, the apparent viscosity increases as the solids concentration increases.

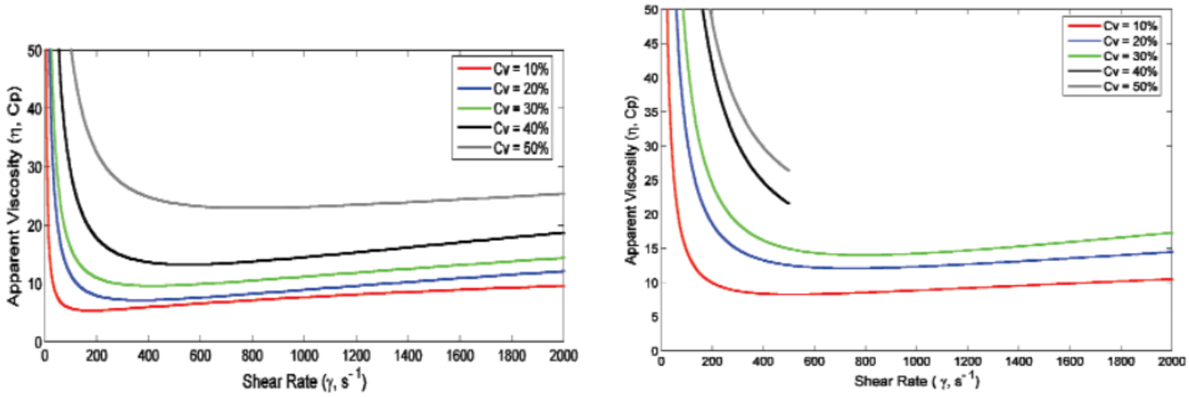

(a) Apparent viscosity of $d_{50} = 90\mu m$ sand as a function of shear rate.

(b) Apparent viscosity of $d_{50} = 180\mu m$ sand as a function of shear rate.

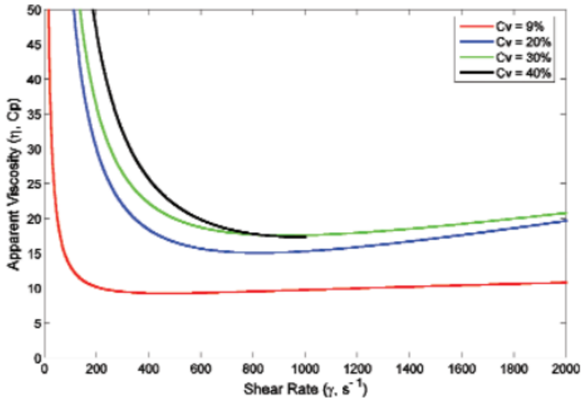

(c) Apparent viscosity of $d_{50} = 300\mu m$ sand as a function of shear rate.

Figure 1.22 – Comparing the effect of solid concentrations on the viscosity as a function of shear rate [102].

Shafiei et al. [103] examined the rheological properties and microstructure of nanocrystalline cellulose (NCC) aqueous suspensions. It has been investigated at different concentrations. They showed in Fig. 1.23 that the variation of viscosity with respect to the shear rate is affected with the concentration of the particles in the medium. As concentration increases, the viscosity increases. These results agree with the work of Li et al. [104], who studied the rheology of aqueous suspensions of chitin crystallites. It is also consistent with the work of Jia et al. [105], who worked on the amorphous cellulose suspension.

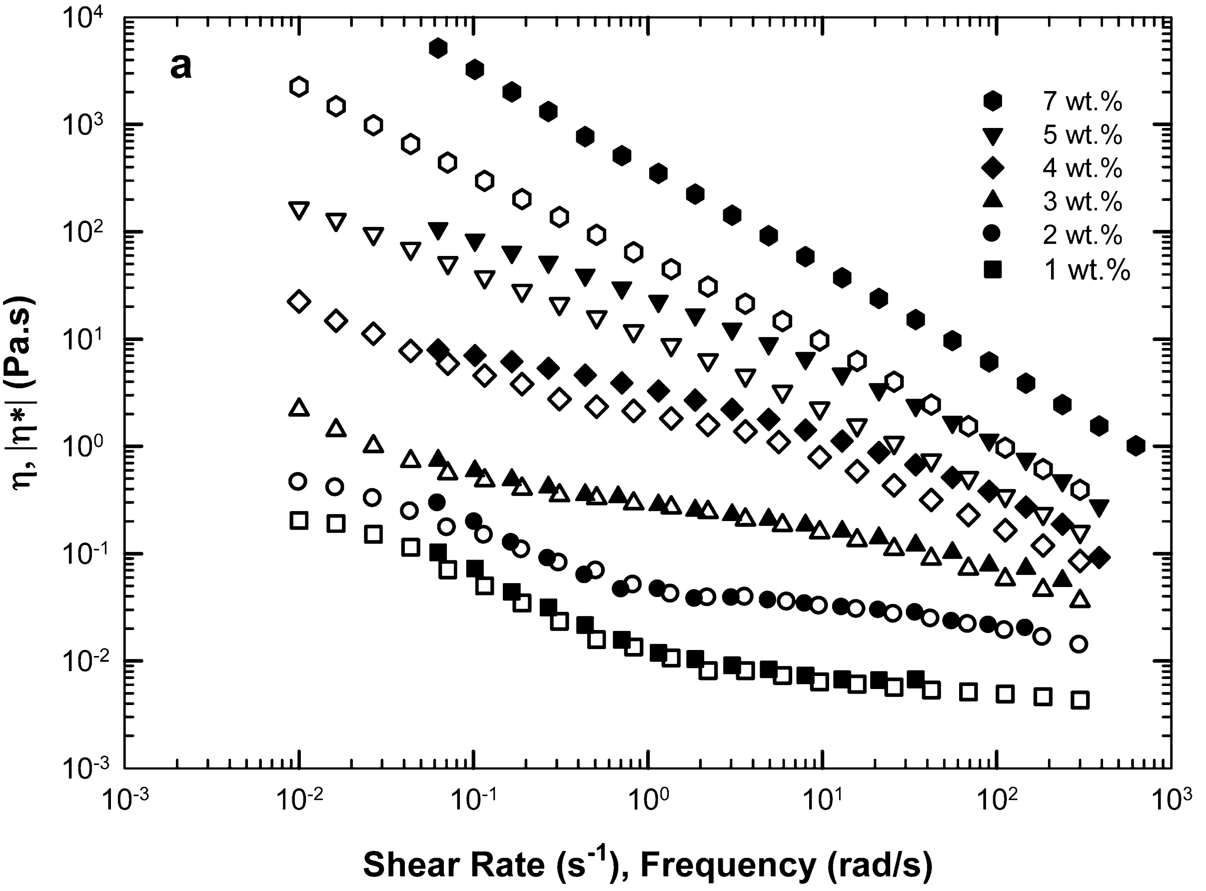

Figure 1.23 – Comparison of the viscosity as a function of shear rate of NCC samples of different concentrations [103].

### 1.9.2 Rheology of active systems

While swimming, an active particle suspended in a fluid creates a local flow. This flow can be captured by a far-field force dipole, as shown in Eq. 1.61, and it contributes to the particle's stress on the outer fluid. The swimmer's shear flow is super imposed on the imposed shear flow, causing a rheological response that is dependent on the swimmer's mean orientation with the shear flow. The phenomenology of active particle rheology can be captured by imposing shear flows similar to those produced by the particles. The use of extremely precise experimental setups capable of generating flows with shear rates of $\dot{\gamma} \leq 1/s$ is then required. Micro-rheology setups [106], microfluidic rheometers [107], and low-shear Couette rheometers [108, 109] have all been developed for this purpose. The findings of these studies reveal some interesting aspects of the rheology of active particles of the puller and pusher types.

Solomon et al. [110] show the relationship between shear rate and viscosity for concentrated rod suspensions with an aspect ratio of 8.4 and an ionic strength of $0.002M$. As the concentration of the rods increases, three qualitative effects become apparent (as shown in Fig. 1.24). First, the magnitude of viscosity increases. Second, the characteristic shear rate for the onset of shear thinning behavior decreases. Third, the severity of shear thinning, as characterized by the power-law exponent, increases. These observations were consistent across all the concentrated suspensions studied, regardless of their ionic strength or aspect ratio. For pushers, Sokolov et al. [106] have demonstrated the effect of viscosity reduction in Bacillus subtilis suspensions for the first time (Fig 1.25). Bacillus subtilis is a flagellated elongated pusher bacterium, similar to E. coli. Gachelin et al. [107] later demonstrated a similar behavior for E. coli suspension using a microfluidic setup (Fig. 1.26) that allowed them to vary the shear rate of the imposed flow (Fig. 1.27). Fig. 1.27(a) shows the relative viscosity of suspensions of motile and non-motile bacteria as a function of the maximum shear rate for a concentration of 0.8%. The relative viscosity is plotted as a function of the maximum shear rate. The plot reveals that the relative viscosity of the motile bacteria is non-monotonic, with a minimum value below 1 at small shear rates, an increase in viscosity with increasing shear rate (shear-thickening), and then shear-thinning at higher shear rates. The viscosity of the non-motile bacteria does not show a decrease in viscosity below one or shear-thickening behavior. Fig. 1.27(b) illustrates that the qualitative behavior of the relative viscosity is the same for all concentrations. Fig. 1.27(c) demonstrates changes in relative viscosity as a function of the volume fraction for various shear rates. The plot reveals that a decrease in viscosity below one is observed for the small shear rates. With increasing concentration, a sharp increase in viscosity takes place for all shear rates, corresponding to a semi-dilute regime.

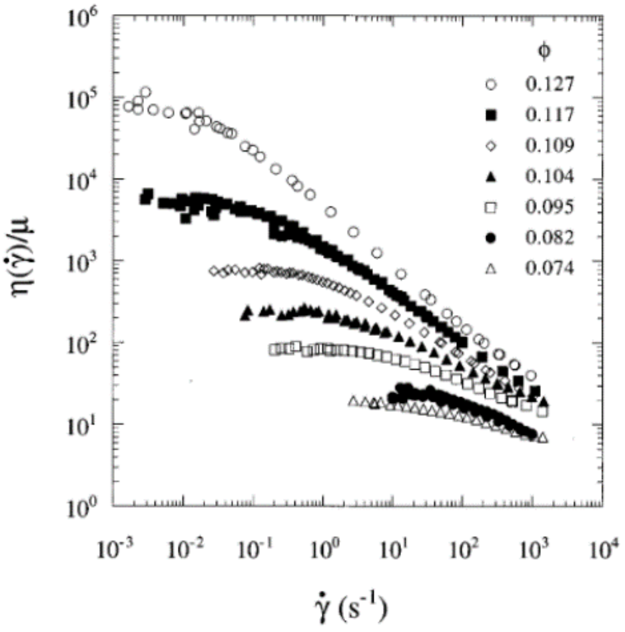

Figure 1.24 – Shear-thinning rheology of colloidal hematite rods. The shear viscosity, normalized by the viscosity of the carrying fluid, is plotted as a function of the shear rate for different rods concentrations [110]

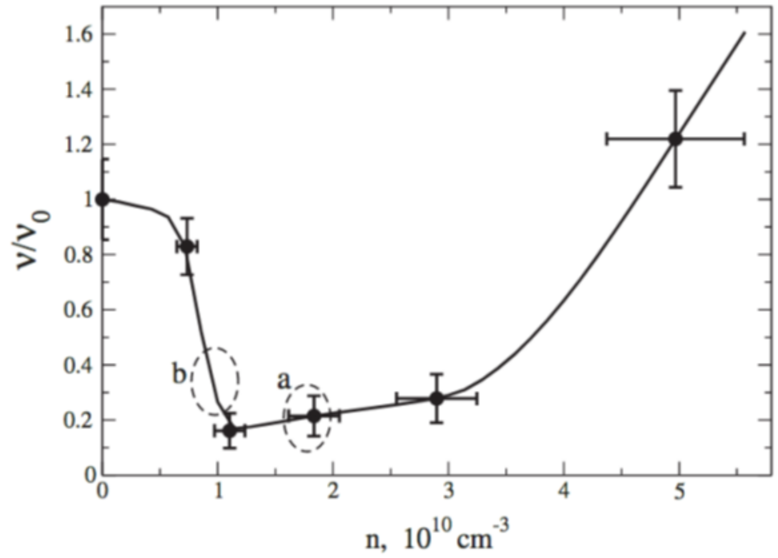

Figure 1.25 – Reduction of viscosity in Bacillus subtilis suspensions. Ratio of the effective shear viscosity over the viscosity of the bacteria medium, measured for a suspension of Bacillus subtilis (pusher bacteria) at different cell concentration n [106]

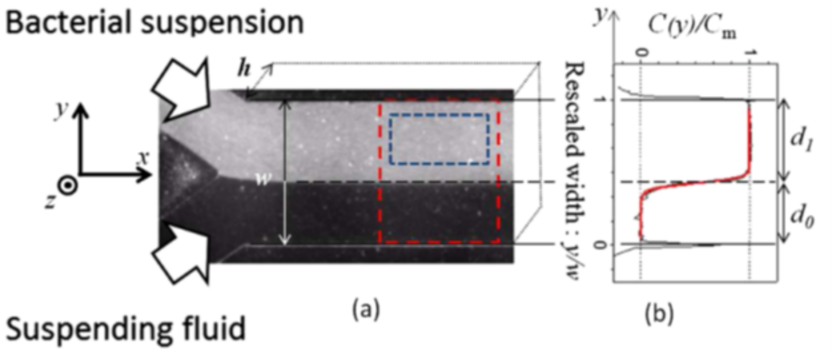

Figure 1.26 – Microfluidic rheometer to measure the viscosity of bacteria suspensions [107]

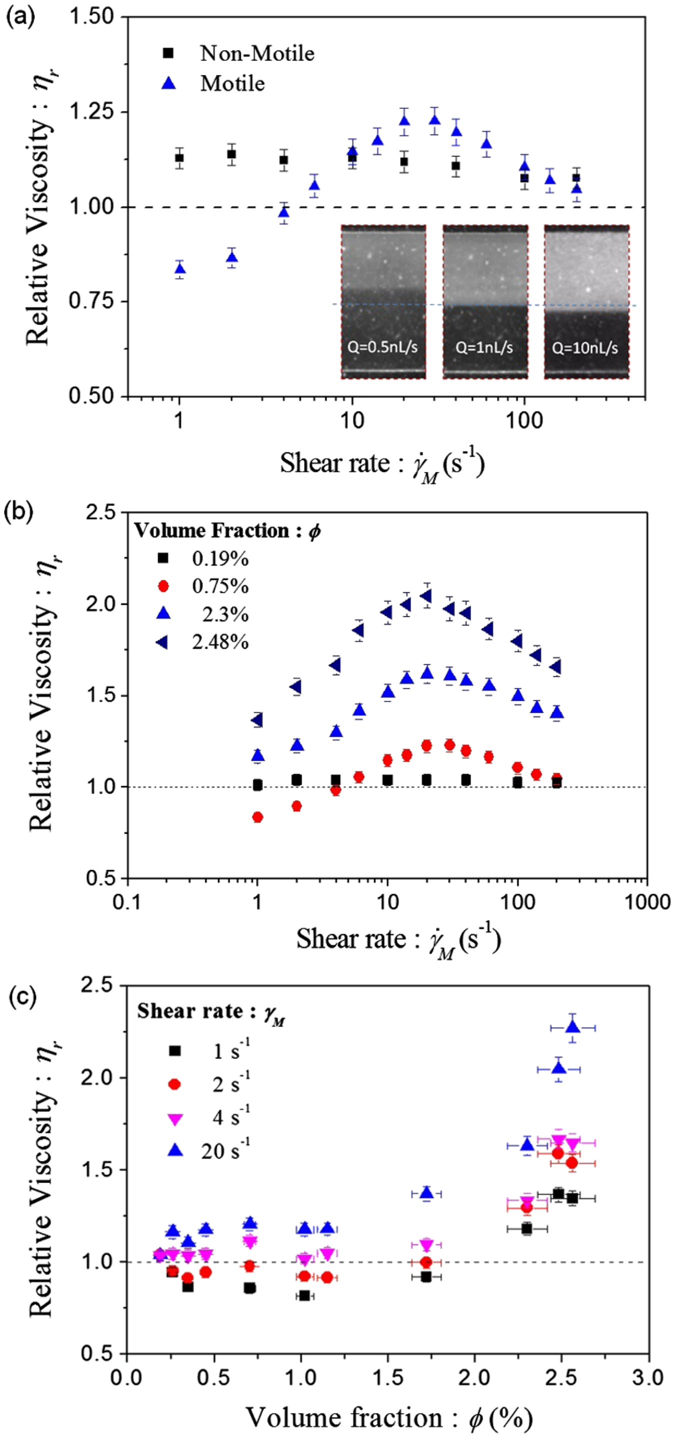

Figure 1.27 – Non-Newtonian behavior of E. coli suspensions [107]

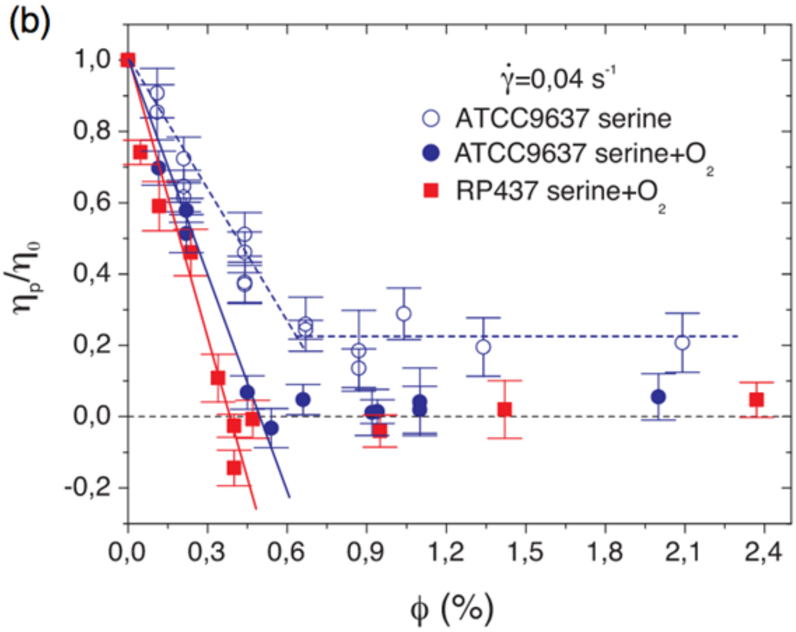

Figure 1.28 – Superfluid state of E. coli suspensions [109]

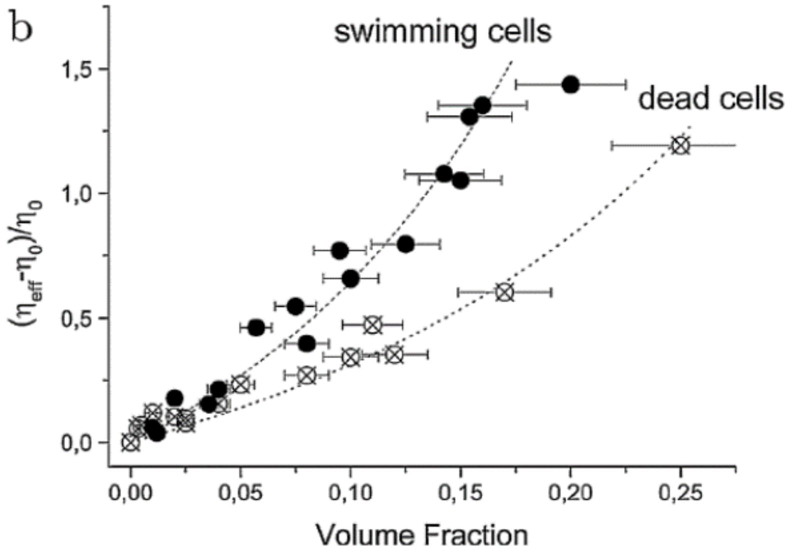

Figure 1.29 – Viscosity of puller swimmers : the example of Chlamydomonas reinhardtii [108]

Lopez et al. [109] carried out these experiments in a low-shear rheometer, which allowed them to apply Couette flows at shear rates as low as $\dot{\gamma} = 0.04/s$. They discovered that, under certain medium conditions and at a fixed shear rate, E. coli viscosity drops to zero for a wide range of cell concentrations, resembling a superfluid regime (Fig.1.28).

For pullers, using a Couette rheometer, Rafai et al. [108] determined the effective viscosity of Chlamydomonas reinhardtii. Their findings show an increase in viscosity at low shear rates, with a minimum of $\dot{\gamma} = 4/s$ being investigated. When compared to non-motile algae, activity also plays an important role in the increase of effective shear viscosity depending on the rotary diffusion (Fig.1.30).

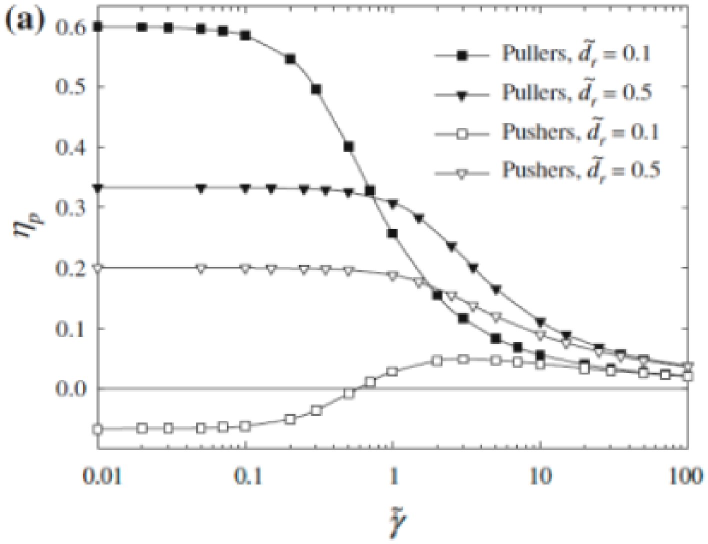

Figure 1.30 – Rheology of non-tumblers (smooth) and slender ($\lambda = 1$) swimmers (pushers and pullers) [70]

### 1.9.3 Cross-stream migration in non-rheological flow

Experimental investigations were carried out in Newtonian liquids by Karnis et al. [111], employing single rigid spheres, rods, and disks. These particles were characterized by densities matching those of the liquids. The flow conditions subjected them to particle Reynolds numbers ranging between $3 \times 10^{-6}$ and $7 \times 10^{-3}$. Notably, the rods and disks exhibited the same tubular pinch effect that was previously observed with rigid spheres at these particular Reynolds numbers. During the experiments, particles initially positioned near the tube wall displayed an inward migration phenomenon, while particles situated closer to the tube axis underwent an outward movement. This dynamic persisted until an equilibrium radial position ($r$) was attained, approximating one-half of the tube radius ($R$), as depicted in Fig. 1.31.

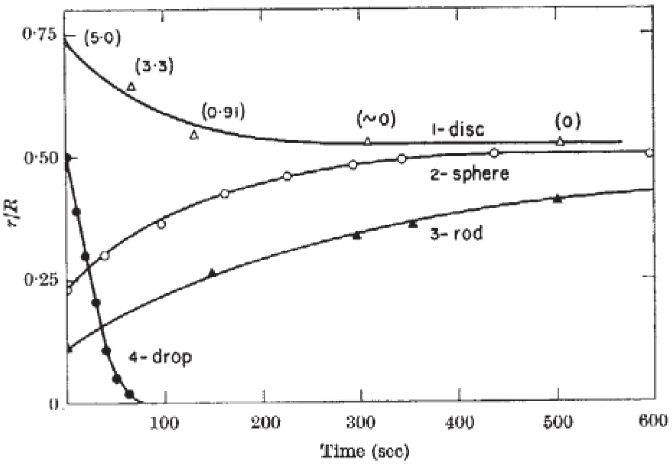

Figure 1.31 – Radial migration to the equilibrium position $r/R = 1/2$ approximately, exhibited by spheres, rods and disks at high Reynold number when suspended in polyglycol oils flowing through a tube of radius $R = 0.2cm$ [111].

Nitsche and Hinch [112] addressed the cross-stream migration of rigid rods undergoing diffusion and advection in parabolic flow between flat plates. Clear and unequivocal findings regarding the observable concentration profiles across the channel are extracted through the implementation of a finite-difference solution for the full Fokker-Planck equation in the lateral position $y$ and azimuthal angle $\theta$ dimensions. Notably, this analysis excludes the influences of steric confinement and hydrodynamic wall effects, which predominantly manifest within narrow boundary layers. The computational outcomes strongly suggest the propensity for rods to undergo migration towards the channel walls (see Fig. 1.32).

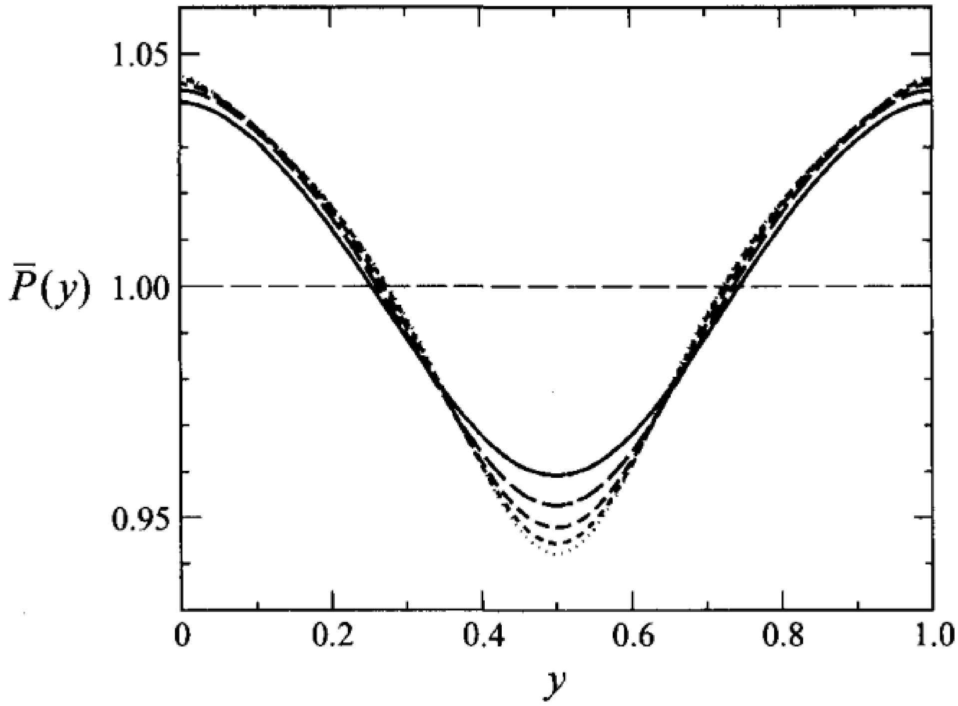

Figure 1.32 – Steady-state angle-averaged probability density functions at $Pe_r = 10$ [112].

Schiek and Shaqfeh [113] considered slender particle migrations across streamlines in a suspension under plane Poiseuille flow. They considered the weak flow limit such that Brownian motion strongly affects the particle position and orientation. They found that at steady state the particles centre-of-mass distribution function shows a net migration of particles away from the centre of the channel and towards the channel walls.

The tendency of swimming particles to accumulate near boundaries distinguishes confined active suspensions. Rothschild [114] measured the concentration of swimming bull spermatozoa in a glass chamber and reported a nonuniform distribution across the channel with a significant concentration spike near the walls, as seen in Fig. 1.33. This was the first study to demonstrate this.

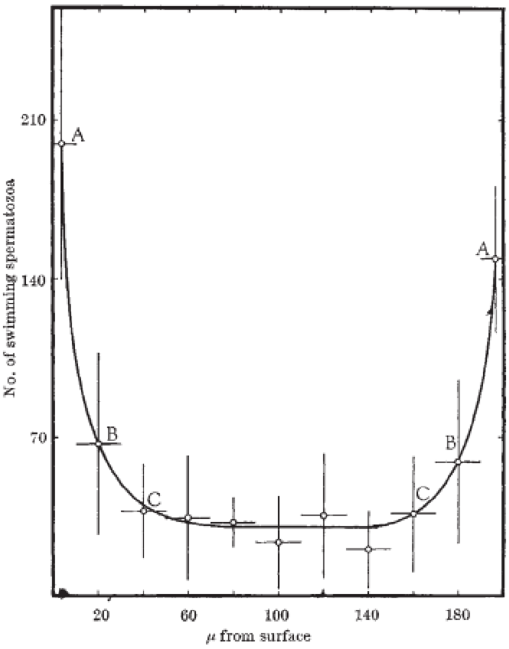

Figure 1.33 – Distribution of swimming bull spermatozoa (semen diluted 1/30) in a Hawksley hremocytometer chamber 200$\mu m$ [114].

When Berke et al. [115] carried out the same experiment again with Escherichia coli suspensions in microchannels, they also noticed bacterial buildup at the channel walls (see Fig. 1.34).

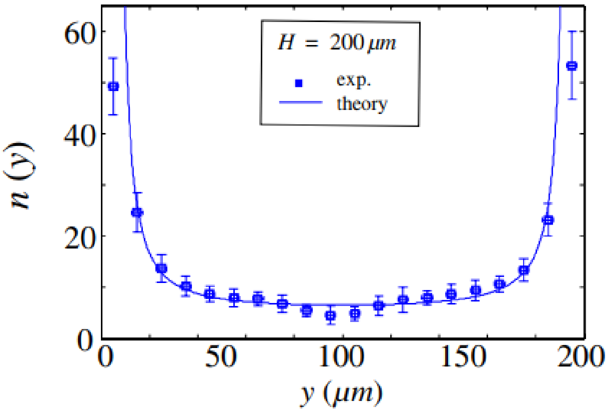

Figure 1.34 – Experimental data: number of swimming cells $n$ as a function of the distance to the bottom cover slip $y$ when the distance between the surfaces is $H = 200\mu m$ [115].

Sartori et al. [116] conducted empirical investigations into the concentration profiles of bacterial suspensions constrained within slits characterized by heights $h$ comparable to the typical persistence length of the cells. Specifically, they focused on MG1655 E. coli and wild-type P.

aeruginosa bacteria. These experimental observations were complemented by numerical simulations employing a simplified model of self-propelling particles. In both the experimental studies and numerical simulations, a consistent pattern emerges that the concentration profiles exhibit similarity, regardless of the specific motility pattern (see Fig. 1.35). This accumulation is an effect of a longer detention time close to the walls which is due to the cells alignment induced by steric interactions with solid walls.

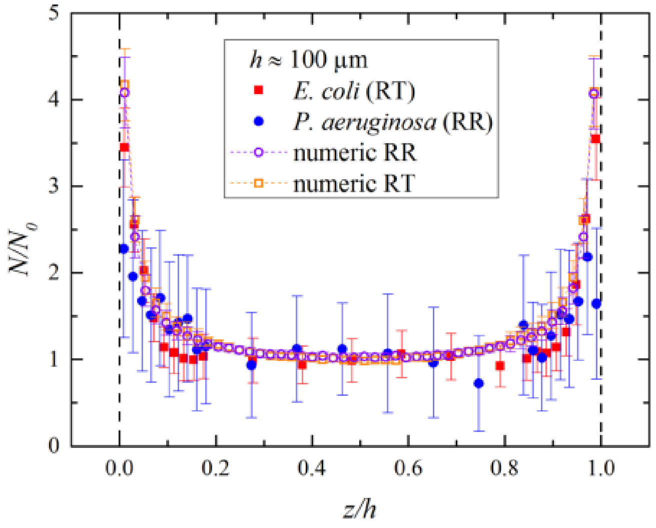

Figure 1.35 – Experimental concentration profiles obtained for MG1655 E. coli (full squares) and wild-type P. aerugionosa (full circles). The corresponding results from the simulations of the Run and Tumble [117] (RT) (empty squares) and Run and Reverse [118] (RR) (empty circles) models are reported for comparison. In this case the slit height $h = 100\mu m$ and 75% of the bacteria are motile [116].

## 1.10 Conclusion of the chapter

This chapter presents a state of the art on the suspension of active particles. However, the various questions, several parts are presented to allow the suspension of non-Brownian and Brownian particles in the flow. Firstly, the interest is focused on understanding the anisometric particle properties, its orientation and its position. Also, in this part, the difference between a Brownian and non-Brownian particle and a passive and active particle are introduced. Then, the description of particle movement in fluid flows is made clearer. Jeffery's equation gives a description of particle orientation in the case of a diluted fiber solution. Thus, this model is a base for the evolution of the orientation of the particles by adding other terms. The second part of this chapter is dedicated to describing the different concentration regimes, in addition to introducing the probability distribution function and its moments that are used to depict the suspension of particles sample. After that, the Fokker-Planck equation is introduced to solve the evolution of the probability density function before explaining the stress tensor generated by the presence of particles in the flow. In the third part, the various numerical methods employed to model the flow of particles are shown, including the finite volume and finite element methods used for solving the Fokker-Planck equation and the closure approximations used for solving the evolution of the second-order orientation tensors. Final part of this chapter gives a background of the experimental studies done on the anisometric particles. It starts with showing the rheological features for different concentration regimes, then it sheds light on the rheology of active particles. Finally, it displays cross-stream migrations in non-rheological flows.

CHAPTER 2

# MODELING AND NUMERICAL SIMULATIONS OF BROWNIAN RODLIKE PARTICLES WITH ANISOTROPIC TRANSLATIONAL DIFFUSION

A new kinetic macromodel based on moments of the probability distribution function is proposed to investigate the flow of rodlike Brownian particle suspensions. The rods concentration-orientation coupling is taken into account. A numerical study is presented for rods through the planar channel, with and without introducing a circular obstacle which develops a nonhomogeneous flow. To verify this macromodel, the results are compared with the solution of the associated Fokker-Planck equation taking into consideration an anisotropic translational diffusion tensor. This tensor depends on the local orientation of the rod. Low (smaller than $10^3$ ) Brownian translational Peclet number causes rod migrations across the flow streamlines.

Un nouveau macromodèle cinétique basé sur les moments de la fonction de distribution de probabilité est proposé pour étudier l'écoulement de suspensions de particules browniennes en forme de bâtonnets. Le couplage concentration-orientation des bâtonnets est pris en compte. Une étude numérique est présentée pour des tiges à travers un canal planaire, avec et sans introduction d'un obstacle circulaire qui développe un écoulement non homogène. Pour vérifier ce macromodèle, les résultats sont comparés à la solution de l'équation de Fokker-Planck associée qui prend en compte un tenseur de diffusion translationnelle anisotrope. Ce tenseur dépend de l'orientation locale de la tige. Un nombre de Peclet brownien de translation faible (inférieur à $10^3$) provoque des migrations de la tige à travers les lignes de courant.

## 2.1 Introduction

Mechanical, thermal, or electrical properties are influenced significantly by the concentration and orientation distributions of nanoparticles in composite materials. Thus, predicting and controlling the concentration and orientation state of particle suspensions is critical for designing a successful manufacturing process of advanced materials [119–121].

Researchers have theoretically studied the evolution of the orientation of anisotropic particles homogeneously suspended during flow. Jeffery [22] derived the equation of motion of one isolated, inertialess, and axisymmetric particle in a Newtonian fluid with a uniform velocity gradient. When a dilute fiber suspension is exposed to a constant shear flow, fibers tend to align in the flow direction [122, 123]. Folgar and Tucker [27] modified Jeffery's equation by introducing a scalar diffusion term to capture phenomenologically the interactions between non-Brownian particles in nondilute regimes. According to additional research, various perturbations inherent in flowing channels can have an impact on the reproducibility and endurance of rotations. Small deviations from a perfect axisymmetric rod shape, for example, can result in doubly periodic and chaotic orbits, which have been investigated both theoretically and experimentally [124–126]. Jeffery's orbits are perturbed by the proximity of channel walls [127–131], inertia [126], and the viscoelasticity of the shearing fluid [132, 133]. The Fokker-Planck equation (FP) for Brownian particles is derived from the work of Kirkwood and Auer [134] by Doi and Edwards [40]. Rheo-optical techniques have been used to measure rod distributions [135, 136], and these results were compared to theoretical expectations and Brownian dynamics simulations [137–140]. Brownian fluctuations and their effect on orbits of individual Brownian rods in a microchannel flow have been studied theoretically [141]. In both the spatial and configurational spaces, some numerical strategies have been developed to solve the Fokker-Planck equation directly [98, 142–147]. Park and Park [148] and Férec et al. [149] provided thorough reviews of the fundamentals and numerical simulations for predicting fiber orientation during the injection molding of polymer composites.

When dispersed in a Newtonian liquid, isolated particles may exhibit cross-stream migration. Schiek and Shaqfeh [113] considered fiber migration across streamlines in a suspension under a plane Poiseuille flow in the weak flow limit, such that Brownian motion strongly affects the fiber position and orientation. At steady state, the center-of-mass distribution of fibers shows a net migration of fibers away from the center of the channel and toward the channel walls. Nitsche and Hinch [112] addressed the cross-stream migration of rigid rods undergoing diffusion and advection in a parabolic flow between flat plates. Results are obtained from using a finite-difference scheme for the solution of the Fokker-Planck equation. The results indicate that rods migrate toward the walls and toward the higher shear zone. Park et al. [150] used a kinetic theory to study the cross-stream migration of a rigid polymer undergoing rectilinear flow in the vicinity of a wall. In a simple shear flow, polymers migrate away from the wall, while in a pressure-driven flow, the center-of-mass distribution has an off-center maximum. This is because of the competition between the hydrodynamic interactions with the wall and the anisotropic diffusivity induced by the inhomogeneous flow field. Sharaf et al. [151] established that Brownian motion plays a significant role in the deposition of nanoparticles on the channel walls at low Reynolds number.

Solving a multidimensional Fokker-Planck equation has high computational costs. Developing an equivalent kinetic macromodel is a strategy to render the numerical solution of detailed physics overall more accessible. There is a large amount of published literature showing the use of macromodels for predicting particle orientation or concentration. Advani and Tucker [152] used a set of even-order tensors related to the coefficients of a Fourier series expansion of the probability distribution function to describe fiber orientation in suspensions containing short rigid fibers. Phillips et al. [153] proposed a constitutive equation for computing particle concentration and velocity fields in concentrated monomodal, spherical suspensions. Shapley et al. [154] compared the predictions of several models of particle migration to laser Doppler velocimetry measurements in various concentrated suspensions of noncolloidal spheres in a Couette flow. The models predict the observed macroscopic shear rate and concentration profiles well at moderate bulk particle concentration but diverge from one another at high concentrations. These models are either used to predict the orientation or the concentration, without studying the correlation between both. Saintillan and Shelley [12] derived a basic kinetic model for a suspension of self-propelled rodlike particles and discussed its stability and nonlinear dynamics. Weady et al. [76] restated and coarse grained a continuum kinetic model for an active suspension. These two models approximate the translational diffusion to a constant, while in fact, this diffusion is anisotropic and depends on the orientation of the particle. A macromodel that considers the coupling of concentration and orientation of Brownian rods is not yet available in the literature. This mutual coupling is especially interesting in the context of active nematic suspensions. Typical models of active nematic suspensions assume isotropic diffusion, and therefore uniform concentration; however many physical systems show significant fluctuations [155]. This work aims to build a new macromodel to solve the motion of suspended rodlike particles in flows in a nonhomogeneous system taking into consideration the coupling of particle concentration and orientation. To verify this model, a new numerical strategy is developed to solve the configurational and spatial Fokker-Planck equation of suspension of Brownian particles in a Newtonian viscous fluid. Particle suspensions are studied in a planar channel, and with the presence of a circular obstacle. The structure of this article is as follows. Sec. 2.2 focuses on the theoretical modeling. Then Sec. 2.3 describes the flow problem used to solve the rodlike particle suspensions. Finally, before the conclusion, Sec. 2.4 shows the numerical results in the two geometries, planar channel with and without a circular obstacle, and the verification of the macromodel.

## 2.2 Theoretical model

### 2.2.1 Hypotheses

Let us consider a suspension of Brownian rodlike particles of length $L$ and width $d$. The particles are monodisperse, neutrally buoyant, and rigid. The suspension is considered in the dilute regime of concentration, where $c << (d/L)^2$. Each particle is described with a position vector of the particle's centroid $\mathbf{r}_c$ and an orientation unit vector $\mathbf{p}$.

### 2.2.2 Kinetic model equation

A suspension of Brownian particles can be described via a probability distribution function $\Psi(\mathbf{r}_c, \mathbf{p}, t)$. It represents the probability to find a particle at location $\mathbf{r}_c$, at the level of elementary volume [see Fig. 2.1a], with orientation $\mathbf{p}$ at time $t$. In the dilute regime, a single-particle Smoluchowski equation can be obtained as follows [22, 26, 27, 40]:

$$\frac{\partial \Psi}{\partial t} = -\nabla_{\mathbf{x}} \cdot (\dot{\mathbf{r}}_c \Psi) - \nabla_{\mathbf{p}} \cdot (\dot{\mathbf{p}} \Psi) . \tag{2.1}$$

The evolution of the position of a Brownian particle with respect to time, $\dot{\mathbf{r}}_c$, is

$$\dot{\mathbf{r}}_c = \mathbf{u} - \mathbf{D}_t \cdot \nabla_{\mathbf{x}} \log \Psi, \tag{2.2}$$

and the evolution of its orientation with respect to time, $\dot{\mathbf{p}}$, can be written as

$$\dot{\mathbf{p}} = \dot{\mathbf{p}}_j - D_r \nabla_{\mathbf{p}} \log \Psi, \tag{2.3}$$

where $\dot{\mathbf{p}}_j$ is the Jeffery's equation and it is given by

$$\dot{\mathbf{p}}_j = -\frac{1}{2} \boldsymbol{\omega} \cdot \mathbf{p} + \frac{\lambda}{2} \left( \dot{\boldsymbol{\gamma}} \cdot \mathbf{p} - \dot{\boldsymbol{\gamma}} : \mathbf{ppp} \right) . \tag{2.4}$$

$D_r$ and $\mathbf{D}_t$ are the rotary diffusion coefficient and translational diffusion tensor, respectively. The latter for nonspherical, rigid particles are defined by $\mathbf{D}_t = D_{\|} \mathbf{pp} + D_{\perp} (\boldsymbol{\delta} - \mathbf{pp})$, where $D_{\|}$ and $D_{\perp}$ are constants that characterize the diffusion parallel and perpendicular to the particle axis. The rotary diffusion can also have a tensorial form similar to $\mathbf{D}_t$. However, the scalar product of $\mathbf{p}$ with $\nabla_{\mathbf{p}}$ equals zero, which reduces the rotary diffusion to a scalar [40]. $\mathbf{u}$ is the external flow velocity vector at location $\mathbf{r}_c$. $\nabla_{\mathbf{p}}$ and $\nabla_{\mathbf{x}}$ denote the gradient operators in configurational and spatial spaces, respectively. $\boldsymbol{\omega}$, $\dot{\boldsymbol{\gamma}}$, and $\boldsymbol{\delta}$ are the vorticity, strain rate, and identity tensors, respectively. $\lambda$ is a constant form factor as a function of the rod aspect ratio $a_r = L/d$. Hence, the expanded version of Eq. (2.1), by taking into account the fluid incompressibility condition, is

$$\frac{D\Psi}{Dt} = \nabla_{\mathbf{x}} \cdot (\mathbf{D}_t \cdot \nabla_{\mathbf{x}}\Psi) - \nabla_{\mathbf{p}} \cdot (\dot{\mathbf{p}}_j\Psi) + D_r\nabla^2_{\mathbf{p}}\Psi, \tag{2.5}$$

where $\frac{D(...)}{Dt} = \frac{\partial(...)}{\partial t} + \mathbf{u} \cdot \nabla_{\mathbf{x}}(...)$ is the material derivative operator and $\nabla^2_{\mathbf{p}}$ is the Laplacian operator in configurational domain. In what follows, we derive an equivalent evolution equation based on the second-order moment of $\Psi$.

### 2.2.3 Second-order moment of $\Psi$

The second-order moment of $\Psi$, $\mathbf{A}_2$, contains information on the local concentration and orientation of particles and is defined as

$$\mathbf{A}_2 = \frac{1}{V}\int_{\mathbf{p}}\int_{\mathbf{r}_c} \mathbf{pp}\Psi d\mathbf{r}_c d\mathbf{p}. \tag{2.6}$$

The trace of $\mathbf{A}_2$ is the concentration field $c$, which represents the mean number density in the suspension, it is the zeroth-order moment of $\Psi$

$$c = \frac{1}{V}\int_{\mathbf{p}}\int_{\mathbf{r}_c} \Psi d\mathbf{r}_c d\mathbf{p}. \tag{2.7}$$

$V$ represents the volume, which is large enough to contain a statistically significant number of particles but smaller than the characteristic length scale of the macroscopic properties of the system under consideration. Figure 2.1 provides two-dimensional (2D) examples on how $\mathbf{A}_2$ can describe the particle concentration and orientation in the elementary volume. It represents $\mathbf{A}_2$ for two concentrations $c_1$ and $c_2$, with $c_2 \geq c_1$. At the macroscopic level, $\mathbf{A}_2 = \mathbf{A}_2(\boldsymbol{x}, t)$, where $\mathbf{x}$ is the position vector of the elementry volume.

The evolution of $\mathbf{A}_2$ is obtained by premultiplying Eq. (2.5) with the tensor $\mathbf{pp}/V$ and integrating it over the spatial and configurational spaces. We focus here on the first term on the right-hand side of Eq. (2.5), since the material derivative of the orientational divergence part of Eq. (2.5) is similarly derived in the literature [152]. First, the divergence operator is expanded to obtain

$$\begin{aligned} \frac{1}{V}\int_{\mathbf{p}}\int_{\mathbf{r}_c} \nabla_{\mathbf{x}} \cdot (\mathbf{D}_t \cdot \nabla_{\mathbf{x}}\Psi)\, \mathbf{pp} d\mathbf{r}_c d\mathbf{p} &= \frac{1}{V}\nabla_{\mathbf{x}} \cdot \nabla_{\mathbf{x}} \cdot \int_{\mathbf{p}}\int_{\mathbf{r}_c} \mathbf{D}_t\mathbf{pp}\Psi d\mathbf{r}_c d\mathbf{p} \\ &= D_\perp \nabla^2_{\mathbf{x}}\mathbf{A}_2 + \left(D_\parallel - D_\perp\right) \nabla_{\mathbf{x}}\nabla_{\mathbf{x}} : \mathbf{A}_4, \end{aligned} \tag{2.8}$$

Where $\mathbf{A}_4 = \frac{1}{V}\int_{\mathbf{p}}\int_{\mathbf{r}_c} \mathbf{pppp}\Psi d\mathbf{r}_c d\mathbf{p}$ is the fourth-order moment of $\Psi$. After the full derivation, the evolution of the tensor $\mathbf{A}_2$ is obtained

$$\begin{aligned} \frac{D\mathbf{A}_2}{Dt} =& -\frac{1}{2}(\boldsymbol{\omega} \cdot \mathbf{A}_2 - \mathbf{A}_2 \cdot \boldsymbol{\omega}) + \frac{\lambda}{2}(\dot{\boldsymbol{\gamma}} \cdot \mathbf{A}_2 + \mathbf{A}_2 \cdot \dot{\boldsymbol{\gamma}} - 2\mathbf{A}_4 : \dot{\boldsymbol{\gamma}}) \\ &+ 2D_r(c\boldsymbol{\delta} - \alpha\mathbf{A}_2) + D_\perp\nabla^2_{\mathbf{x}}\mathbf{A}_2 + \left(D_\parallel - D_\perp\right)\nabla_{\mathbf{x}}\nabla_{\mathbf{x}} : \mathbf{A}_4. \end{aligned} \tag{2.9}$$

(a) Two-dimensional random rods with concentration $c_1$.

(b) Perfectly aligned rods in the $x$ direction with concentration $c_1$.

(c) Two-dimensional random rods with concentration $c_2$.

(d) Perfectly aligned rods in the $x$ direction with concentration $c_2$.

Figure 2.1 – Representation of $\mathbf{A}_2$ in an elementary surface for different concentrations and orientations.

where $\alpha$ equals 2 in 2D and 3 in 3D. The full derivation of Eq. (2.9) is reported in Appendix A.1. It can be noticed that the time evolution of the tensor $\mathbf{A}_2$ depends on higher-order moments of $\Psi$. Hence, the problem requires a closure approximation. Fortunately, the standard closure approximations [44, 46, 156] can be applied for this case, where the particles are axisymmetric, by being careful to normalize the tensor $\mathbf{A}_2$ by $c$ to maintain the condition of having a unitary trace. The Tucker and coworkers model is recovered from Eq. (2.9) by setting the translational diffusion to zero (i.e., $D_\perp = D_\parallel = 0$) and then dividing by the trace of $\mathbf{A}_2$ [152]. The last term in Eq. (2.9) is the Hessian operator and the last two terms of Eq. (2.9) show implicitly the coupling between the local concentration and the local orientation of Brownian particles. It is explained in Sec. 2.2.4. The last two terms have been omitted in recent works but they can change drastically the obtained microstructures as we will discuss below [76, 153, 157, 158]. The derived macromodel enables one to solve a set of partial differential equations (PDEs) rather than a full 5D Fokker-Planck equation [Eq. (2.5)], to be discussed below, drastically simplifying the problem.

### 2.2.4 Concentration field of Brownian rods

The concentration field $c$ is represented by the trace of $\mathbf{A}_2$. So the evolution of concentration of the Brownian rods in a suspending fluid can be derived from Eq. (2.9)

$$\frac{Dc}{Dt} = D_\perp \nabla^2_{\mathbf{x}} c + (D_\parallel - D_\perp) \nabla_{\mathbf{x}} \nabla_{\mathbf{x}} : \mathbf{A}_2. \tag{2.10}$$

The last term in Eq. (2.10) (Hessian operator) shows the coupling between the concentration and the local orientation of the Brownian rods and it requires knowledge of $\mathbf{A}_2$, while $\mathbf{A}_2$ does not appear in the concentration equation when diffusion is isotropic (i.e., $D_\parallel = D_\perp$) .

### 2.2.5 Dimensionless formulation of the problem

The problem identified by Eq. (2.5) or by Eq. (2.9) in its tensor form, describes the evolution of spatial and orientational configurations of a suspension of Brownian rodlike particles in a flow field. These systems of equations will be analyzed numerically in the following sections. Choosing the particle length $L$ as the characteristic length and the characteristic strain rate $|\dot{\gamma}| = U_{avg}/L$, where $U_{avg}$ is the average flow velocity, the definitions of the dimensionless variables for the problem, denoted with an asterisk, are

$$t^* = t\,|\dot{\gamma}|\,, \tag{2.11}$$

$$\mathbf{u}^* = \frac{\mathbf{u}}{L\,|\dot{\gamma}|}, \tag{2.12}$$

$$Pe_r = \frac{|\dot{\gamma}|}{D_r}, \tag{2.13}$$

$$\dot{\mathbf{p}}_{\mathbf{j}}{}^* = \frac{\dot{\mathbf{p}}_{\mathbf{j}}}{|\dot{\gamma}|}, \tag{2.14}$$

and

$$\mathbf{D}^* = \frac{\mathbf{D}_t}{L^2\,|\dot{\gamma}|} = \frac{1}{Pe_\parallel}\mathbf{pp} + \frac{1}{Pe_\perp}\left(\boldsymbol{\delta} - \mathbf{pp}\right). \tag{2.15}$$

The rotary Peclet number ($Pe_r$) appears, which measures the distortion of the suspension orientation state from the anisotropic equilibrium orientation configuration, i.e., changing $Pe_r$ tends to affect the final orientation. It also shows the two translational Brownian Peclet numbers ($Pe_\parallel = L^2\,|\dot{\gamma}|\,/D_\parallel$) and ($Pe_\perp = L^2\,|\dot{\gamma}|\,/D_\perp$), along and orthogonal to the long axis of the rod, respectively. The dimensionless form of the Fokker-Planck equation becomes after dropping the asterisk

$$\frac{D\Psi}{Dt} = \nabla_{\mathbf{x}} \cdot \left\{ \left[ \frac{1}{Pe_\parallel}\mathbf{pp} + \frac{1}{Pe_\perp}\left(\boldsymbol{\delta} - \mathbf{pp}\right) \right] \cdot \nabla_{\mathbf{x}} \Psi \right\} - \nabla_{\mathbf{p}} \cdot (\dot{\mathbf{p}}_j \Psi) + \frac{1}{Pe_r} \nabla^2_{\mathbf{p}} \Psi. \tag{2.16}$$

For very long and thin rodlike particles, the relation $Pe_{\perp} = 2Pe_{\parallel}$ applies [40], and Eq. (2.15) simplifies as $\mathbf{D} = \frac{1}{Pe_{\perp}}(\mathbf{pp} + \boldsymbol{\delta})$ and $\lambda = 1$. Equation (2.16) is written as

$$\frac{D\Psi}{Dt} = \nabla_{\mathbf{x}} \cdot \left\{ \left[ \frac{1}{Pe_{\perp}}(\mathbf{pp} + \boldsymbol{\delta}) \right] \cdot \nabla_{\mathbf{x}}\Psi \right\} - \nabla_{\mathbf{p}} \cdot (\dot{\mathbf{p}}_j \Psi) + \frac{1}{Pe_r} \nabla^2_{\mathbf{p}} \Psi. \tag{2.17}$$

Using the same dimensionless variables, the evolution equation for the second-order moment of the probability distribution function in dimensionless form is

$$\begin{aligned} \frac{D\mathbf{A}_2}{Dt} =& -\frac{1}{2}(\boldsymbol{\omega} \cdot \mathbf{A}_2 - \mathbf{A}_2 \cdot \boldsymbol{\omega}) + \frac{1}{2}(\dot{\boldsymbol{\gamma}} \cdot \mathbf{A}_2 + \mathbf{A}_2 \cdot \dot{\boldsymbol{\gamma}} - 2\dot{\boldsymbol{\gamma}} : \mathbf{A}_4) \\ &+ \frac{2}{Pe_r}(c\boldsymbol{\delta} - \alpha \mathbf{A}_2) + \frac{1}{Pe_{\perp}} \nabla^2_{\mathbf{x}} \mathbf{A}_2 + \frac{1}{Pe_{\perp}} \nabla_{\mathbf{x}} \nabla_{\mathbf{x}} : \mathbf{A}_4. \end{aligned} \tag{2.18}$$

## 2.3 Flow problem

Under the assumptions of a Newtonian, isothermal, steady and incompressible fluid, the governing equations for the pressure, $P$, and velocity fields in the dimensionless form are

$$\nabla_{\mathbf{x}} \cdot \mathbf{u} = 0, \tag{2.19}$$

$$\nabla^2_{\mathbf{x}} \mathbf{u} - \nabla_{\mathbf{x}} P = \mathbf{0}. \tag{2.20}$$

For simplicity, we do not consider here the coupling between flow and the extra stresses induced by rods since the goal is first to verify the obtained macromodel predictions and compare them with the full numerical solution of Eq. (2.16). This coupling will be explored in future works. This hypothesis is acceptable here in the assumption of dilute concentration regimes. Hence the problem is fully characterized by two Peclet numbers, $Pe_r$ and $Pe_{\perp}$.

The work is performed in a planar channel [Fig 2.2(b)] of width $2H$ and length $W = 3H$, except for the case of the homogeneous inlet in a planar channel (Sec. 2.4.2), where $W = 9H$. These dimensions do not affect our conclusions. $H/L = 10^6$ ($H >> L$). In the second part of the work, a circular obstacle of radius $R = 0.5H$ is introduced [Fig. 2.2(b)], the center of the obstacle is at $x = H$. Four types of boundary conditions, marked by BC1 to BC4, are defined for this model. BC1 is the inlet velocity profile condition $U/U_{max} = 1 - (y/H)^2$ and the Dirichlet boundary conditions for $\Psi$; BC2 is the no slip condition at walls ($\mathbf{u} = \mathbf{0}$ ); BC3 is the outlet condition where the relative pressure is set to zero, $(-P\boldsymbol{\delta} + \nabla_{\mathbf{x}}\mathbf{u}) : \mathbf{nn} = 0$, where $\mathbf{n}$ is the normal vector to the surface; and BC4 is the symmetry boundary condition ($\mathbf{u} \cdot \mathbf{n} = 0$ and $\dot{\boldsymbol{\gamma}} - (\dot{\boldsymbol{\gamma}} \cdot \mathbf{n})\mathbf{n} = \mathbf{0}$). Due to BC4, half of the domain is considered in simulations to reduce computational efforts [see Fig. (2.2)]. The homogeneous Neumann boundary conditions (zero flux) is applied for the probability density function $\Psi$ in method 1 ($\mathbf{n} \cdot \nabla_{\mathbf{x}}\Psi = 0$ for spatial BCs (BC2, BC3 and BC4)

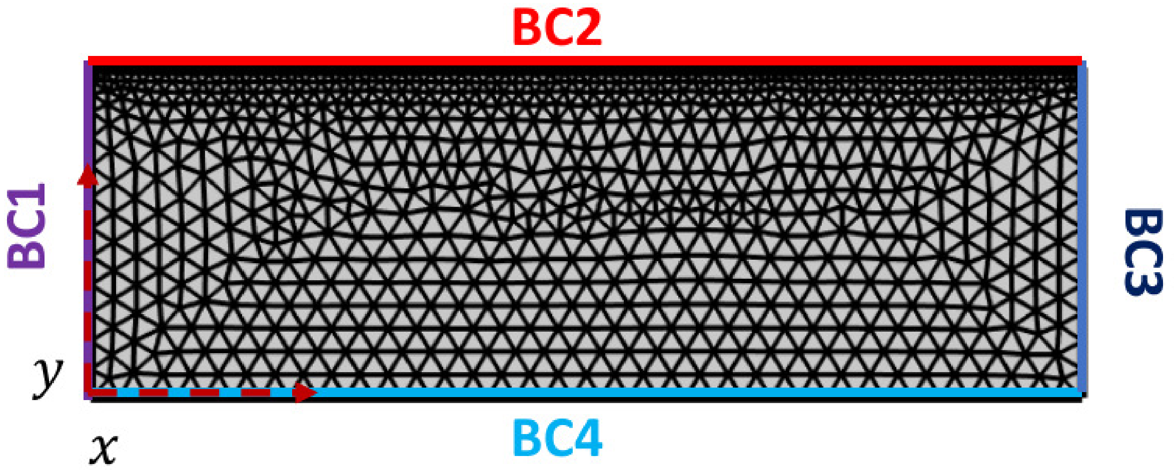

(a) Rectangular planar channel.

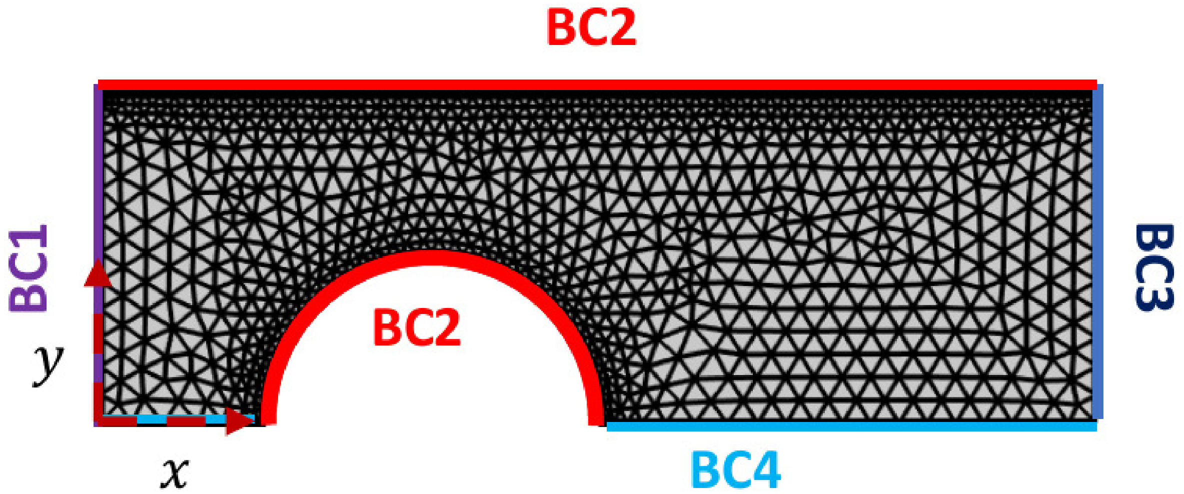

(b) Planar channel with circular obstacle.

Figure 2.2 – FE mesh for a planar channel. BC1,laminar inflow; BC2,pressure outlet; BC3,zero-slip condition; BC4,symmetry condition.

and $\mathbf{n} \cdot \nabla_{\mathbf{p}} \Psi = 0$ for configurational BCs [all the surfaces in Fig. A.1b except BC5)]. It is also used for $\mathbf{A}_2$ and $c$ in method 2 ($\mathbf{n} \cdot \nabla_{\mathbf{x}} \cdot A_{ij} = 0$. Where $A_{ij}$ are the components of $\mathbf{A}_2$ and $\mathbf{n} \cdot \nabla_{\mathbf{x}} c = 0$).

## 2.4 Numerical results

The steady state form of Eq. (2.17) is

$$\mathbf{u} \cdot \nabla_{\mathbf{x}} \Psi = \nabla_{\mathbf{x}} \cdot \left\{ \left[ \frac{1}{Pe_{\perp}} (\mathbf{pp} + \boldsymbol{\delta}) \right] \cdot \nabla_{\mathbf{x}} \Psi \right\} - \nabla_{\mathbf{p}} \cdot (\dot{\mathbf{p}}_j \Psi) + \frac{1}{Pe_r} \nabla_{\mathbf{p}}^2 \Psi, \tag{2.21}$$

and of Eq. (2.18) is

$$\begin{aligned} \mathbf{u} \cdot \nabla_{\mathbf{x}} \mathbf{A}_2 = &- \frac{1}{2} (\boldsymbol{\omega} \cdot \mathbf{A}_2 - \mathbf{A}_2 \cdot \boldsymbol{\omega}) + \frac{1}{2} (\dot{\boldsymbol{\gamma}} \cdot \mathbf{A}_2 + \mathbf{A}_2 \cdot \dot{\boldsymbol{\gamma}} - 2\dot{\boldsymbol{\gamma}} : \mathbf{A}_4) \\ &+ \frac{2}{Pe_r} (c\boldsymbol{\delta} - \alpha \mathbf{A}_2) + \frac{1}{Pe_{\perp}} \nabla_{\mathbf{x}}^2 \mathbf{A}_2 + \frac{1}{Pe_{\perp}} \nabla_{\mathbf{x}} \nabla_{\mathbf{x}} : \mathbf{A}_4. \end{aligned} \tag{2.22}$$

Equations (2.19), (2.20) and (2.21), and Eqs. (2.19), (2.20) and (2.22) are solved numerically using method 1 and method 2, respectively [see Appendix (A.2)]. Both methods use the finite-element method (FEM). The numerical solutions are tested at steady state and for 2D flows to reduce computational time. Method 1 is based on the linear extrusion of 2D flow channel, represents the spatial distribution in $xy$ plane, to a third dimension, which stands for the probability of finding a rod of orientation angle with the $x$ axis $\phi$. Method 2 is based on solving the set of equations of evolution of $A_{11}$, $A_{12}$, and $A_{22}$ in the flow.

### 2.4.1 Method 1 verification

**Homogeneous systems**

To verify the numerical solution of the model, we compare the model with published data in the case of an homogeneous system [96, 98]. The flow field is assumed to be at steady state. In this case, the streamlines are parallel to each other and parallel to the wall. No Brownian translational diffusion is taken into consideration. The flow inside the channel is described as a planar Poiseuille flow in the direction of $x$. These assumptions allow us to study the rod orientations in the flow channel, since the shear rate in the Poiseuille flow is constant along each streamline. Rods are assumed to have a random-planar distribution of homogeneous concentration at the inlet, which means a Dirichlet boundary condition of $\Psi = 1/2\pi$.

To verify the results of the FEM in a homogeneous system, rod orientations at a chosen streamline is compared with the results found in the literature [see Fig. (2.3)]. Equation (2.21) is solved using a homogenous numerical diffusion to stabilize the numerical scheme, which gives

$$\mathbf{u} \cdot \nabla_{\mathbf{x}} \Psi = \frac{1}{Pe_{num}} \nabla_{\mathbf{x}}^2 \Psi - \nabla_{\mathbf{p}} \cdot (\dot{\mathbf{p}}_j \Psi) + \frac{1}{Pe_r} \nabla_{\mathbf{p}}^2 \Psi. \tag{2.23}$$

$Pe_{num}$ is an artificial diffusion Peclet number, set to value $10^9$, which has no physical effect except for stabilizing the numerical scheme. The study is done for values of rotary Peclet number $Pe_r$= 1, 10, 100, and 1000. The orientation state of the rods is represented by the components of the second-order orientation tensor $\boldsymbol{a}_2$ ($\boldsymbol{a}_2 = \int_{\mathbf{p}} \mathbf{pp}\psi d\mathbf{p}$, where $\psi$ is the probability distribution function of finding a rod of orientation $\mathbf{p}$ at time $t$ in a homogeneous systems [152]) [see Fig. (2.3)]. In addition, these quantities are traced spatially along the channel for $Pe_r = 100$ and compared with the results in the literature (Fig 2.4).
The $a_{11}$ and $a_{12}$ components are directly computed from the FP equation for planar orientations and compared with the results obtained by Férec *et al.* [96] solving the configurational part of Eq. (2.5) with a finite-volume method approach. Figure 2.3 shows the very good agreement between the two methods. Figure 2.4 shows that rods along the fixed wall become highly oriented and reach its final orientation almost instantly, whereas rods further downstream must travel quite a distance to reach the steady state. These results (Fig 2.4) show agreement with the work done by Mezi *et al.* [98], where we get $\mathbf{A}_2/c = \boldsymbol{a}_2$.

**Nonhomogeneous systems**

A concentration gradient is imposed at the inlet along the $y$ axis. The Dirichlet boundary condition is set to be $\Psi = \frac{c_0}{2\pi}$, where $c_0 = 1 - 0.6\,(y/H)^2$ is the concentration at the inlet. This parabolic concentration gradient is chosen to have a nonzero concentration in the domain ($c_0 = 0.4$ at the walls and $c_0 = 1$ at the center). Rod orientations are planar random at the inlet and no Brownian translational diffusion is considered. BC1, BC2, BC3, and BC4 are taken into account. In these conditions, the rods are affected by pure translational convection of the flow, and no rod migration across the streamlines is expected. The effect of concentration gradients on rod orientation distribution is a major concern. $A_{11}/c$ and $A_{12}/c$ components are directly computed from the FP equation in the channel for $Pe_r$ = 1, 10, 100, and 1000. The results are similar to the previous part when homogeneous concentration along the channel is examined [see Figs. (2.3 )and (2.4)].

### 2.4.2 Effect of translational diffusion

We aim now to study the effect of the anisotropic translational diffusion on rod suspensions in a planar channel. Equations (2.19), (2.20) and (2.21) are solved based on method 1. Three regimes of translational and orientational diffusions are studied. The first regime, $Pe_\perp \ll Pe_r$, explores the case when the timescale for translational diffusion is longer than the rotational diffusion

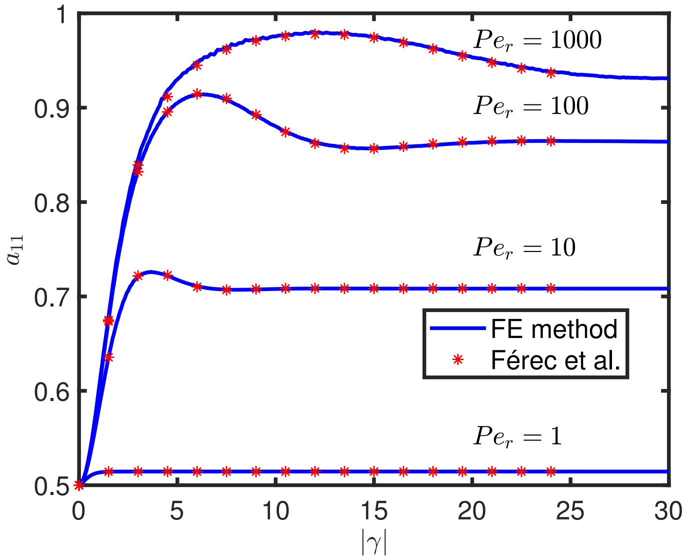

(a) Evolution of orientation component $a_{11}$ as a function of strain $|\gamma|$.

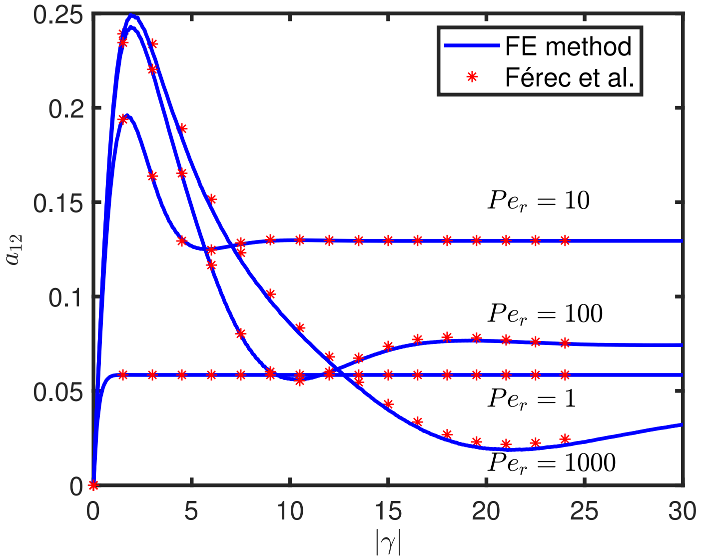

(b) Evolution of orientation component $a_{12}$ as a function of strain $|\gamma|$.

Figure 2.3 – $a_{11}$ and $a_{12}$ versus strain for the streamline along the line $y = 0.9H$ in a planar channel, with $|\dot{\gamma}| = 1.8/s$. Method 1 is verified with the work of Férec *et al.* [96]

.

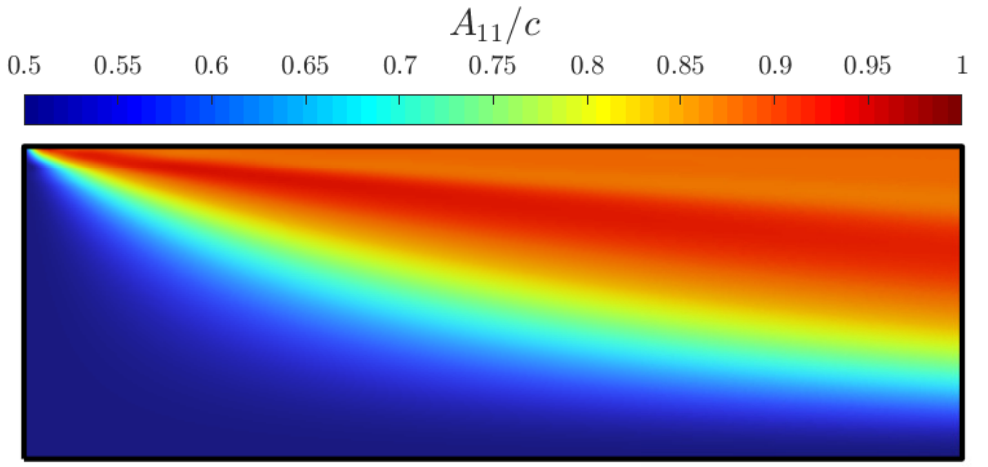

(a) Distribution of the orientation component $A_{11}/c$ in the $xy$ plane of a planar channel.

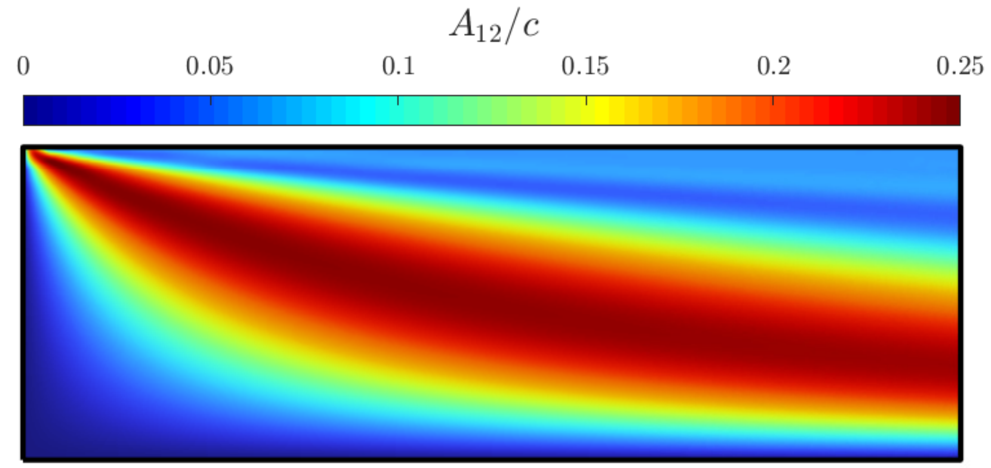

(b) Distribution of the orientation component $A_{12}/c$ in the $xy$ plane of a planar channel.

Figure 2.4 – (a) $A_{11}/c$ and (b) $A_{12}/c$ components of the orientation tensor, $\mathbf{A}_2$, along the channel in a homogeneous system, where concentration equals 1 at the inlet and no rod migrations occur.

one. The second regime, $Pe_{\perp} = Pe_r$, considers the case where both timescales are equal, and the third regime, $Pe_{\perp} \gg Pe_r$, investigates the case where the rotary diffusion is faster than the translational diffusion. A local rotary, perpendicular, and parallel Peclet numbers are introduced depending on the local strain rate, $\dot{\gamma}_l = \sqrt{\frac{1}{2}(\dot{\gamma} : \dot{\gamma})}$, $Pe_{r_{local}} = |\dot{\gamma}_l| / D_r$, $Pe_{\perp_{local}} = (|\dot{\gamma}_l| \, H^2)/D_{\perp}$, and $2Pe_{\|_{local}} = Pe_{\perp_{local}}$, respectively. In a planar channel, the local Peclet numbers are constant along the flow direction ($x$ axis). The variation of local rotational and perpendicular Peclet numbers along the $y$ axis are shown in Figs. 2.5a and 2.5b. The rod suspensions are affected by the global and local Peclet numbers.

### Homogeneous concentration and planar random orientation at the inlet

The rod concentration and orientation predictions are examined for a Dirichlet boundary condition $\Psi = 1/2\pi$. Figures (2.6) and (2.7) show that Brownian rods exhibit an inhomogeneous orientation through the channel. This is because of the competition between shear flow, which tends to align the rods in the flow direction, and Brownian motion, which tends to randomize their orientations [123, 138, 159]. The overshoot in the rod orientations before reaching the final orientation [see Fig. (2.3)] is noticed in the channel. Depending on the rotary Peclet number, rods near the wall reaches their final orientation faster than the rods at the center due to the higher value of $Pe_{r_{local}}$ near the wall. For all the studied cases, $A_{12}/c$ range between 0 and 0.25, which means that the angle between the rod and $x$ axis ranges from 0 to $\frac{\pi}{2}$. Figure (2.8) shows that rods tend to migrate toward the walls, where $Pe_{\perp_{local}}$ is high.
This phenomenon was also predicted by Schiek and Shaqfeh [113], and by Nitsche and Hinch [112]. In Fig. 2.8(a) (where the high translational Peclet number, $Pe_{\perp} = 10^3$, and low rotary Peclet number, $Pe_r = 10$, are considered), rods migrate toward the wall. While in Fig. 2.8(b) (where the high translational Peclet number, $Pe_{\perp} = 10^3$, and high rotary Peclet number, $Pe_r = 10^3$, are considered) a high concentration is observed at the wall after the inlet. After a distance, rods accumulate between the center and the wall ($0.3 \leq y/H \leq 0.8$). This accumulation is due to the overshoot in rod orientations. Rods higher alignment leads to low migrations across the streamlines. At lower $Pe_{\perp}$, rod migration is more evident. In Fig. (2.8c), rod migration occurs and a concentration gradient is observed at the outlet. In this case, rods are less aligned, mainly in the center, which enhances rod migration toward the wall (higher local Peclet numbers). For the case of low translational Peclet number and high rotational Peclet number ( $Pe_{\perp} = 10$ and $Pe_r = 10^3$), rods are highly aligned at the outlet and almost homogeneous [Fig 2.6(d)]. Since the rod orientations tend to equilibrate significantly at lower strain than their center of mass translate in the flow direction. While the values of $A_{11}/c$ is low near the wall [comparing with Fig. 2.6(b)] due to the migration of less aligned rods toward the wall.

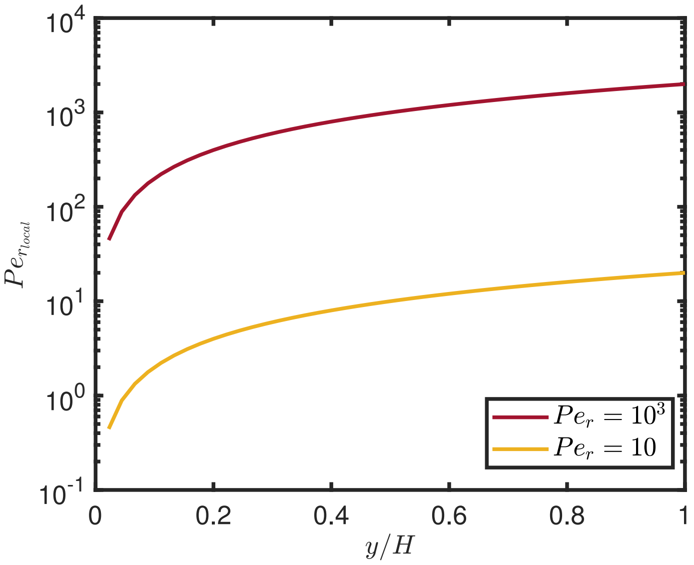

(a) Evolution of the local rotary Peclet number, $Pe_{r_{local}}$, with respect to the normalized channel width, $y/H$, independent on the translational Peclet number.

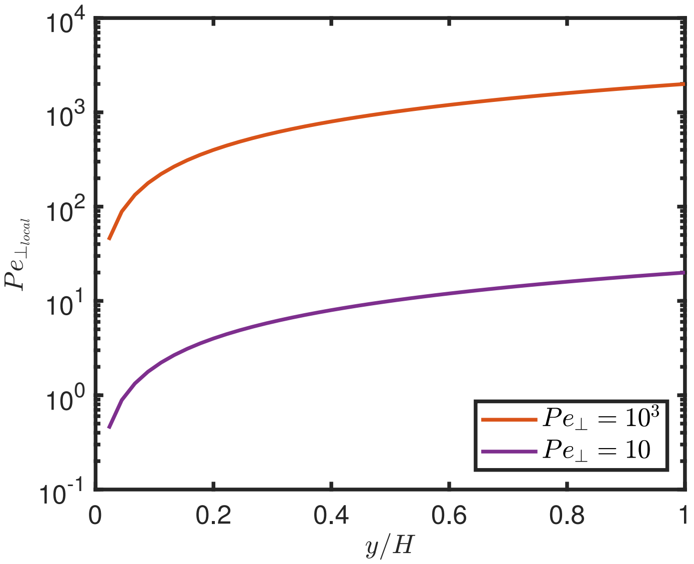

(b) Evolution of the local translational Peclet number, $Pe_{\perp_{local}}$, with respect to the normalized channel width $y/H$ independent on the rotary Peclet number.

Figure 2.5 – Variation of local Peclet numbers with respect to the normalized channel width in a planar channel for the global Peclet numbers $Pe_\perp = 10, 10^3$ and $Pe_r = 10, 10^3$.

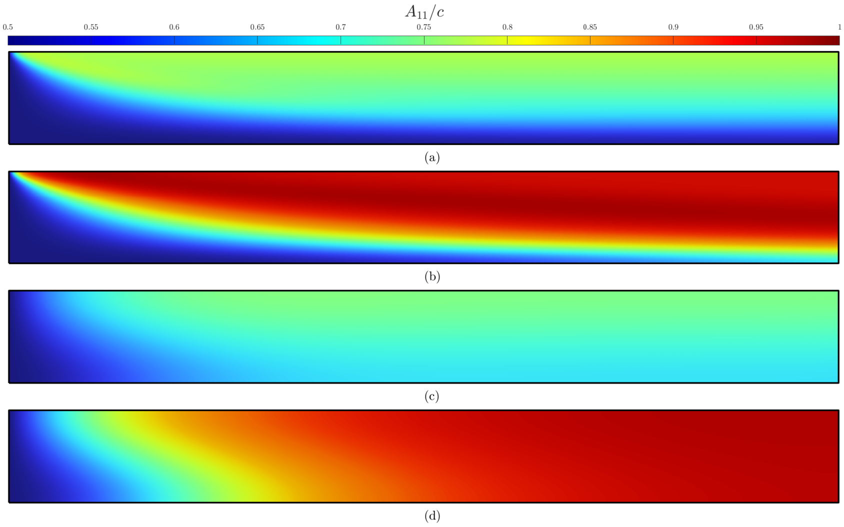

Figure 2.6 – Orientation component $A_{11}/c$ using method 1, across the planar channel, where homogeneous concentration and random orientation of the rods are prescribed at the inlet for a) $Pe_r = 10, Pe_\perp = 10^3$, b) $Pe_r = 10^3, Pe_\perp = 10^3$, c) $Pe_r = 10, Pe_\perp = 10$, d) $Pe_r = 10^3, Pe_\perp = 10$.

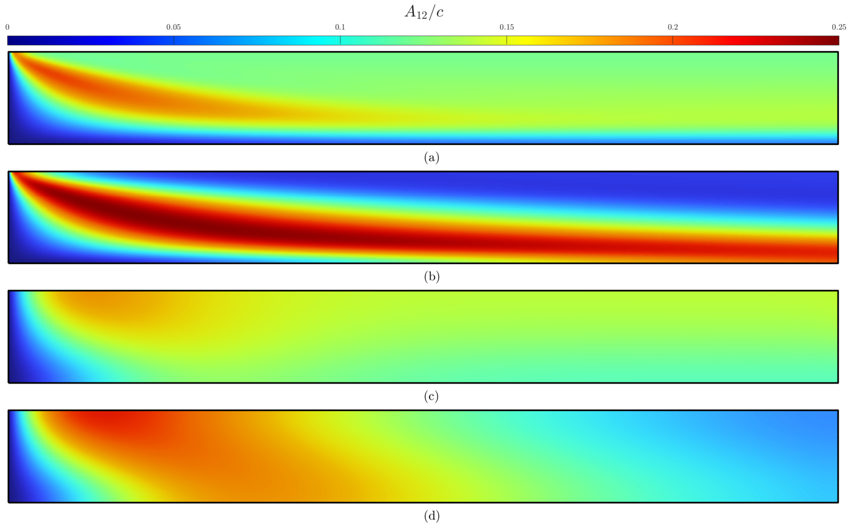

Figure 2.7 – Orientation component $A_{12}/c$ using method 1, across the planar channel, where homogeneous concentration and random orientation of the rods are prescribed at the inlet for a) $Pe_r = 10, Pe_\perp = 10^3$, b) $Pe_r = 10^3, Pe_\perp = 10^3$, c) $Pe_r = 10, Pe_\perp = 10$, d) $Pe_r = 10^3, Pe_\perp = 10$.

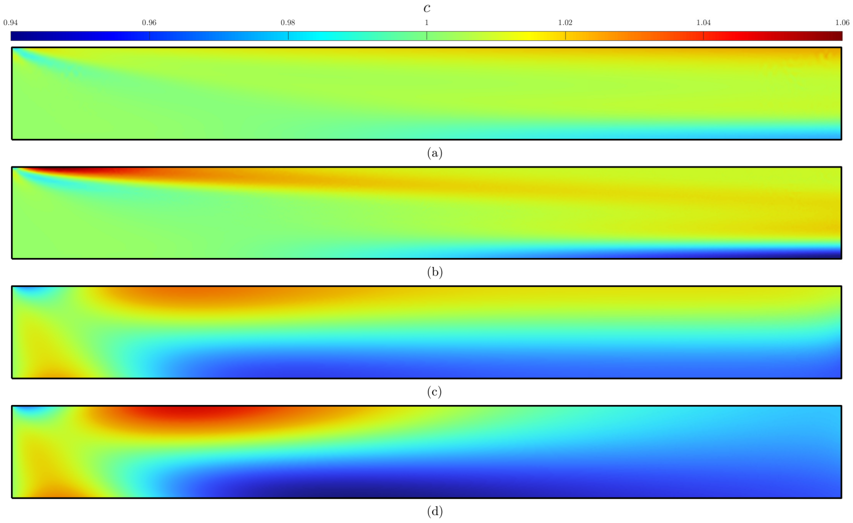

Figure 2.8 – Concentration distribution $c$ using method 1, across the planar channel, where homogeneous concentration and random orientation of the rods are prescribed at the inlet for a) $Pe_r = 10, Pe_\perp = 10^3$, b) $Pe_r = 10^3, Pe_\perp = 10^3$, c) $Pe_r = 10, Pe_\perp = 10$, d) $Pe_r = 10^3, Pe_\perp = 10$.

### Effect of concentration gradient at the inlet

A concentration gradient is introduced with a planar random orientation at the inlet $\Psi = c_i/(2\pi)$ to study its effect on the final rod suspension microstructures. Four different parabolic concentration profiles at the inlet are tested according to $c_i = -\frac{10-2i}{10}(y/H)^2 + 1$ for $i = 1, 2, 3,$ and 4. Same effect of translational and rotational Peclet numbers is figured qualitatively as the previous section (Sec. 2.4.2). No notable effect of concentration gradient on the orientation is shown. Rods are oriented similar to the case where homogeneous concentration is applied at the inlet (same plots for $A_{11}/c$ and $A_{12}/c$ in Figs. 2.6 and 2.7). This agrees with the results in Sec. 2.4.1. However, concentration gradient at the inlet has a significant effect on rod migration rates. The relative changes in concentration ($\frac{|c-c_i|}{average(c_i)}$) are plotted at the outlet for $Pe_\perp = 10$ and $Pe_r = 10^3$ in Fig. 2.9. Figure 2.9 shows that rod migrations are higher near the wall, where the concentration is the lowest for the four cases explored, and the gradient of local translational Peclet number is the highest. As concentration gradient increases, rods migrate at higher rates due to rod migration from low to high translational $Pe_{\perp_{local}}$ regions.

## 2.4.3 Effect of rod orientations gradient at the inlet

To study the effect of rod orientations on its migration across streamlines, an orientation gradient is introduced at the inlet, where the Dirichlet boundary condition is $\Psi = [\frac{1}{2\pi}\left(e^{\beta}\ sin^2\phi + e^{-\beta}cos^2\phi\right)^{-1}]/2,$

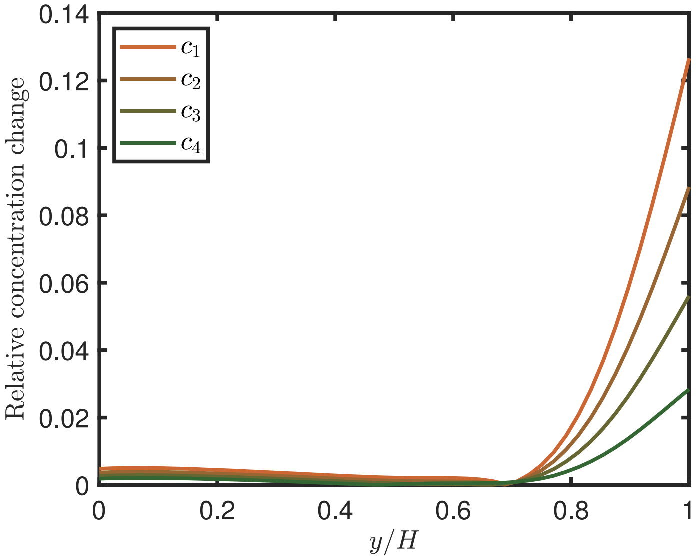

Figure 2.9 – Relative change in concentration with respect to the normalized channel width, $y/H$, at the outlet, for $Pe_r = 10^3$ and $Pe_\perp = 10$, for the four concentration gradients $c_1$, $c_2$, $c_3$ and $c_4$.

and $\beta = \frac{5y}{2H}$, where rods are planar random at the center of the channel and highly aligned in the direction of the flow near the walls [see Fig. (2.10)] for $A_{11}$, and $A_{12} = 0$]. The concentration is homogeneous and equals one at the inlet. Figure 2.11 shows that rods migrate toward the wall, where higher $Pe_{\perp_{local}}$. Comparing with the case of homogeneous concentration and planar random orientation at the inlet (Sec. 2.4.2), the concentration at the center is almost the same, while near the wall, rods are more accumulated in the case of planar random at the inlet (comparing the case $Pe_r = 10^3, Pe_\perp = 10^3$ directly after the inlet. $c = 1.02$ where rods are perfectly aligned [Fig 2.11(b) ] and $c = 1.06$ where rods are planar random [Fig 2.8(b)]. For lower translational Peclet number, $Pe_\perp = 10$, rods are accumulated at the upper part [Figs. 2.11(c) and 2.11(d)]. In this zone, the migration of aligned particles is difficult.

Qualitatively, the effect of orientation gradient at the inlet with the presence of the circular obstacle is similar to its effect in the absence of the obstacle.

### 2.4.4 Results of flow in a channel with a circular obstacle

Modeling the interaction between suspended rods and obstacles encountered in their flow is critical for understanding particulate suspension transport in various engineering applications [160, 161]. A complex flow field is also interesting to explore here because of the expected variation of both local Peclet numbers along and perpendicular to the flow direction. The velocity magnitude with some streamlines Fig. 2.12 depicts the variation of local Peclet numbers along a horizontal

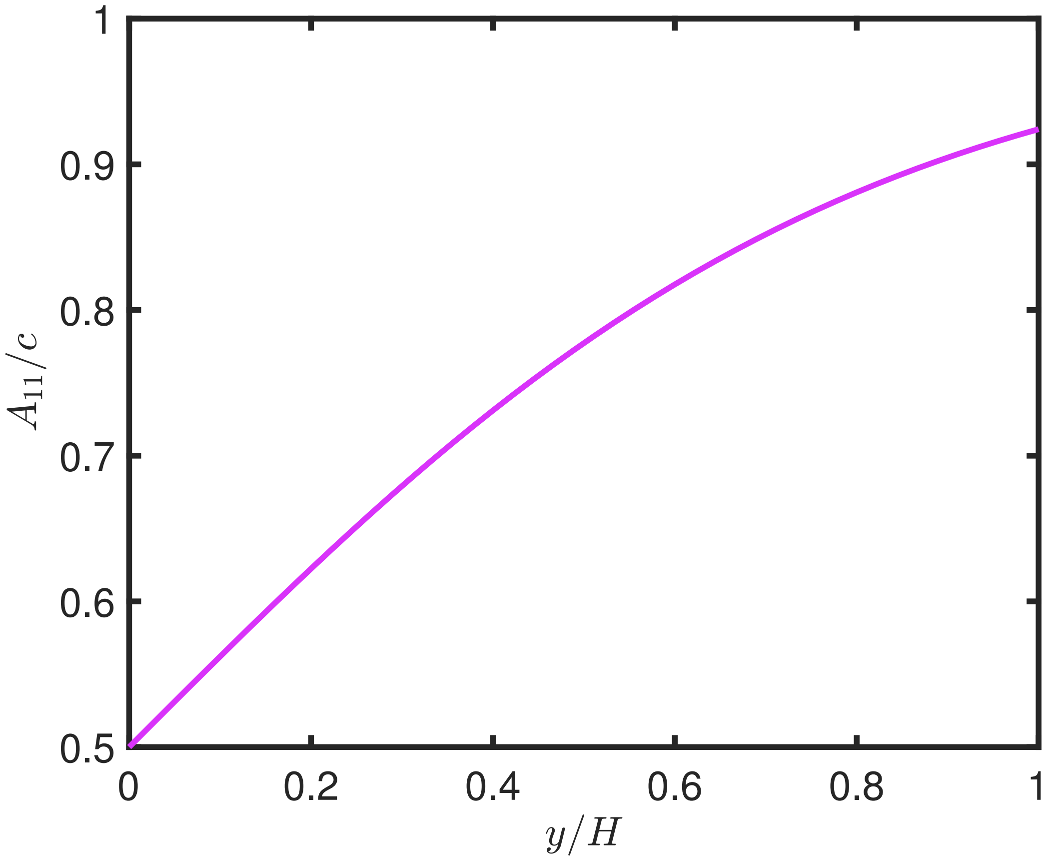

Figure 2.10 – Orientation component $A_{11}/c$ with respect to the normalized channel width, $y/H$, at the inlet.

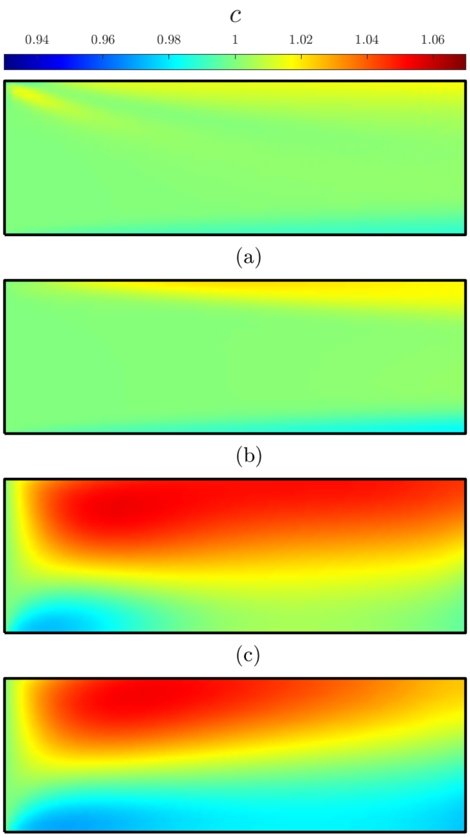

(a)

(b)

(c)

(d)

Figure 2.11 – Concentration distribution $c$ using method 1, across the planar channel, where homogeneous concentration and random orientation of the rods are at the inlet for a) $Pe_r = 10, Pe_\perp = 10^3$, b) $Pe_r = 10^3, Pe_\perp = 10^3$, c) $Pe_r = 10, Pe_\perp = 10$, d) $Pe_r = 10^3, Pe_\perp = 10$.

line at $y = 0.7H$. It shows that the local Peclet numbers have minima above the center ($x = H$) of the obstacle, and maxima around the level of the extremities of the obstacle ($x = 0.5H$ and $x = 1.5H$). Figure 2.13 shows the variation of local Peclet numbers along a vertical line $x = H$. It shows that the local Peclet numbers have maxima near the wall and the obstacle, where the highest shear rate is found. Simulations are performed to study the effect of circular obstacles in the channel on the concentration and orientation.

In the presence of circular obstacle, rods are highly concentrated at the back of the obstacles and depleted in the front [162] as seen in Fig. 2.14. Even in the presence of the obstacle, rods have higher tendency to migrate toward the wall. Rods are more aligned at the back of the obstacle, as in Fig. 2.15 than at the front. This was also found by Phan-Thien and Graham [163], who used a single falling sphere in semiconcentrated systems, and by Kumar and Natale [164], who studied at low Reynolds values, two settling non-Brownian rigid spheres in a dilute suspension of Brownian rods. At the front of the obstacle, we find that the local orientation of the rods are aligned in the $y$ direction ($A_{11}/c \leq 0.5$, and $A_{12}/c \leq 0$ ), as in Figs. (2.15) and (2.16). This is caused by the high shear rate zone, located above the obstacle. There, rods are less concentrated and less aligned because lower local Peclet numbers [see Fig. (2.13)]. Also, we see that rods have high alignment near the wall, even in the presence of circular obstacle due to the high local rotational Peclet numbers.

### 2.4.5 Macromodel

Although solving the Fokker-Planck equation is precise and general, it requires high computational effort. The second-moment tensor evolution [Eq. (2.22)] provides a concise description requiring less computational power. It is necessary to utilize a closure approximation to relate the fourth-order moment tensor with the second-order moment tensor to solve Eq. (2.22). Closure approximations found in the literature can be applied for this model. The numerical method 2 mentioned in Appendix A.2 is used to solve Eq. (2.22), using quadratic [156] and IBOF [46] closures. We applied the quadratic closure for its simplicity, while the IBOF for its precision. This macromodel is tested for homogeneous concentration, and planar random rod orientations at the inlet (Dirichlet BC6 $A_{11}/c = A_{22}/c = 0.5$ and $A_{12}/c = 0$ ). Figures (2.17) and (2.19) show the concentration results of rods in the channel for quadratic and IBOF closures, respectively. Figures (2.18) and (2.20) show the orientation component $A_{11}/c$ using the mentioned closures. These figures show a quantitative agreement between the full solution of the FP equation and the macromodel nevertheless the use of the closure approximations. Tables 2.1 and 2.2 show the maximum and mean absolute error percentage values along the channel for concentration $c$ and orientation component $A_{11}/c$, respectively. The IBOF closure provides an excellent agreement for the concentration and orientation, better than the quadratic. For IBOF, the errors with respect to the solutions obtained solving the FP equation [Eq. (2.16)]

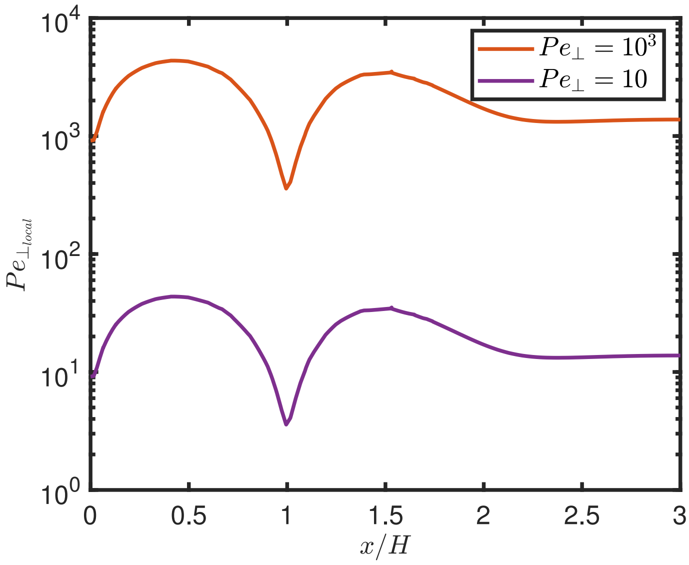

(a) Evolution of the local translational Peclet number, $Pe_{\perp_{local}}$, with respect to the normalized channel length, $x/H$, independent on the translational Peclet number.

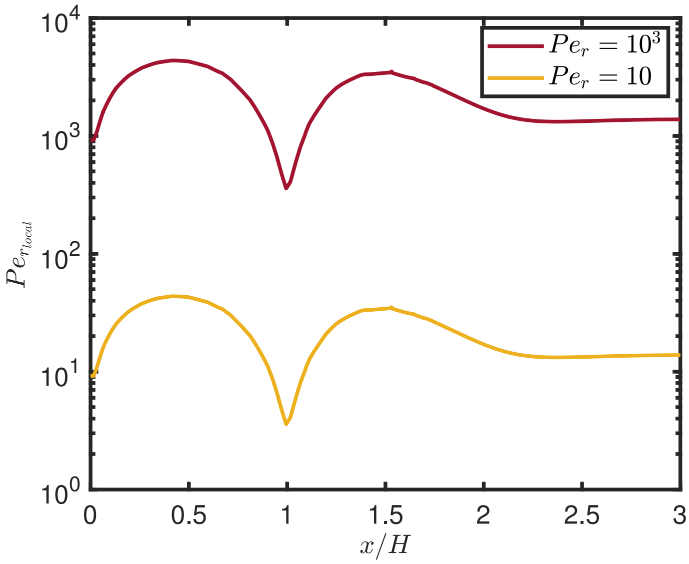

(b) Evolution of the local rotary Peclet number, $Pe_{r_{local}}$, with respect to the normalized channel length $x/H$ independent on the rotary Peclet number.

Figure 2.12 – Variation of local Peclet numbers with respect to the normalized channel width at the streamline $y = 0.7H$ in a planar channel with the presence of circular obstacle.

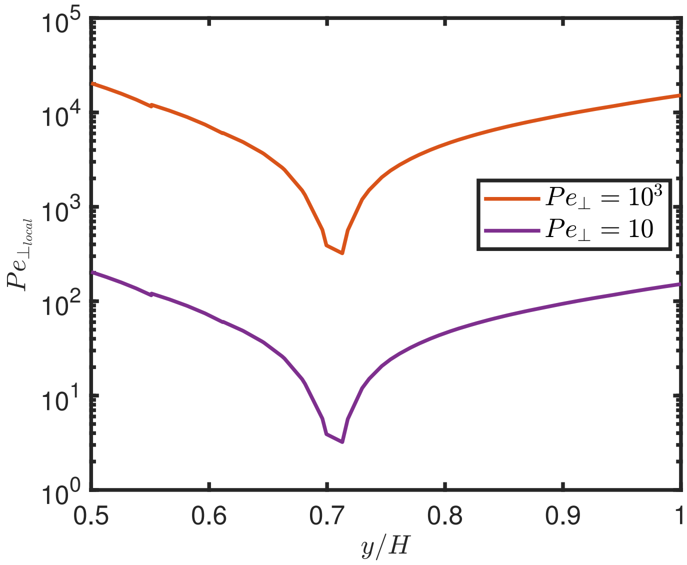

(a) Evolution of the local translational Peclet number, $Pe_{\perp_{local}}$, with respect to the normalized channel width, $y/H$, independent on the translational Peclet number.

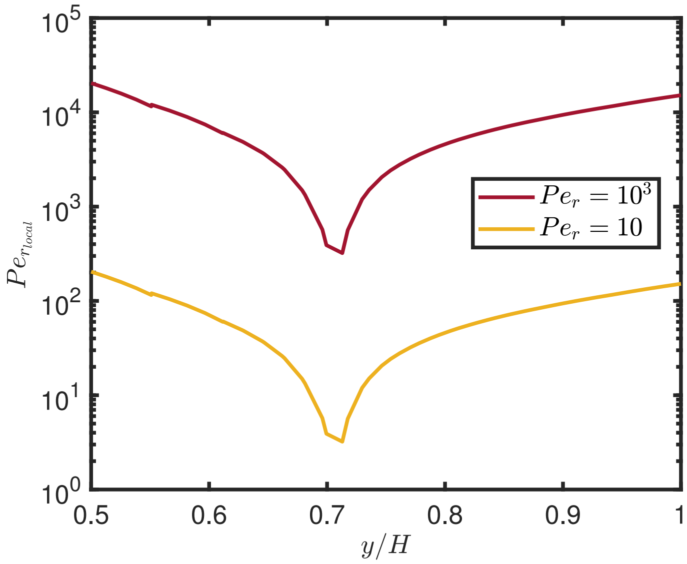

(b) Evolution of the local rotary Peclet number, $Pe_{r_{local}}$, with respect to the normalized channel width, $y/H$, independent on the rotary Peclet number.

Figure 2.13 – Variation of local Peclet numbers with respect to the normalized channel length at $x = H$ in a planar channel with the presence of circular obstacle.

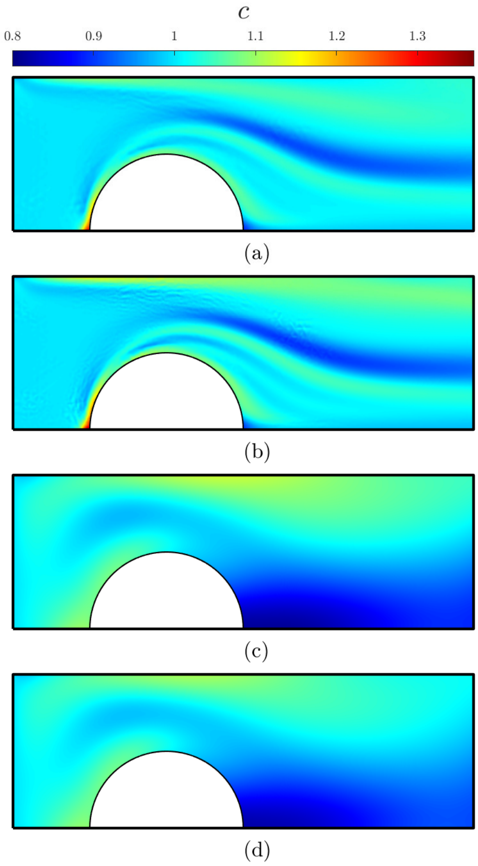

Figure 2.14 – Concentration distribution $c$ using method 1, across the planar channel with the presence of circular obstacle, where homogeneous concentration and random orientation of the rods are prescribed at the inlet for a) $Pe_r = 10, Pe_\perp = 10^3$, b) $Pe_r = 10^3, Pe_\perp = 10^3$, c) $Pe_r = 10, Pe_\perp = 10$, d) $Pe_r = 10^3, Pe_\perp = 10$.

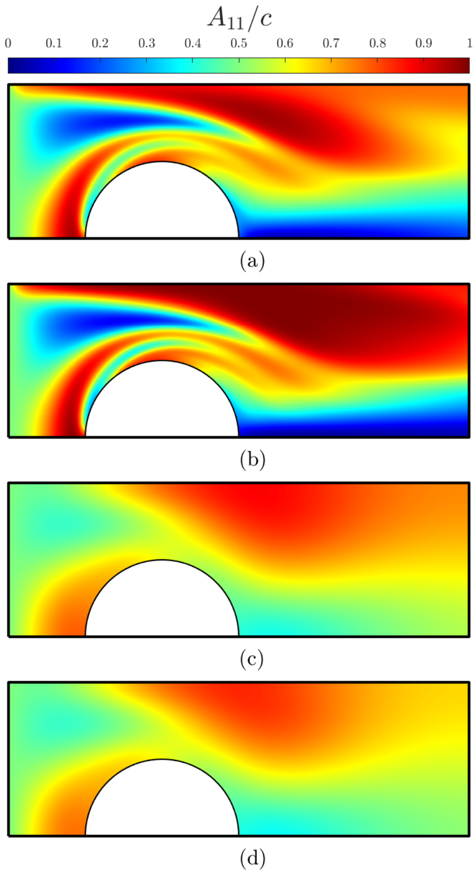

(a)

(b)

(c)

(d)

Figure 2.15 – Orientation component $A_{11}/c$ using method 1, across the planar channel with the presence of circular obstacle, where homogeneous concentration and random orientation of the rods are prescribed at the inlet for a) $Pe_r = 10, Pe_\perp = 10^3$, b) $Pe_r = 10^3, Pe_\perp = 10^3$, c) $Pe_r = 10, Pe_\perp = 10$, d) $Pe_r = 10^3, Pe_\perp = 10$.

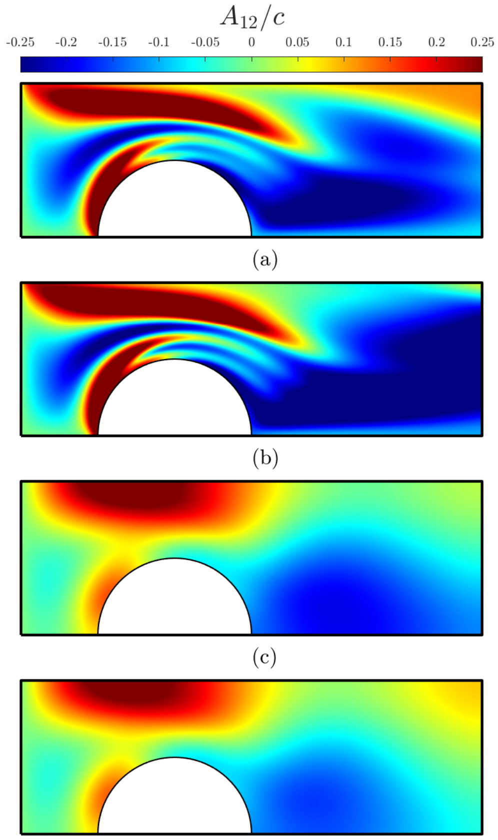

(a)

(b)

(c)

(d)

Figure 2.16 – Orientation component $A_{12}/c$ orientation component using method 1, across the planar channel with the presence of circular obstacle, where homogeneous concentration and random orientation of the rods are prescribed at the inlet for a) $Pe_r = 10, Pe_\perp = 10^3$, b) $Pe_r = 10^3, Pe_\perp = 10^3$, c) $Pe_r = 10, Pe_\perp = 10$, d) $Pe_r = 10^3, Pe_\perp = 10$.

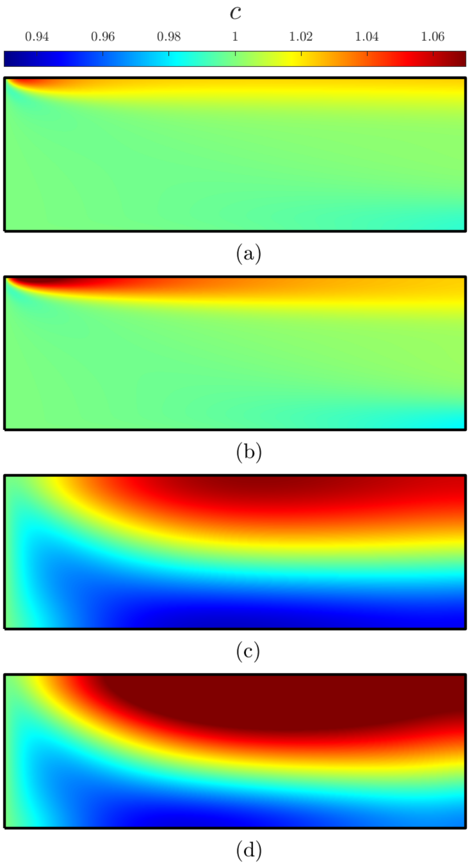

Figure 2.17 – Concentration distribution $c$ results using a quadratic closure approximation, across the planar channel, where homogeneous concentration and random orientation of the rods are prescribed at the inlet for a) $Pe_r = 10, Pe_\perp = 10^3$, b) $Pe_r = 10^3, Pe_\perp = 10^3$, c) $Pe_r = 10, Pe_\perp = 10$, d) $Pe_r = 10^3, Pe_\perp = 10$.

across the channel does not exceed 5% for both concentration and orientation component $A_{11}/c$ for the tested cases (Tables 2.1 and 2.2 ), while the mean absolute errors are much lower than the error values obtained using the quadratic closure. These results further demonstrate the validity of the derived macromodel also for nonhomogeneous systems. The mean absolute error is affected by $Pe_r$ and $Pe_\perp$. The tested cases using the quadratic closure show that the mean absolute errors for both orientation and concentration increase with decreasing the rotary and the perpendicular Peclet numbers. While for IBOF, the relation between the Peclet numbers and the mean absolute errors is unclear.

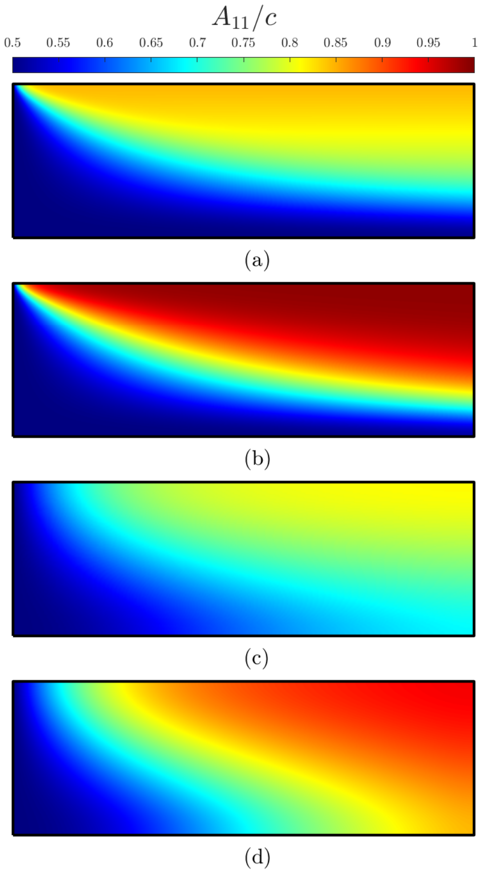

(a)

(b)

(c)

(d)

Figure 2.18 – Orientation component $A_{11}/c$ results using a quadratic closure approximation, across the planar channel, where homogeneous concentration and random orientation of the rods are prescribed at the inlet for a) $Pe_r = 10, Pe_\perp = 10^3$, b) $Pe_r = 10^3, Pe_\perp = 10^3$, c) $Pe_r = 10, Pe_\perp = 10$, d) $Pe_r = 10^3, Pe_\perp = 10$.

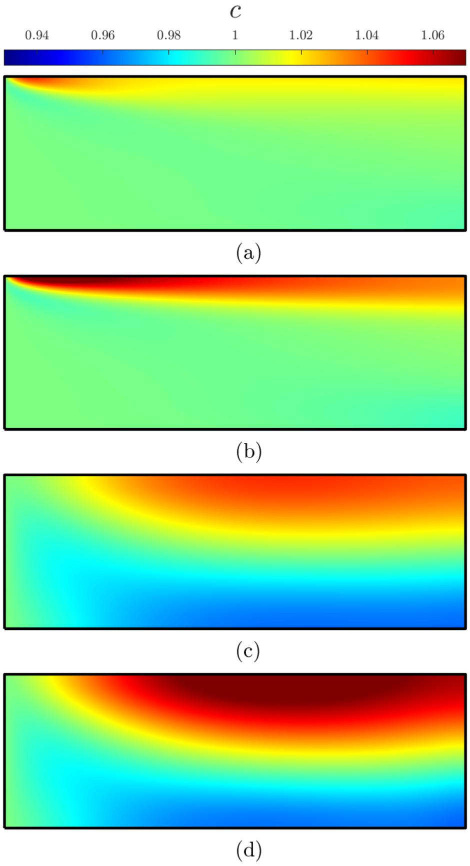

Figure 2.19 – Concentration distribution $c$ results using the IBOF closure approximation, across the planar channel, where homogeneous concentration and random orientation of the rods are prescribed at the inlet for a) $Pe_r = 10, Pe_\perp = 10^3$, b) $Pe_r = 10^3, Pe_\perp = 10^3$, c) $Pe_r = 10, Pe_\perp = 10$, d) $Pe_r = 10^3, Pe_\perp = 10$.

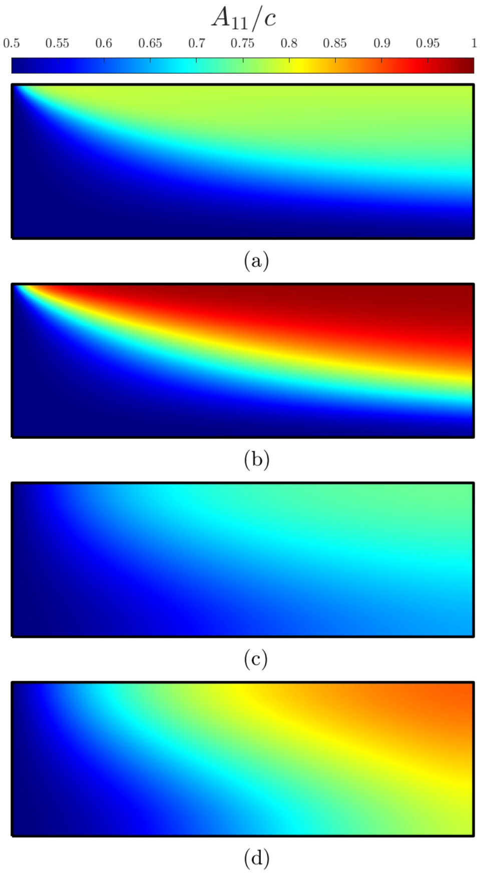

Figure 2.20 – Orientation component $A_{11}/c$ results using the IBOF closure approximation, across the planar channel, where homogeneous concentration and random orientation of the rods are prescribed at the inlet for a) $Pe_r = 10, Pe_\perp = 10^3$, b) $Pe_r = 10^3, Pe_\perp = 10^3$, c) $Pe_r = 10, Pe_\perp = 10$, d) $Pe_r = 10^3, Pe_\perp = 10$.

Tableau 2.1 – Values of the maximum percentage error and the mean absolute percentage error for concentration $c$, $CE_{max}$ and $CE_{mean}$, respectively, using the IBOF and quadratic closures with respect to the results in method 1.

| | Percentage error of concentration $c$ (CE) | | | |
|---|---|---|---|---|
| | IBOF closure | | Quadratic closure | |
| | $CE_{max}$ | $CE_{mean}$ | $CE_{max}$ | $CE_{mean}$ |
| $Pe_r = 10$<br>$Pe_{\perp} = 10^3$ | 4.89% | 2.45% | 7.08% | 3.94% |
| $Pe_r = 10^3$<br>$Pe_{\perp} = 10^3$ | 4.62% | 0.42% | 5.88% | 0.46% |
| $Pe_r = 10$<br>$Pe_{\perp} = 10$ | 4.14% | 1.39% | 6.38% | 2.46% |
| $Pe_r = 10^3$<br>$Pe_{\perp} = 10$ | 4.24% | 0.28% | 5.27% | 0.44% |

Tableau 2.2 – Values of the maximum percentage error and the mean absolute percentage error for orientation component $A_{11}/c$, $OE_{max}$ and $OE_{mean}$, respectively, using the IBOF and quadratic closures with respect to the results in method 1.

| | Percentage error of orientation $A_{11}/c$ (OE) | | | |
|---|---|---|---|---|
| | IBOF closure | | Quadratic closure | |
| | $OE_{max}$ | $OE_{mean}$ | $OE_{max}$ | $OE_{mean}$ |
| $Pe_r = 10$<br>$Pe_{\perp} = 10^3$ | 3.07% | 1.31% | 16.01% | 6.62% |
| $Pe_r = 10^3$<br>$Pe_{\perp} = 10^3$ | 3.17% | 0.29% | 14.92% | 5.3% |
| $Pe_r = 10$<br>$Pe_{\perp} = 10$ | 1.7% | 0.78% | 14.45% | 7.32% |
| $Pe_r = 10^3$<br>$Pe_{\perp} = 10$ | 2.21% | 0.84% | 13.51% | 6.56% |

## 2.5 Conclusion

The major contribution of this work is the derivation of a macromodel to investigate the flow of Brownian particle suspensions taking into account the coupling between the concentration and the orientation of particles. Such macromodel reduces drastically the computational time required to numerically solve a full FP equation for the 2D case explored here. The effect of anisotropic translational diffusion, depending on the orientation, is studied in a planar channel with and without the presence of a circular obstacle. The Brownian translational diffusion favors the rod migrations toward the walls. The concentration gradient does not affect the orientation of rods, but it favors their migration. Aligned rods are slower to migrate than planar random ones. These results are in qualitative agreement with the results in the literature. A circular obstacle in a planar channel causes complexity in the flow field which affects the rod suspensions. The macromodel is verified based on the solution of the Fokker-Planck equation. Future works will focus in exploring the effect between particle and Brownian stresses, the stress terms will be developed and added to Stokes equation as in the work of Saintillan and Shelley [12]. On the other hand, the effect of anisotropic translational diffusion in the case of active particles will be investigated.

## 2.6 Acknowledgments

H.I. particularly wishes to acknowledge the Brittany Region and ISblue for their financial supports. G.N. acknowledges financial support from the Natural Sciences and Engineering Research Council of Canada (NSERC) (03783).

CHAPTER 3

# BROWNIAN ROD-LIKE PARTICLES SUSPENSION IN NON-HOMOGENEOUS SYSTEM: THE EFFECT OF FLOW/ROD COUPLING

This study investigates the behavior of Brownian rod suspensions in flow systems, focusing on rod-fluid interactions and concentration gradients induced by anisotropic translational diffusion. Numerical simulations, based on a kinetic macro-model following the work of Issa et al. [20], are used to analyze these results. In simple shear flow, the presence of rods does not significantly impact the flow, and translational diffusion does not influence the mechanism. However, in Poiseuille flow, the rods cause a flattening of the velocity profile and the formation of concentration variations. The coupling between the flow field and the rods influences their orientation, migration behavior, and rheological properties. In Couette flow, rod-fluid coupling results in outward flow in the vicinity of a fixed cylinder. The translational diffusion plays a crucial role, as higher Peclet numbers lead to pronounced migration of rods towards the channel walls and increased alignment with the flow direction. This coupling effect also affects the velocity profile in Couette flow. The findings of this study provide valuable insights into the complex behavior of suspended Brownian rods in different flow regimes.

Cette étude examine le comportement des suspensions de bâtonnets Browniens dans les systèmes d'écoulement, en se concentrant sur les interactions bâtonnets-fluide et les gradients de concentration induits par la diffusion translationnelle anisotrope. Des simulations numériques, basées sur un macro-modèle cinétique suivant le travail d'Issa et al. [20], sont utilisées pour analyser ces résultats. Dans un écoulement de cisaillement simple, la présence de tiges n'a pas d'impact significatif sur l'écoulement, et la diffusion translationnelle n'influence pas le mécanisme. Cependant, dans un écoulement de Poiseuille, les tiges provoquent un aplatissement du profil de vitesse et la formation de variations de concentration. Le couplage entre le champ d'écoulement et les bâtonnets influence leur orientation, leur comportement migratoire et leurs propriétés rhéologiques. Dans l'écoulement de Couette, le couplage tige-fluide entraîne un écoulement vers l'extérieur à proximité d'un cylindre fixe. La diffusion translationnelle joue un rôle crucial, car des nombres de Peclet plus élevés entraînent une migration prononcée des bâtonnets vers les parois du canal et un alignement accru avec la direction de l'écoulement. Cet effet de couplage affecte également le profil de vitesse dans l'écoulement de Couette. Les résultats de cette étude fournissent des indications précieuses sur le comportement complexe des bâtonnets Browniens en suspension dans différents régimes d'écoulement.

## 3.1 Introduction

Predicting and controlling the local configuration (i.e., concentration and orientation) state of particle suspensions is critical to design advanced materials manufacturing processes [119–121]. Simulating suspensions of colloids is a difficult undertaking that requires resolving particle-particle interactions, thermal fluctuations, and long-range many-body hydrodynamic interactions that lead to complex suspension microstructures [165, 166].

The evolution of the orientation of anisometric particles homogeneously suspended during flow has been theoretically studied by researchers. Jeffery [22] was the pioneer who derived the equation of motion for a single isolated, inertialess, ellipsoidal, non-Brownian particle in a Newtonian fluid with a uniform velocity gradient. In a specific case where a dilute slender fiber suspension is subjected to constant shear flow, particles orient in the flow direction and spent most of their time aligned in this latter direction [122, 123]. This phenomenon has similarities with the behavior of Brownian particles, for which Doi and Edwards [40] gave the associated Fokker-Planck equation (FP) for Brownian particles. Dhont and Briels [167] focused on extending the Doi-Edwards framework to account for the dynamical correlations and to better understand the behavior of suspensions of rod-like particles under shear flow conditions. Férec et al. [96] examined the rheological behavior of a short fiber-filled polypropylene in simple shear flow using the Folgar-Tucker-Lipscomb (FTL) model without any closure approximation. They discussed the accuracy of commonly used closure approximations and highlights the aspects of the FTL model that requires further improvement. Natale et al. [168] developed a new set of rheological equations to explain the shear-thinning behavior of attractive rod suspensions in a Newtonian matrix. The particle-particle interactions were modeled by a nonlinear lubrication force, a function of the relative velocity at the contact point and weighted by the contact probability.

In recent years, researchers have been developing numerical techniques to predict and experimental methods to observe particle orientation and concentration. Rheo-optical studies have been used to investigate the effect of Brownian motion on sheared suspensions, as reported by Frattini and Fuller [135]. The findings provided experimental evidence for evaluating closure approximations and understanding the orientation dynamics of rigid, axisymmetric particles in dilute suspensions subjected to simple shearing flow. Schiek and Shaqfeh [113] studied the cross-streamline migration of slender Brownian rods in plane Poiseuille flow. It provides insights into the occurrence of migration and the distribution patterns of particles on scales comparable to the particle length within the channel. Nitsche and Hinch [112] investigated the shear-induced lateral migration of Brownian rigid rods in parabolic channel flow, and quantitatively confirmed the accumulation of rods at the channel walls. Xie et al. [136] used experimental techniques to study the shear-induced alignment of low aspect ratio gold nanorods in Newtonian fluids. Their observations highlight the alignment phenomenon and numerical simulations support the understanding of the nanorods' behavior, including the impact of Brownian motion even at high Peclet numbers.

Hinch and Leal [137] reveals the intricate interplay between shear flow alignment and Brownian disorientations in a dilute suspension of axisymmetric particles. The rheological behavior exhibits oscillatory features tied to particle rotation and a fading memory effect due to Brownian diffusion. Hijazi and Zoaeter [138] used Brownian dynamics simulations to study rod-like particles in dilute flowing solution. Their results demonstrated the impact of the hydrodynamic shear rate and rotational Brownian diffusion on the average orientations, with the maximum orientation angle exhibiting a strong dependence on the flow conditions. Leahy et al. [139] examined the effect of shear flow on the rotational diffusion of a single axisymmetric particle. Their study provided new insights into the time-dependent rheological properties of suspensions containing non-spherical Brownian particles. The study highlights the complex interplay between shear-induced rotations and diffusion, revealing the importance of particle shape and orientation dynamics in determining the behavior and properties of such suspensions. Palanisamy and den Otter [140] developed an efficient Brownian dynamics simulation method for rigid colloids in linear flow fields based on the grand mobility matrix. This study on suspensions of non-spherical Brownian particles revealed that the rheological properties in continuous shear flow is influenced by two distinct diffusive time scales, which depend on the particle aspect ratio. Kumar and Natale [164] investigated the settling dynamics of two spheres in a suspension of Brownian rods using numerical simulations. They found that the presence of Brownian rods introduces non-Newtonian contributions, resulting in repulsive interactions between the settling spheres that depend on the Peclet number and the distance between their centers.

Fokker-Planck-like equations in multiple dimensions are computationally expensive to solve. The creation of an equivalent kinetic macro-model is a tactic used to make the numerical solution of complex physics problems more accessible. Macro-models have been used extensively in the literature to forecast particle concentration or orientation. To describe fiber orientation in suspensions containing short rigid fibers, Advani and Tucker [152] used a set of even-order moments of the probability distribution function. In concentrated monomodal, spherical suspensions, Phillips et al. [153] proposed a constitutive equation for computing particle concentration and velocity fields. Shapley et al. [154] compared the predictions of various particle migration models to laser Doppler velocimetry measurements. At moderate bulk particle concentrations, the models accurately predict the macroscopic shear rate and concentration profiles, but at high concentrations, they start to diverge. Without considering the correlation between the two, these models are either used to predict the orientation or the concentration. Saintillan and Shelley [12] developed a fundamental kinetic model and discussed the stability and nonlinear dynamics of a suspension of self-propelled rod-like particles. For an active suspension, Weady et al. [76] restated and coarse-grained a continuum kinetic model. Although the translational diffusion is anisotropic and depends on the particle's orientation, these two models roughly represent it as a constant. That is why Issa et al. [20] derived a new kinetic macro-model based on moments of the probability distribution function to investigate the flow of Brownian particle suspensions with taking into account the anisotropic translational diffusion. This is a key element in predicting the rheological behavior of particle suspensions in a flow inside complex geometries while addressing the coupling between the flow field and the particle orientations and concentrations distribution [98, 169–171].

In a series of influential papers [77, 172, 173], Batchelor and coworkers established that microstructural asymmetry, not just distortion, is required to produce non–Newtonian rheology. They established expressions for the average suspension stress in diluted colloidal dispersion, as well as the non-equilibrium Smoluchowski framework that governs the evolution of a flowing microstructure under the influence of thermodynamic and hydrodynamic forces.

Several studies have confirmed that particles alter the flow pattern of suspensions. Bagnold [174] reported the appearance of normal stresses during shear flow on flow-induced non-Newtonian rheology of suspensions of noncolloidal spherical particles. He proposed that non-Newtonian rheology was caused by the presence of a particle microstructure and shear-flow-induced changes in its shape. The existence of a shear-induced structure in concentrated noncolloidal suspensions was conclusively suggested by several studies after this innovative work [175, 176]. Mezi et al. [98] developed a numerical simulation for 2D planar flows for fiber suspension with a Newtonian and a power-law suspending fluids. Then, they extended this model to examine a 2D axisymmetric capillary die swell for fiber suspensions, which occurs in 3D printing extrusion processes [170]. The particles extra stress effect flattens the velocity profile but has little effect on the distribution of fiber orientation in the suspension flow. Yasuda et al. [177] measured the velocity profile of short fibers in a Newtonian matrix flow inside a channel with a rectangular cross-section. They observed that the velocity profile becomes flatter as the fiber volume fraction increases. Mazahir et al. [178, 179] used slow orientation kinetics such as the reduced strain closure model [180] to conduct coupled transient simulations to predict fiber orientation in a center-gated disc. They discovered that the numerical data of the coupling effect is very small when compared to experimental data measured in the shell, transition, and core layers, but there is an improvement in the frontal flow region. A two-way coupled, which refers to the mutual influence between the fluid flow and the suspended particles, direct simulation technique is proposed by Moosaie and Manhart [144] for the numerical solution of Brownian rod suspension flows in complex geometries. They observed that, in the case of channel flow, the bulk velocity in the channel decreases by the effect of extra stress generated by the rods. Krochak et al. [145] examined the effect of two-way coupling between the flow field and the orientation state of rigid-fiber suspensions flowing through a tapered channel with an orientation distribution function that evolves according to a Fokker-Planck-type equation. They demonstrated that

when the two-way coupling is present, the orientation anisotropy changes significantly.
The objective of this work is to investigate the effect of flow/Brownian rod micro-structure coupling in non-homogeneous systems while considering the particle concentration and orientation. The study employs a kinetic macro-model derived in a previous work [20] and examines particle suspensions in a planar infinite channel during transient study.
The article is organized as follows: Section 3.2 focuses on theoretical modeling and the flow problem for rod suspensions. Finally, section 3.3 presents the numerical results, including the effect of particle extra stresses, the effect of translational diffusion, and the effect of both initial concentration and orientation gradients, before the conclusion.

## 3.2 Governing equations

Let's consider a suspension of Brownian rod-like particles of length $L$, circular cross-section of diameter $d$ and an aspect ratio $a_r = L/d$. The particles are assumed to be rigid, monodisperse, neutrally buoyant, and immersed in a Newtonian fluid. The rod suspension is supposed to be diluted in a volume of interest $V$. Hence the mean number of rods per unit volume $n$ verified that $nL^3 << 1$ (this corresponds to a volume fraction $\phi_p << (d/L)^2$). The fluid is presumed to be isothermal and incompressible. Below are presented the equations that describe the flow problem and the kinetic macro-model of the suspending rods. Subsequently, these equations are written in dimensionless form for further analysis and simplification.

### 3.2.1 Flow problem

The problem is governed by the continuity and Cauchy momentum equations in the limit of creeping flow (low Reynolds number)

$$\nabla_{\mathbf{x}} \cdot \mathbf{u} = 0, \tag{3.1}$$

$$\nabla_{\mathbf{x}} P - \eta_0 \nabla_{\mathbf{x}}^2 \mathbf{u} = \nabla_{\mathbf{x}} \cdot \mathbf{\Sigma}. \tag{3.2}$$

In the above equations, $\nabla_{\mathbf{x}}$ and $\nabla_{\mathbf{x}}^2$ are the gradient and Laplacian operators in the spatial space, respectively. $\mathbf{u}$ is the velocity vector of the suspension, $P$ denotes the pressure, $\eta_0$ is the Newtonian dynamic viscosity of the suspending fluid and $\mathbf{\Sigma}$ represents the particle extra stress tensor. Indeed, the presence of particles in a Newtonian medium develops extra stress contributions, which are obtained by configurational averages of force dipoles exerted by the particle on the fluid. In a dilute regime, the particle extra stress tensor arises from two contributions [12]

$$\mathbf{\Sigma} = \mathbf{\Sigma}_B + \mathbf{\Sigma}_F. \tag{3.3}$$

The first contribution is due to the fact that particles are Brownian

$$\boldsymbol{\Sigma}_B = k_B T(3\mathbf{A}_2 - \mathbf{A}_2 : \boldsymbol{\delta}\boldsymbol{\delta}), \tag{3.4}$$

where $k_B$ and $T$ are the Boltzmann constant and the absolute temperature, respectively, and $\boldsymbol{\delta}$ is the identity tensor. The second contribution comes from the inextensibility condition of the particles and is expressed as

$$\boldsymbol{\Sigma}_F = \sigma_F \left[ \left( \mathbf{A}_4 - \frac{1}{3}\boldsymbol{\delta}\mathbf{A}_2 \right) : \dot{\boldsymbol{\gamma}} \right], \tag{3.5}$$

where $\sigma_F = \pi\eta_0 L^3/6 \log(2a_r)$ from slender body theory, and $\dot{\boldsymbol{\gamma}}$ is the strain-rate tensor. $\mathbf{A}_2$ and $\mathbf{A}_4$, which will be defined below, represent the second and fourth-order conformation tensors, respectively.

### 3.2.2 Kinetic based model

In a local volume, which is large enough to contain a statistically significant number of particles but smaller than the characteristic length scale of the macroscopic properties of the system under consideration, a Brownian particle suspension can be characterized by a distribution function $\Psi(\mathbf{r}_c, \mathbf{p}, t)$. It reflects the probability of finding a particle at position $\mathbf{r}_c$ with orientation $\mathbf{p}$, at time $t$. Therefore, $\Psi(\mathbf{r}_c, \mathbf{p}, t)d\mathbf{r}_c d\mathbf{p}$ represents the number of particles with center of mass and orientation vectors in a range $d\mathbf{r}_c d\mathbf{p}$ about $\mathbf{r}_c$ and $\mathbf{p}$ at the current time $t$.

A single particle Smoluchowski equation can be obtained in the dilute regime as follows [40, 98]

$$\frac{\partial \Psi}{\partial t} = -\nabla_{\mathbf{x}} \cdot (\dot{\mathbf{r}}_{\mathbf{c}} \Psi) - \nabla_{\mathbf{p}} \cdot (\dot{\mathbf{p}} \Psi), \tag{3.6}$$

where $\nabla_{\mathbf{p}}$ is the gradient operator in the configurational space. The time-dependent evolution of the position of a Brownian particle, $\dot{\mathbf{r}_c}$, is

$$\dot{\mathbf{r}_c} = \mathbf{u} - \mathbf{D}_t \cdot \nabla_{\mathbf{x}} \log \Psi, \tag{3.7}$$

and the time-dependent evolution of its orientation, $\dot{\mathbf{p}}$, can be written as

$$\dot{\mathbf{p}} = \dot{\mathbf{p}}_j - D_r \nabla_{\mathbf{p}} \log \Psi, \tag{3.8}$$

where $\dot{\mathbf{p}}_j$ is the Jeffery's equation such as

$$\dot{\mathbf{p}}_j = -\frac{1}{2}\boldsymbol{\omega} \cdot \mathbf{p} + \frac{\lambda}{2} (\dot{\boldsymbol{\gamma}} \cdot \mathbf{p} - \dot{\boldsymbol{\gamma}} : \mathbf{ppp}). \tag{3.9}$$

The rotational diffusion coefficient and translational diffusion tensor are denoted by $D_r$ and $\mathbf{D}_t$, respectively. The latter is defined for non-spherical, rigid particles as $\mathbf{D}_t = D_{\parallel}\mathbf{pp}+D_{\perp}\left(\boldsymbol{\delta}-\mathbf{pp}\right)$, where $D_{\parallel}$ and $D_{\perp}$ are constants that characterize the diffusion parallel and perpendicular to the particle axis, respectively. The vorticity tensor is denoted by $\boldsymbol{\omega}$ and $\lambda$ is a constant shape factor as a function of the rod aspect ratio $a_r$. The combination of the above equations, with the help of the continuity equation, leads to

$$\frac{D\Psi}{Dt} = \nabla_{\mathbf{x}} \cdot \left(\mathbf{D}_t \cdot \nabla_{\mathbf{x}}\Psi\right) - \nabla_{\mathbf{p}} \cdot \left(\dot{\mathbf{p}}_j\Psi\right) + D_r\nabla^2_{\mathbf{p}}\Psi, \tag{3.10}$$

where $D(...)/Dt = \partial(...)/\partial t + \mathbf{u}\cdot\nabla_{\mathbf{x}}(...)$ is the material derivative. Based on the distribution function, some moments can be derived. Specifically, the fourth-order the second-order and the zeroth-order moments of $\Psi$ are respectively defined as [20]

$$\mathbf{A}_4 = \int_{\mathbf{p}} \mathbf{pppp}\Psi d\mathbf{p}, \tag{3.11}$$

$$\mathbf{A}_2 = \mathbf{A}_4 : \boldsymbol{\delta} = \int_{\mathbf{p}} \mathbf{pp}\Psi d\mathbf{p}, \tag{3.12}$$

$$c = \mathbf{A}_2 : \boldsymbol{\delta} = \int_{\mathbf{p}} \Psi d\mathbf{p}, \tag{3.13}$$

where $c$ represents to the local number density of the suspension, which is directly linked to the trace of $\mathbf{A}_2$. The moments $\mathbf{A}_4$ and $\mathbf{A}_2$ contain information on the local concentration and orientation of particles. For instance, a local population of rods oriented randomly with a number density $c_1$ is given by $\mathbf{A}_2 = c_1\boldsymbol{\delta}/3$, whereas a group of rods having the same direction with a number density $c_2$ leads that $\mathbf{A}_2$ has only one non-zero component in the alignment direction equals to $c_2$. Therefore, it is found that the distribution function $\Psi$ is normalized such as

$$\frac{1}{V}\int_{\mathbf{x}}\int_{\mathbf{p}} \Psi d\mathbf{p}d\mathbf{x} = n. \tag{3.14}$$

After some straightforward algebraic manipulations, an evolution equation of the tensor $\mathbf{A}_2$ can be derived [20]

$$\begin{aligned}\frac{D\mathbf{A}_2}{Dt} =& -\frac{1}{2}\left(\boldsymbol{\omega}\cdot\mathbf{A}_2 - \mathbf{A}_2\cdot\boldsymbol{\omega}\right) + \frac{\lambda}{2}\left(\dot{\boldsymbol{\gamma}}\cdot\mathbf{A}_2 + \mathbf{A}_2\cdot\dot{\boldsymbol{\gamma}} - 2\mathbf{A}_4 : \dot{\boldsymbol{\gamma}}\right) + 2D_r\left(c\boldsymbol{\delta} - 3\mathbf{A}_2\right) \\ &+ D_{\perp}\nabla^2_{\mathbf{x}}\mathbf{A}_2 + \left(D_{\parallel} - D_{\perp}\right)\nabla_{\mathbf{x}}\nabla_{\mathbf{x}} : \mathbf{A}_4.\end{aligned} \tag{3.15}$$

Since Eq. (3.15) involves on $\mathbf{A}_4$, it requires a closure approximation to express $\mathbf{A}_4$ in terms of $\mathbf{A}_2$. Fortunately, standard closure approximations [44, 46, 156] can be used for this case, where the particles are axisymmetric, by being cautious to normalise $\mathbf{A}_2$ by $c$ in order to maintain the unitary trace condition. In our previous investigation [20], the IBOF closure was tested and yielded more than 95% accurate results as compared to the exact solution obtained by solving the Fokker-Planck equation given by Eq. (B.2). Hence, all the cases presented in this work involved the IBOF closure [46] for the analysis. Eq. (3.15), called macro-model, allows for solving of a set of partial differential equations (i.e., 6 PDEs in 3D, which are the evolution of $A_{11}$, $A_{22}$, $A_{33}$, $A_{12}$, $A_{13}$ and $A_{23}$) rather than a full 6D Fokker-Planck equation (i.e., 3D in spatial space, 2D in configurational space and 1D in time), greatly simplifying the numerical simulation.

### 3.2.3 Dimensionless formulation of the problem

.

To render the problem dimensionless, the particle length $L$ and the Newtonian viscosity of the suspending fluid $\eta_0$ are chosen as the characteristic length and viscosity, respectively. Therefore, the characteristic strain rate is $\dot{\gamma} = U_{avg}/L$, where $U_{avg}$ is the average flow velocity. We also introduce a dimensionless mean number density such as $c^* = c/n$, where $n$ is the mean number density. The dimensionless form of the Cauchy equation can be written as

$$\nabla^*_{\mathbf{x}} P^* - \nabla^{*2}_{\mathbf{x}} \mathbf{u}^* = \nabla^*_{\mathbf{x}} \cdot \left\{ c^* \left[ N_p \left( \mathbf{A}^*_4 - \frac{1}{3} \boldsymbol{\delta} \mathbf{A}^*_2 \right) : \dot{\boldsymbol{\gamma}}^* + N_b \left( 3\mathbf{A}^*_2 - \boldsymbol{\delta} \right) \right] \right\}. \tag{3.16}$$

As a result, the dimensionless form of the stress tensor is

$$\boldsymbol{\Sigma}^* = c^* \left[ N_p \left( \mathbf{A}_4 - \frac{1}{3} \boldsymbol{\delta} \mathbf{A}_2 \right) : \dot{\boldsymbol{\gamma}}^* + N_b \left( 3\mathbf{A}^*_2 - \boldsymbol{\delta} \right) \right], \tag{3.17}$$

where $N_p = \frac{\pi n L^3}{6 log(a_r)}$ is the particle coupling coefficient, and $N_b = \frac{n k_B T}{\eta_0 \dot{\gamma}}$ is the Brownian coupling coefficient.

Following the previous work [20], $Pe_r = |\dot{\gamma}| / D_r$, $Pe_\perp = L^2 |\dot{\gamma}| / D_\perp$ and $Pe_\parallel = L^2 |\dot{\gamma}| / D_\parallel$ are the rotary, perpendicular and parallel Peclet numbers, respectively. For very long and thin rod-like particles, $\lambda = 1$ and the relation $Pe_\perp = 2 Pe_\parallel$ applies [40]. The evolution equation for $\mathbf{A}_2$ in dimensionless form becomes

$$\begin{aligned} \frac{D\mathbf{A}^*_2}{Dt^*} = & -\frac{1}{2} \left( \boldsymbol{\omega}^* \cdot \mathbf{A}^*_2 - \mathbf{A}^*_2 \cdot \boldsymbol{\omega}^* \right) + \frac{1}{2} (\dot{\boldsymbol{\gamma}}^* \cdot \mathbf{A}^*_2 + \mathbf{A}^*_2 \cdot \dot{\boldsymbol{\gamma}}^* - 2\dot{\boldsymbol{\gamma}}^* : \mathbf{A}^*_4) + \frac{2}{Pe_r} \left( \boldsymbol{\delta} - 3\mathbf{A}^*_2 \right) \\ & + \frac{1}{Pe_\perp} \nabla^{*2}_{\mathbf{x}} \mathbf{A}^*_2 + \frac{1}{Pe_\perp} \nabla^*_{\mathbf{x}} \nabla^*_{\mathbf{x}} : \mathbf{A}^*_4, \end{aligned} \tag{3.18}$$

where $t^* = t\dot{\gamma}$. The evolution equation of concentration $c$ is

$$\frac{Dc^*}{Dt^*} = \frac{D\mathbf{A}^*_2}{Dt^*} : \boldsymbol{\delta} = \frac{1}{Pe_\perp} \nabla^{*2}_{\mathbf{x}} c^* + \frac{1}{Pe_\perp} \nabla^*_{\mathbf{x}} \nabla^*_{\mathbf{x}} : \mathbf{A}^*_2. \tag{3.19}$$

Eqs. 3.18 and 3.19 show the coupling between the concentration and the local orientation of the

Brownian rods. This coupling clearly appears in the last term of Eq. 3.19. In what follows the asterisks indicating the non-dimensional quantities have been dropped for clarity.

## 3.3 Numerical results

In this work, three flow problems (simple shear flow, Poiseuille flow and Couette flow) are tested using the kinetic macro-model with the IBOF closure, Eqs. 3.1, 3.16 and 3.18 are solved. The accuracy of this model has been verified in Appendix B.1 with comparing the results with the solution of the full Fokker-Planck equation for simple shear flow (uncoupled model). The dimensionless first and second normal stress differences $N_1$ and $N_2$ are, respectively,

$$N_1 = \Sigma^*_{11} - \Sigma^*_{22} \tag{3.20}$$

$$N_2 = \Sigma^*_{22} - \Sigma^*_{33} \tag{3.21}$$

and the dimensionless shear viscosity is $\Sigma^*_{12}$.
Actually, the indices $1, 2$ and 3 represent the flow direction, the velocity gradient direction and the vorticity direction, respectively. Therefore in a simple shear flow and Poiseuille flow, they refer to $x, y$ and $z$, respectively, while in the Couette flow, they refer to $\theta, r$ and $z$, respectively.

### 3.3.1 Simple shear flow

First, it is considered a suspension flow between two moving parallel plates. The geometry is a 2D square channel of side $H$, where $H/L = 10^6$. A simple shear flow is imposed in the $xy$-plane, where the upper wall at $y = H/2$ translates at $\dot{\gamma}H/2 = 0.5$ in the $x$-direction whereas the lower wall at $-y = H/2$ translates in the opposite direction. It results that the $x$, $y$ and $z$ axes denote the flow direction, the velocity gradient direction and the vorticity direction, respectively. Due to the symmetric conditions along the $y = 0$ axis, all results in the rectangular channel are plotted for $0 < y/H < 0.5$. Periodic flow conditions with $\Delta P = 0$ at ($x = 0$ and $x = H$) are used to simulate the flow in an infinite channel. Initial conditions for the conformation tensor (unless otherwise mentioned) are $A_{ii} = c_0/3$ and $A_{ij} = 0$ for $i \neq j$, where $c_0$ is the initial concentration.

#### Homogeneous systems

Under the one-way coupling assumption ($N_p = 0$ and $N_b = 0$), we first explore the flow-microstructure coupling for a homogeneous system in a simple shear flow. Numerical simulations are performed for $Pe_\perp = 0.01, 0.1, 1$ and 10, with a fixed value of $Pe_r = 10$. It is observed that there is no effect of translational diffusion on the system, where no rod migrations occur and no effect on the rod orientation dynamics, normal stress differences, and shear viscosity (results not shown). This is confirmed by the fact that the right-hand side of Eq. 3.19 is always null.

We then examine the flow-microstructure coupling coefficients for $N_b = 0, 10, 100, 250$ and 1000 and $N_p = 0, 10, 100$ with $Pe_\perp = Pe_r = 10$. It is found that the two-way coupling does not change the velocity profile in simple shear flows and does not modify the rod orientations as well as the rheological properties (shear viscosity and normal stress differences).

### Non-homogeneous systems - Effect of concentration gradient

We now investigate the effect of various initial concentration on the transient rheological properties of Brownian rod suspensions. As depicted in Fig. (3.1), six initial concentration gradient cases along the $y$-direction are examined, $c_1 = 0.7$, $c_2 = -1.8(y/H)^2 + 0.85$, $c_3 = -2.4(y/H)^2 + 0.9$, $c_4 = -3.6(y/H)^2 + 1$, $c_5 = 0.9995$ for $0 < y/H < 0.35$ else $c_5 = 0.001$ and $c_6 = 1.998$ for $0 < y/H < 0.1755$ else $c_6 = 0.001$. The average concentration in the channel is kept constant to 0.7 for all the cases. Particles are initially isotropically oriented. Two ways coupling assumptions are taken into consideration. In order to examine the impact of concentration, it is necessary to keep the other parameters influencing the study constant, such as maintaining fixed values for $N_b = 250$, $N_p = 10$, and $Pe_r = Pe_\perp = 10$. In these cases, the presence of an initial concentration gradient leads to a non-uniform distribution of particles within the channel. As a result, particle migration occurs across the streamlines due to translational diffusion. The presence of a concentration gradient in the $y-$direction leads that the term $\frac{1}{Pe_\perp}\nabla_{\mathbf{x}}$ in Eq. 3.19 becomes non-zero, which subsequently induces particle migrations. Indeed, since $t$ increases, the concentration gradient gradually changes as reported in Fig. 3.2, until reaching an uniform concentration distribution $c = 0.7$ at the steady state at $t = 0.2$. However, in these cases it is worth mentioning that the migration of rods have a minimal impact on their orientation dynamics. As a result, the transient rheological properties, which is specifically related to the orientation distributions of the rods, remains unaffected by rod migrations.

### Non-homogeneous systems - Effect of orientation gradient

In order to explore the influence of orientation along the $y$-direction, an orientation gradient is imposed in a simple shear flow keeping the concentration constant and homogeneous. Four initial orientation gradient cases are examined, as shown in Fig. 3.3, for which $A_{yy}/c = A_{zz}/c$ and $A_{xy}/c = 0$. The first case is referred as "ISO", where the rods are isotropic, i.e., $\mathbf{A}_2 = \boldsymbol{\delta}/3$. In the second case "ALI", particles are perfectly aligned in the flow direction ($A_{xx}/c = 1$). "LIN" corresponds to the situation, where the orientation gradient has a linear profile. $A_{xx}/c = 1$ and $A_{yy}/c = 0$ at the walls ($y/H = 0.5$), whereas $A_{xx}/c = 0$ and $A_{yy}/c = 0.5$ at center-line $y = 0$. The latest case called "QUA" considers a quadratic form for the orientation gradient, where rods are aligned in the flow direction at centerline $y = 0$, $A_{xx}/c = 1$ and $A_{yy}/c = 0$ while at walls $y/H = 0.5$, $A_{xx}/c = 0$ and $A_{yy}/c = 0.5$ . In order to isolate the effect of orientation, parameters are fixed to $N_b = 250$, $N_p = 10$, and $Pe_\perp = Pe_r = 10$. No cross-streamline migrations of the

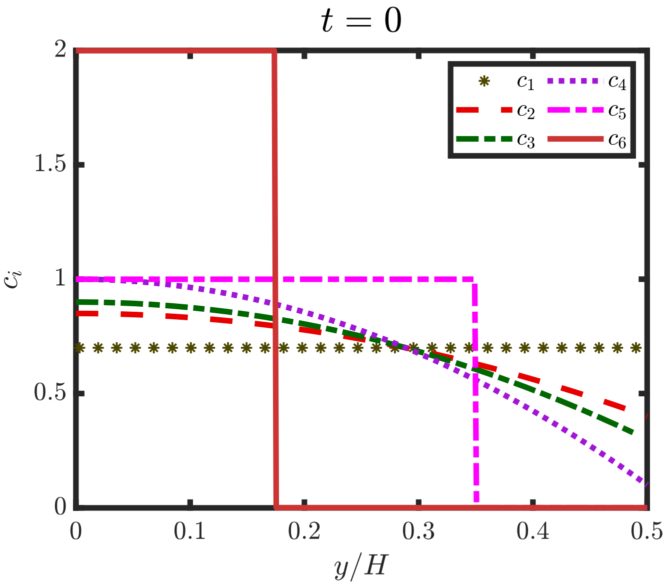

Figure 3.1 – Initial concentration gradients $c_1 = 0.7$, $c_2 = -1.8y^2 + 0.85$, $c_3 = -2.4y^2 + 0.9$, $c_4 = -3.6y^2 + 1$, $c_5 = 0.9995$ for $0 < y/H < 0.35$ else $c_5 = 0.001$ and $c_6 = 1.998$ for $0 < y/H < 0.1755$ else $c_6 = 0.001$.

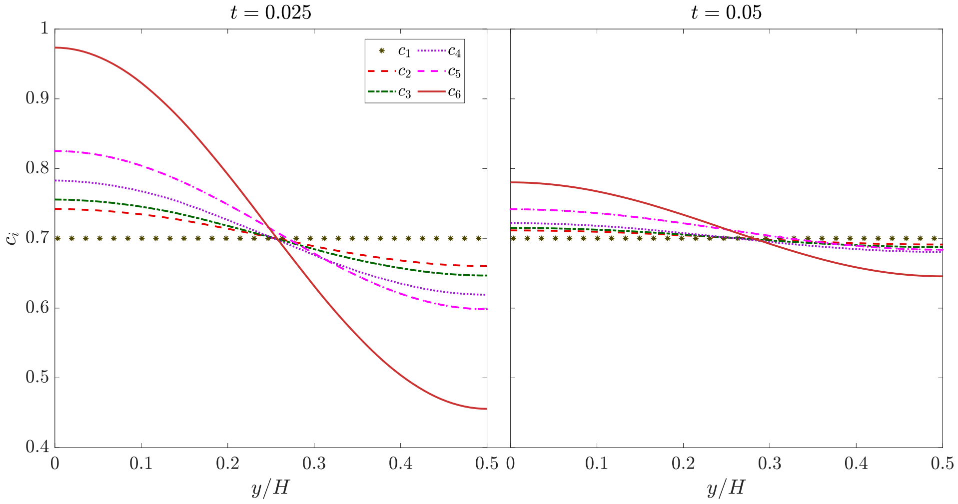

Figure 3.2 – Evolution of concentration distribution along the $y$-direction for various initial concentration gradients at $t = 0.025$ and $0.05$.

rods are observed. Furthermore, the various initial orientations of rods does not modify their final orientation distributions and consequently the final rheological properties of the system. However, it does influence the transient rheological properties of the system.

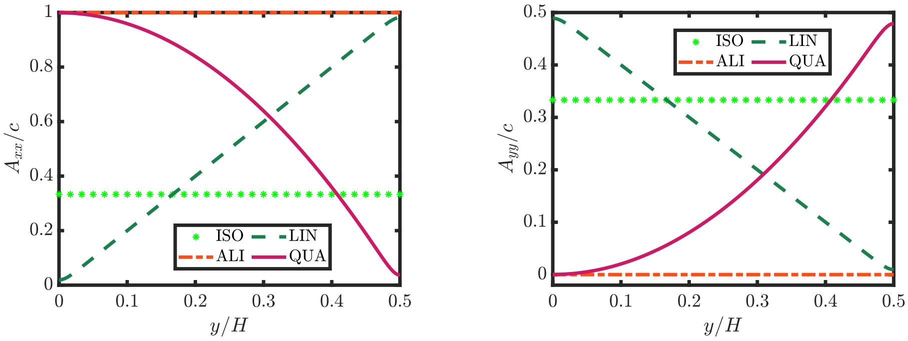

(a) The initial distribution of $A_{xx}$ along the $y$-direction.

(b) The initial distribution of $A_{yy}$ along the $y$-direction.

Figure 3.3 – The initial rod orientations, "ISO", "LIN", "ALI", and "QUA" for (a) $A_{xx}/c$ and (b)$A_{yy}/c$ in the $y$-direction.

Evaluated at $x/H = 0$, Fig. 3.4, Fig. 3.5, and Fig. 3.6 depict the time evolution along the $y$-direction for the shear stress $\Sigma_{xy}$, the first normal stress difference $N_1 = \Sigma_{xx} - \Sigma_{yy}$ and the second normal stress difference $N_2 = \Sigma_{yy} - \Sigma_{zz}$, respectively. These figures provide valuable information about how the rheological properties of the system evolve over time in response to changes in the initial orientation of the rods. The study reveals that rheological properties are strongly linked with rod orientation distributions.

### 3.3.2 Poiseuille flow

The work is now focused on the planar Poiseuille flow problem. The geometry consists in a 2D square of side $H$ and, therefore, the flow occurs in the $xy$-plane, $x$ denotes the flow direction, $y$ is the velocity gradient direction and $z$ corresponds to the vorticity direction. The two fixed walls are located at $y \pm H/2$. Periodic flow conditions of constant flow rate are used to simulate an infinite flow in the channel. The prescribed initial condition for velocity is parabolic with $U/(\dot{\gamma}H) = 1 - 4(y/H)^2)$, where $\dot{\gamma}H = 1$. Initial conditions for the conformation tensor are $A_{ii} = c_0/3$ and $A_{ij} = 0$ for $i \neq j$, where $c_0$ is the initial concentration.

#### Effect of particle extra stress

By taking into account the two-way coupling effects in homogeneous systems, it is known that the presence of particles in the fluid causes a flattening of the standard parabolic velocity profile in a Poiseuille flow [170]. However, in our study, we focus on non-homogeneous systems, where

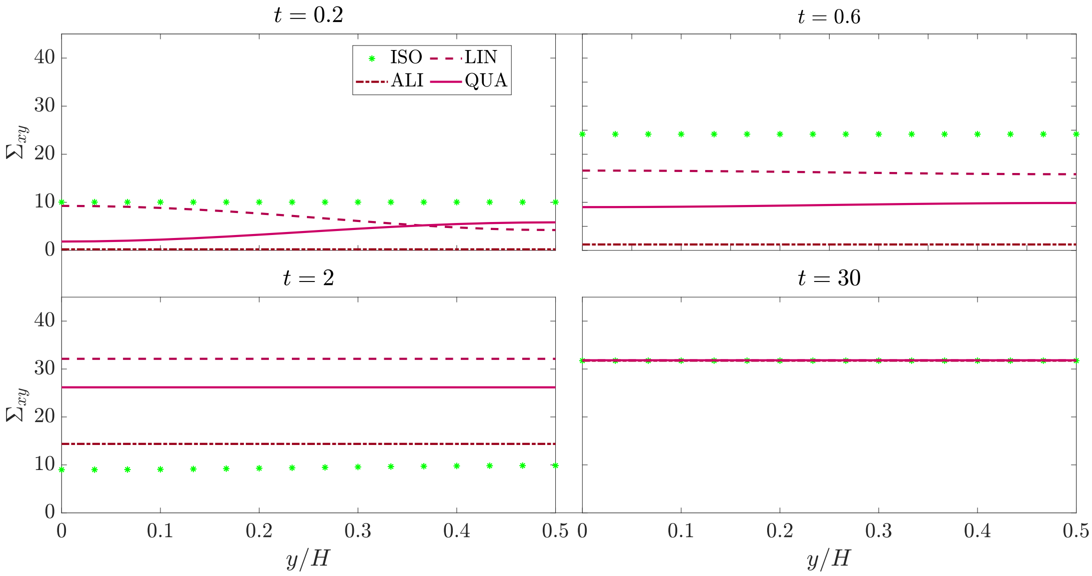

Figure 3.4 – Evolution of the shear stress along the $y$-direction for various initial rod orientations at $t = 0.2, 0.6, 2$ and $30$.

migrating rods lead to the formation of concentration variations, thus deviating from homogeneity. Hence, in order to investigate the impact of particle extra stress on the system, we keep constant the translational and rotational Peclet numbers at a value of 10 (i.e., $Pe_r = Pe_\perp = 10$). This allows us to isolate and analyze the specific influence of the additional stress on the system (i.e., the effect of two-way coupling).

Fig. 3.7a presents the numerical results obtained by investigating the coupled flow field and rod micro-structures, in particular the effect of Brownian stress contribution through $N_b$. Starting from a prescribed parabolic velocity profile with an isotropic orientation distribution and $c_0(t = 0) = 1$, the velocity profile tends to flatten out with time (results not shown). The system is fully developed at $t = 30$. As increasing $N_b$, the velocity profile tends to be more flatten. For $N_b = 10$, the effect on the velocity profile is relatively small. However, as $N_b$ increases, particle stresses increase leading to a more significant deviation from the standard parabolic profile.

Fig. 3.7b depicts the effect of Brownian stresses on the concentration profile at $t = 30$ (i.e., at steady-state). Particle stress hinders the rod orientations toward the flow direction in the channel. It also favours the migration of rods toward the walls as aligned rods have less tendency to migrate across the streamlines [20].

Then, the effect of hydrodynamic stress contribution through $N_p$ is tested. Values of $N_p$ up to 100 shows no significant modifications on the velocity profile and concentration distribution. Note that the limit of convergence of this numerical model is $N_p = 100$, for higher values the numerical model diverges.

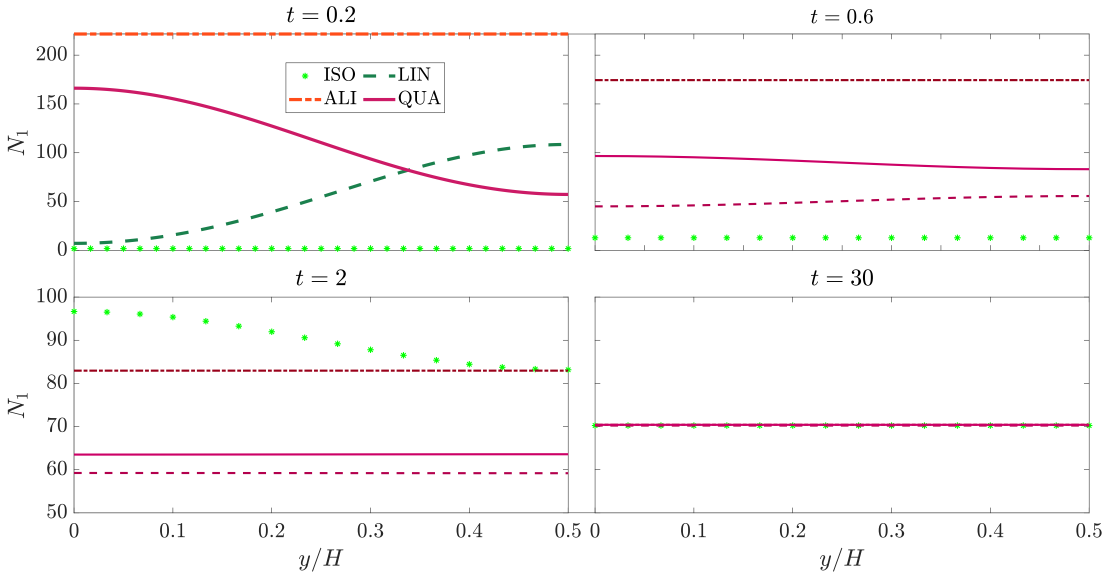

Figure 3.5 – Evolution of the first normal stress difference along the $y$-direction for various initial rod orientations at $t = 0.2, 0.6, 2$ and 30.

### Effect of translational diffusion

In our previous work [20], the effect of translational diffusion in a limited planar channel is studied without flow coupling. We aim now to explore the effect of translational diffusion in an infinite channel by taking into account the two ways coupling effects in a transient study. Therefore, the coupling coefficients and the rotary Peclet number are maintained at fixed values, such as $N_b = 250$, $N_p = 10$ and $Pe_r = 10$ with varying the values of $Pe_\perp$.

Fig. 3.8a shows the effect of translational diffusion on the velocity profile compared with the initial velocity. It is found that extra stress has a more pronounced impact on the velocity profile at higher translational diffusion Peclet numbers.

Fig. 3.8b illustrates the influence of translational diffusion on the concentration distribution of the rods. At high values of $Pe_\perp$, there is a notable migration of the rods towards the walls of the channel. However, as $Pe_\perp$ decreases, this migration becomes less pronounced. When $Pe_\perp$ drops below $10^{-1}$, the rods tend to remain more uniformly distributed along the channel without significant concentration variations. It is also observed that the rods tend to maintain an isotropic distribution at low values of $Pe_\perp$ (results not shown). Consequently, the rheological properties of the suspension are closed to the ones of the suspending fluid when $Pe_\perp$ becomes low (for more details, see Appendix B.2).

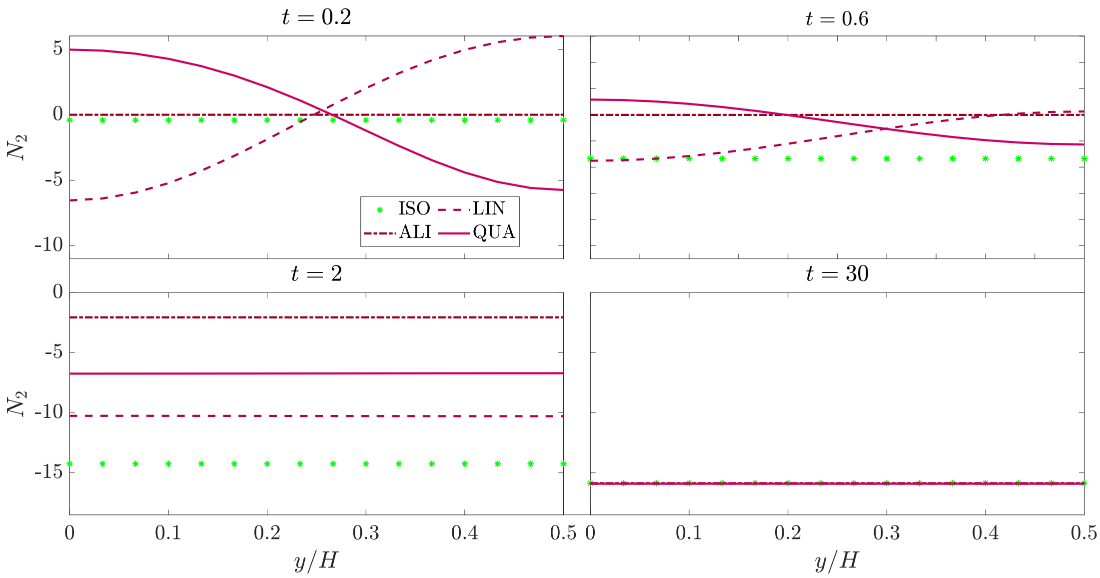

Figure 3.6 – Evolution of the second normal stress difference along the $y$-direction for various initial rod orientations at $t = 0.2, 0.6, 2$ and 30.

### Effect of concentration gradient

A concentration gradient is now introduced with keeping the rod orientation distribution isotropic. The same concentration gradient cases are considered as in 3.3.1. The numerical simulations are performed with $N_b = 250$, $N_p = 10$ and $Pe_r = Pe_\perp = 10$. No significant effect on the rod orientation are observed.

Figs. 3.9, 3.10, 3.11, and 3.12 show that the initial concentration gradients change the transient behavior of the velocity profile, shear stress and both normal stresses differences. In a suspension of Brownian rods, the shear stress and normal stress differences can undergo transient changes. These variations are caused by the presence of a concentration gradient within the suspension, which in turn affects the generation of extra stress on the fluid. However, it is crucial to emphasize that these transient changes do not impact the final steady-state values. As the rods migrate across streamlines, the concentration gradient gradually diminishes, leading the system to reach a steady-state characterized by a well-developed and consistent concentration distribution. In this steady-state condition, the system achieves a stable equilibrium, with final shear stress and normal stress difference values that are the same across the channel for all the studied cases. Once the concentration becomes homogeneously distributed and the system reaches this equilibrium state, the rheological properties no longer exhibit transient changes and maintain their steady-state values throughout the channel.

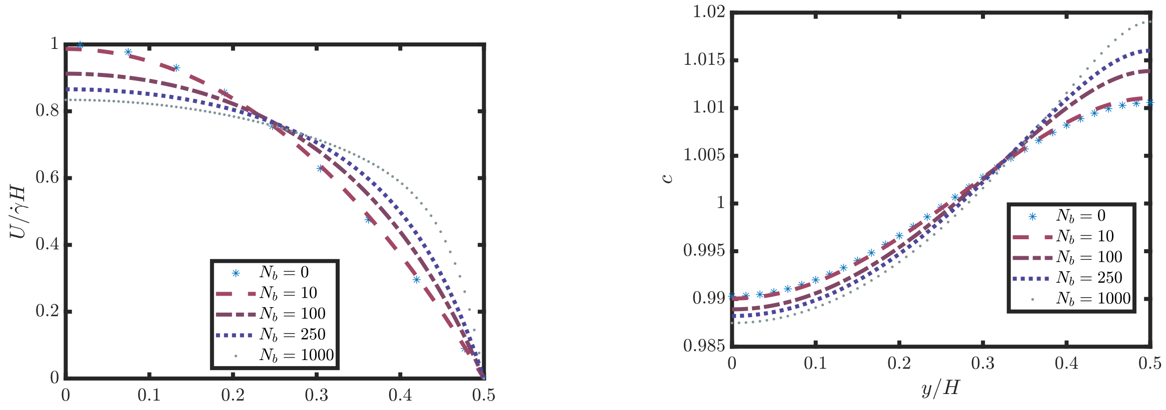

(a) Velocity profiles along the $y$-direction for $N_p = 0$ and for various values of $N_b$ at $t = 30$.

(b) Concentration distributions along the $y$-direction for $N_p = 0$ and for various values of $N_b$ at $t = 30$.

Figure 3.7 – Effect of Brownian stress contribution on the (a) velocity profile and the (b) concentration distribution along the $y$-direction for $N_b = 0, 10, 100, 250$ and $1000$ at $t = 30$ at $t = 30$ with $N_p = 0$.

### 3.3.3 Couette flow

The Couette flow is commonly used to study fluid dynamics and transport phenomena in cylindrical geometries. Fig. 3.13 shows the Couette flow geometry studied in this section, which consists of two concentric cylinders with radii $H$ and $0.8H$. The outer cylinder is fixed, while the inner cylinder is rotating at angular velocity $U/(\dot{\gamma}H) = 0.36$. Fig. 3.13 also displays the magnitude of the velocity field between the coaxial cylinders, which varies with the radial distance. All the results in this section are plotted at the "Baseline"(see Fig. 3.13), at this line the velocity vector has only one component in the direction of $\theta$. Using a cylindrical coordinate system $(r, \theta, z)$ is suitable to present the results.

#### Small gap

We first consider a flow between two concentric cylinders with a very small gap, known as Taylor-Couette flow ($R_{in}/R_{out} = 0.99$). The difference in shear rates between the inner and outer cylinders is found to be around 2.8% ($\dot{\gamma} = 1 \pm 2.8\% s^{-1}$). The rotary diffusion is fixed to a value of $Pe_r = 10$ and the coupling coefficients are fixed to a values of $N_p = 10$ and $N_b = 250$. We observed that even a small difference in the shear rates between the inner and outer cylinders can have a significant effect on the system. The particles do not introduce any noticeable alterations to the flow field, and there is no migration of particles across the streamlines (Homogeneous concentration). However, the orientation of the rods in the Taylor-Couette flow is influenced by the translational Peclet number, as shown in Fig. 3.14. The changes in particle orientation have

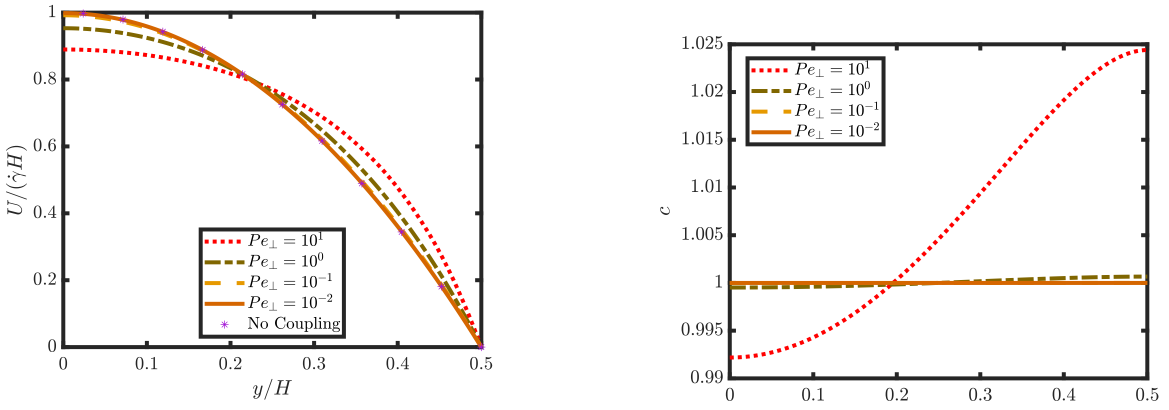

(a) Velocity profiles along the $y$-direction for various $Pe_\perp$ at $t = 30$ compared with velocity profile with no coupling.

(b) Concentration along the $y$-direction for various $Pe_\perp$ at $t = 30$

Figure 3.8 – Effect of the translational Peclet number on the (a) velocity profile and the (b) concentration distribution along the $y$-direction for $Pe_\perp = 10^{-2}, 10^{-1}, 10^0$ and $10^1$ at $t = 30$.

notable consequences on the rheological properties of the system, as depicted in Fig. 3.15. The isotropic distribution of rods at these conditions led to a minimal value of the shear viscosity comparable to the case of aligned rods, as well as for both normal stress differences. This behavior highlights the significant impact of rod orientation on the rheological properties of the suspension. The findings provide valuable insights into the interplay between translational diffusion, particle orientation, and the flow behavior of Brownian particle suspensions in Taylor-Couette flow.

### Effect of particle extra stresses

Fig. 3.16a illustrates the effect of Brownian stress contribution on the velocity profile in a Couette flow with suspended rods. It shows that as the Brownian coupling increases, the velocity profile becomes more flattened. This is because the orientation of the elongated particles affects the stress contributions, which in turn changes the shear viscosity. As a result, the velocity profile deviates from the initial profile observed in a Couette flow

$$v_\theta/(\dot{\gamma}R_{out}) = \frac{1}{R_{out}^2 - R_{in}^2}\left[(-0.45R_{in}^2)r + \frac{0.45R_{in}^2 R_{out}^2}{r}\right]. \tag{3.22}$$

When $N_b = 100$ or 250, the coupling between the flow-field and rod orientation is strong enough to cause the formation of a reverse flow near the fixed cylinder. This occurs because the orientation of the rods affects the flow field, leading to the formation of a pressure gradient that opposes the initial flow direction (last term in Eq. 3.16). As a result, the velocity near the fixed

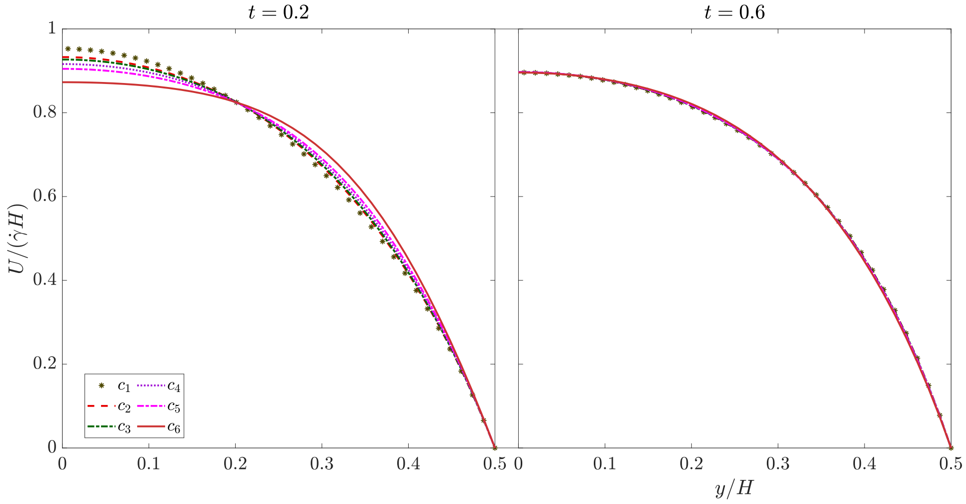

Figure 3.9 – Effect of the initial concentration on the velocity profile along the $y$-direction at $t = 0.2$, and 0.6.

cylinder becomes negative.

Fig. 3.16b depicts the effect of Brownian coupling on the concentration of the rods. It indicates that as $N_b$ increases, the concentration of rods near the fixed wall decreases and becomes more concentrated near the moving wall. This is due to the change in the velocity profile mentioned earlier.

### Effect of translational diffusion

The effect of translational diffusion on the behavior of Brownian particles in the Couette flow is investigated by simulating the flow for various values of $Pe_\perp$. The results show that the behavior of the suspension in the Couette flow is qualitatively similar to that observed in the Poiseuille flow. Fig. 3.17a reports the velocity profile between the coaxial cylinders at $t = 30$. As expected, the velocity profile changes as the coupling between the particles and the flow increases. Furthermore, the effect of coupling decreases as the translational Peclet number decreases. Fig. 3.17b depicts the concentration distribution between the coaxial cylinders at $t = 30$. It demonstrates that at high values of $Pe_\perp$, the rods exhibit a migration towards the walls. Conversely, as $Pe_\perp$ decreases, this migration becomes less pronounced.
At low values of $Pe_\perp$, the rods tend to maintain an isotropic distribution. This isotropic behavior significantly influences the rheological properties. The concentration distribution and migration of the rods play a crucial role in determining the overall rheology and behavior of the suspension in a Couette flow.

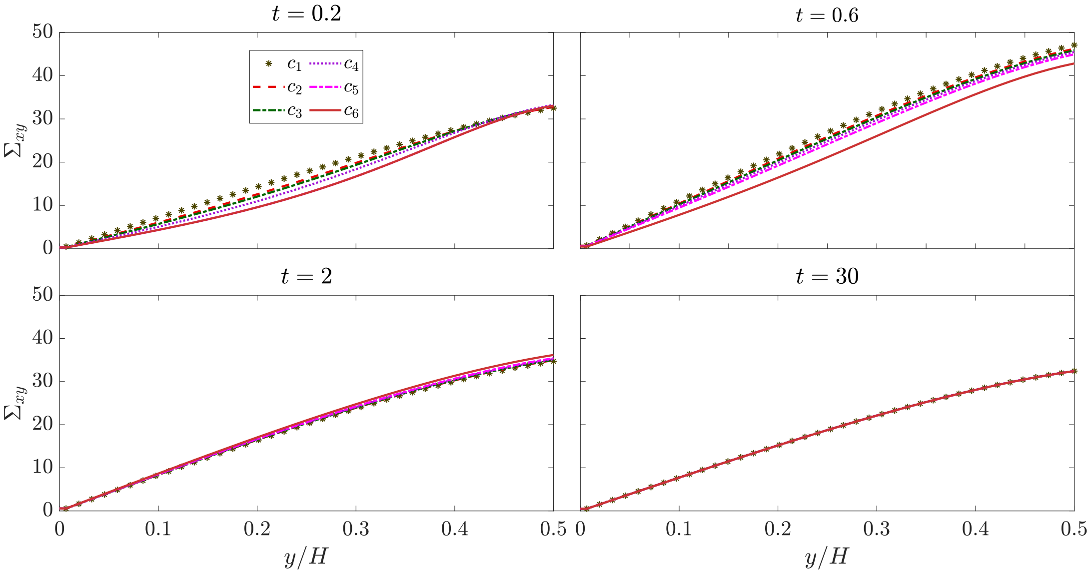

Figure 3.10 – Effect of the initial concentration on the shear viscosity along the $y$-direction at $t = 0.2, 0.6, 2$ and 30.

## 3.4 Conclusion

This numerical work investigates the rheological behavior of Brownian rod suspensions in a simple shear flow, a Poiseuille flow, and a Couette flow. The effects of rod-fluid coupling, concentration gradients, and translational diffusion are explored based on a kinetic macro-model. The findings reveal that the presence of rods in simple shear flows does not significantly alter the flow behavior, and translational diffusion has minimal impact on the system. However, in Poiseuille flows, the rods cause deviations from the standard parabolic velocity profile, leading to a flattened profile and the formation of concentration gradients. The coupling between the flow-field and rod orientation affects their orientation, migration behavior, and rheological properties, which have implications for the overall flow dynamics. In Couette flows, the rod-fluid coupling leads to an interesting phenomenon of inverse flow near the fixed cylinder, driven by the interplay between rod orientation and flow field.

Also, this study highlights the influence of translational Peclet numbers on the behavior of Brownian rod suspensions in flow systems. The findings reveal that low values of the translational Peclet number hinder the effects of rod-flow couplings, resulting in minimal alterations to the flow behavior. However, as the translational Peclet number increases, pronounced migration of rods towards the channel walls and increased alignment with the flow direction are observed.

These results have significant implications for various applications involving rod-like particle suspensions. Understanding the influence of translational Peclet numbers can aid in the design and optimization of microfluidic devices, biophysical processes, and industrial applications, where

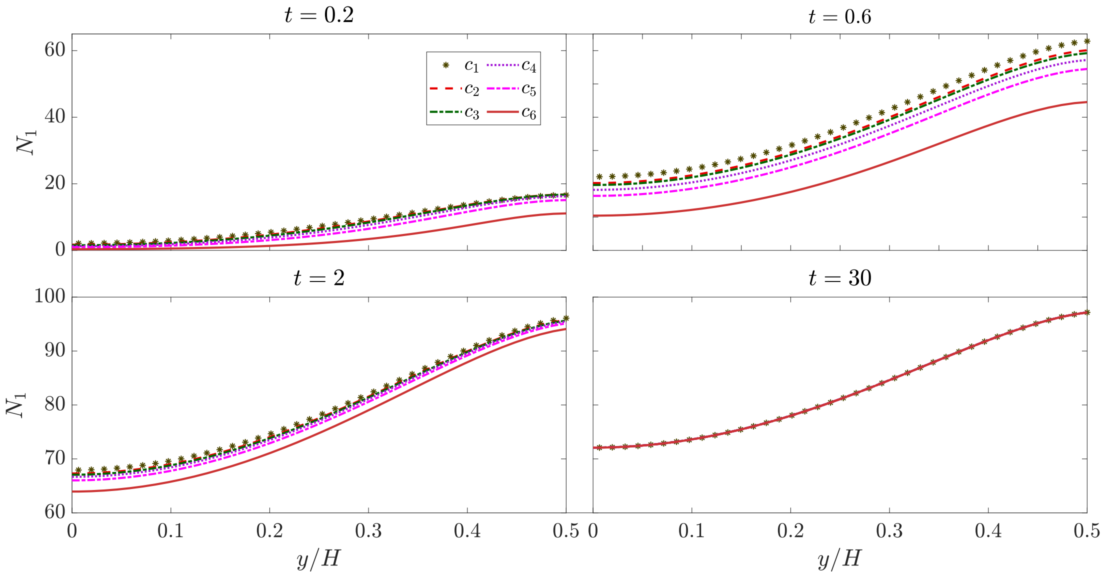

Figure 3.11 – Effect of the initial concentration on the first normal stress differences along the $y$-direction at $t = 0.2, 0.6, 2$ and 30.

the control and manipulation of rod-like particles in flow systems are crucial. Further research and experimental investigations are necessary to validate and expand upon these findings, exploring the interplay between translational diffusion and rod-flow couplings. Future works will focus on exploring the effect of anisotropic translational diffusion in the case of active Brownian particles as well as the effect of the stresses on the system.

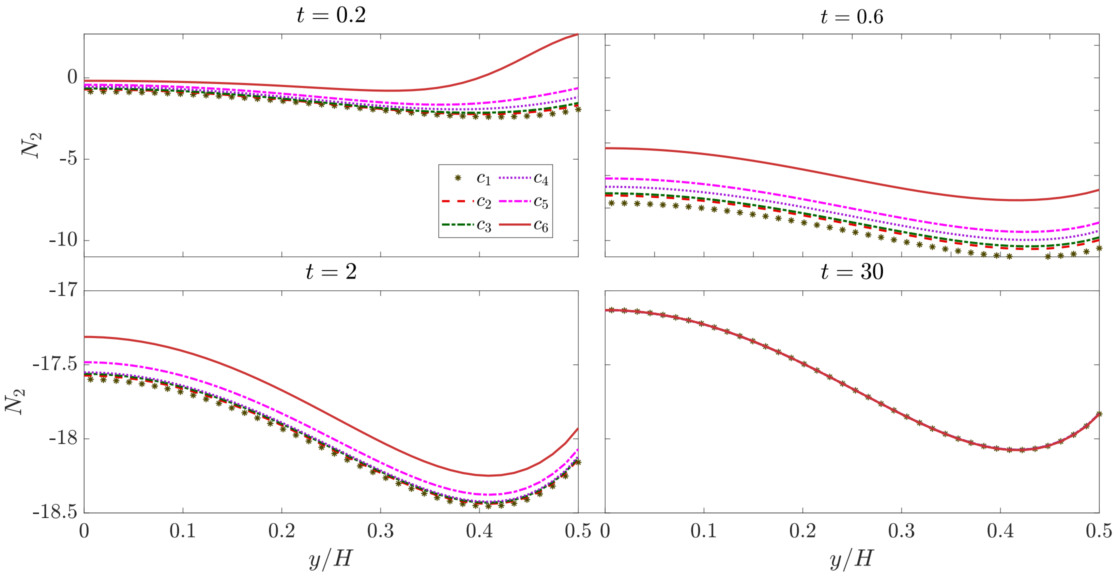

Figure 3.12 – Effect of the initial concentration on the second normal stress differences along the $y$-direction at $t = 0.2, 0.6, 2$ and 30.

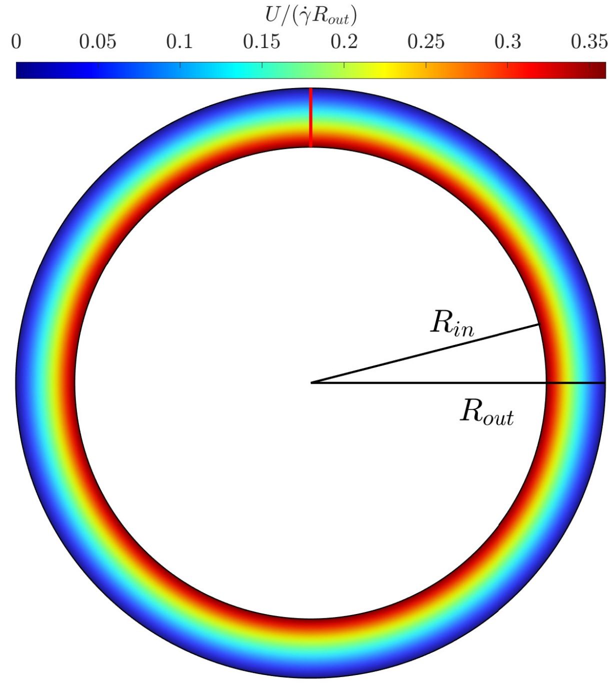

Figure 3.13 – Initial dimensionless velocity magnitude in the Couette flow. The red vertical line will be referred to as "the base line" in this work

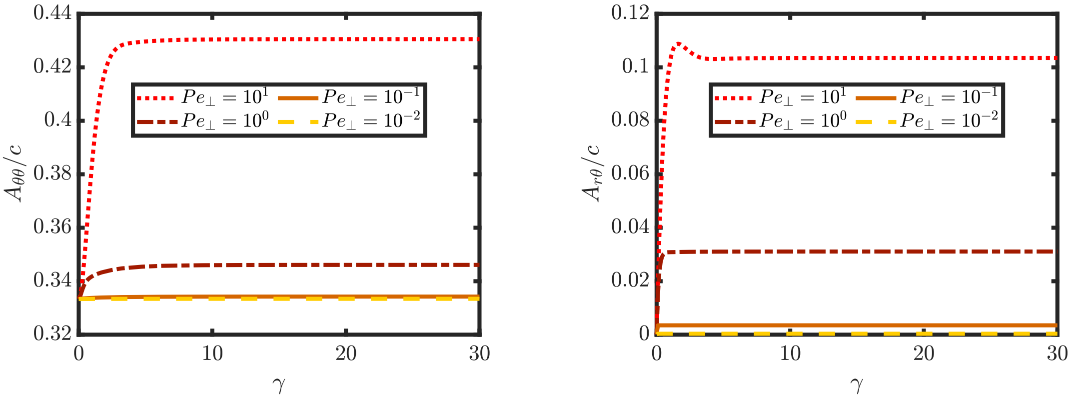

(a) Evolution of $A_{\theta\theta}/c$ with respect to the strain. (b) Evolution of $A_{r\theta}/c$ with respect to the strain.

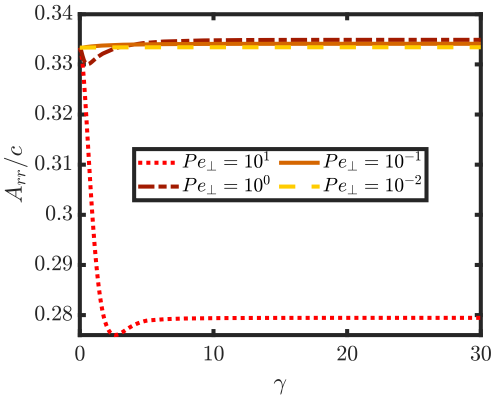

(c) Evolution of $A_{rr}/c$ with respect to the strain.

Figure 3.14 – Effect of the translational Peclet number on the evolution of the orientation components of (a) $A_{\theta\theta}/c$, (b)$A_{r\theta}/c$ and (c) $A_{rr}/c$ as a function of strain ($\gamma$) at $r = (R_{in}+R_{out})/2$ ($\dot{\gamma} = 1/s$).

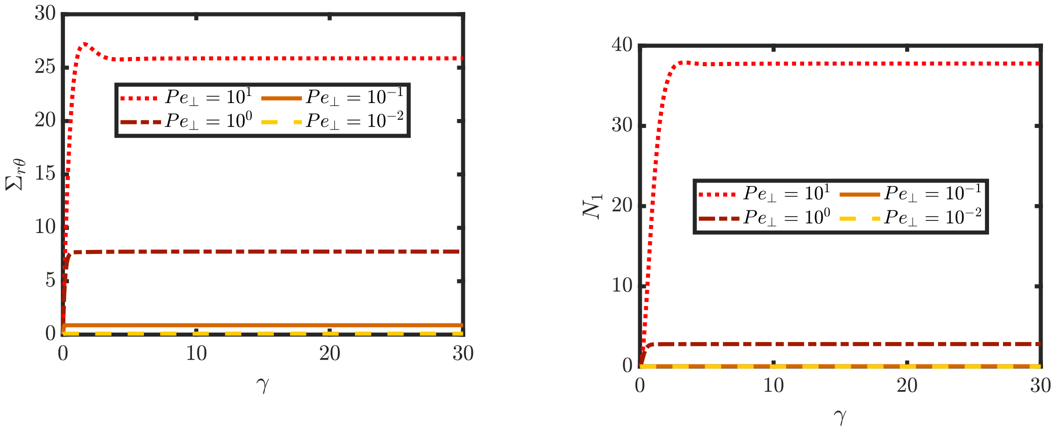

(a) Evolution of the shear viscosity ($\Sigma_{r\theta}$) with respect to the strain.

(b) Evolution of the first normal stress difference ($N_1$) with respect to the strain.

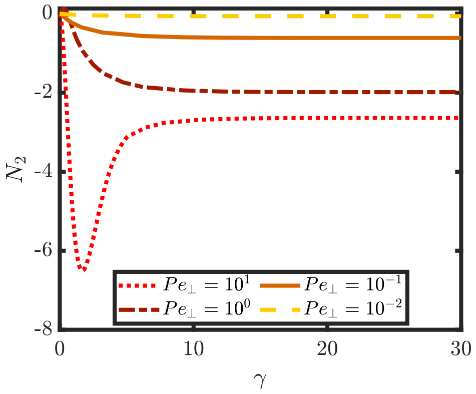

(c) Evolution of the second normal stress difference ($N_2$) with respect to the strain.

Figure 3.15 – Effect of the translational Peclet number on the evolution of the normalized rheological properties (a) shear viscosity ($\Sigma_{r\theta}$), (b) first normal stress difference ($N_1$) and (c) second normal stresses difference ($N_2$) as a function of strain ($\gamma$) at $r = (R_{in} + R_{out})/2$ ($\dot{\gamma} = 1/s$).

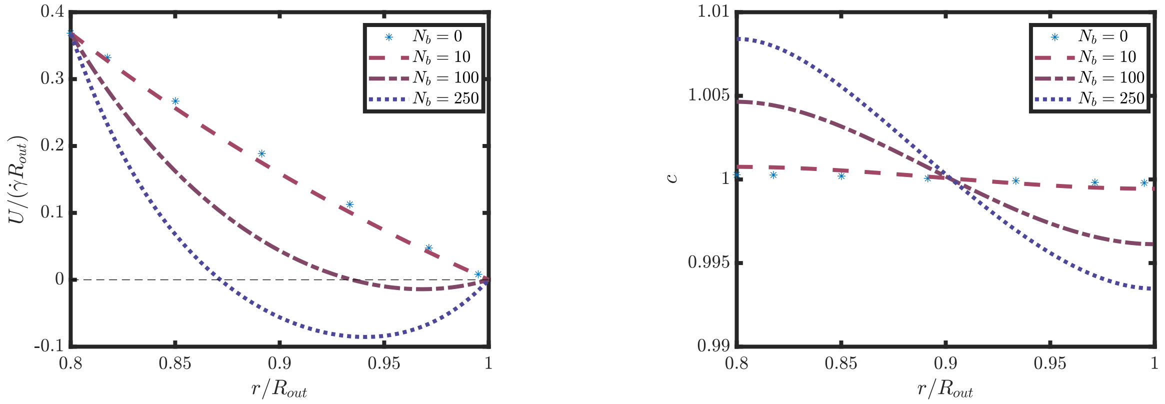

(a) Velocity profiles along the $r$-direction for $N_b = 0, 10, 100$ and 250 at $t = 30$.

(b) Concentration distributions along the $r$-direction for $N_b = 0, 10, 100$ and 250 at $t = 30$.

Figure 3.16 – Effect of Brownian stress contribution on the (a) velocity profile and (b) concentration distribution along the $r$-direction for $N_b = 0, 10, 100$ and 250, and $N_p = 0$ at $t = 30$.

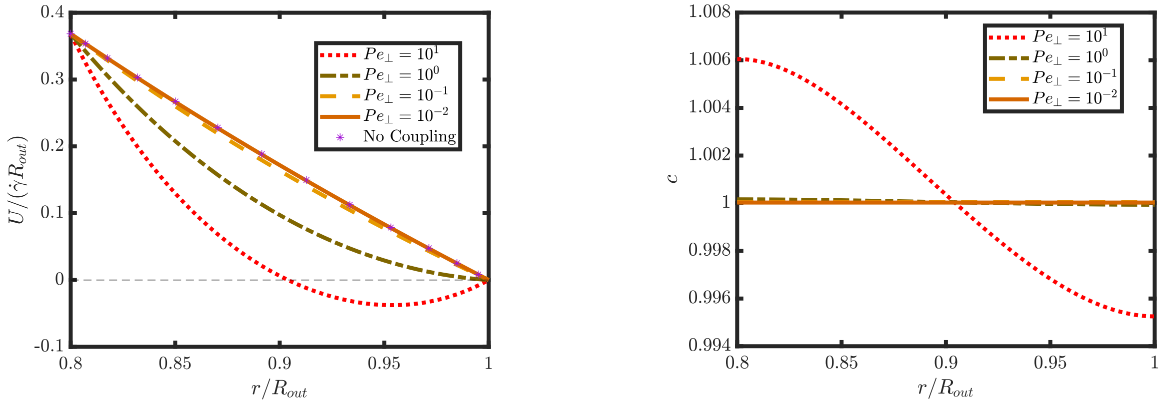

(a) Effect of the translational Peclet number on the velocity profile along the $r$-direction of the base line for $Pe_\perp = 10^{-2}, 10^{-1}, 10^0$ and $10^1$ at $t = 30$.

(b) Effect of the translational Peclet number on the concentration along the $r$-direction of the base line for $Pe_\perp = 10^{-2}, 10^{-1}, 10^0$ and $10^1$ at $t = 30$.

Figure 3.17 – Effect of the translational Peclet number on ((a) velocity profile and (b) concentration along the $r$-direction for $Pe_\perp = 10^{-2}, 10^{-1}, 10^0$ and $10^1$ at $t = 30$.

Chapter 4

# SUSPENSION OF ACTIVE ROD-LIKE PARTICLES IN COMPLEX FLOWS

This study explores the dynamics of active rodlike particles in flow systems, focusing on the active particles-fluid interactions and particles accumulation induced by anisotropic translational diffusion. Numerical simulations based on the work of Mezi et al. [98] are used to analyse the results. In Poiseuille flow, active rods are accumulated at the walls with high alignment in the flow direction and nematic order in the wall directions. A circular obstacle is introduced in the Poiseuille flow which develops non-homogeneous flow. The results of this study offer important new understandings into the intricate behavior of suspended active rods under various flow conditions.

Cette étude explore la dynamique des particules actives en forme de bâtonnet dans les systèmes d'écoulement, en se concentrant sur les interactions particules actives-fluide et l'accumulation des particules induite par la diffusion translationnelle anisotrope. Des simulations numériques basées sur les travaux de Mezi et al. [98] sont utilisées pour analyser les résultats. Dans l'écoulement de Poiseuille, les tiges actives sont accumulées sur les parois avec un alignement élevé dans la direction de l'écoulement et un ordre nématique dans les directions des parois. Un obstacle circulaire est introduit dans l'écoulement de Poiseuille, ce qui entraîne un écoulement non homogène. Les résultats de cette étude permettent de mieux comprendre le comportement complexe des tiges actives en suspension dans diverses conditions d'écoulement.

## 4.1 Introduction

The movement of active particles within confined spaces and their interaction with solid boundaries are crucial in various biological processes. Spermatozoa accumulate at surfaces [181], which is important for sperm behavior and interactions during fertilization. Bacterias tend to gather and interact with external flows near surfaces, significantly impacting their adhesion and biofilm formation capabilities. Lecuyer et al. [182] found that Pseudomonas aeruginosa PA14 bacteria stick to surfaces for longer time with increasing shear stress. Additionally, the concentration of bacteria near surfaces affects how they interact with the gastrointestinal wall during digestion, which has implications for a number of pathologies [183, 184]. The tendency of swimming particles to accumulate near boundaries is the most noticeable characteristic of confined active suspensions. This was first discovered by Rothschild [114], who examined the distribution of swimming bull spermatozoa in a glass chamber and reported that there was a strong concentration peak close to the walls. When Berke et al. [115] carried out the same experiment again with Escherichia coli suspensions in microchannels, they also noticed a substantial accumulation of bacteria on the channel walls. They also mentioned how bacteria tended to align parallel to boundaries.

Hill et al. [185] conducted experiments tracking Escherichia coli trajectories near a rigid surface in a microfluidic channel, proposing a complex mechanism for their upstream swimming involving flagellar bundles chirality and hydrodynamic interactions. Subsequently, Kaya and Koser [186] further characterized their hydrodynamic interactions, showing that Escherichia coli cells undergo modified Jeffery orbits near walls [22]. Measuring and characterizing this hydrodynamic phenomenon has been a major objective of their work [186] as a first step in modeling and understanding shear-assisted orientation and upstream migration. Yet more recent research by Kaya and Koser [187], who methodically examined Escherichia coli motility near a surface as a function of the local shear rate, provided a clearer understanding of this phenomenon. They deduced that individual bacteria entering a flow system can rapidly migrate upstream. As previously explained by Lauga et al. [188], circular trajectories were seen at low shear rates because of the chirality of the cells. Positive rheotaxis was reported at higher shear rates, and it was accompanied by swift and continuous upstream motility. The combined effects of surface hydrodynamic interactions and orientation by the shear flow, which aligns the cells against the flow, were used to explain this directional swimming. The majority of confinement-based experimental studies have concentrated on swimming dynamics and near-wall aggregation. Secchi et al. [189] established that fluid flow predominantly governs the colonization of non-planar surfaces by motile bacteria. This was demonstrated through microfluidic experiments on Pseudomonas aeruginosa and Escherichia coli bacteria. Velocity gradients on curved surfaces dictate preferential attachment to specific regions. This is contrary to the case of nonmotile cells that attach at namely the leeward side of cylinders and immediately below apexes on corrugated sur-

faces [189]. Vennamneni et al. [190] investigated shear-induced migration of microswimmers in a dilute suspension. They found thatThe steady state concentration profile is a function of the rotary Peclet number and the particle aspect ratio. Hernandez-Ortiz et al. [191, 192] performed direct numerical simulations of hydrodynamically interacting swimming particles contained in a gap between two plates using a straightforward dumbbell model. They found a strong particle accumulation at the boundaries in diluted systems. Elgeti and Gompper [193] introduced a Fokker-Planck description of active Brownian suspensions. They observed excellent agreement between analytical solutions and numerical results in simulations of self-propelled spheres in limits of narrow channels or small propulsion velocities despite completely ignoring hydrodynamic interactions. This study suggests that neither shape anisotropy nor wall hydrodynamic interactions are necessary to understand migration. Lee [194] proposed a comparable continuum model and derived analytical expressions for the ratio of particles in the bulk to those in the near-wall region for weak and strong rotational diffusion limits. Li and Ardekani [195] conducted direct numerical simulations of confined suspensions of spherical squirmers propelled by an imposed slip velocity, observing substantial accumulation at the boundaries irrespective of propulsion details. They also observed a tendency of particles to align perpendicularly to the wall in the near-wall region. Saintillan and Shelley [196, 197] introduced a class of models to elucidate the emergence of collective motion in semi-dilute suspensions. These models relie on a conservation equation for the distribution function representing particle positions and orientations. These models consider fluxes resulting from self-propulsion, advection, rotation by the background fluid flow, and diffusive processes. Baskaran and Marchetti [198] derived a continuum description of a suspension of active organisms that includes fluid-mediated, long-range hydrodynamic interactions among swimmers, showing that these interactions offer a straightforward, universal explanation for various nonequilibrium phenomena observed in the literature [5, 199–202], independent of the microscopic physical model of individual swimmers. Forest et al. [203] developed a kinetic model for active polar liquid crystalline polymers, which exhibits a variety of excitable and stationary patterns in dilute regimes. Ezhilan and Saintillan [204] investigated the dynamics of confined suspensions of active particles subjected to pressure-driven flow using a kinetic model that incorporates detailed treatment of boundary conditions. They found peculiar dynamics, including wall accumulation, upstream swimming, centerline depletion, and shear-trapping, and provide analytical expressions for concentration and polarization profiles, demonstrating excellent agreement with numerical simulations and experimental observations.
In the previous numerical studies, the translational diffusion is addressed as an isotropic constant, while in fact the translational diffusion is anisotropic that depends on particle orientations. This work focuses on tackling the absence of consideration for anisotropic translational diffusion in previous numerical researches regarding the active particles. A numerical method based on the approach of Férec et al. [96] and Mezi et al. [98], utilizing the finite volume method, is updated,

by changing the translational diffusion into an anisotropic tensor, to solve for the orientation of active Brownian particles. The extra stress contributions exerted by the active particles are not taken into consideration to clearly highlight the effect of the anisotropic diffusion on the suspensions.

The structure of this chapter is as follows. Sec. 4.2 focuses on the theoretical modeling. Then Sec. 4.3 describes the numerical model used to solve the active particle suspensions. Finally before the conclusion, Sec. 4.4 shows the numerical results in two geometries, planar infinite channel then a planar channel with introducing a circular obstacle.

## 4.2 Hypothesis

Consider a suspension of Brownian rodlike active particles of length $L$ and width $d$. The active rods are mono-dispersed, neutrally buoyant, and rigid. The suspension is considered in the dilute concentration regime. Active rods are polar (the head of the rod is not identical to its tail). A position vector $\mathbf{r}_c$ and an orientation unit vector $\mathbf{p}$ describe each rod. For simplification, the extra stress contribution is not considered in this work.

### 4.2.1 Kinetic model equation

A suspension of active Brownian particles can be described via a probability distribution function $\Psi(\mathbf{r}_c, \mathbf{p}, t)$. It represents the probability to find particles at location $\mathbf{r}_c$ with orientation $\mathbf{p}$, at the instant $t$. In a dilute regime, a single-particle Smoluchowski equation can be obtained as

$$\frac{\partial \Psi}{\partial t} = -\nabla_{\mathbf{x}} \cdot (\dot{\mathbf{r}}_c \Psi) - \nabla_{\mathbf{p}} \cdot (\dot{\mathbf{p}} \Psi) \,. \tag{4.1}$$

The evolution of the position of an active Brownian particle with respect to time , $\dot{\mathbf{r}}_c$, is [197]

$$\dot{\mathbf{r}}_c = \mathbf{u} + V_s \mathbf{p} - \mathbf{D}_t \cdot \nabla_{\mathbf{x}} \log \Psi, \tag{4.2}$$

where $V_s$ is the particle velocity. The evolution of its orientation with respect to time, $\dot{\mathbf{p}}$, can be written as

$$\dot{\mathbf{p}} = \dot{\mathbf{p}}_j - D_r \nabla_{\mathbf{p}} \log \Psi, \tag{4.3}$$

where $\dot{\mathbf{p}}_j$ is the Jeffery's equation and it is given by [22]

$$\dot{\mathbf{p}}_j = -\frac{1}{2} \boldsymbol{\omega} \cdot \mathbf{p} + \frac{\lambda}{2} \left( \dot{\boldsymbol{\gamma}} \cdot \mathbf{p} - \dot{\boldsymbol{\gamma}} : \mathbf{ppp} \right) . \tag{4.4}$$

$D_r$ and $\mathbf{D}_t$ are the rotary diffusion coefficient and translational diffusion tensor , respectively. The latter for non-spherical, rigid particles is defined by $\mathbf{D}_t = D_{\parallel} \mathbf{pp} + D_{\perp} (\boldsymbol{\delta} - \mathbf{pp})$, where $D_{\parallel}$

and $D_\perp$ are constants that characterize the diffusion parallel and perpendicular to the particle axis [40]. $\mathbf{u}$ is the external flow velocity vector at location $\mathbf{r}_c$. $\nabla_{\mathbf{p}}$ and $\nabla_{\mathbf{x}}$ denote the gradient operators in configurational and spatial spaces, respectively. $\boldsymbol{\omega}$, $\dot{\boldsymbol{\gamma}}$, and $\boldsymbol{\delta}$ are the vorticity, strain rate, and identity tensors, respectively. $\lambda$ is a constant form factor as a function of the particle aspect ratio $a_r = L/d$, in the case of rods, $\lambda = 1$. Hence, the expanded version of Eq. 4.1, by taking into account the fluid incompressibility condition, is

$$\frac{D\Psi}{Dt} = -\nabla_{\mathbf{x}} \cdot (V_s \mathbf{p} \Psi) + \nabla_{\mathbf{x}} \cdot (\mathbf{D}_t \cdot \nabla_{\mathbf{x}} \Psi) - \nabla_{\mathbf{p}} \cdot (\dot{\mathbf{p}}_j \Psi) + D_r \nabla^2_{\mathbf{p}} \Psi, \tag{4.5}$$

where $\frac{D(...)}{Dt} = \frac{\partial(...)}{\partial t} + \mathbf{u} \cdot \nabla_{\mathbf{x}}(...)$ is the material derivative operator, and $\nabla^2_{\mathbf{p}}$ is the Laplacian operator in configurational domain. In what follows, we derive an equivalent evolution equation based on the second-order moment of $\Psi$.

### 4.2.2 Flow problem

The problem is governed by the Stokes equations in the limit of creeping flow

$$\nabla_{\mathbf{x}} \cdot \mathbf{u} = 0, \tag{4.6}$$

$$-\eta_0 \nabla^2_{\mathbf{x}} \mathbf{u} + \nabla_{\mathbf{x}} P = \mathbf{0}. \tag{4.7}$$

In the above equations, $\nabla^2_{\mathbf{x}}$ is the Laplacian operator in the spatial space, $\eta_0$ is the dynamic viscosity of the Newtonian suspending fluid, $P$ denotes the pressure. The extra stress contribution by the particles and brownian motion is set to zero for simplicity and in order to highlight the effect of the translational diffusion.

### 4.2.3 Dimensionless formulation of the problem

Choosing the active rod length $L$ as the characteristic length and the characteristic strain rate $\dot{\gamma} = U_{avg}/L$, where $U_{avg}$ is the average flow velocity, and the dimensionless concentration $c^* = \frac{c}{n}$, where $n$ is the mean number density. The dimensionless form of FP equation (Eq. 4.5) is

$$\frac{D\Psi}{D\tau} = -Pe_s \nabla^*_{\mathbf{x}} \cdot (\mathbf{p}\Psi) + \nabla^*_{\mathbf{x}} \cdot \left\{ \left[ \frac{1}{Pe_\parallel} \mathbf{pp} + \frac{1}{Pe_\perp} (\boldsymbol{\delta} - \mathbf{pp}) \right] \cdot \nabla^*_{\mathbf{x}} \Psi \right\} - \nabla_{\mathbf{p}} \cdot (\dot{\mathbf{p}}_j \Psi) + \frac{1}{Pe_r} \nabla^2_{\mathbf{p}} \Psi, \tag{4.8}$$

where $Pe_s = \frac{Vs}{L\dot{\gamma}}$ is a dimensionless number that represents the relative velocity of the active rod with respect to the flow velocity. This dimensionless number can provide insights into how active rods respond to the applied shear flow. For example, if $Pe_s$ is much smaller than 1, it suggests that the active rod moves relatively slowly compared to the rate of deformation, indicating a less responsive or less mobile active rod. Conversely, if $Pe_s$ is close to or greater than 1, it suggests that the active rod moves more rapidly in comparison to the flow velocity, indicating a more mobile or responsive active rod. The dimensionless equation of flow is

$$-\nabla_{\mathbf{x}}^{*2}\mathbf{u}^{*}+\nabla_{\mathbf{x}}^{*}P^{*}=\mathbf{0} \tag{4.9}$$

## 4.3 Numerical model

This study focuses on a 2D problem confining the active rod on a plane with one configurational coordinate ($\theta$), and two spatial Cartesian coordinates $x$ and $y$. At each spatial node, this multidimensional problem imposes a mesh for the active rod orientation angle $\theta$ domain. The partial differential equation, Eq. 4.8, is discretized in the configurational space using the finite volume technique (FVM). The FVM is known for having the local conservativeness property required to satisfy the model formalized normalization constraint for the PDF. Following the work of Férec et al. [96] and Mezi et al. [98] the model is updated to solve Eq. 4.8 for active rods with an anisotropic diffusion tensor. In this context, all the possible orientations describe a full circle of unit radius since an active rod is polar. As a result, the perimeter of the circle has been divided into N equal intervals of length $\Delta\theta = 2\pi/N$. The convection-diffusion problem is solved using an upwinding power-law approach in the configurational space [205]. Therefore, the descritized form for nodal points $P$, $E$ and $W$ of the FP equation, Eq. 4.8, is

$$\begin{aligned}\Delta\theta\frac{\partial\Psi_p}{\partial\tau}+\Delta\theta\mathbf{u}\cdot\nabla_{\mathbf{x}}\Psi_p-\Delta\theta\nabla_{\mathbf{x}}\cdot\left\{\left[\frac{1}{Pe_{\perp}}(\mathbf{pp}+\boldsymbol{\delta})\right]\cdot\nabla_{\mathbf{x}}\Psi_p\right\}&\\+\Delta\theta Pe_s\nabla_{\mathbf{x}}\cdot\Psi_p+a_P\Psi_P-a_W\Psi_W-a_E\Psi_E=0.&\end{aligned} \tag{4.10}$$

COMSOL Multiphysics 6.1 is used, which enables coupling of the existing laminar flow interface with partial differential equation (PDE) interfaces, which are necessary for simulating the additional active rod stresses, the whole problem (i.e., flow field and fiber orientation) is solved using this software with livelink with MATLAB R2022B to implement the equations. Given that there are $N$ nodal points involved in discretization of $\Psi$, the coupled system of PDEs is represented by using the matrix coefficient forms.

## 4.4 Numerical results

We employ the Finite Volume method to investigate two flow problems, solving the problem defined in Eqs. 4.6, 4.7 and 4.10. The indices 1 and 2 represent the flow direction and the velocity gradient direction, respectively. In a simple shear flow and Poiseuille flow, they are indicated with x and y, respectively.

### 4.4.1 Poiseuille flow

We conduct simulations within a square 2D channel with a side length of $H$, featuring a Poiseuille flow between two stationary walls defined by $(U/(\dot{\gamma}H)) = 1-4(y/H)^2)$. To simulate an infinitely long channel, periodic flow conditions are employed with a constant flow rate (as depicted in Fig. 4.1). The initial condictions are set to $\Psi = 1/2\pi$, where active rods are assumed to be initially random planar and homogeneously distributed along the channel. This means that the initial conformation tensor conditions are set as $A_{ii} = 1/3$ and $A_{ij} = 0$ for $i \neq j$.

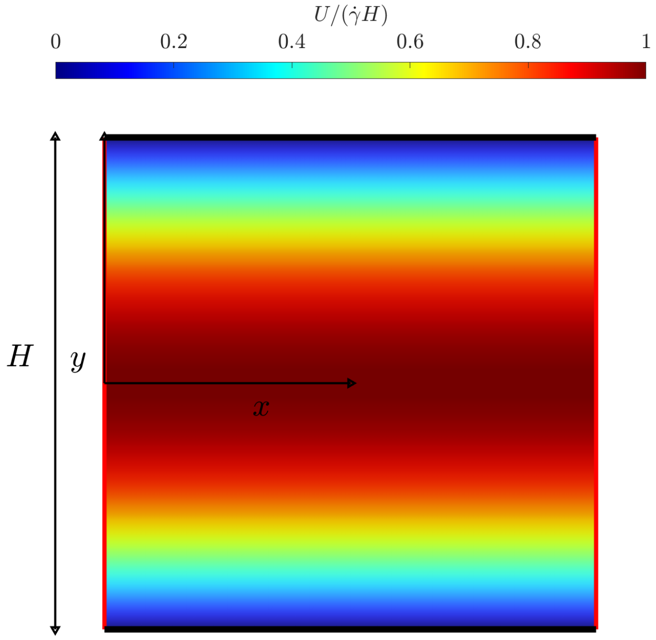

Figure 4.1 – Dimensionless velocity magnitude in the squared channel, of side H, for Poiseuille flow with periodic BC. The vertical red lines represent the periodic conditions.

#### Effect of particles velocity

Based on the diffusion Peclet numbers ($Pe_r$ and $Pe_\perp$) and the active rod self-propulsion Peclet numbers ($Pe_s$), we investigate three different regimes. The first regime ($Pe_s, Pe_r, Pe_\perp$) investigates conditions in which the directed motion resulting from self-propulsion is only marginally present. The second regime ($Pe_s = Pe_r = Pe_\perp$) corresponds to situations in which active motion and diffusion are in competition. The third regime ($Pe_s > Pe_r, Pe_\perp$) examines circumstances in which active motion takes precedence over diffusion. In this instance, $Pe_\perp = Pe_r = 10$ and $Pe_s = 0, 5, 10$, and 15 are the fixed Peclet numbers. No extra stress caused by active rods is taken into account, and the flow issue is derived from Eq. 4.9. The concentration profiles, as depicted in Figure 4.2a, shows active rod accumulation near the walls. This is particularly evident at higher values of the self-propulsion Peclet number ($Pe_s$). This accumulation of active rods near the walls is accompanied by a decrease in their alignment in the flow direction, as indicated in Fig. 4.2b. Moreover, the nematic order parameter, as shown in Figs. 4.2c and 4.2d, indicates a higher nematic alignment near the walls. In this context, the nematic director $n_2$ shares the same direction as the wall-normal coordinate $y$ and exhibits a substantially higher absolute value near the walls, gradually diminishing towards the center of the channel.

Fig. 4.2b provides insight into the alignment of active rods along the $y$-direction at steady state. Increasing the self-propulsion ($Pe_s$) results in a more alignment of the active rods in the direction of the flow. This alignment phenomenon arises due to the interplay between self-propulsion and fluid flow-induced shear. As the active rods exhibit stronger self-propelled motion with higher $Pe_s$, this active motion enhances the rod orientations induced by the flow in the flow direction, with higher alignment around the center of the channel. This alignment effect is particularly pronounced due to the dominance of self-propulsion over diffusion, leading to organized patterns of alignment parallel to the flow direction.

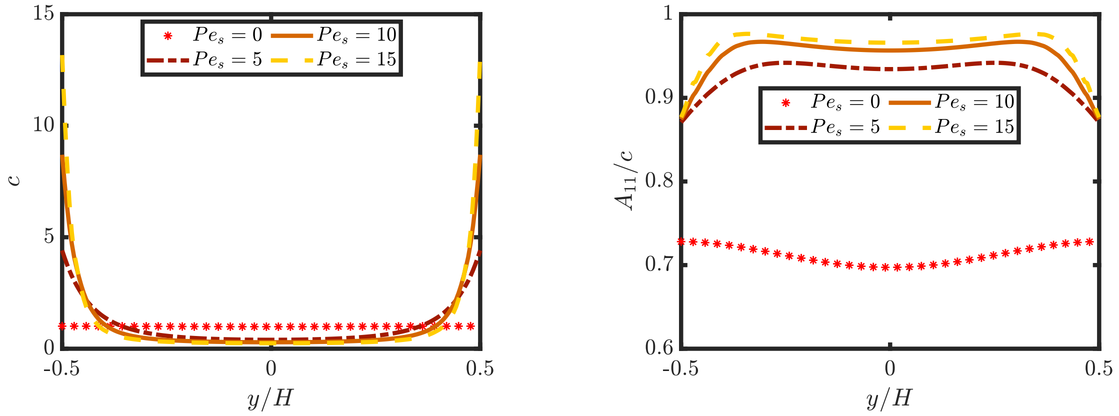

(a) Effect of the particles self-propulsion Peclet number, $Pe_s$, on the concentration distribution, $c$, along the $y$ direction.

(b) Effect of the particles self-propulsion Peclet number, $Pe_s$, on the orientation component, $A_{11}/c$, along the $y$ direction.

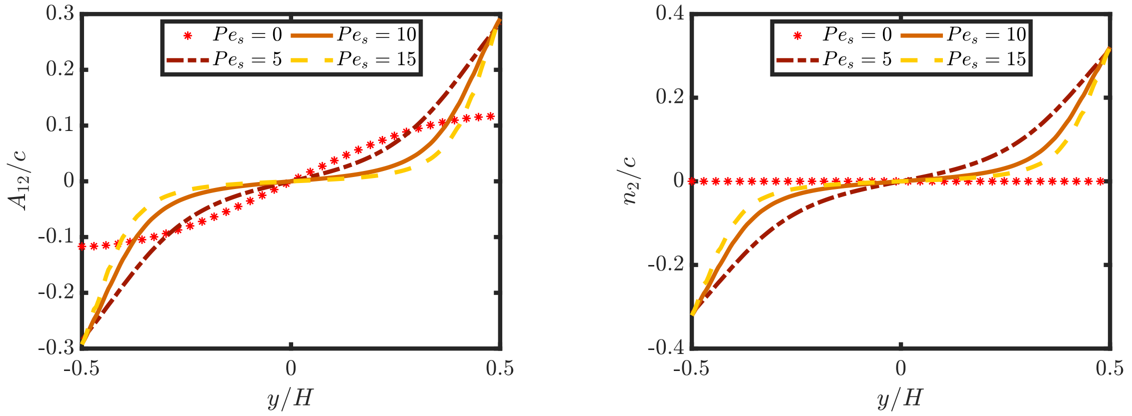

(c) Effect of the particles self-propulsion Peclet number, $Pe_s$, on the orientation component, $A_{12}/c$, along the $y$ direction.

(d) Effect of the particles self-propulsion Peclet number, $Pe_s$, on the nematic order, $n_2/c$, along the $y$ direction.

Figure 4.2 – Showing the effect of the particles self-propulsion Peclet number, $Pe_s = 0, 5, 10$ and 15, (a) on the concentration distribution, $c$, (b) on the orientation component, $A_{11}/c$, (c) on the orientation component, $A_{12}/c$, (d) on the nematic order, $n_2/c$, along the $y$ direction at steady state, in Poiseuille flow.

### Effect of anisotropic translational diffusion

Here, we want to understand how directional diffusion affects the suspension active rods as opposed to the isotropic translational diffusion. We fixed the particles self-propulsion Peclet number $Pe_s = 5$ and the rotary Peclet number $Pe_r = 10$. We compare a constant translational Peclet number (replacing the diffusion tensor in Eq. 4.8) $Pe = \frac{Pe_{\parallel}+Pe_{\perp}}{2}$ ($Pe_{\perp} = 10$), with the case when the translational diffusion is a tensor.

In the case of anisotropic translational diffusion, the active rods experience various effective diffusions depending on their orientations. Figs. 4.3a and 4.3b show the concentration results examining an isotropic translational diffusion and an anisotropic translational diffusion, respectively. Both cases predict the migration of active rods toward the fixed walls. Fig. 4.3b shows strong accumulation of active rods at the wall, while Fig. 4.3a shows a moderate migration. Anisotropic diffusion can also influence the alignment behavior of the active rods. Figs. 4.4a and 4.4b show the orientation of the active rods in the flow direction ($x$ direction). The directional dependence of diffusion contributes to a more pronounced alignment of active rods with the flow direction. In the case of isotropic diffusion, the active rods experience the same diffusion coefficient in all directions, resulting in a more uniform and isotropic exploration of the flow field. While the active rods can still migrate towards low shear regions and align with the flow direction, the isotropic nature of diffusion limits the migration enhancement compared to the anisotropic case. The isotropic diffusion leads to a more moderate alignment of active rods the flow direction, and the migration towards low shear regions is less pronounced compared to the anisotropic case.

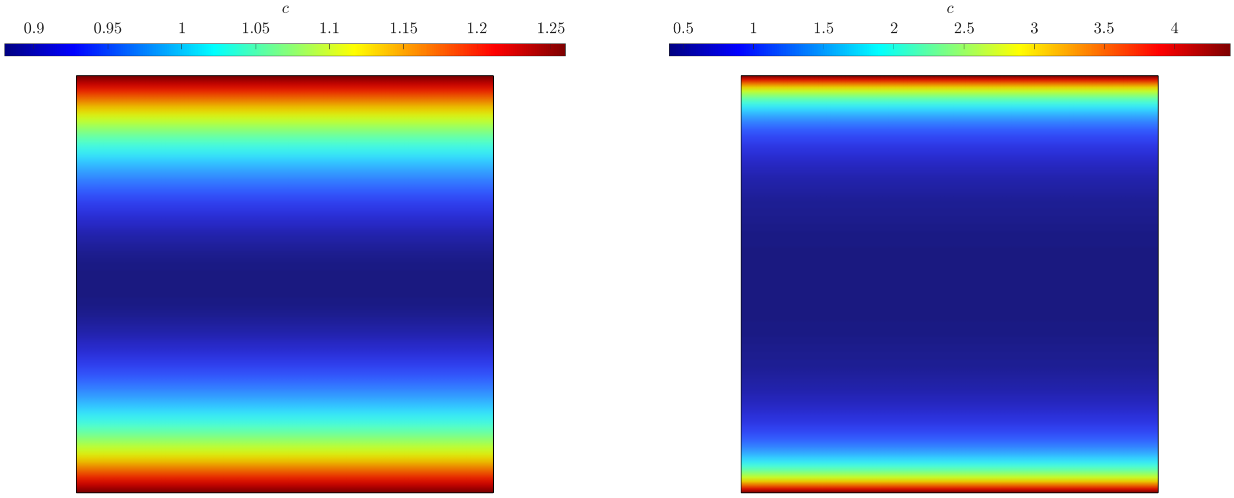

(a) Concentration distribution $c$ at steady state for isotropic traslational diffusion.

(b) Concentration distribution $c$ at steady state for anisotropic translational diffusion.

Figure 4.3 – Showing the effect of (a) isotropic translational diffusion and (b) anisotropic translational diffusion on the concentration distribution $c$ along the channel at steady state.

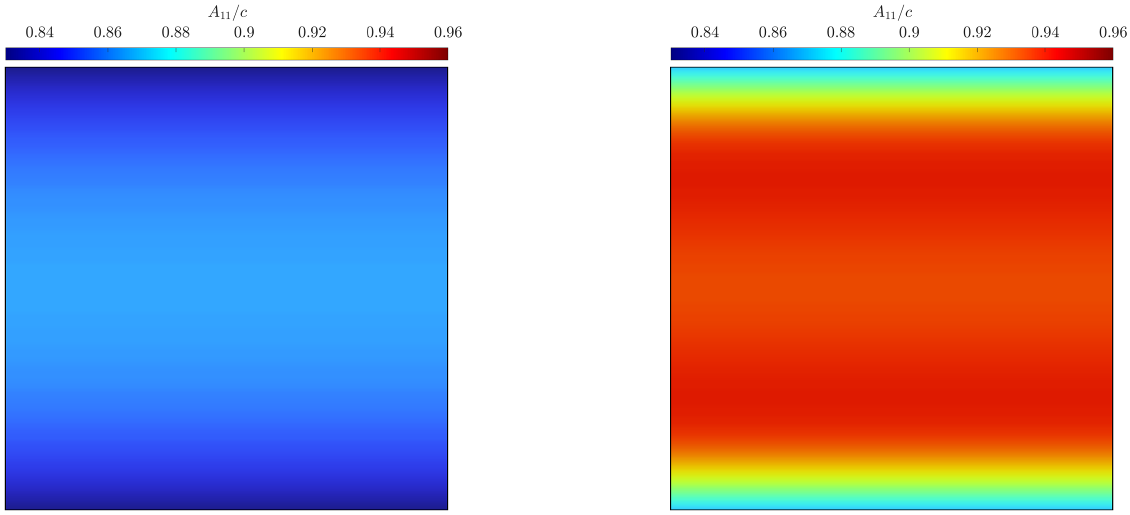

(a) Orientation component distribution $A_{11}/c$ at steady state for isotropic translational diffusion.

(b) Orientation component distribution $A_{11}/c$ at steady state for anisotropic translational diffusion.

Figure 4.4 – Showing the effect of (a) isotropic translational diffusion and (b) anisotropic translational diffusion on the orientation component $A_{11}/c$ along the channel at steady state.

#### Effect of rotary diffusion

We conducted simulations to explore the effects of varying rotary Peclet numbers ($Pe_r$), focusing on cases where $Pe_r$ values were set at $1, 10, 100$, and 1000. To maintain consistency, we kept the particle self-propulsion Peclet number is fixed at $Pe_s = 5$, and the translational diffusion coefficient was maintained at a constant value represented by $Pe_\perp = 10$. As anticipated, the outcomes revealed that higher rotary Peclet numbers tend to attenuate the alignment of active rods in the direction of the flow. Moreover, our investigations unveiled an intriguing trend: increasing in $Pe_r$ led to higher active rod accumulation toward the channel walls (see Fig. 4.5a). This trend mirrors the behavior observed in passive rod systems, where the migration of actively aligned rods becomes less prominent as the value of $Pe_r$ increases. Additionally, Fig. 4.5b indicates that the nematic order of active rods near the walls is influenced by rotary diffusion. Notably, as the rotary Peclet number ($Pe_r$) decreases, the nematic order exhibits a discernible increase. This finding suggests that the interaction between rotary diffusion and the fluid dynamics plays a crucial role in shaping the spatial distribution and alignment of active rods in the channel. These results are in good agreement with the work of Matilla et al. [206], where the increase of the rotary Peclet number leads to more accumulations at the walls.

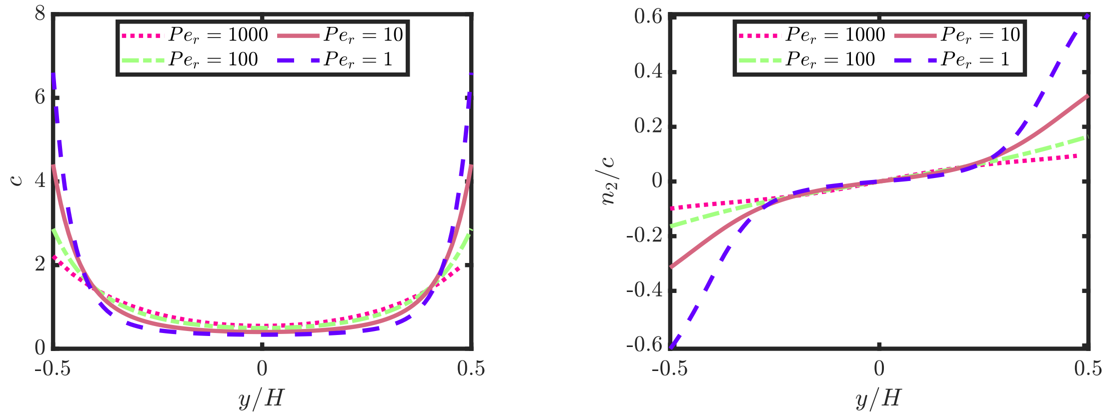

(a) Effect of the rotary diffusion, $Pe_r$, on the concentration distribution, $c$, along the $y$ direction.

(b) Effect of the rotary diffusion, $Pe_r$, on the nematic order, $n_2/c$, along the $y$ direction.

Figure 4.5 – Showing the effect of the rotary diffusion, $Pe_r = 1, 10, 100$ and 1000, (a) on the concentration distribution, $c$, (b) on the nematic order, $n_2/c$, along the $y$ direction at steady state, in Poiseuille flow.

**Effect of translational diffusion**

In the context of parabolic flow, we are investigating the influence of translational diffusion on a system of active rods. To examine this, we maintained a constant particles self-propulsion Peclet number of $Pe_s = 5$ and a rotary diffusion coefficient of $Pe_r = 10$, while systematically varying the translational Peclet number with different values, $Pe_\perp = 0.1, 1,$ and 10. Our findings illustrate that at higher $Pe_\perp$ values, active rods tend to accumulate near the channel walls. Conversely, as $Pe_\perp$ decreases, this wall accumulation tendency diminishes, eventually resulting in a more uniform distribution of active rods along the channel. Notably, when $Pe_\perp = 0.1$, active rods exhibit a nearly homogeneous distribution throughout the channel.

Fig. 4.6b shows that under higher $Pe_\perp$ conditions, active rods exhibit a heightened orientation preference aligned with the flow direction. In contrast, lower $Pe_\perp$ values coincide with active rod orientations that approach a more randomized distribution. This observation implies that the translational Peclet number acts as a constraining factor on the self-propulsion dynamics of active rods. Figs. 4.6c and 4.6d reveal that the quantity $A_{12}/c$ exhibits the same direction in comparison to $y/H$, and $n_2/c$ aligns with the same direction as $y/H$. This alignment pattern suggests that the active rods exhibit polarization towards the flow direction, accompanied by nematic order directed towards the walls of the channel.

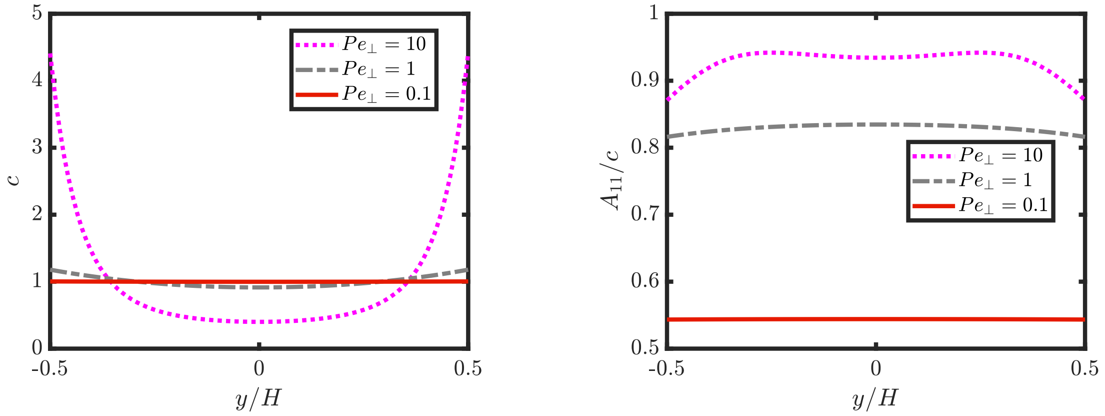

(a) Effect of the particles self-propulsion Peclet number, $Pe_s$, on the concentration distribution, $c$, along the $y$ direction.

(b) Effect of the particles self-propulsion Peclet number, $Pe_s$, on the orientation component, $A_{11}/c$, along the $y$ direction.

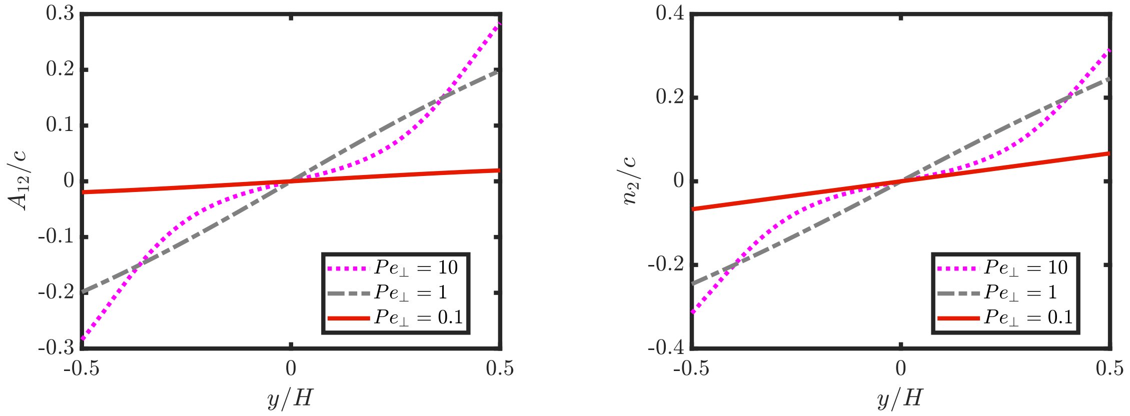

(c) Effect of the particles self-propulsion Peclet number, $Pe_s$, on the orientation component, $A_{12}/c$, along the $y$ direction.

(d) Effect of the particles self-propulsion Peclet number, $Pe_s$, on the nematic order, $n_2/c$, along the $y$ direction.

Figure 4.6 – Showing the effect of the translational diffusion, $Pe_\perp = 0.1, 1$ and 10, (a) on the concentration distribution, $c$, (b) on the orientation component, $A_{11}/c$, (c) on the orientation component, $A_{11}/c$, (d) the nematic order, $n_2/c$, along the $y$ direction at steady state, in Poiseuille flow.

### 4.4.2 Results of flow with a circular obstacle

To thoroughly validate and extend the applicability of this model [160, 161], it is imperative to assess its performance in the context of active rods. This step will contribute significantly to enhancing our understanding of how active rods navigate through complex environments, shedding light on their behavior in real-world situations.Indeed, incorporating a model that captures the interaction between suspended rods and obstacles is crucial for comprehending the dynamics of particulate suspensions in diverse engineering scenarios. In fact, biofilms formation on various things, including industrial and maritime infrastructure, can be a serious issue. The prevention methods can indeed be costly [207], and researchers are continuously exploring ways to address this issue more efficiently and economically [208, 209]. Spoting the biofilms formation areas can help in solving the problems. The study is conducted within a planar channel characterized by a width of $2H$ and a length of $W = 3H$. To introduce complexity, a circular obstacle with a radius of $R = 0.5H$ is placed at the center of the channel ($x = H$) as depicted in Fig. 4.7. This work is performed by Issa et al. [210] for passive rods. The study is conducted for $Pe_r = Pe_\perp = 10$.

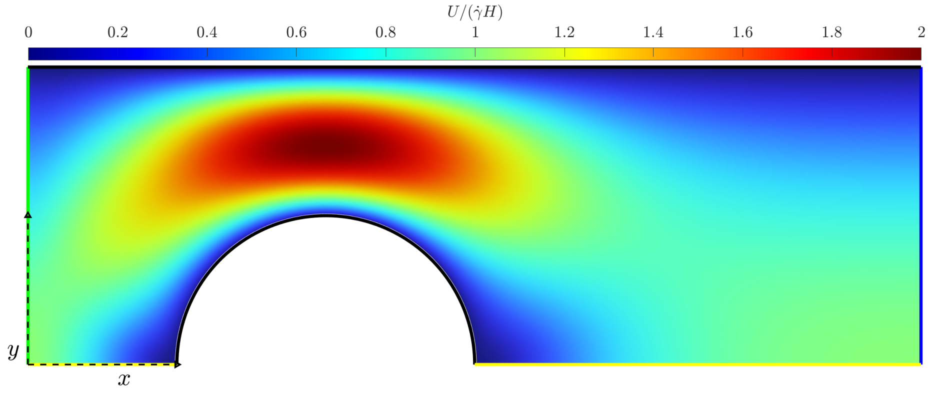

Figure 4.7 – Dimensionless velocity magnitude a rectangular channel, for the precence of circular obstacle. The vertical green line represents the inlet, the horizontal yellow line represents the symmetric and the vertical blue line represents the outlet.

In the context of a Poiseuille flow channel with the inclusion of a circular obstacle, we have investigated the distribution of active rod concentration. The concentration profile, as depicted in Fig. 4.8a, underscores intriguing spatial variations. Specifically, active rods exhibit heightened concentration both near the channel walls and preceding the obstacle. However, there is a substantial decline in active rod concentration downstream of the obstacle. Interestingly, the behavior becomes more pronuanced as the self-propulsion ($Pe_s$) of the active rods increases. In particular, with elevated $Pe_s$, active rods tend to accumulate more prominently along the channel walls and in the region preceding the obstacle. This zone of accumulation becomes narrower with higher active rod concentration. Moreover, Fig. 4.8b sheds light on the orientation of active rods. Specifically, active rods are observed to align in the $x$ direction at the rear of the obstacle and in the upper part of the channel. Conversely, before and after the obstacle, particularly at the center of the channel ($y = 0$), active rods adopt an orientation opposite to the flow direction.

As shown in the study, biofilms are formed at the rear part of the obstacle. These findings are in quantative agreement with the work of Mino et al. [211] were they found accumulation of motile bacteria at the rear of a confined obstacle.

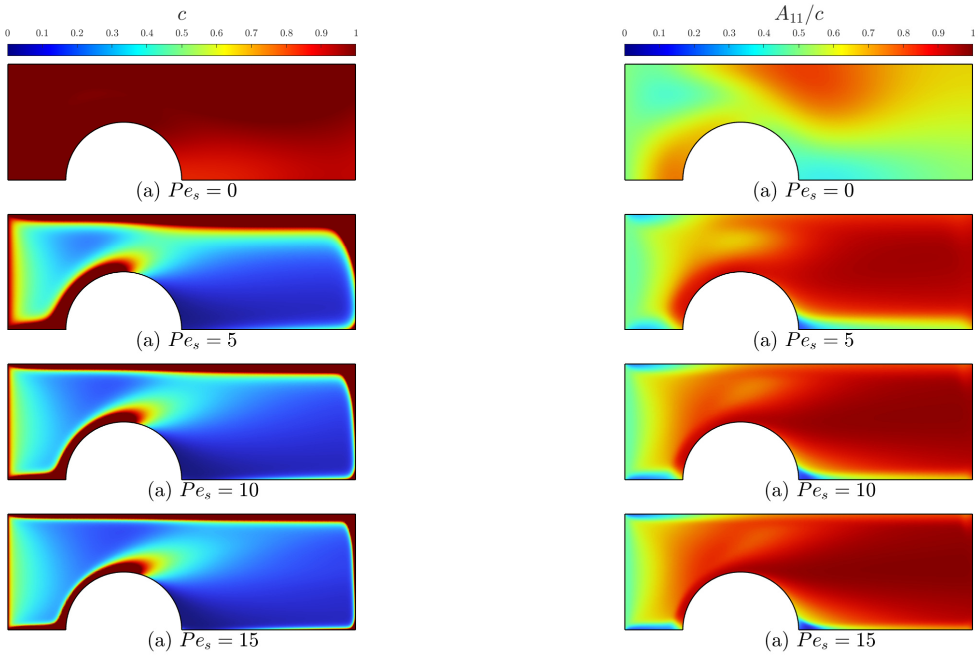

(a) Effect of the particles self-propulsion Peclet number, $Pe_s$, on the concentration distributon, $c$, along the channel, at steady state.

(b) Effect of the particles self-propulsion Peclet number, $Pe_s$, on the orientation component, $A_{11}/c$, along the channel, at steady state.

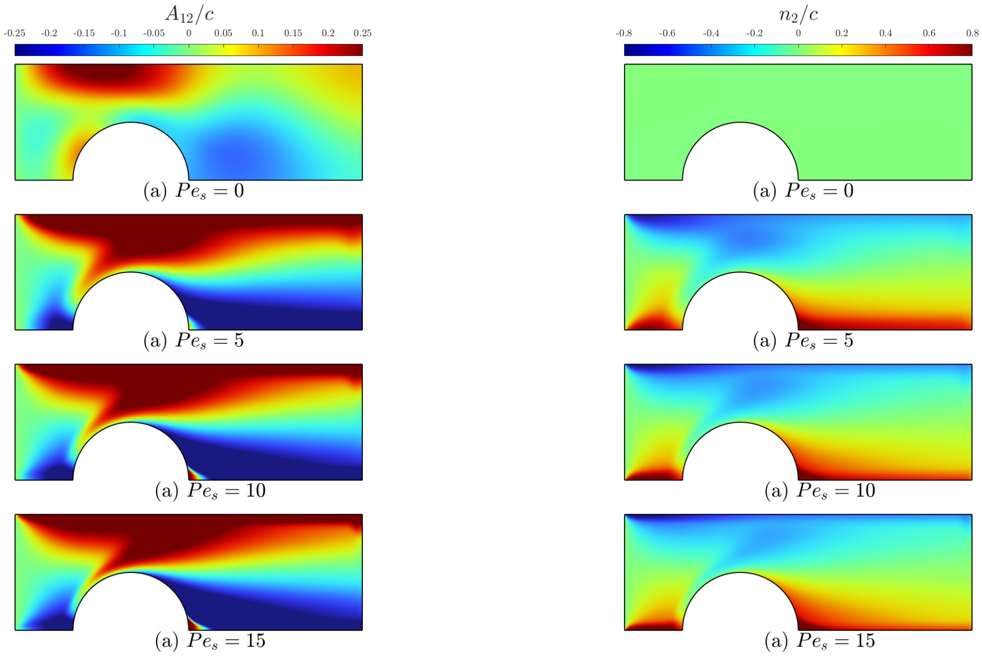

(c) Effect of the particles self-propulsion Peclet number, $Pe_s$, on the orientation component, $A_{12}/c$, along the channel, at steady state.

(d) Effect of the particles self-propulsion Peclet number, $Pe_s$, on the nematic order, $n_2/c$, along the channel, at steady state.

Figure 4.8 – Showing the effect of the particles self-propulsion Peclet number, $Pe_s = 0, 5, 10$ and 15, with the presence of a circular obstacle on (a) the concentration distribution, $c$, (b) the orientation component, $A_{11}/c$, (c) the orientation component, $A_{12}/c$, (d) the nematic order,$n_2/c$, at steady state.

Fig. 4.8c and Fig. 4.8d provide insights into the orientation characteristics of the active rods within the channel containing a circular obstacle. Specifically, Fig. 4.8c depicts the values of the orientation component $A_{12}/c$, while Fig. 4.8d illustrates the nematic order $n_2/c$. In the upper region of the obstacle, extending to the walls, both $A_{12}/c$ and $n_2/c$ exhibit positive values. This indicates that active rods are polarized in the positive $x$ direction and oriented towards the wall. Conversely, at the center of the channel, both $A_{12}/c$ and $n_2/c$ take on negative values. This implies that active rods in this region are polarized in the positive $x$ direction but oriented towards the channel's center.

A distinct behavior is observed immediately after the obstacle in a small area at the center. Here, $A_{12}/c$ remains positive while $n_2/c$ takes on a negative value. This signifies that active rods are polarized in the negative $x$ direction and oriented towards the channel's center in this specific region.

## 4.5 Conclusion

In conclusion, this work explores the behavior of active rod suspensions in different flow systems, Poiseuille flow in infinite channels, and introducing a circular obstacle in channel with Poiseuille flow at the inlet. The study examines the dynamics of active rods including active rod migrations, orientations and the nematic order through a numerical simulations based on the volume method with taking into consideration an anisotropic translational diffusion.

The active rods favor the accumulation at the walls of the channel, in addition active rods are more aligned in the flow direction than the passive rods. Although, randomly aligned active rods at low rotary Peclet numbers $Pe_r$ have more tendency to migrate toward the walls than the aligned active rods. It is shown that translational diffusion hinders the effect of the active rods and at low translational Peclet numbers $Pe_\perp$, the system returns to act as the case of the passive rods. When a circular obstacle is presented, active rods are accumulated at the walls and at the back of obstacle for active rods, while after the obstacle, they are more aligned in the inlet flow direction ($x$ direction) except in the center of the channel, they are aligned in the velocity gradient direction $y$ direction.

To confirm and build upon these findings, additional study and experimentation are required. Future work will focus in expanding this work to 3D. In addition of developing a good closure approximation for the kinetic model that can predict the orientation, concentration and the rheological properties of the active rods with less computational effort.

CHAPTER 5

# ACTIVE ROD-LIKE PARTICLES SUSPENSION IN NON-HOMOGENOEUS SYSTEM: THE EFFECT OF ACTIVE MOTION AND FLOW/ROD COUPLING

This study explores active Brownian rods in simple shear flow, examining the influence of self-propulsion ($Pe_s$), rotary diffusion ($Pe_r$), and translational diffusion ($Pe_\perp$). We observe these rods accumulating near walls, aligning with the flow direction, with more pronounced effects at higher $Pe_s$ and $Pe_\perp$, and lower $Pe_r$. Furthermore, we examine the impact of particle extra stress in simple shear flows, observing shear banding and rheological changes. These findings enhance our understanding of complex effect created by active particles.

Cette étude explore les tiges browniennes actives dans un écoulement cisaillé simple, en examinant l'influence de l'autopropulsion ($Pe_s$), de la diffusion rotative ($Pe_r$) et de la diffusion translationnelle ($Pe_\perp$). Nous observons que ces bâtonnets s'accumulent près des parois, s'alignant avec la direction de l'écoulement, avec des effets plus prononcés pour des $Pe_s$ et $Pe_\perp$ plus élevés, et des $Pe_r$ plus faibles. En outre, nous examinons l'impact de la contrainte supplémentaire des particules dans les écoulements à cisaillement simple, en observant des bandes de cisaillement et des changements rhéologiques. Ces résultats améliorent notre compréhension de l'effet complexe créé par les particules actives.

## 5.1 Introduction

Several biological processes depend on the mobility of active self-propelled particles and their interactions with solid boundaries. Numerous studies have looked into the mobility of biological particles in confined spaces experimentally [114, 115, 185, 189] and numerically [190–192]. The accumulation of active particles on channel walls has been observed. In their additional analysis of the hydrodynamic interactions, Kaya and Koser [186] demonstrated that Escherichia coli cells undergo modified Jeffery orbits near walls [22]. Understanding the upstream migration phenomenon requires knowing this specific information. A greater understanding of this phenomena was offered by more recent study by Kaya and Koser [187], who carefully investigated Escherichia coli motility near a surface as a function of the local shear rate. Swimming dynamics and near-wall aggregation have been the main topics of most confinement-based experimental research. To explain how collective motion emerged in semi-dilute suspensions, Saintillan and Shelley developed a group of models [196, 197] to explain how collective motion emerged in semi-dilute suspensions.In these models, the particle positions and orientations are represented by a distribution function that is based on a conservation equation.The fluxes brought on by diffusive, advective, rotating, and self-propelled processes are all taken into consideration by these models. They examined the stability of aligned suspensions and showed that they are consistently unstable to fluctuations, a finding that confirms earlier hypotheses by Simha and Ramaswamy [93]. They also demonstrated that an instability for the particle stress occurs when isotropic suspensions are taken into account. An active particle impose a net force dipole on the surrounding fluid [191, 196] as it moves forward due to the balance between the propulsive force and viscous drag on its body. This force dipole can take either a positive or a negative sign depending on how the particle drives itself through the fluid: a pusher particle will produce a negative dipole while a puller particle will produce a positive dipole. Hatwalne et al. [212], who generalized liquid crystal kinetic equations to represent the rheology of active suspensions, discovered that for pushers the effective viscosity would decrease and for pullers it would increase. Ishikawa and Pedley [213] then carried out simulations of Stokesian dynamics of suspensions of spherical 'squirmers' that swim as a result of a specified slip velocity on their surface. They discovered that swimming had no influence on effective viscosity in the dilute limit. A result of the spherical shape, which generates an isotropic distribution of orientation. Haines et al. [214] demonstrated through analytical calculations that swimming does definitely cause a change in viscosity if the orientation distribution is considered to be anisotropic. Additionally, they saw a reduction in the viscosity of pusher suspensions. Saintillan [70] discovered that tail-actuated swimmers significantly reduce the fluid's effective shear viscosity and that the rheology is characterized by much higher normal stress differences than for passive suspensions. Recent research has found that bacterial suspensions exhibit counter-intuitive behavior when subjected to external shear, including regimes of apparent superfluidity [109, 215]. By demonstrating a novel concentration-shear coupled mechanism, Vennamneni et al. [216] show how fluctuations in bacterial suspensions can grow and eventually reach banded steady states. In stark contrast to the passive complex fluids [217–219] and active fluids [67, 220] studied earlier, the proposed mechanism is shown to result in shear bands, with concentration inhomogeneities, in the dilute regime. Previously, shear banding was only observed or predicted in the semi-dilute and concentrated regimes.

Here we explore the effect of the active particles extra stress contribution in the simple shear flow. After the introduction, the theoretical modeling and the flow problem for active rods are derived in Sec. 5.2. Then, before conclusion Sec. 5.3 presents the numerical results in simple shear flow including the effects of rotary and translational Peclet numbers, in addition to the effect of extra stress generated by active particles.

## 5.2 Hypothesis

Consider a suspension of active particles that resemble Brownian rods and have length $L$ and width $d$. The active rods are rigid, neutrally buoyant, and mono-dispersed. The suspension is taken into account in the regime of diluted concentration. Active rods are polar, meaning that their heads and tails aren't exactly the same. Each rod is described by a position vector $\mathbf{r}_c$ and an orientation unit vector $\mathbf{p}$.

### 5.2.1 Kinetic model equation

A probability distribution function $\Psi(\mathbf{r}_c, \mathbf{p}, t)$ can be used to characterize a suspension of active Brownian particles. It represents the probability that particles will be present at position $\mathbf{r}_c$ and orientation $\mathbf{p}$ at time $t$. A single-particle Smoluchowski equation can be derived in a diluted state as

$$\frac{\partial \Psi}{\partial t} = -\nabla_{\mathbf{x}} \cdot (\dot{\mathbf{r}}_c \Psi) - \nabla_{\mathbf{p}} \cdot (\dot{\mathbf{p}} \Psi) \,. \tag{5.1}$$

The evolution of the position of an active Brownian particle with respect to time , $\dot{\mathbf{r}}_c$, is [197]

$$\dot{\mathbf{r}}_c = \mathbf{u} + V_s \mathbf{p} - \mathbf{D}_t \cdot \nabla_{\mathbf{x}} \log \Psi, \tag{5.2}$$

where $V_s$ is the particle velocity. The evolution of its orientation with respect to time, $\dot{\mathbf{p}}$, can be written as

$$\dot{\mathbf{p}} = \dot{\mathbf{p}}_j - D_r \nabla_{\mathbf{p}} \log \Psi, \tag{5.3}$$

where $\dot{\mathbf{p}}_j$ is the Jeffery's equation and it is given by [22]

$$\dot{\mathbf{p}}_j = -\frac{1}{2}\boldsymbol{\omega}\cdot\mathbf{p} + \frac{\lambda}{2}\left(\dot{\boldsymbol{\gamma}}\cdot\mathbf{p} - \dot{\boldsymbol{\gamma}}:\mathbf{ppp}\right). \tag{5.4}$$

$D_r$ and $\mathbf{D}_t$ are the rotary diffusion coefficient and translational diffusion tensor , respectively. The latter for non-spherical, rigid particles is defined by $\mathbf{D}_t = D_{\|}\mathbf{pp} + D_{\perp}\left(\boldsymbol{\delta} - \mathbf{pp}\right)$, where $D_{\|}$ and $D_{\perp}$ are constants that characterize the diffusion parallel and perpendicular to the particle axis [40]. $\mathbf{u}$ is the external flow velocity vector at location $\mathbf{r}_c$. $\nabla_{\mathbf{p}}$ and $\nabla_{\mathbf{x}}$ denote the gradient operators in configurational and spatial spaces, respectively. $\boldsymbol{\omega}$, $\dot{\boldsymbol{\gamma}}$, and $\boldsymbol{\delta}$ are the vorticity, strain rate, and identity tensors, respectively. $\lambda$ is a constant form factor as a function of the particle aspect ratio $a_r = L/d$, in the case of rods, $\lambda = 1$. Hence, the expanded version of Eq. 5.1, by taking into account the fluid incompressibility condition, is

$$\frac{D\Psi}{Dt} = -\nabla_{\mathbf{x}}\cdot\left(V_s\mathbf{p}\Psi\right) + \nabla_{\mathbf{x}}\cdot\left(\mathbf{D}_t\cdot\nabla_{\mathbf{x}}\Psi\right) - \nabla_{\mathbf{p}}\cdot\left(\dot{\mathbf{p}}_j\Psi\right) + D_r\nabla^2_{\mathbf{p}}\Psi, \tag{5.5}$$

where $\frac{D(...)}{Dt} = \frac{\partial(...)}{\partial t} + \mathbf{u}\cdot\nabla_{\mathbf{x}}(...)$ is the material derivative operator, and $\nabla^2_{\mathbf{p}}$ is the Laplacian operator in configurational domain. In what follows, we derive an equivalent evolution equation based on the second-order moment of $\Psi$.

### 5.2.2 Flow problem

The problem is governed by the continuity and Cauchy momentum equations in the limit of creeping flow

$$\nabla_{\mathbf{x}}\cdot\mathbf{u} = 0, \tag{5.6}$$

$$-\eta_0\nabla^2_{\mathbf{x}}\mathbf{u} + \nabla_{\mathbf{x}}P = \nabla_{\mathbf{x}}\cdot\boldsymbol{\Sigma}. \tag{5.7}$$

In the above equations, $\nabla^2_{\mathbf{x}}$ is the Laplacian operator in the spatial space, $\eta_0$ is the dynamic viscosity of the Newtonian suspending fluid, $P$ denotes the pressure and $\boldsymbol{\Sigma}$ represents the extra stress tensor. Indeed, the presence of active particles in a Newtonian medium develops extra stress contributions, which are obtained by configurational averages of force dipoles exerted by the particle on the fluid. In the case of interest, the dipole arises from several contributions, including hydrodynamic stress, Brownian stresses, and the permanent dipole due to self-propulsion. The extra stress is calculated following the work of saintillan et al. [70].

$$\boldsymbol{\Sigma} = \boldsymbol{\Sigma}_s + \boldsymbol{\Sigma}_B + \boldsymbol{\Sigma}_F. \tag{5.8}$$

The first contribution is resulting from the particle swimming and can be expressed as

$$\boldsymbol{\Sigma}_s = \sigma_0(\mathbf{A}_2 - \mathbf{A}_2:\boldsymbol{\delta\delta}/3), \tag{5.9}$$

where $\sigma_0$ is the dipole or stresslet strength, which depends on the swimming mechanism. It is a constant and can be used to measure the particle activity. It should be noted that depending on the type of swimmer, $\sigma_0$ can be either positive or negative. For example, it can be demonstrated that $\sigma_0 < 0$ for most swimming bacteria (such as Escherichia coli and Bacillus subtilis) and $\sigma_0 > 0$ for head-actuated swimmers or pullers, such as the alga Chlamydomonas Reinhardtii [197].

The second contribution is due to the fact that particles are Brownian. It is

$$\boldsymbol{\Sigma}_B = k_B T(3\mathbf{A}_2 - \mathbf{A}_2 : \boldsymbol{\delta\delta}), \tag{5.10}$$

where $k_B$ and $T$ are the Boltzmann constant and the absolute temperature, respectively. The third contribution comes from the inextensibility of the particles and is expressed as

$$\boldsymbol{\Sigma}_F = \sigma_F \left[(\mathbf{A}_4 - \boldsymbol{\delta}\mathbf{A}_2/3) : \dot{\boldsymbol{\gamma}}\right], \tag{5.11}$$

where $\sigma_F = \pi\eta_0/6\log(2a_r)$ from slender body theory.

Substituting Eqs. 5.9, 5.10 and 5.11 into Eq. 5.8 gives the detailed expression of the particle extra stress

$$\boldsymbol{\Sigma} = (\sigma_0 + 3k_B T)(\mathbf{A}_2 - \mathbf{A}_2 : \boldsymbol{\delta\delta}/3) + \sigma_F\left[(\mathbf{A}_4 - \boldsymbol{\delta}\mathbf{A}_2/3) : \dot{\boldsymbol{\gamma}}\right] \tag{5.12}$$

### 5.2.3 Dimensionless formulation of the problem

Choosing the active rod length $L$ as the characteristic length and the characteristic strain rate $\dot{\gamma} = U_{avg}/L$, where $U_{avg}$ is the average flow velocity, and the dimensionless concentration $c^* = \frac{c}{n}$, where $n$ is the mean number number density. The dimensionless form of FP equation (Eq. 5.5) is

$$\frac{D\Psi}{D\tau} = -Pe_s\nabla^*_{\mathbf{x}}\cdot(\mathbf{p}\Psi) + \nabla^*_{\mathbf{x}}\cdot\left\{\left[\frac{1}{Pe_\parallel}\mathbf{pp} + \frac{1}{Pe_\perp}(\boldsymbol{\delta} - \mathbf{pp})\right]\cdot\nabla^*_{\mathbf{x}}\Psi\right\} - \nabla_{\mathbf{p}}\cdot(\dot{\mathbf{p}}_j\Psi) + \frac{1}{Pe_r}\nabla^2_{\mathbf{p}}\Psi, \tag{5.13}$$

where the dimensionless number $Pe_s = \frac{Vs}{L\dot{\gamma}}$ denotes the active rod's relative velocity to the flow velocity. This dimensionless value can shed light on how active rods react to the shear flow that is being applied.

The dimensionless of the continuity equation is

$$\nabla^*_{\mathbf{x}} \cdot \mathbf{u}^* = 0, \tag{5.14}$$

The dimensionless form of the Cauchy equation can be written as

$$\nabla^*_{\mathbf{x}} P^* - \nabla^{*2}_{\mathbf{x}} \mathbf{u}^* = \nabla^*_{\mathbf{x}} \cdot \left\{ c^* \left[ N_p \left( \mathbf{A}^*_4 - \frac{1}{3} \boldsymbol{\delta} \mathbf{A}^*_2 \right) : \dot{\boldsymbol{\gamma}}^* + (N_b + N_s)\left(3\mathbf{A}^*_2 - \boldsymbol{\delta}\right) \right] \right\}. \qquad (5.15)$$

As a result, the dimensionless form of the stress tensor is

$$\boldsymbol{\Sigma}^* = c^* \left[ N_p \left( \mathbf{A}_4 - \frac{1}{3} \boldsymbol{\delta} \mathbf{A}_2 \right) : \dot{\boldsymbol{\gamma}}^* + (N_b + N_s)\left(3\mathbf{A}^*_2 - \boldsymbol{\delta}\right) \right], \qquad (5.16)$$

where $N_p = \frac{\pi n L^3}{6log(a_r)}$ is the particle coupling coefficient, $N_b = \frac{nk_BT}{\eta_0 \dot{\gamma}}$ is the Brownian coupling coefficient and $N_s = \frac{n\sigma_0}{\eta_0 \dot{\gamma}}$ is the self propulsion coupling coefficient.

## 5.3 Numerical results

We employ the finite volume method to investigate two flow problems, solving the problem defined in Eqs. 5.13, 5.14 and 5.15 . The indices 1 and 2 represent the flow direction and the velocity gradient direction, respectively. In a simple shear flow and Poiseuille flow, they are indicated with x and y, respectively.

### 5.3.1 Simple shear flow

A squared 2D channel with side length $H$ undergoes a simple shear flow between opposing moving walls. Here, the aspect ratio is defined as $H/L = 10^6$. To emulate an infinite flow channel, periodic flow conditions with $\Delta P = 0$ are employed (refer to Fig. 5.1). The initial conditions for the conformation tensor are set as $A_{ii} = 1/3$ and $A_{ij} = 0$ for $i \neq j$. The initial concentration is homogeneous and equals to one.

#### Effect of self-propulsion

We examine three distinct regimes based on the active rods relative velocity Peclet number ($Pe_s$) and the diffusion Peclet numbers ($Pe_r$ and $Pe_\perp$). The first regime ($Pe_s < Pe_r, Pe_\perp$) explores scenarios where the directed motion due to self-propulsion is relatively weak. The second regime ($Pe_s = Pe_r = Pe_\perp$) corresponds to cases where there is a competition between active motion and diffusion. Lastly, the third regime ($Pe_s > Pe_r, Pe_\perp$), investigates situations where active motion dominates over diffusion. The Peclet numbers in this case are fixed to $Pe_\perp = Pe_r = 10$ while the value of $Pe_s$ equals $0, 5, 10$ and 15. In this section, no active rods extra stresses is taken into consideration and the flow problem is developed from Eq. 5.15.
With an increase in $Pe_s$, there is a noticeable accumulation of active rods near the moving walls (see Fig. 5.2a). The stronger is the active rod self-propulsion velocity, the more pronounced is the active rods clustering in regions where the flow velocity is higher. As depicted in Fig.5.2b,

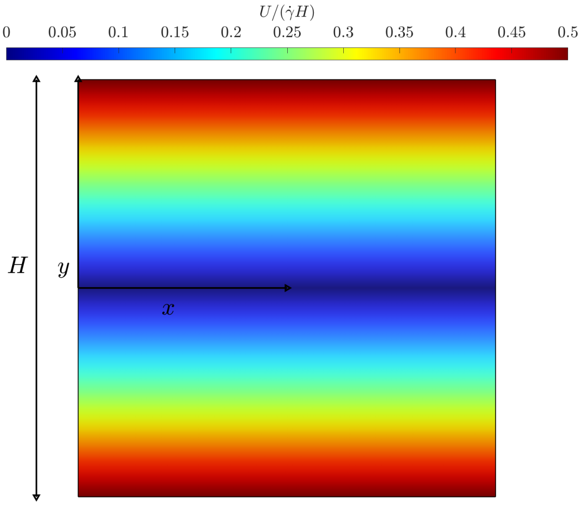

Figure 5.1 – Dimensionless velocity magnitude in the squared channel, of side $H$, for simple shear flow with periodic BC.

active rods exhibit enhanced alignment in the flow direction at the center of the channel as the self-propulsion Peclet number ($Pe_s$) increases. Conversely, active rods near the walls present reduced alignment. This behavior illustrates that higher particle velocities promote stronger alignment in the central region, while the alignment weakens towards the channel walls. Fig. 5.2c shows that $A_{12}/c$ is positive near the walls and negative at the center, while Fig. 5.2d shows that $n_2/c$ has the same sign as $y/H$ with maximum absolute values at the walls and zero at the center. This means that at walls active rods are aligned in the direction of the flow with nematic order toward the walls, while at the center active rods are aligned opposite to the flow with nematic order toward the walls.

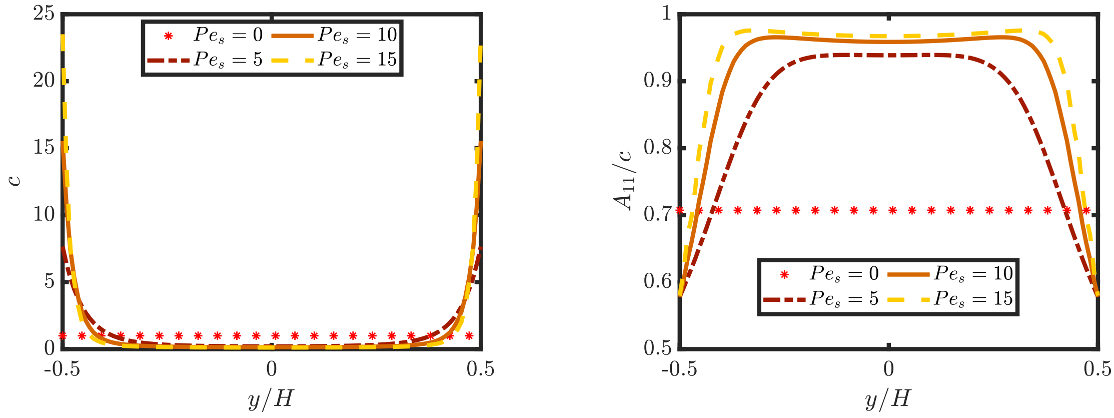

(a) Effect of the The self-propulsion Peclet number, $Pe_s$, on the concentration distribution, $c$, along the $y$ direction.

(b) Effect of the self-propulsion Peclet number, $Pe_s$, on the orientation component, $A_{11}/c$, along the $y$ direction.

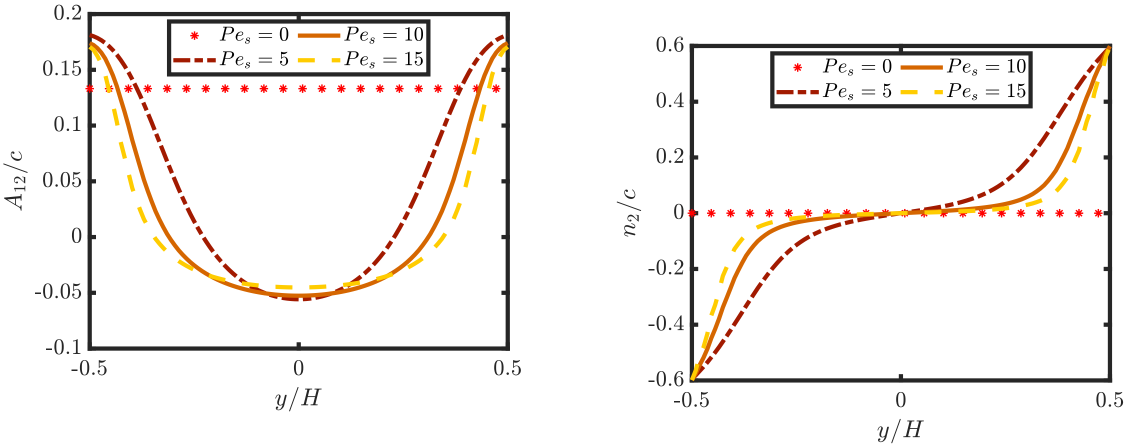

(c) Effect of the self-propulsion Peclet number, $Pe_s$, on the orientation component, $A_{12}/c$, along the $y$ direction

(d) Effect of the self-propulsion Peclet number, $Pe_s$, on the nematic order, $n_2/c$, along the $y$ direction.

Figure 5.2 – Showing the effect of the self-propulsion Peclet number, $Pe_s = 0, 5, 10$ and $15$,(a) on the concentration distribution, $c$, (b) on the orientation component, $A_{11}/c$, (c) on the orientation component, $A_{12}/c$, (d) on the nematic order, $n_2/c$, along the $y$ direction at steady state, in simple shear flow.

### Effect of rotary diffusion

With fixed values of $Pe_s = 5$ and $Pe_\perp = 10$, we focus on the impact of rotary diffusion on the migration behavior of active rods. As shown in Fig. 5.3a, a decrease in the rotary Peclet number ($Pe_r$) corresponds to a stronger tendency for active rods to accumulate at the walls. This observation implies that, even in the case of active rods, isotropic active rods have more tendency to migrate across streamlines than the aligned ones [210]. Fig. 5.3b demonstrates that active rods display a nematic ordering directed toward the walls, with varying degrees of alignment corresponding to different rotary Peclet values. Remarkably, as the rotary Peclet number ($Pe_r$) decreases, the nematic order ($n_2$) becomes increasingly prominent.

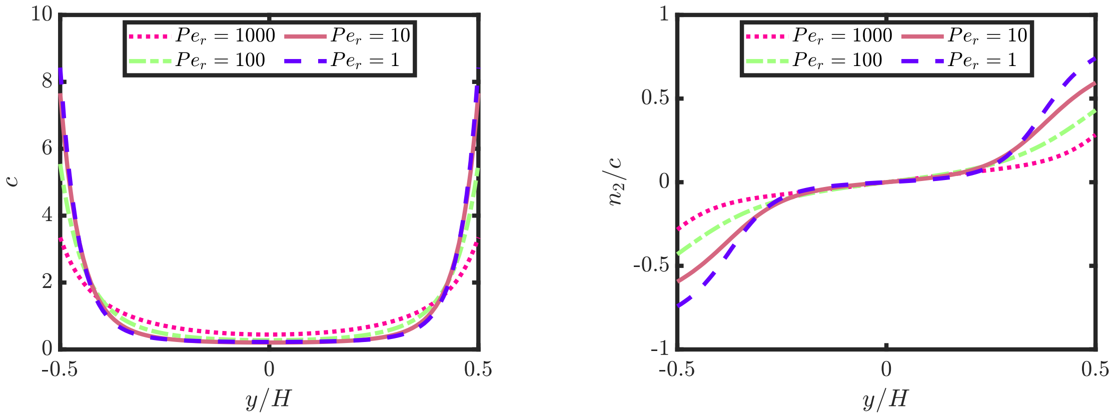

(a) Effect of the rotary diffusion, $Pe_r$, on the concentration distribution, $c$, along the $y$ direction.

(b) Effect of the rotary diffusion, $Pe_r$, on the nematic order, $n_2/c$, along the $y$ direction.

Figure 5.3 – Showing the effect of the rotary diffusion, $Pe_r = 1, 10, 100$ and $1000$, (a) on the concentration distribution, $c$, (b) on the nematic order, $n_2/c$, along the $y$ direction at steady state, in simple shear flow.

### Effect of translational diffusion

For passive rods subjected to simple shear flow, the translational diffusion exhibits negligible influence on both rod migration and orientation. However, for active rods experiencing simple shear flows, distinct behaviors emerge. To isolate the effect of translational Peclet numbers on the system, the other Peclet numbers are fixed at $Pe_r = 10$ and $Pe_s = 5$. At higher translational Peclet numbers, active rods tend to accumulate near the walls, whereas as the translational Peclet number increases, active rod distribution becomes more uniform along the channel (see Fig. 5.4a). Concerning active rod orientations, under high Peclet numbers, active rods align predominantly in the flow direction at the center of the channel, while exhibiting a nearly isotropic arrangement near the high-concentration walls. Decreasing the Peclet number leads to a reduction in the gradient of active rod orientation along the $y$ direction, as shown in Fig. 5.4b. Translational diffusion dominates the behavior of passive rods in simple shear flows. This causes an homogeneous distribution of passive rods in simple shear flow, while for active rods, when the self-propulsion is dominant at high $Pe_\perp$, active rods are accumulated near the walls and highly aligned in the flow directions. As $Pe_\perp$ increases, translational diffusion dominates and returns the system to its homogeneous state. Figs. 5.4c and 5.4d shows that active rods exhibit a distinct orientation toward the walls within the vicinity of the walls. However, as one moves towards the center of the channel, the orientation of active rods is more randomized. As the effect of translational diffusion becomes increasingly dominant, active rods appear to lose any preferential alignment along the flow direction. This shift towards a more homogeneous distribution of active rod orientations highlights the role of diffusion in counteracting any alignment tendencies induced by the active flow.

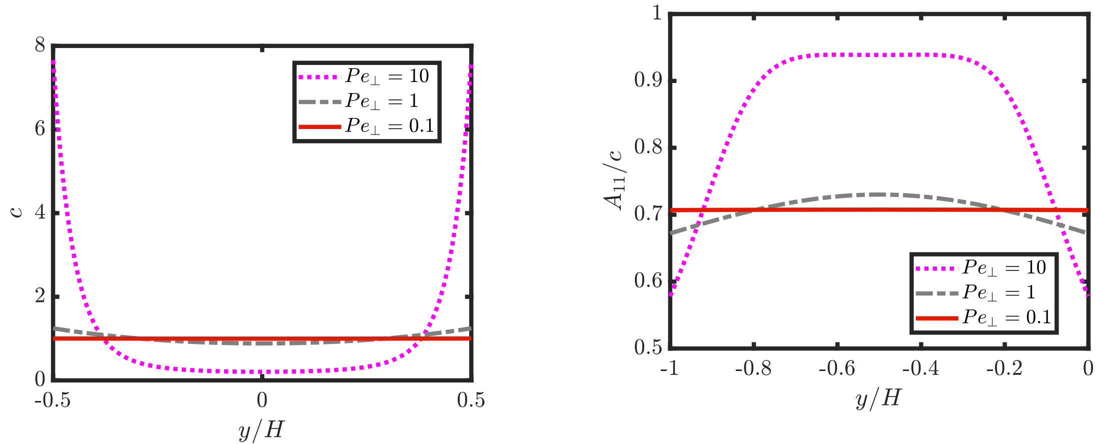

(a) Effect of the translational diffusion, $Pe_\perp$, on the concentration distribution, $c$, along the $y$ direction.

(b) Effect of the translational diffusion, $Pe_\perp$, on the orientation component, $A_{11}/c$, along the $y$ direction.

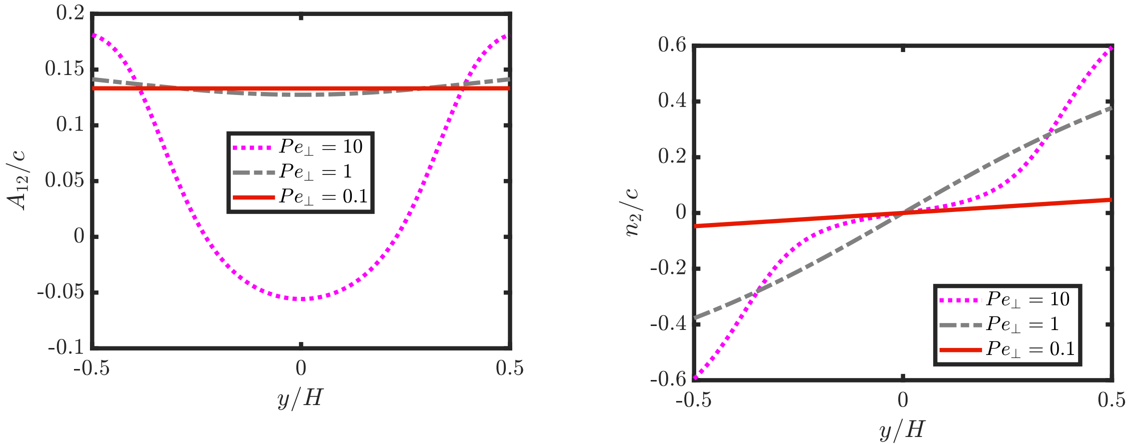

(c) Effect of the translational diffusion, $Pe_\perp$, on the orientation component, $A_{12}/c$, along the $y$ direction.

(d) Effect of the translational diffusion, $Pe_\perp$, on the nematic order, $n_2/c$, along the $y$ direction.

Figure 5.4 – Showing the effect of the translational diffusion, $Pe_\perp = 0.1, 1$ and 10, (a) on the concentration distribution, $c$, (b) on the orientation component, $A_{11}/c$, (c) on the orientation component, $A_{11}/c$, (d) the nematic order, $n_2/c$, along the $y$ direction at steady state, in simple shear flow.

### Effect of particles extra stress

We examined the influence of particle stress in a simple shear flow. Specifically, we maintained a fixed Peclet numbers of $Pe_r = Pe_\perp = 10$ and a constant coupling coefficient of $N_p = 0$. We examine $Pe_s = 0, 5, 10$, and 15. Unlike the scenario with passive rods, where the simple shear flow is not significantly affected by particle stress, our findings revealed that active particles do exhibit alterations in response to particle stress. We focus on exploring the impact of $Pe_s$ on the rheological behavior of the system.

- Pusher rods

  In the case of pusher active rods, the extra stress generated by the rod is positive, here $N_b + N_s = -10$. Fig. 5.5 provides insights into this behavior by depicting the changes in velocity profiles at the steady state for different $Pe_s$ values. Considering only one half of the simple shear flow profile, the results unveil the occurrence of a reverse flow in a direction opposite to the moving wall. The system predicts shear banding, where shear deformation occurs. This results have a good confirmation with the work of Vennamneni et al. [216], where they observed shear bands with concentration inhomogeneities, in the dilute regime.

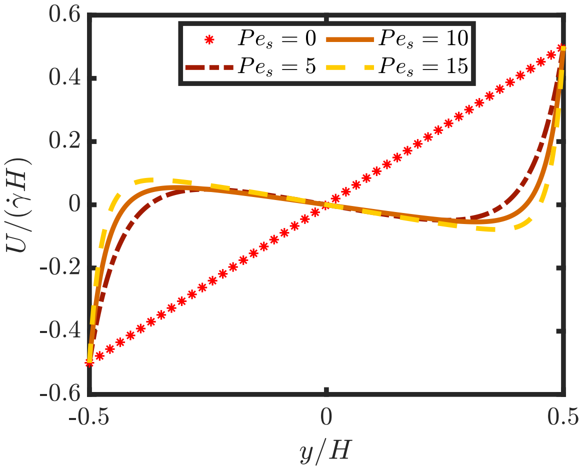

Figure 5.5 – Effect of the self-propulsion Peclet number, $Pe_s$, on the velocity profile at steady state, initially simple shear flow, for $N_b = 10$.

Fig. 5.6a illustrates the impact of self-propulsion Peclet number on the evolution of shear viscosity with respect to strain. Notably, the results reveal a direct correlation between the shear viscosity values and $Pe_s$. The decrease in shear viscosity with the increase of $Pe_s$ attributed to the complex interactions between the active rods and the surrounding fluid. As a result, pushers tend to decrease the suspension viscosity. Fig. 5.6b illustrates the impact of self-propulsion Peclet number on the evolution of the normal stress differences with respect to deformation at the moving wall. As the self-propulsion Peclet number ($Pe_s$) increases, the values of the normal stress differences also increase. As the self-propulsion ($Pe_s$) increases, the intensity of self-propulsion also increases. This enhanced activity leads to more frequent and stronger active rod-fluid interactions, causing the suspension to exhibit higher resistance to deformation. In essence, the active rods energetic motion contributes to greater resistance to the flow, resulting in elevated viscosity values and enhanced stress contributions. In this case, the orientation and concentration distributions are qualitatively the same as the results in Sec. 5.3.1.

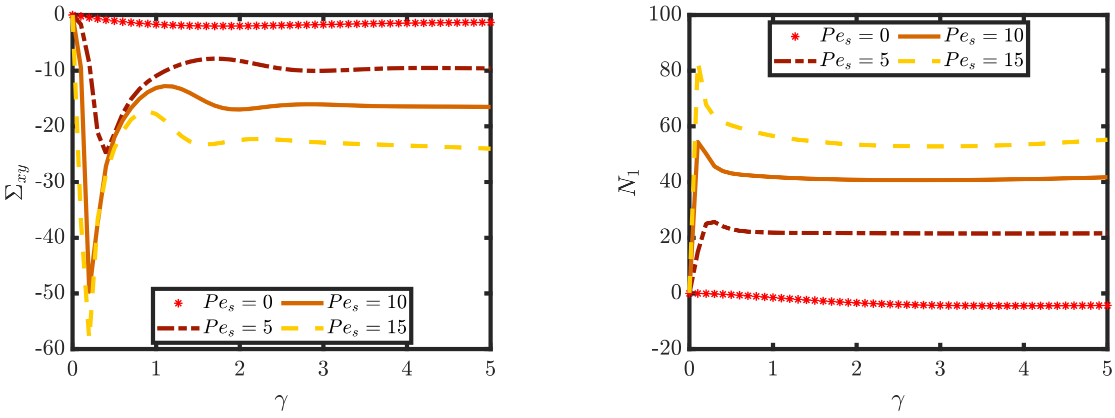

(a) Effect of self-propulsion Peclet number, $Pe_s$, on the evolution of the shear viscosity with respect to deformation.

(b) Effect of self-propulsion Peclet number, $Pe_s$, on the evolution of the normal stresses difference with respect to deformation.

Figure 5.6 – Showing the effect of the self-propulsion Peclet number, $Pe_s$, on the rheological properties (a) shear viscosity, $\eta$, (b) the normal stress differences, $N_1$, with respect to the deformation, $\gamma$, in simple shear flow.

— Puller rods

In the case of puller active rods, the extra stress generated by the rod is negative, here $N_b + N_s = 10$. Fig. 5.7 illustrates how the particle extra stress and changing $Pe_s$ values affect the velocity profiles at steady state. A small deviation from the typical linear profile of standard simple shear flow is shown in the figure. Notably, higher $Pe_s$ values are associated with faster flow rates. It also shows shear banding opposite to the case of pushers with less deformation.

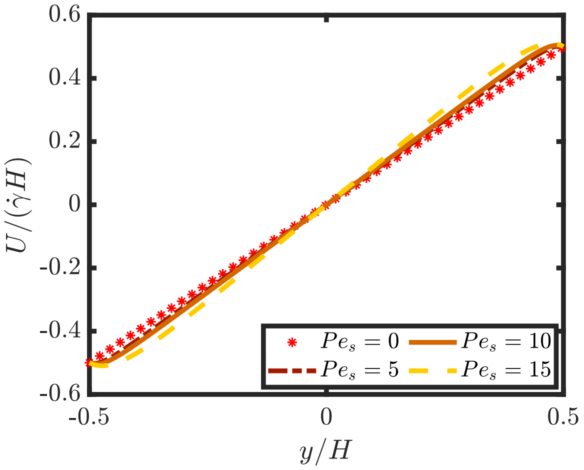

Figure 5.7 – Effect of self-propulsion Peclet number, $Pe_s$, on the velocity profile at steady state, initially simple shear flow, for $N_b = 10$.

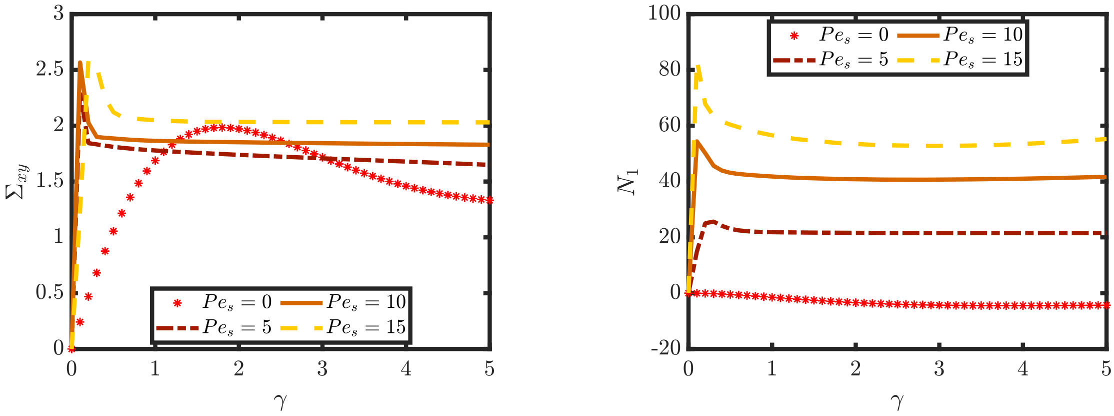

(a) Effect of self-propulsion Peclet number, $Pe_s$, on the evolution of the shear viscosity with respect to deformation.

(b) Effect of self-propulsion Peclet number, $Pe_s$, on the evolution of the normal stresses difference with respect to deformation.

Figure 5.8 – Showing the effect of the self-propulsion Peclet number, $Pe_s$, on the rheological properties (a) shear viscosity, $\eta$, (b) the normal stress differences, $N_1$, with respect to the deformation, $\gamma$, in simple shear flow.

For the case of pullers, the effect of active suspension increases the shear viscosity of the suspended flow as shown in Fig. 5.8a. As well as increasing the normal stress differences as shown in Fig.5.8b. These results are in agreement with the work of Matilla et al. [206] which they found that pushers tend to decrease the suspension viscosity whereas pullers enhance it. For both pusher and puller active rods the effect of $Pe_s$ on the concentration, orientation and the nematic order are qualitatively the same as Sec. 5.3.1. As $Pe_s$ increases, active rods are more accumulated to the walls and more aligned in the flow direction with nematic order toward the walls.

## 5.4 Conclusion

In conclusion, this work explores the rheology of active rod suspensions in simple shear flow, including simple shear flow. The study examines the dynamics of active rods including active rod migrations, orientations and the nematic order in addition to effect of active rod-fluid coupling in simple shear flow, through numerical simulations based on the volume method with taking into consideration an anisotropic translational diffusion.

The active rods are more aligned with the flow direction than the passive rods, favoring accumulation near the channel walls. However, compared to aligned active rods, randomly aligned active rods with low rotational Peclet numbers $Pe_r$ have a stronger propensity to orient in the direction of the walls. The action of the active rods is demonstrated to be hindered by translational diffusion, and for low translational Peclet numbers $Pe_{perp}$, the system resumes acting as in the case of the passive rods.

In simple shear flow, the presence of active rods causes shear banding, a divergence from the typical linear velocity profile. Rheological characteristics, viscosity, and normal stress differences alter when active rods' relative velocities and Peclet numbers increase. Additional research and testing are needed to validate and expand upon these findings. Future work will concentrate on studying the 3D cases in addition of expanding the rheological studies into more complex fluids.

# General Conclusion and Perspectives

# Conclusion

In conclusion, this thesis has examined the complex dynamics of particle suspensions in a variety of flow systems, shedding light on their actions, interactions, and implications in various contexts. Our understanding of the intricate interactions between particle concentration, orientation, and fluid flow has been enriched by the unique yet connected findings presented in each chapter.

After a general introduction, the first chapter made it possible to define the various studies to be carried out in order to respond to the problem addressed. This thesis starts with decribing the single anisometric particle and its dynamics including orientation and center of mass position according to previous studies. Then, it goes through defining the Brownian passive particle before extending to the active particles. After describing the suspension of anisometric particles and defining the moments of the Fokker-Planck equation for the probability distribution function, it goes on to discuss the stress tensor, the flow problem, and the numerical solutions used to solve these problems. Afterwards, it shows some experimental previous researches including the rheological features of active and passive particles in addition to the cross stream migrations of non rheological systems.

In Chapter 2, it was shown how a novel macromodel could be developed and put into use while still substantially reducing down on computation time and maintaining simulation fidelity. By exploring Brownian rod suspensions using this novel method, it has become clear that anisotropic translational diffusion is crucial for determining migration patterns and rod distributions. This macromodel is verified by comparing to the results got by solving the Fokker-Planck equation using finite element method in 2D. The orientations and migrations of Brownian particles are examined in different flow systems. Further research is now possible thanks to these new understandings of particle transport in constrained geometries.

Chapter 3 extended this analysis to suspension rods focusing on the extra stress generated by these rods, examining their behavior in different infinite flow systems. The combination of flow and rod orientations emerged as a key determinant, highlighting the impact of translational Peclets affecting migration development, rheological properties, and overall flow dynamics, and providing important guidelines for management from microfluidic devices to industrial processes.

With the introduction of self-propulsion, the study of active particle suspensions in Chapter 4 revealed a deeper layer of complexity. The intricate alignment patterns of active particles and their tendency to accumulate at channel walls have revealed the complex interplay between particle activity, particle extra stress, flow, and confinement. The importance of translational diffusion has been highlighted, clarifying its function in limiting the effects of active particles and getting bqck passive-like behavior. The work is done by solving the Fokker Planck equation for active particles in 2D using finite volume method.

These chapters have collectively improved the understanding of particle-fluid interactions by

providing new information with broad implications. The conclusions made here offer helpful direction for the design and optimization of a wide range of applications in addition to adding to the basic understanding of complex flows.
This thesis has shed light on the complex interactions that control particle suspensions in various flow environments while accounting for anisotropic translational diffusion. It proposes powerful numerical models, which makes it possible to describe and to calculate the distribution of particles, the coupling between the flow of the fluid and the contribution of the particles. What's been added here represent a significant advancement in the field and encourage further research and creativity to understand the complexities of multiphase flows and their numerous applications as these numerical models present a very good database to allow other work to study the flow of suspensions in different processes.

## Perspectives

As a result of this work, different perspectives are opening up in terms of numerical work. By expanding the proposed numerical model to the 3D and study the behavior of the suspension of particles in more real life applications systems represents a continuation of this work. Few examples of these systems are pipelines, biological flows, porous media and etc, where numerical simulations can give useful information about the interactions between fluid dynamics, particle behavior, and both. Each system offers different problems to be solved and chances for research and application. Materials with adaptive properties, such as self-healing materials that repair damage on their own or materials that alter their stiffness or shape in response to environmental factors, can incorporate active particles. These materials are 3D printed, and the properties of the finished material depends on the suspensoion of the particles during the printing processes. Modeling the 3D printing systems technology of Brownian and active particles will offer some answers on how to optimise these systems and the printing conditions. This will provide a database of the mechanical properties of the composite which will be then used. In addition to extending this model to work in different concentration regimes such as modeling the particle-particle and particle-walls interactions term. Furthermore, these models can be used in viscoelastic flows. Also adapting this model to study the suspension of polydispersed suspensions is a huge jump in the research work which will helps to understand more complicated systems. A periodic sinusoidal flows can be simulated to model the mechanism of sea waves and tides in a medium full of active particles and sediments. This study can help in understanding the mechanism of formation of biofilms in the marine nature, which is a good step to prevent biofouling.

### Taylor dispertion

It is now broadly acknowledged that when exposed to a background shear flow, confined rod-shaped particles have a propensity to migrate towards channel walls [112, 113, 221–224]. On the other hand, Taylor [225] calculated the dispersion of spherical solute particles undergoing Poiseuille flow in a cylindrical pipe in a seminal paper [225]. When a uniform patch of a solute is injected in a laminar flow, according to Taylor's original physical model, it spreads due to the interaction of advection and diffusion. Early on, the solute patch mimics the parabolic flow profile, causing lateral concentration gradients that fuel molecular diffusion to cause net lateral transport. In the end, the shear flow facilitates the solute's spreading, a process now known as Taylor dispersion. In a two-dimensional Poiseuille flow with one degree of rotational freedom, Peng and Brady [226] explored the upstream swimming and dispersion of active Brownian particles for spherical and rod-shaped particles. They found that the swimming of the active Brownian particles increased the dispersion factor. Kumar et al. [227] studied the Taylor dispersion of Brownian elongated rods in a two-dimensional Poiseuille flow, the study demonstrates that elongated rods exhibit an enhanced longitudinal dispersion. They found that when rotational diffusion dominates, the classical Taylor dispersion result for the longitudinal spreading rate is recovered using an orientationally averaged translational diffusivity for the rods. Taylor dispersion arises due to the combined effects of rods diffusion and the velocity gradient across the channel. As the rods are transported by the flowing fluid, their diffusion causes random fluctuations in their positions. These fluctuations become amplified by the velocity gradient, leading to the dispersion and spreading of the rods across the channel. Fig. 5.9 illustrates the initial conditions of the concentration distribution in the channel. The rods concentration $c = 1$ for $0.2 < x/H < 0.3$, means that there is a localized region within the channel where the concentration is elevated. Outside this region, the concentration is set to $c = 0$ indicating a lack of rods. The rod orientations are isotropic initially, $Pe_{\perp} = 10, N_b = 250$ and $N_p = 10$. Fig. 5.10 shows the evolution of the concentration distribution in the channel over $\tau$. During the early stages, rods mimic the shape of the flow, indicating that they move and deform in a manner similar to the fluid flow in the channel. The presence of a shear flow induces lateral concentration gradients, meaning that there are variations in concentration across the channel width. Later, rod advection continues longitudinal spreading of rods becomes prominent. This refers to the dispersion of rods in the direction of the flow. At the final stage, the rods spread out longitudinally until the concentration becomes homogeneous along each streamline. In addition to the observed evolution of concentration in the flow direction, rods migrate toward the channel walls in this study. Fig. 5.11 illustrates the concentration profile in the channel at a specific time ($\tau = 0.6$) for different rotary Peclet numbers. It shows that an increase in the rotary Peclet number leads to a decrease in the velocity of the rods in the flow direction. This means that rods with higher rotary Peclet numbers experience a slower motion in the direction of the flow compared to rods with lower rotary Peclet numbers. Additionally, it indicates that as the rotary Peclet number increases, the rods tend to concentrate more toward the walls of the channel. To investigate the dispersion behavior and rod velocity in the channel, the following governing equation for Taylor dispersion was employed [227],

$$\frac{\partial \mathcal{C}_m}{\partial \tau} + \mathrm{Pe} U_m \frac{\partial \mathcal{C}_m}{\partial x} = \kappa \mathrm{Pe}^2 \frac{\partial^2 \mathcal{C}_m}{\partial x^2}, \tag{5.17}$$

where $\mathcal{C}_m$ represents the average lateral concentration, $U_m$ denotes the average rods velocity, and $\kappa$ corresponds to the Taylor dispersion coefficient. In our study, we considered the translational Peclet number, $Pe$, as the average of the perpendicular Peclet number ($Pe_\perp$) and the parallel Peclet number ($Pe_{||}$). This equation describes the evolution of the average lateral concentration with respect to time and position in the channel. The first term on the left-hand side represents the temporal change of the concentration, while the second term accounts for the convective transport along the flow direction. The right-hand side captures the effect of diffusion, quantified by the Taylor dispersion coefficient and the second spatial derivative of the concentration. To analyze the dispersion behavior and estimate the rod velocity, Eq. 5.17 was solved numerically. Fig. 5.12 presents the variation of the Taylor dispersion coefficient ($\kappa$) as a function of the rotary Peclet number ($Pe_r$). It shows an increase in the rotary Peclet number corresponds to a decrease in the dispersion coefficient. These results do not match with the work of Kumar et al. [227]. It is good to model a mathmatical equation related to our marcomodel that calculates the Taylor dispersion coefficient and the particle average velocity similar to the work of Kumar et al. [227]. In addition, it is good to extend this work to 3D and study the Taylor dispersion of active particles.

### Closure approximation

In this work, the mathematical calculations of the kinetic macromodel is extended to the work of active particles, although this macromodel needs closure approximations unlike the closures used in the work of the passive particles. Constructing an accurate closure model for these kinetic models is essential for preserving the multi-scale dynamics and capturing the correct physics, as the equations of motion depend on unknown fields that require approximation [228]. Closures have a history of application in computational models for rheology and many-particle systems [229], and more recently, they have been utilized in active fluids research [230–233]. These models not only provide efficient computational frameworks but also offer alternative analytical approaches [234, 235]. Weady et al. [76] present a robust, accurate, and efficient numerical scheme for evaluating the Bingham closure [236, 237] in a coarse-grained continuum model for a suspension of active particles, enabling high-resolution simulations in parameter regimes inaccessible to kinetic theories. Developing an accurate closure for this model will help

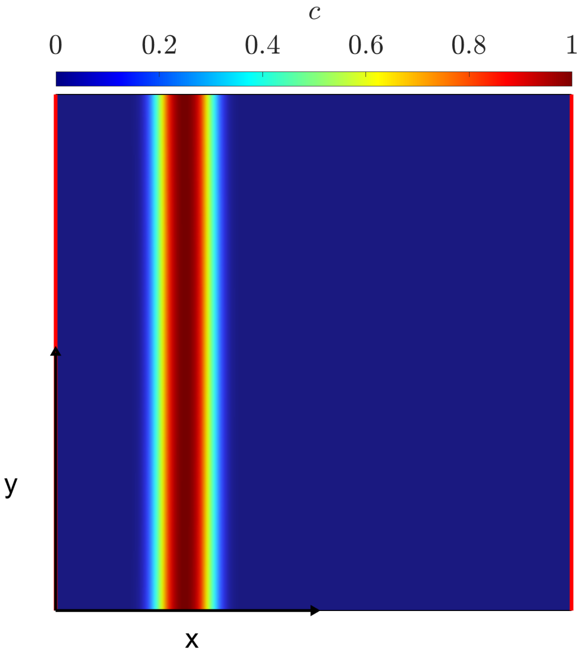

Figure 5.9 – Initial concentration distribution in the channel, the red vertical lines represent the flow periodic boundary conditions

in reducing the cost of the numerical simulations and the needed time. This will open the door to extend the work into more complicated geometries.

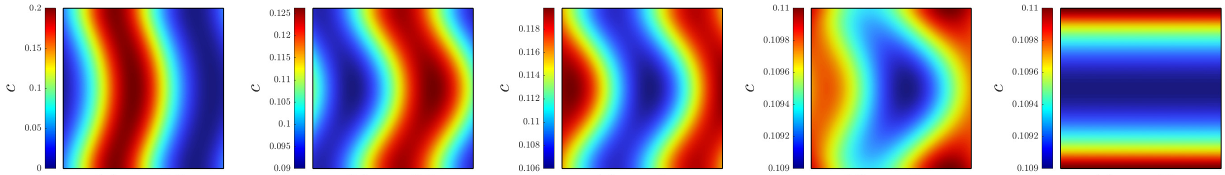

(a) $\tau = 0.2$ (b) $\tau = 0.6$ (c) $\tau = 1$ (d) $\tau = 5$ (e) $\tau = 30$

Figure 5.10 – Brownian rods concentration $c$ in a Poiseuille flow, with $\tau$ increasing, demonstrating the diffusive spread caused by Tayor dispersion

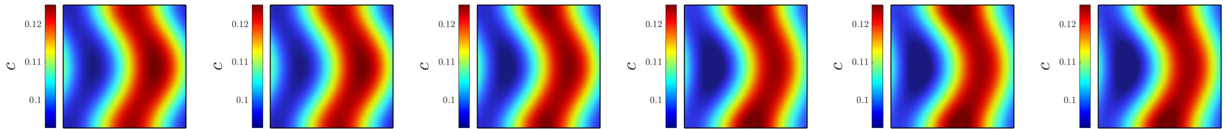

(a) $Pe_r = 10^{-2}$ (b) $Pe_r = 10^{-1}$ (c) $Pe_r = 10^{1}$ (d) $Pe_r = 10$ (e) $Pe_r = 10^{2}$ (e) $Pe_r = 10^{3}$

Figure 5.11 – Brownian rod concentration $c$ in a Poiseuille flow, with the values of $Pe_r$ increasing, demonstrating the diffusive spread caused by Tayor dispersion, at $\tau = 0.6$

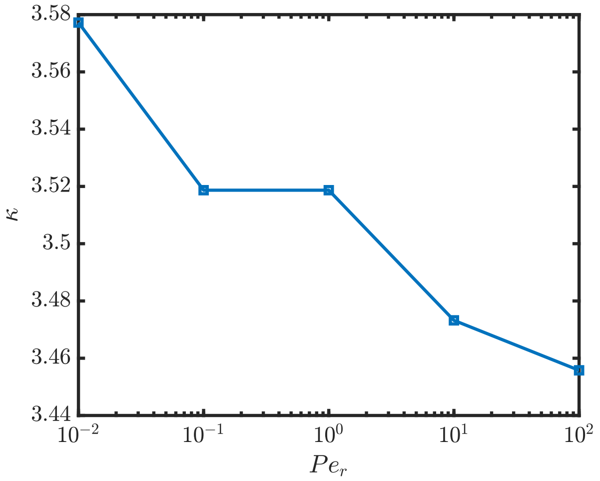

Figure 5.12 – Variation of Taylor dispersion coefficient ($\kappa$) as a function of rotary Peclet number ($Pe_r$)

# BIBLIOGRAPHY

1. Callow, J. A. & Callow, M. E., Trends in the development of environmentally friendly fouling-resistant marine coatings, *Nature communications* **2,** 244 (2011).
2. Lacoste, E. & Gaertner-Mazouni, N., Biofouling impact on production and ecosystem functioning: a review for bivalve aquaculture, *Reviews in Aquaculture* **7,** 187–196 (2015).
3. Xiao, R. & Zheng, Y., Overview of microalgal extracellular polymeric substances (EPS) and their applications, *Biotechnology advances* **34,** 1225–1244 (2016).
4. Roager, L. & Sonnenschein, E. C., Bacterial candidates for colonization and degradation of marine plastic debris, *Environmental science & technology* **53,** 11636–11643 (2019).
5. Dombrowski, C, Cisneros, L, Chatkaew, S, Goldstein, R. & Kessler, J., Self-concentration and large-scale coherence in bacterial dynamics, *Physical review letters* **93,** 098103 (2004).
6. Cisneros, L., Kessler, J., Ganguly, S & Goldstein, R., Dynamics of swimming bacteria: Transition to directional order at high concentration, *Physical Review E* **83,** 061907 (2011).
7. Dunkel, J *et al.,* Fluid dynamics of bacterial turbulence, *Physical review letters* **110,** 228102 (2013).
8. Kudrolli, A, Lumay, G, Volfson, D & Tsimring, L., Swarming and swirling in self-propelled polar granular rods, *Physical review letters* **100,** 058001 (2008).
9. Deseigne, J, Dauchot, O & Chaté, H, Collective motion of vibrated polar disks, *Physical review letters* **105,** 098001 (2010).
10. Ramaswamy, S, The mechanics and statistics of active matter, *Annu. Rev. Condens. Matter Phys.* **1,** 323–345 (2010).
11. Marchetti, M. *et al.,* Hydrodynamics of soft active matter, *Reviews of Modern Physics* **85,** 1143 (2013).
12. Saintillan, D & Shelley, M., Active suspensions and their nonlinear models, *Comptes Rendus Physique* **14,** 497–517 (2013).
13. Purcell, E., Life at low Reynolds number, *American journal of physics* **45,** 3–11 (1977).
14. Brennen, C & Winet, H, Fluid mechanics of propulsion by cilia and flagella, *Annual Review of Fluid Mechanics* **9,** 339–398 (1977).

---

15. Paxton, W. *et al.,* Catalytic nanomotors: autonomous movement of striped nanorods, *Journal of the American Chemical Society* **126,** 13424–13431 (2004).

16. Villa, K *et al.,* Chemical Microrobots as Self-Propelled Microbrushes against Dental Biofilm, *Cell Reports Physical Science* **1,** 100181 (2020).

17. Saintillan, D & Shelley, M., *in Complex Fluids in biological systems* 319–355 (Springer, 2015).

18. Drescher, K., Dunkel, J., Cisneros, L. H., Ganguly, S. & Goldstein, R. E., Fluid dynamics and noise in bacterial cell–cell and cell–surface scattering, *Proceedings of the National Academy of Sciences* **108,** 10940–10945 (2011).

19. Guasto, J. S., Johnson, K. A. & Gollub, J. P., Oscillatory flows induced by microorganisms swimming in two dimensions, *Physical review letters* **105,** 168102 (2010).

20. Issa, H., Natale, G., Ausias, G. & Férec, J., Modeling and numerical simulations of Brownian rodlike particles with anisotropic translational diffusion, *Phys. Rev. Fluids* **8,** 033302, `https://link.aps.org/doi/10.1103/PhysRevFluids.8.033302` (3 2023).

21. Einstein, A. *et al.,* On the motion of small particles suspended in liquids at rest required by the molecular-kinetic theory of heat, *Annalen der physik* **17,** 208 (1905).

22. Jeffery, G., The motion of ellipsoidal particles immersed in a viscous fluid, *Proceedings of the Royal Society of London. Series A, Containing papers of a mathematical and physical character* **102,** 161–179 (1922).

23. Trevelyan, B. & Mason, S., Particle motions in sheared suspensions. I. Rotations, *Journal of Colloid Science* **6,** 354–367 (1951).

24. Darabaner, C. & Mason, S., Particle motions in sheared suspensions xxii: Interactions of rigid spheres (experimental), *Rheologica Acta* **6,** 273–284 (1967).

25. Batchelor, G., *Theoretical Introduction to Fluid Mechanics* (Cambridge University Press, 1972).

26. Dinh, S. & Armstrong, R., A rheological equation of state for semiconcentrated fiber suspensions, *Journal of Rheology* **28,** 207–227 (1984).

27. Folgar, F & Tucker III, C., Orientation behavior of fibers in concentrated suspensions, *Journal of reinforced plastics and composites* **3,** 98–119 (1984).

28. Advani, S. & Tucker III, C., The use of tensors to describe and predict fiber orientation in short fiber composites, *Journal of rheology* **31,** 751–784 (1987).

29. Doi, M., Molecular dynamics and rheological properties of concentrated solutions of rodlike polymers in isotropic and liquid crystalline phases, *Journal of Polymer Science: Polymer Physics Edition* **19,** 229–243 (1981).

30. Redjeb, A., *Simulation numérique de l'orientation de fibres en injection de thermoplastique renforcé* PhD thesis (École Nationale Supérieure des Mines de Paris, 2007).
31. Dogossy, G., Morauszki, T. & Ronkay, F., Experimental investigation and applicability of multi-stage simulations in the case of a thick-walled injection-moulded composite, *Applied Sciences* **12,** 8415 (2022).
32. Bay, R. S., *Fiber orientation in injection-molded composites: a comparison of theory and experiment* PhD thesis (University of Illinois at Urbana-Champaign, 1991).
33. Ranganathan, S. & Advani, S., Fiber–fiber interactions in homogeneous flows of nondilute suspensions, *Journal of Rheology* **35,** 1499–1522 (1991).
34. Ramazani SA, A, Ait-Kadi, A & Grmela, M, Rheology of fiber suspensions in viscoelastic media: Experiments and model predictions, *Journal of Rheology* **45,** 945–962 (2001).
35. Park, J. M. & Kwon, T. H., Irreversible thermodynamics based constitutive theory for fiber suspended polymeric liquids, *Journal of Rheology* **55,** 517–543 (2011).
36. Koch, D. L., A model for orientational diffusion in fiber suspensions, *Physics of Fluids* **7,** 2086–2088 (1995).
37. Phan-Thien, N., Fan, X.-J. & Zheng, R., A numerical simulation of suspension flow using a constitutive model based on anisotropic interparticle interactions, *Rheologica acta* **39,** 122–130 (2000).
38. Phelps, J. H. & Tucker III, C. L., An anisotropic rotary diffusion model for fiber orientation in short-and long-fiber thermoplastics, *Journal of Non-Newtonian Fluid Mechanics* **156,** 165–176 (2009).
39. Hand, G. L., A theory of anisotropic fluids, *Journal of Fluid Mechanics* **13,** 33–46 (1962).
40. Doi, M & Edwards, S., *The theory of polymer dynamics* (oxford university press, 1988).
41. Altan, M., Advani, S., Güçeri, S. & Pipes, R., On the description of the orientation state for fiber suspensions in homogeneous flows, *Journal of Rheology* **33,** 1129–1155 (1989).
42. Hinch, E. & Leal, L., Constitutive equations in suspension mechanics. Part 2. Approximate forms for a suspension of rigid particles affected by Brownian rotations, *Journal of Fluid Mechanics* **76,** 187–208 (1976).
43. Verleye, V, Couniot, A & Dupret, F, Numerical prediction of fibre orientation in complex injection-moulded parts, *WIT Transactions on Engineering Sciences* **4** (1970).
44. Cintra Jr, J. S. & Tucker III, C. L., Orthotropic closure approximations for flow-induced fiber orientation, *Journal of Rheology* **39,** 1095–1122 (1995).
45. Verleye, V *et al., in Rheology Series* 1347–1398 (Elsevier, 1999).

46. Chung, D. H. & Kwon, T. H., Invariant-based optimal fitting closure approximation for the numerical prediction of flow-induced fiber orientation, *Journal of rheology* **46,** 169–194 (2002).
47. Brown, R., XXVII. A brief account of microscopical observations made in the months of June, July and August 1827, on the particles contained in the pollen of plants; and on the general existence of active molecules in organic and inorganic bodies, *The philosophical magazine* **4,** 161–173 (1828).
48. Mörters, P. & Peres, Y., *Brownian motion* (Cambridge University Press, 2010).
49. Wiener, N, Differential space, *Journal of Mathematics and Physics* **2,** 131–174 (1923).
50. Feynman, R, Leighton, R. B. & Sands, M, The brownian movement, *The Feynman lectures of physics* **1,** 41–1 (1964).
51. Burgers, J. M., On the motion of small particles of elongated form suspended in a viscous liquid, *Kon. Ned. Akad. Wet. Verhand.(Eerste Sectie)* **16,** 113–184 (1938).
52. Leal, L. & Hinch, E., The effect of weak Brownian rotations on particles in shear flow, *Journal of Fluid Mechanics* **46,** 685–703 (1971).
53. Brenner, H., Rheology of a dilute suspension of axisymmetric Brownian particles, *International journal of multiphase flow* **1,** 195–341 (1974).
54. Gallily, I. & Cohen, A.-H., On the stochastic nature of the motion of nonspherical aerosol particles. I. The aerodynamic radius concept, *Journal of Colloid and Interface Science* **56,** 443–459 (1976).
55. Gentry, J., Spurny, K. & Schörmann, J, The diffusion coefficients for ultrathin chrysotile fibers, *Journal of aerosol science* **22,** 869–880 (1991).
56. Lavenda, B. H., Brownian motion, *Scientific American* **252,** 70–85 (1985).
57. Bird, R. B., Curtiss, C. F., Armstrong, R. C. & Hassager, O., *Dynamics of polymeric liquids, volume 2: Kinetic theory* (Wiley, 1987).
58. Baglietto, G. & Albano, E. V., Finite-size scaling analysis and dynamic study of the critical behavior of a model for the collective displacement of self-driven individuals, *Physical Review E* **78,** 021125 (2008).
59. Kulinskii, V. & Chepizhko, A., The kinetic regime of the Vicsek model, *Mathematical and Statistical Physics* **1198,** 25 (2009).
60. Chate, H., Ginelli, F., Grégoire, G., Peruani, F. & Raynaud, F., Modeling collective motion: variations on the Vicsek model, *The European Physical Journal B* **64,** 451–456 (2008).

61. ZhiXin, L. & Lei, G., Connectivity and synchronization of Vicsek model, *Science China Series F: Information Sciences* **51,** 848–858 (2008).

62. Jadbabaie, A., Lin, J. & Morse, A., Coordination of groups of mobile autonomous agents using nearest neighbor rules, *IEEE Transactions on Automatic Control* **48,** 988–1001 (2003).

63. Ginelli, F., Peruani, F., Bär, M. & Chate, H., Large-scale collective properties of self-propelled rods, *Physical Review Letters* **104,** 184502 (2010).

64. Vicsek, T., Czirok, A., Ben-Jacob, E., Cohen, I. & Shochet, O., Novel type of phase transition in a system of self-driven particles, *Physical review letters* **75,** 1226 (1995).

65. Solon, A. P. *et al.,* Pressure is not a state function for generic active fluids, *Nature Physics* **11,** 673–678 (2015).

66. Bialké, J., Speck, T. & Löwen, H., Crystallization in a dense suspension of self-propelled particles, *Physical review letters* **108,** 168301 (2012).

67. Cates, M., Fielding, S., Marenduzzo, D, Orlandini, E & Yeomans, J., Shearing active gels close to the isotropic-nematic transition, *Physical review letters* **101,** 068102 (2008).

68. Giomi, L., Liverpool, T. B. & Marchetti, M. C., Sheared active fluids: Thickening, thinning, and vanishing viscosity, *Physical Review E* **81,** 051908 (2010).

69. Słomka, J. & Dunkel, J., Geometry-dependent viscosity reduction in sheared active fluids, *Physical Review Fluids* **2,** 043102 (2017).

70. Saintillan, D, The dilute rheology of swimming suspensions: A simple kinetic model, *Experimental Mechanics* **50,** 1275–1281 (2010).

71. Woodhouse, F. G. & Goldstein, R. E., Spontaneous circulation of confined active suspensions, *Physical review letters* **109,** 168105 (2012).

72. Gao, T. & Li, Z., Self-driven droplet powered by active nematics, *Physical Review Letters* **119,** 108002 (2017).

73. Chen, S., Gao, P. & Gao, T., Dynamics and structure of an apolar active suspension in an annulus, *Journal of Fluid Mechanics* **835,** 393–405 (2018).

74. Theillard, M. & Saintillan, D., Computational mean-field modeling of confined active fluids, *Journal of Computational Physics* **397,** 108841 (2019).

75. Chaubal, C. V. & Leal, L. G., A closure approximation for liquid-crystalline polymer models based on parametric density estimation, *Journal of Rheology* **42,** 177–201 (1998).

76. Weady, S., Shelley, M. J. & Stein, D. B., A fast Chebyshev method for the Bingham closure with application to active nematic suspensions, *Journal of Computational Physics* **457,** 110937 (2022).

77. Batchelor, G., The stress system in a suspension of force-free particles, *Journal of fluid mechanics* **41,** 545–570 (1970).

78. Batchelor, G., The stress generated in a non-dilute suspension of elongated particles by pure straining motion, *Journal of Fluid Mechanics* **46,** 813–829 (1971).

79. Hinch, E. & Leal, L., The effect of Brownian motion on the rheological properties of a suspension of non-spherical particles, *Journal of Fluid Mechanics* **52,** 683–712 (1972).

80. Lipscomb II, G., Denn, M. M., Hur, D. & Boger, D. V., The flow of fiber suspensions in complex geometries, *Journal of Non-Newtonian Fluid Mechanics* **26,** 297–325 (1988).

81. Shaqfeh, E. S. & Fredrickson, G. H., The hydrodynamic stress in a suspension of rods, *Physics of Fluids A: Fluid Dynamics* **2,** 7–24 (1990).

82. Ausias, G., *Etude de l'extrusion de tubes en polymeres thermoplastiques charges de fibres courtes* PhD thesis (Paris, ENMP, 1991).

83. Megally, A., *Etude et modélisation de l'orientation de fibres dans des thermoplastiques renforcés* PhD thesis (École Nationale Supérieure des Mines de Paris, 2005).

84. Mazo, R. M., *Brownian motion: fluctuations, dynamics, and applications* (OUP Oxford, 2008).

85. Phan-Thien, N., Constitutive equation for concentrated suspensions in Newtonian liquids, *Journal of Rheology* **39,** 679–695 (1995).

86. Phan-Thien, N., Fan, X. J. & Khoo, B. C., A new constitutive model for monodispersed suspensions of spheres at high concentrations, *Rheologica Acta* **38,** 297–304 (1999).

87. Narumi, T. *et al.,* Transient response of concentrated suspensions after shear reversal, *Journal of Rheology* **46,** 295–305 (2002).

88. Mason, T. G. & Weitz, D. A., Optical measurements of frequency-dependent linear viscoelastic moduli of complex fluids, *Physical review letters* **74,** 1250 (1995).

89. Crocker, J. C. & Grier, D. G., Methods of digital video microscopy for colloidal studies, *Journal of colloid and interface science* **179,** 298–310 (1996).

90. Dhont, J. K. & Briels, W. J., Gradient and vorticity banding, *Rheologica acta* **47,** 257–281 (2008).

91. Lauga, E. & Powers, T. R., The hydrodynamics of swimming microorganisms, *Reports on Progress in Physics* **72,** 096601 (2009).

92. Izri, Z., Van Der Linden, M. N., Michelin, S. & Dauchot, O., Self-propulsion of pure water droplets by spontaneous Marangoni-stress-driven motion, *Physical review letters* **113,** 248302 (2014).

93. Simha, R. & Ramaswamy, S, Hydrodynamic fluctuations and instabilities in ordered suspensions of self-propelled particles, *Physical review letters* **89,** 058101 (2002).

94. Hatwalne, Y., Ramaswamy, S., Rao, M. & Aditi Simha, R, *Dynamics and Rheology of Active-Particle Suspensions in APS March Meeting Abstracts* **2004** (2004), L9–012.

95. Saintillan, D., Extensional rheology of active suspensions, *Physical Review E* **81,** 056307 (2010).

96. Férec, J., Heniche, M., Heuzey, M. C., Ausias, G. & Carreau, P. J., Numerical solution of the Fokker-Planck equation for fiber suspensions: application to the Folgar–Tucker–Lipscomb model, *Journal of non-Newtonian Fluid Mechanics* **155,** 20–29 10.1016/j.jnnfm.2008.04.004 (2008).

97. Advani, S. G., *Prediction of fiber orientation during processing of short fiber composites* (University of Illinois at Urbana-Champaign, 1987).

98. Mezi, D., Ausias, G., Advani, S. G. & Férec, J., Fiber suspension in 2D nonhomogeneous flow: The effects of flow/fiber coupling for Newtonian and power-law suspending fluids, *Journal of Rheology* **63,** 405–418 10.1122/1.5081016 (2019).

99. Assaad Al Ayoubi, N. *et al.,* Simulation of the Fiber Orientation Through a Finite Element Approach to Solve the Fokker-Planck Equation, https://dx.doi.org/10.2139/ssrn.4216630, *Hugues and Da Silva, Luisa Rocha and Binetruy, Christophe and Renault, Thierry and Comas-Cardona, Sebastien, Simulation of the Fiber Orientation Through a Finite Element Approach to Solve the Fokker-Planck Equation.*

100. Wegener, K., Kuzmin, D. & Turek, S., Efficient numerical solution of the Fokker-Planck equation using physics-conforming finite element methods, *Journal of Numerical Mathematics* (2023).

101. Lohmann, C., *Physics-compatible finite element methods for scalar and tensorial advection problems* (Springer, 2019).

102. Mangesana, N *et al.,* The effect of particle sizes and solids concentration on the rheology of silica sand based suspensions, *Journal of the Southern African Institute of Mining and Metallurgy* **108,** 237–243 (2008).

103. Shafiei-Sabet, S., Hamad, W. Y. & Hatzikiriakos, S. G., Rheology of nanocrystalline cellulose aqueous suspensions, *Langmuir* **28,** 17124–17133 (2012).

104. Li, J, Revol, J. & Marchessault, R., Rheological properties of aqueous suspensions of chitin crystallites, *Journal of Colloid and Interface Science* **183,** 365–373 (1996).

105. Jia, X. *et al.,* Rheological properties of an amorphous cellulose suspension, *Food Hydrocolloids* **39,** 27–33 (2014).

106. Sokolov, A. & Aranson, I. S., Reduction of viscosity in suspension of swimming bacteria, *Physical review letters* **103,** 148101 (2009).

107. Gachelin, J. *et al.,* Non-Newtonian viscosity of Escherichia coli suspensions, *Physical review letters* **110,** 268103 (2013).

108. Rafaï, S., Jibuti, L. & Peyla, P., Effective viscosity of microswimmer suspensions, *Physical Review Letters* **104,** 098102 (2010).

109. López, H. M., Gachelin, J., Douarche, C., Auradou, H. & Clément, E., Turning bacteria suspensions into superfluids, *Physical review letters* **115,** 028301 (2015).

110. Solomon, M. & Boger, D., The rheology of aqueous dispersions of spindle-type colloidal hematite rods, *Journal of Rheology* **42,** 929–949 (1998).

111. Karnis, A, Goldsmith, H. & Mason, S., Axial migration of particles in Poiseuille flow, *Nature* **200,** 159–160 (1963).

112. Nitsche, L. C. & Hinch, E. J., Shear-induced lateral migration of Brownian rigid rods in parabolic channel flow, *Journal of Fluid Mechanics* **332,** 1–21 (1997).

113. Schiek, R. L. & Shaqfeh, E. S. G., Cross-streamline migration of slender Brownian fibres in plane Poiseuille flow, *Journal of Fluid Mechanics* **332,** 23–39 (1997).

114. ROTHSCHILD, Non-random distribution of bull spermatozoa in a drop of sperm suspension, *Nature* **198,** 1221–1222 (1963).

115. Berke, A. P., Turner, L., Berg, H. C. & Lauga, E., Hydrodynamic attraction of swimming microorganisms by surfaces, *Physical Review Letters* **101,** 038102 (2008).

116. Sartori, P. *et al.,* Wall accumulation of bacteria with different motility patterns, *Physical Review E* **97,** 022610 (2018).

117. Elgeti, J. & Gompper, G., Run-and-tumble dynamics of self-propelled particles in confinement, *Europhysics Letters* **109,** 58003 (2015).

118. Stocker, R., Reverse and flick: Hybrid locomotion in bacteria, *Proceedings of the National Academy of Sciences* **108,** 2635–2636 (2011).

119. Houshyar, S., Shanks, R. A. & Hodzic, A., The effect of fiber concentration on mechanical and thermal properties of fiber-reinforced polypropylene composites, *Journal of applied polymer science* **96,** 2260–2272 10.1002/app.20874 (2005).

120. Thomason, J. L. & Groenewoud, W. M., The influence of fibre length and concentration on the properties of glass fibre reinforced polypropylene: 2. Thermal properties, *Composites Part A: Applied Science and Manufacturing* **27,** 555–565 10.1016/1359–835X(96)00016–4 (1996).

121. Li, M. *et al.,* Stress induced carbon fiber orientation for enhanced thermal conductivity of epoxy composites, *Composites Part B: Engineering* **208,** 108599 (2021).

122. Rahnama, M., Koch, D. L., Iso, Y. & Cohen, C., Hydrodynamic, translational diffusion in fiber suspensions subject to simple shear flow, *Physics of Fluids A: Fluid Dynamics* **5,** 849–862 10.1063/1.858890 (1993).

123. Stover, C. A., Koch, D. L. & Cohen, C., Observations of fibre orientation in simple shear flow of semi-dilute suspensions, *Journal of Fluid Mechanics* **238,** 277–296 10.1017/S002211209200171X (1992).

124. Hinch, E. J. & Leal, L. G., Rotation of small non-axisymmetric particles in a simple shear flow, *Journal of Fluid Mechanics* **92,** 591–607 (1979).

125. Yarin, A. L., Gottlieb, O. & Roisman, I. V., Chaotic rotation of triaxial ellipsoids in simple shear flow, *Journal of Fluid Mechanics* **340,** 83–100 (1997).

126. Einarsson, J. *et al.,* Tumbling of asymmetric microrods in a microchannel flow, *Physics of Fluids* **28,** 013302 (2016).

127. Hijazi, A. & Khater, A., Brownian dynamics simulations of rigid rod-like macromolecular particles flowing in bounded channels, *Computational materials science* **22,** 279–290 (2001).

128. Zurita-Gotor, M., Bławzdziewicz, J. & Wajnryb, E., Motion of a rod-like particle between parallel walls with application to suspension rheology, *Journal of Rheology* **51,** 71–97 (2007).

129. Atwi, A., Khater, A. & Hijazi, A., Three-dimensional simulations for the dynamics of dilute colloidal suspensions of ellipsoidal-like particles flowing in the bulk and near solid boundaries, *Polymer* **54,** 1555–1566 (2013).

130. Holmstedt, E., Åkerstedt, H. O., Staffan Lundström, T. & Högberg, S. M., Modeling Transport and Deposition Efficiency of Oblate and Prolate Nano-and Micro-particles in a Virtual Model of the Human Airway, *Journal of Fluids Engineering* **138** (2016).

131. Monjezi, S., Jones, J. D., Nelson, A. K. & Park, J., The effect of weak confinement on the orientation of nanorods under shear flows, *Nanomaterials* **8,** 130 (2018).

132. Gunes, D. Z., Scirocco, R., Mewis, J. & Vermant, J., Flow-induced orientation of non-spherical particles: Effect of aspect ratio and medium rheology, *Journal of non-Newtonian Fluid Mechanics* **155,** 39–50 (2008).

133. Férec, J., Bertevas, E., Khoo, B. C., Ausias, G. & Phan-Thien, N., Rigid fiber motion in slightly non-Newtonian viscoelastic fluids, *Physics of Fluids* **33,** 103320 (2021).

134. Kirkwood, J. G. & Auer, P. L., The visco-elastic properties of solutions of rod-like macromolecules, *The Journal of Chemical Physics* **19,** 281–283 10.1103/PhysRevLett.107.250603 (1951).

135. Frattini, P. L. & Fuller, G. G., Rheo-optical studies of the effect of weak Brownian rotations in sheared suspensions, *Journal of Fluid Mechanics* **168,** 119–150 (1986).

136. Xie, D., Lista, M., Qiao, G. G. & Dunstan, D. E., Shear induced alignment of low aspect ratio gold nanorods in Newtonian fluids, *The Journal of Physical Chemistry Letters* **6,** 3815–3820 (2015).

137. Hinch, E. J. & Leal, L. G., Time-dependent shear flows of a suspension of particles with weak Brownian rotations, *Journal of Fluid Mechanics* **57,** 753–767 (1973).

138. Hijazi, A. & Zoaeter, M., Brownian dynamics simulations for rod-like particles in dilute flowing solution, *European Polymer Journal* **38,** 2207–2211 (2002).

139. Leahy, B. D., Koch, D. L. & Cohen, I., The effect of shear flow on the rotational diffusion of a single axisymmetric particle, *Journal of Fluid Mechanics* **772,** 42–79 (2015).

140. Palanisamy, D. & den Otter, W. K., Efficient Brownian Dynamics of rigid colloids in linear flow fields based on the grand mobility matrix, *The Journal of Chemical Physics* **148,** 194112 (2018).

141. Zöttl, A. *et al.,* Dynamics of individual Brownian rods in a microchannel flow, *Soft Matter* **15,** 5810–5814 (2019).

142. Lozinski, A. & Chauviere, C., A fast solver for Fokker-Planck equation applied to viscoelastic flows calculations: 2D FENE model, *Journal of Computational Physics* **189,** 607–625 10.1016/S0021–9991(03)00248–1 (2003).

143. Chauviere, C. & Lozinski, A., Simulation of complex viscoelastic flows using theFokker-Planck equation: 3D FENE model, *Journal of non-Newtonian Fluid Mechanics* **122,** 201–214 10.1016/j.jnnfm.2003.12.011 (2004).

144. Moosaie, A. & Manhart, M., A direct numerical simulation method for flow of Brownian fiber suspensions in complex geometries, *Journal of dispersion science and technology* **34,** 427–440 10.1080/01932691.2011.634750 (2013).

145. Krochak, P. J., Olson, J. A. & Martinez, D. M., Fiber suspension flow in a tapered channel: The effect of flow/fiber coupling, *International journal of multiphase flow* **35,** 676–688 10.1016/j.ijmultiphaseflow.2009.03.005 (2009).

146. Ammar, A., Mokdad, B., Chinesta, F. & Keunings, R., A new family of solvers for some classes of multidimensional partial differential equations encountered in kinetic theory modeling of complex fluids, *Journal of non-Newtonian Fluid Mechanics* **139,** 153–176 10.1016/j.jnnfm.2006.07.007 (2006).

147. Ammar, A., Mokdad, B., Chinesta, F. & Keunings, R., A new family of solvers for some classes of multidimensional partial differential equations encountered in kinetic theory modelling of complex fluids: Part II: Transient simulation using space-time separated representations, *Journal of non-Newtonian Fluid Mechanics* **144,** 98–121 10.1016/j.jnnfm.2007.03.009 (2007).

148. Park, J. M. & Park, S. J., Modeling and simulation of fiber orientation in injection molding of polymer composites, *Mathematical Problems in Engineering* **2011** (2011 year).

149. Férec, J., Ausias, G., Heuzey, M. C. & Carreau, P. J., Modeling fiber interactions in semiconcentrated fiber suspensions, *Journal of Rheology* **53,** 49–72 (2009).

150. Park, J., Bricker, J. M. & Butler, J. E., Cross-stream migration in dilute solutions of rigid polymers undergoing rectilinear flow near a wall, *Physical Review E* **76,** 040801 (2007).

151. Sharaf, O. Z., Al-Khateeb, A. N., Kyritsis, D. C. & Abu-Nada, E., Numerical investigation of nanofluid particle migration and convective heat transfer in microchannels using an Eulerian-Lagrangian approach, *Journal of Fluid Mechanics* **878,** 62–97 (2019).

152. Advani, S. G. & Tucker III, C. L., The use of tensors to describe and predict fiber orientation in short fiber composites, *Journal of Rheology* **31,** 751–784 10.1122/1.549945 (1987).

153. Phillips, R. J., Armstrong, R. C., Brown, R. A., Graham, A. L. & Abbott, J. R., A constitutive equation for concentrated suspensions that accounts for shear-induced particle migration, *Physics of Fluids A: Fluid Dynamics* **4,** 30–40 10.1063/1.858498 (1992).

154. Shapley, N. C., Armstrong, R. C. & Brown, R. A., Laser Doppler velocimetry measurements of particle velocity fluctuations in a concentrated suspension, *Journal of Rheology* **46,** 241–272 10.1122/1.1427908 (2002).

155. Sanchez, T., Chen, D. T., DeCamp, S. J., Heymann, M. & Dogic, Z., Spontaneous motion in hierarchically assembled active matter, *Nature* **491,** 431–434 (2012).

156. Advani, S. G. & Tucker III, C. L., Closure approximations for three-dimensional structure tensors, *Journal of Rheology* **34,** (1990).

157. Tseng, H. C., Chang, R. Y. & Hsu, C. H., Cross-streamline migration of slender Brownian fibres in plane Poiseuille flow, *Journal of Rheology* **62,** 313–320 10.1122/1.4998520 (2018).

158. Ezhilan, B., Shelley, M. J. & Saintillan, D., Instabilities and nonlinear dynamics of concentrated active suspensions, *Physics of Fluids* **25,** 070607 10.1063/1.4812822 (2013).

159. Chen, S. B. & Jiang, L., Orientation distribution in a dilute suspension of fibers subject to simple shear flow, *Physics of Fluids* **11,** 2878–2890 (1999).

160. Du, Y., Jiang, H. & Hou, Z., Study of active Brownian particle diffusion in polymer solutions, *Soft Matter* **15,** 2020–2031 (2019).

161. Ghernaout, D. *et al.,* Brownian motion and coagulation process, *American Journal of Environmental Protection* **4,** 1–15 (2015).

162. Haddadi, H., Shojaei-Zadeh, S., Connington, K. & Morris, J. F., Suspension flow past a cylinder: particle interactions with recirculating wakes, *Journal of Fluid Mechanics* **760 10.1017/jfm.2014.613** (2014).

163. Phan-Thien, N. & Graham, A. L., A new constitutive model for fibre suspensions: flow past a sphere, *Rheologica acta* **30,** 44–57 (1991).

164. Kumar, G. & Natale, G., Settling dynamics of two spheres in a suspension of Brownian rods, *Physics of Fluids* **31,** 073104 (2019).

165. Russel, W., Brownian motion of small particles suspended in liquids, *Annual Review of Fluid Mechanics* **13,** 425–455 (1981).

166. Ladd, A. & Verberg, R, Lattice-Boltzmann simulations of particle-fluid suspensions, *Journal of statistical physics* **104,** 1191–1251 (2001).

167. Dhont, J. K. & Briels, W. J., Rod-like Brownian particles in shear flow, *Soft Matter: Complex Colloidal Suspensions, edited by G. Gompper, M. Schick* **2** (2006).

168. Natale, G, Heuzey, M., Carreau, P., Ausias, G. & Férec, J, Rheological modeling of carbon nanotube suspensions with rod–rod interactions, *AIChE Journal* **60,** 1476–1487 (2014).

169. VerWeyst, B. E. & Tucker III, C. L., Fiber suspensions in complex geometries: Flow/orientation coupling, *The Canadian Journal of Chemical Engineering* **80,** 1093–1106 (2002).

170. Mezi, D., Ausias, G., Grohens, Y. & Férec, J., Numerical simulation and modeling of the die swell for fiber suspension flows, *Journal of Non-Newtonian Fluid Mechanics* **274,** 104205 (2019).

171. Férec, J., Mezi, D., Advani, S. G. & Ausias, G., Axisymmetric flow simulations of fiber suspensions as described by 3D probability distribution function, *Journal of Non-Newtonian Fluid Mechanics* **284,** 104367 (2020).

172. Batchelor, G. & Green, J., The determination of the bulk stress in a suspension of spherical particles to order c2, *Journal of Fluid Mechanics* **56,** 401–427 (1972).

173. Batchelor, G., The effect of Brownian motion on the bulk stress in a suspension of spherical particles, *Journal of fluid mechanics* **83,** 97–117 (1977).

174. Bagnold, R. A., Experiments on a gravity-free dispersion of large solid spheres in a Newtonian fluid under shear, *Proceedings of the Royal Society of London. Series A. Mathematical and Physical Sciences* **225,** 49–63 (1954).

175. Gadala-Maria, F. A., *The rheology of concentrated suspensions.* (Stanford University, 1979).

176. Gadala-Maria, F & Acrivos, A., Shear-induced structure in a concentrated suspension of solid spheres, *Journal of Rheology* **24,** 799–814 (1980).

177. Yasuda, K., Ohara, N. & Muguruma, M., Velocity profiles of suspension flows through an abrupt contraction measured by magnetic resonance imaging, *Chemical Engineering & Technology: Industrial Chemistry-Plant Equipment-Process Engineering-Biotechnology* **30,** 1036–1044 (2007).

178. Mazahir, S., Vélez-García, G., Wapperom, P & Baird, D, Evolution of fibre orientation in radial direction in a center-gated disk: Experiments and simulation, *Composites Part A: Applied Science and Manufacturing* **51,** 108–117 (2013).

179. Mazahir, S., Vélez-García, G., Wapperom, P & Baird, D, Fiber orientation in the frontal region of a center-gated disk: Experiments and simulation, *Journal of Non-Newtonian Fluid Mechanics* **216,** 31–44 (2015).

180. Wang, J., O'Gara, J. F. & Tucker III, C. L., An objective model for slow orientation kinetics in concentrated fiber suspensions: Theory and rheological evidence, *Journal of Rheology* **52,** 1179–1200 (2008).

181. Woolley, D., Motility of spermatozoa at surfaces, *REPRODUCTION-CAMBRIDGE-* **126,** 259–270 (2003).

182. Lecuyer, S. *et al.,* Shear stress increases the residence time of adhesion of Pseudomonas aeruginosa, *Biophysical journal* **100,** 341–350 (2011).

183. Lu, L. & Walker, W. A., Pathologic and physiologic interactions of bacteria with the gastrointestinal epithelium, *The American journal of clinical nutrition* **73,** 1124S–1130S (2001).

184. Celli, J. P. *et al.,* Helicobacter pylori moves through mucus by reducing mucin viscoelasticity, *Proceedings of the National Academy of Sciences* **106,** 14321–14326 (2009).

185. Hill, J., Kalkanci, O., McMurry, J. L. & Koser, H., Hydrodynamic surface interactions enable Escherichia coli to seek efficient routes to swim upstream, *Physical review letters* **98,** 068101 (2007).

186. Kaya, T. & Koser, H., Characterization of hydrodynamic surface interactions of Escherichia coli cell bodies in shear flow, *Physical review letters* **103,** 138103 (2009).

187. Kaya, T. & Koser, H., Direct upstream motility in Escherichia coli, *Biophysical journal* **102,** 1514–1523 (2012).

188. Lauga, E., DiLuzio, W. R., Whitesides, G. M. & Stone, H. A., Swimming in circles: motion of bacteria near solid boundaries, *Biophysical journal* **90,** 400–412 (2006).

189. Secchi, E. *et al.,* The effect of flow on swimming bacteria controls the initial colonization of curved surfaces, *Nature communications* **11,** 2851 (2020).

190. Vennamneni, L., Nambiar, S. & Subramanian, G., Shear-induced migration of microswimmers in pressure-driven channel flow, *Journal of Fluid Mechanics* **890,** A15 (2020).

191. Hernandez-Ortiz, J. P., Stoltz, C. G. & Graham, M. D., Transport and collective dynamics in suspensions of confined swimming particles, *Physical review letters* **95,** 204501 (2005).

192. Hernandez-Ortiz, J. P., Underhill, P. T. & Graham, M. D., Dynamics of confined suspensions of swimming particles, *Journal of Physics: Condensed Matter* **21,** 204107 (2009).

193. Elgeti, J. & Gompper, G., Wall accumulation of self-propelled spheres, *EPL (Europhysics Letters)* **101,** 48003 (2013).

194. Lee, C. F., Active particles under confinement: aggregation at the wall and gradient formation inside a channel, *New Journal of Physics* **15,** 055007 (2013).

195. Li, G.-J. & Ardekani, A. M., Hydrodynamic interaction of microswimmers near a wall, *Physical Review E* **90,** 013010 (2014).

196. Saintillan, D. & Shelley, M. J., Instabilities, pattern formation, and mixing in active suspensions, *Physics of Fluids* **20** (2008).

197. Saintillan, D. & Shelley, M. J., Instabilities and pattern formation in active particle suspensions: kinetic theory and continuum simulations, *Physical Review Letters* **100,** 178103 (2008).

198. Baskaran, A. & Marchetti, M. C., Statistical mechanics and hydrodynamics of bacterial suspensions, *Proceedings of the National Academy of Sciences* **106,** 15567–15572 (2009).

199. Igoshin, O. A., Welch, R., Kaiser, D. & Oster, G., Waves and aggregation patterns in myxobacteria, *Proceedings of the National Academy of Sciences* **101,** 4256–4261 (2004).

200. Riedel, I. H., Kruse, K. & Howard, J., A self-organized vortex array of hydrodynamically entrained sperm cells, *Science* **309,** 300–303 (2005).

201. Nedelec, F. J., Surrey, T., Maggs, A. C. & Leibler, S., Self-organization of microtubules and motors, *Nature* **389,** 305–308 (1997).

202. Narayanan, V., Ramaswamy, S. & Menon, N., Long-lived giant number fluctuations in a swarming granular nematic, *Science* **317,** 105–108 (2007).

203. Forest, M. G., Wang, Q. & Zhou, R., Kinetic theory and simulations of active polar liquid crystalline polymers, *Soft Matter* **9,** 5207–5222 (2013).

204. Ezhilan, B. & Saintillan, D., Transport of a dilute active suspension in pressure-driven channel flow, *Journal of Fluid Mechanics* **777,** 482–522 (2015).

205. Versteeg, H. K. & Malalasekera, W., *An introduction to computational fluid dynamics: the finite volume method* (Pearson education, 2007).

206. Alonso-Matilla, R., Ezhilan, B. & Saintillan, D., Microfluidic rheology of active particle suspensions: Kinetic theory, *Biomicrofluidics* **10,** 043505 (2016).

207. Xu, D, Jia, R, Li, Y & Gu, T, Advances in the treatment of problematic industrial biofilms, *World Journal of Microbiology and Biotechnology* **33,** 1–10 (2017).

208. Rasamiravaka, T., Labtani, Q., Duez, P., El Jaziri, M., *et al.,* The formation of biofilms by Pseudomonas aeruginosa: a review of the natural and synthetic compounds interfering with control mechanisms, *BioMed research international* **2015** (2015).

209. Saxena, P., Joshi, Y., Rawat, K. & Bisht, R., Biofilms: architecture, resistance, quorum sensing and control mechanisms, *Indian journal of microbiology* **59,** 3–12 (2019).

210. Issa, H., Natale, G., Ausias, G. & Férec, J., Modeling and numerical simulations of Brownian rodlike particles with anisotropic translational diffusion, *Physical Review Fluids* **8,** 033302 (2023).

211. Miño, G. L. *et al.,* E coli accumulation behind an obstacle (2018).

212. Hatwalne, Y., Ramaswamy, S., Rao, M. & Aditi Simha, R, Rheology of active-particle suspensions, *Phys Rev Lett* **92,** 118101 (2004).

213. Ishikawa, T. & Pedley, T. J., The rheology of a semi-dilute suspension of swimming model micro-organisms, *J Fluid Mech* **588,** 399–435 (2007).

214. Haines, B. M., Aranson, I. S., Berlyand, L. & Karpeev, D. A., Effective viscosity of dilute bacterial suspensions: a two-dimensional model, *Phys Biol* **5,** 1–9 (2008).

215. Guo, S., Samanta, D., Peng, Y., Xu, X. & Cheng, X., Symmetric shear banding and swarming vortices in bacterial superfluids, *Proceedings of the National Academy of Sciences* **115,** 7212–7217 (2018).

216. Vennamneni, L., Garg, P. & Subramanian, G., Concentration banding instability of a sheared bacterial suspension, *Journal of Fluid Mechanics* **904,** A7 (2020).

217. Cates, M. E. & Fielding, S. M., Rheology of giant micelles, *Adv. Phys.* **55,** 799–879 (2006).

218. Olmsted, P. D., Perspectives on shear banding in complex fluids, *Rheol. Acta* **47,** 283–300 (2008).

219. Divoux, T., Fardin, M. A., Manneville, S. & Lerouge, S., Shear banding of complex fluids, *Annu. Rev. Fluid Mech.* **48,** 81–103 (2016).

220. Loisy, A., Eggers, J. & Liverpool, T. B., Active suspensions have nonmonotonic flow curves and multiple mechanical equilibria, *Phys. Rev. Lett.* **121,** 018001 (2018).

221. Agarwal, U, Dutta, A & Mashelkar, R, Migration of macromolecules under flow: The physical origin and engineering implications, *Chemical engineering science* **49,** 1693–1705 (1994).

222. Jendrejack, R. M., Schwartz, D. C., De Pablo, J. J. & Graham, M. D., Shear-induced migration in flowing polymer solutions: simulation of long-chain DNA in microchannels, *The Journal of chemical physics* **120,** 2513–2525 (2004).

223. Marcos, H. C., Fu, H., Powers, T. & Stocker, R, Separation of microscale chiral objects by shear flow, *Physical review letters* **102,** 158103 (2009).

224. Makino, M & Doi, M, Migration of twisted ribbon-like particles in simple shear flow, *Physics of Fluids* **17,** 103605 (2005).

225. Aris, R., On the dispersion of a solute in a fluid flowing through a tube, *Proceedings of the Royal Society of London. Series A. Mathematical and Physical Sciences* **235,** 67–77 (1956).

226. Peng, Z. & Brady, J. F., Upstream swimming and Taylor dispersion of active Brownian particles, *Physical Review Fluids* **5,** 073102 (2020).

227. Kumar, A. H., Thomson, S. J., Powers, T. R. & Harris, D. M., Taylor dispersion of elongated rods, *Physical Review Fluids* **6,** 094501 (2021).

228. Feng, J, Chaubal, C. & Leal, L., Closure approximations for the Doi theory: Which to use in simulating complex flows of liquid-crystalline polymers?, *Journal of Rheology* **42,** 1095–1119 (1998).

229. Levermore, C. D., Entropy-based moment closures for kinetic equations, *Transport Theory and Statistical Physics* **26,** 591–606 (1997).

230. Woodhouse, F. G. & Goldstein, R. E., Spontaneous circulation of confined active suspensions, *Phys. Rev. Lett.* **109,** 168105 (2012).

231. Gao, T. & Li, Z., Self-driven droplet powered by active nematics, *Phys. Rev. Lett.* **119,** 108002 (2017).

232. Chen, S., Gao, P. & Gao, T., Dynamics and structure of an apolar active suspension in an annulus, *Journal of Fluid Mechanics* **835,** 393–405 (2018).

233. Theillard, M. & Saintillan, D., Computational mean-field modeling of confined active fluids, *Journal of Computational Physics* **397,** 108841 (2019).

234. Han, J., Luo, Y., Wang, W., Zhang, P. & Zhang, Z., From microscopic theory to macroscopic theory: a systematic study on modeling for liquid crystals, *Archive for Rational Mechanics and Analysis* **215,** 741–809 (2015).

235. Li, S., Wang, W. & Zhang, P., Local well-posedness and small deborah limit of a molecule-based q-tensor system, *Discrete and Continuous Dynamical Systems - B* **20,** 2611 (2015).

236. Chaubal, C. V. & Leal, L. G., A closure approximation for liquid-crystalline polymer models based on parametric density estimation, *Journal of Rheology* **42,** 177–201 (1998).

237. Bingham, C., An antipodally symmetric distribution on the sphere, *Ann. Statist.* **2,** 1201–1225 (1974).

238. Saintillan, D, Rheology of active fluids, *Annual Review of Fluid Mechanics* **50,** 563–592 (2018).

239. Saintillan, D & Shelley, M., Instabilities and pattern formation in active particle suspensions: kinetic theory and continuum simulations, *Physical Review Letters* **100,** 178103 (2008).

240. Saintillan, D & Shelley, M., Instabilities, pattern formation, and mixing in active suspensions, *Physics of Fluids* **20,** 123304 (2008).

241. Aranson, I., Sokolov, A, Kessler, J. & Goldstein, R., Model for dynamical coherence in thin films of self-propelled microorganisms, *Physical Review E* **75,** 040901 (2007).

242. Stocker, R, Microorganisms in vortices: a microfluidic setup, *Limnology and Oceanography: Methods* **4,** 392–398 (2006).

243. Pahlavan, A. & Saintillan, D, Instability regimes in flowing suspensions of swimming micro-organisms, *Physics of Fluids* **23,** 011901 (2011).

244. Batchelor, G. K., Transport properties of two-phase materials with random structure, *Annual Review of Fluid Mechanics* **6,** 227–255 (1974).

245. Hinch, E. & Leal, L., Constitutive equations in suspension mechanics. Part 1. General formulation, *Journal of Fluid Mechanics* **71,** 481–495 (1975).

246. Chen, S. B. & Koch, D. L., Rheology of dilute suspensions of charged fibers, *Physics of Fluids* **8,** 2792–2807 (1996).

247. Koch, D. & Subramanian, G, Collective hydrodynamics of swimming microorganisms: living fluids, *Annual Review of Fluid Mechanics* **43,** 637–659 (2011).

248. Mazo, R., *Brownian motion: fluctuations, dynamics, and applications* **112** (Oxford University Press on Demand, 2002).

249. Bechinger, C. *et al.,* Active particles in complex and crowded environments, *Reviews of Modern Physics* **88,** 045006 (2016).

250. Elgeti, J., Winkler, R. G. & Gompper, G., Physics of microswimmers—single particle motion and collective behavior: a review, *Reports on progress in physics* **78,** 056601 (2015).

251. Wensink, H. H. *et al.,* Meso-scale turbulence in living fluids, *Proceedings of the national academy of sciences* **109,** 14308–14313 (2012).

252. Narayan, V., Ramaswamy, S. & Menon, N., Long-lived giant number fluctuations in a swarming granular nematic, *Science* **317,** 105–108 (2007).

253. Zhang, H.-P., Be'er, A., Florin, E.-L. & Swinney, H. L., Collective motion and density fluctuations in bacterial colonies, *Proceedings of the National Academy of Sciences* **107,** 13626–13630 (2010).

254. Wu, X.-L. & Libchaber, A., Particle diffusion in a quasi-two-dimensional bacterial bath, *Physical review letters* **84,** 3017 (2000).

255. Mino, G., Dunstan, J., Rousselet, A., Clément, E & Soto, R., Induced diffusion of tracers in a bacterial suspension: theory and experiments, *Journal of Fluid Mechanics* **729,** 423–444 (2013).

256. Morozov, A. & Marenduzzo, D., Enhanced diffusion of tracer particles in dilute bacterial suspensions, *Soft Matter* **10,** 2748–2758 (2014).

257. Peng, Y. *et al.,* Diffusion of ellipsoids in bacterial suspensions, *Physical review letters* **116,** 068303 (2016).

258. Yang, O. *et al.,* Dynamics of ellipsoidal tracers in swimming algal suspensions, *Physical Review E* **94,** 042601 (2016).

259. Haines, B. M., Sokolov, A., Aranson, I. S., Berlyand, L. & Karpeev, D. A., Three-dimensional model for the effective viscosity of bacterial suspensions, *Physical Review E* **80,** 041922 (2009).

260. Ryan, S. D., Haines, B. M., Berlyand, L., Ziebert, F. & Aranson, I. S., Viscosity of bacterial suspensions: Hydrodynamic interactions and self-induced noise, *Physical Review E* **83,** 050904 (2011).

261. Moradi, M. & Najafi, A., Rheological properties of a dilute suspension of self-propelled particles, *EPL (Europhysics Letters)* **109,** 24001 (2015).

262. Bechtel, T. M. & Khair, A. S., Linear viscoelasticity of a dilute active suspension, *Rheologica Acta* **56,** 149–160 (2017).

263. Stokes, G. G. *et al.,* On the effect of the internal friction of fluids on the motion of pendulums (1851).

264. Navier, C., On the laws of motion of fluids taking into consideration the adhesion of the molecules, *Ann. Chim. Phys* **19,** 234–245 (1822).

265. Asgharian, B., Yu, C. & Gradon, L, Diffusion of fibers in a tubular flow, *Aerosol science and technology* **9,** 213–219 (1988).

266. Chen, Y. & Yu, C., Monte Carlo simulation of fiber orientation in a shear flow with Brownian rotation, *Aerosol science and technology* **16,** 255–264 (1992).

267. Tian, L., Ahmadi, G. & Tu, J., Brownian diffusion of fibers, *Aerosol Science and Technology* **50,** 474–486 (2016).

268. Toner, J., Tu, Y. & Ramaswamy, S., Hydrodynamics and phases of flocks, *Annals of Physics* **318,** 170–244 (2005).

269. Redner, G. S., Hagan, M. F. & Baskaran, A., Structure and dynamics of a phase-separating active colloidal fluid, *Physical review letters* **110,** 055701 (2013).

270. Cates, M. E. & Tailleur, J., Motility-induced phase separation, *Annu. Rev. Condens. Matter Phys.* **6,** 219–244 (2015).

271. Wysocki, A., Winkler, R. G. & Gompper, G., Cooperative motion of active Brownian spheres in three-dimensional dense suspensions, *EPL (Europhysics Letters)* **105,** 48004 (2014).

272. Stenhammar, J., Marenduzzo, D., Allen, R. J. & Cates, M. E., Phase behaviour of active Brownian particles: the role of dimensionality, *Soft matter* **10,** 1489–1499 (2014).

273. Wysocki, A., Winkler, R. G. & Gompper, G., Propagating interfaces in mixtures of active and passive Brownian particles, *New journal of physics* **18,** 123030 (2016).

274. Stenhammar, J., Wittkowski, R., Marenduzzo, D. & Cates, M. E., Activity-induced phase separation and self-assembly in mixtures of active and passive particles, *Physical review letters* **114,** 018301 (2015).

275. Digregorio, P. *et al.,* Full phase diagram of active Brownian disks: From melting to motility-induced phase separation, *Physical review letters* **121,** 098003 (2018).

276. Fily, Y., Henkes, S. & Marchetti, M. C., Freezing and phase separation of self-propelled disks, *Soft matter* **10,** 2132–2140 (2014).

277. Fily, Y., Baskaran, A. & Hagan, M. F., Dynamics of self-propelled particles under strong confinement, *Soft matter* **10,** 5609–5617 (2014).

278. Wysocki, A. & Rieger, H., Capillary action in scalar active matter, *Physical review letters* **124,** 048001 (2020).

279. Das, S., Gompper, G. & Winkler, R. G., Local stress and pressure in an inhomogeneous system of spherical active Brownian particles, *Scientific reports* **9,** 1–11 (2019).

280. Takatori, S. C., Yan, W. & Brady, J. F., Swim pressure: stress generation in active matter, *Physical review letters* **113,** 028103 (2014).

281. Winkler, R. G., Wysocki, A. & Gompper, G., Virial pressure in systems of spherical active Brownian particles, *Soft matter* **11,** 6680–6691 (2015).

282. Fily, Y., Kafri, Y., Solon, A. P., Tailleur, J. & Turner, A., Mechanical pressure and momentum conservation in dry active matter, *Journal of Physics A: Mathematical and Theoretical* **51,** 044003 (2017).

283. Pasquino, R., Snijkers, F., Grizzuti, N. & Vermant, J., The effect of particle size and migration on the formation of flow-induced structures in viscoelastic suspensions, *Rheologica Acta* **49,** 993–1001 10.1007/s00397–010–0466–5 (2010).

284. Rashedi, A. *et al.,* Shear-induced migration and axial development of particles in channel flows of non-Brownian suspensions, *AIChE Journal* **66,** e17100 10.1002/aic.17100 (2020).

285. Perumal, V., Gupta, R. K., Bhattacharya, S. N. & Costa, F. S., Fiber migration in shear flow: Model predictions and experimental validation, *Polymer Composites* **40,** 3573–3581 10.1002/pc.25219 (2019).

286. Kang, C. & Mirbod, P., Shear-induced particle migration of semi-dilute and concentrated Brownian suspensions in both Poiseuille and circular Couette flow, *International Journal of Multiphase Flow* **126,** 103239 10.1016/j.ijmultiphaseflow.2020.103239 (2020).

287. Frank, M., Anderson, D., Weeks, E. R. & Morris, J. F., Particle migration in pressure-driven flow of a Brownian suspension, *Journal of Fluid Mechanics* **493,** 363–378 (2003).

288. Jeong, J. T. & Yoon, S. H., Two-dimensional Stokes flow around a circular cylinder in a microchannel, *Journal of Mechanical Science and Technology* **28,** 573–579 10.1007/s12206–013–1162–z (2014).

289. Franceschini, A., Filippidi, E., Guazzelli, E. & Pine, D. J., Transverse alignment of fibers in a periodically sheared suspension: an absorbing phase transition with a slowly varying control parameter, *Physical review letters* **107,** 250603 (2011).

290. Olla, P., Orientation dynamics of weakly Brownian particles in periodic viscous flows, *Physical Review E* **73,** 041406 10.1103/PhysRevE.73.041406 (2006).

291. Strednak, S., Shaikh, S., Butler, J. E. & Guazzelli, É., Shear-induced migration and orientation of rigid fibers in an oscillatory pipe flow, *Physical Review Fluids* **3,** 091301 10.1103/PhysRevFluids.3.091301 (2018).

292. Naillon, A. *et al.,* Dynamics of particle migration in confined viscoelastic Poiseuille flows, *Physical Review Fluids* **4,** 053301 10.1103/PhysRevFluids.4.053301 (2019).

293. Li T.and Luyé, J. F., Flow-fiber coupled injection molding simulations with non-uniform fiber concentration effects (2018 /hal-01958510).

294. Ozenda, O., Saramito, P. & Chambon, G., Shear-induced migration in concentrated suspensions: particle mass conservation, contact pressure and jamming (2021 /hal-03331262).

295. Bahiraei, M., Particle migration in nanofluids: a critical review, *International Journal of Thermal Sciences* **109,** 10.1016/j.ijthermalsci.2016.05.033 (2016).

296. Einarsson, J., Candelier, F., Lundell, F., Angilella, J. R. & Mehlig, B., Effect of weak fluid inertia upon Jeffery orbits, *Physical Review E* **91,** 041002 (2015).

297. Férec, J., Bertevas, E., Ausias, G. & Phan-Thien, N., *in Flow-Induced Alignment in Composite Materials* 77–121 (Elsevier, 2022).

298. Chrit, F. E., Bowie, S. & Alexeev, A., Inertial migration of spherical particles in channel flow of power law fluids, *Physics of Fluids* **32,** 083103 (2020).

299. Fabrice, S., *Understanding Stabilization Methods* (accessed: 22.06.2022).

300. Lai, X., *Shear Thickening of Silica Rod Suspensions* PhD thesis (Georgetown University, 2020).

301. Bossis, G & Brady, J., The rheology of Brownian suspensions, *The Journal of chemical physics* **91,** 1866–1874 (1989).

302. Brady, J. F. & Morris, J. F., Microstructure of strongly sheared suspensions and its impact on rheology and diffusion, *Journal of Fluid Mechanics* **348,** 103–139 (1997).

303. Russel, W. B., The Huggins coefficient as a means for characterizing suspended particles, *Journal of the Chemical Society, Faraday Transactions 2: Molecular and Chemical Physics* **80,** 31–41 (1984).

304. Marrucci, G, The Doi-Edwards model without independent alignment, *Journal of non-Newtonian fluid mechanics* **21,** 329–336 (1986).

305. Rusconi, R., Guasto, J. S. & Stocker, R., Bacterial transport suppressed by fluid shear, *Nature physics* **10,** 212–217 (2014).

306. Durbin, P. A., Some recent developments in turbulence closure modeling, *Annual Review of Fluid Mechanics* **50,** 77–103 (2018).

307. Anand, S. K. & Singh, S. P., Behavior of active filaments near solid-boundary under linear shear flow, *Soft Matter* **15,** 4008–4018 (2019).

APPENDIX A

# APPENDICES: MODELING AND NUMERICAL SIMULATIONS OF BROWNIAN RODLIKE PARTICLES WITH ANISOTROPIC TRANSLATIONAL DIFFUSION

## A.1 Derivation for the equation of change of $\mathbf{A}_2$

This part focuses on the derivation of Eq. (2.9). First, Eq. (2.5) is multiplying with the tensor $\mathbf{pp}/V$ and integrating over all orientations and the spatial domain to give

$$\begin{aligned}\frac{1}{V}\int_{\mathbf{p}}\int_{\mathbf{r}_c}\frac{D\Psi}{Dt}\mathbf{pp}d\mathbf{r}_c d\mathbf{p} =& \frac{1}{V}\int_{\mathbf{p}}\int_{\mathbf{r}_c}\nabla_{\mathbf{x}}\cdot\left(\mathbf{D}_t\cdot\nabla_{\mathbf{x}}\Psi\right)\mathbf{pp}d\mathbf{r}_c d\mathbf{p}\\ &-\frac{1}{V}\int_{\mathbf{p}}\int_{\mathbf{r}_c}\nabla_{\mathbf{p}}\cdot(\dot{\mathbf{p}}_j\Psi)\mathbf{pp}d\mathbf{r}_c d\mathbf{p}+\frac{D_r}{V}\int_{\mathbf{p}}\int_{\mathbf{r}_c}\nabla^2_{\mathbf{p}}\Psi\mathbf{pp}d\mathbf{r}_c d\mathbf{p}.\end{aligned} \tag{A.1}$$

The left-hand side of the above equation is simply the material derivative of $\mathbf{A}_2$, i.e., $D\mathbf{A}_2/Dt$. The first term on the right-hand side of Eq. (A.1) has already been addressed in Eq. (2.8). As for the second term on the right-hand side of Eq. (A.1), application of the integration by parts formula leads to [152]

$$-\frac{1}{V}\int_{\mathbf{p}}\int_{\mathbf{r}_c}\nabla_{\mathbf{p}}\cdot(\dot{\mathbf{p}}_j\Psi)\mathbf{pp}d\mathbf{r}_c d\mathbf{p} \;=\; -\frac{1}{2}\left(\boldsymbol{\omega}\cdot\mathbf{A}_2-\mathbf{A}_2\cdot\boldsymbol{\omega}\right)+\frac{\lambda}{2}\left(\dot{\boldsymbol{\gamma}}\cdot\mathbf{A}_2+\mathbf{A}_2\cdot\dot{\boldsymbol{\gamma}}-2\mathbf{A}_4:\dot{\boldsymbol{\gamma}}\right). \tag{A.2}$$

In obtaining the above equation, the Jeffery's equation [Eq. (2.4)] has been used. Finally, the integration by parts formula is applied two times in the last term of Eq. (A.1) to yield [152]

$$\frac{D_r}{V}\int_{\mathbf{p}}\int_{\mathbf{r}_c}\nabla^2_{\mathbf{p}}\Psi\mathbf{pp}d\mathbf{r}_c d\mathbf{p} = 2D_r\left(c\boldsymbol{\delta}-\alpha\mathbf{A}_2\right), \tag{A.3}$$

where $\alpha$ equals 2 in 2D and 3 in 3D. Gathering these results together, we obtain the expression for the material derivative of $\mathbf{A}_2$ given in Eq. (2.9).

## A.2 Numerical method

For this work, two different numerical methods have been used. The first problem is to solve the FP equation [Eq. (2.5)] in a direct numerical computation. This numerical model is referred by method 1 in this article. While the other method is demonstrated to compute the macromodel ($\mathbf{A}_2$) by solving the partial differential equation of evolution of $\mathbf{A}_2$ [Eq. (2.9)]. This numerical model is referred by method 2 in this article. For both problems, the finite-element method is applied. Utilized software is COMSOL Multiphysics 5.5 to solve the problems including the fluid flow field, and the partial differential equations.

### A.2.1 Method 1

In order to solve the FP equation for $\Psi$ [Eq. (2.16)] for particle orientation and concentration in 2D, a numerical model is composed of two components (a model component in COMSOL Multiphysics is a fundamental section of the model that includes a geometry, physics interface, mesh, variables, and other definitions that are specific to that component), a 2D component and a 3D component. Benefiting from the COMSOL advantage of linear extrusion coupling operator which maps an expression defined on a source to an expression that can be evaluated in the destination (mapping two different components), and general projection operator, which integrates along curves defined via expressions that can be Cartesian coordinates. Component 1 is a 2D rectangular geometry, the creeping flow is defined by solving Eqs. 2.19 and 2.20 and with the given boundary conditions, the spatial discretization of the pressure and velocity fields are done on P1+P2 element. Component 2 is a 3D rectangular block, the base rectangle has the dimensions as component 1, and the horizontal coordinates are defined as spatial coordinates, where component 1 is extruded, while the vertical coordinate are defined as the discretization of $\phi$, considering $\phi$ is the angle of orientation of the particle. $\phi = 0$ means the rod is aligned in the direction of flow since the rods are symmetry, so the head of the rod is identical to its tail. $\phi$ is discretized from 0 to $\pi$, respecting the periodic conditions of symmetric particles

$$\Psi\left(\mathbf{r}_c, \phi, t\right) = \Psi\left(\mathbf{r}_c, \phi + \pi, t\right). \tag{A.4}$$

Equation (2.16) is then projected in the $\phi$ direction to yield for

$$\frac{D\Psi}{Dt} = \nabla_{\mathbf{x}} \cdot \left(\mathbf{D}_t \cdot \nabla_{\mathbf{x}}\Psi\right) - \nabla_{\phi} \cdot \left(\mathbf{p}_j \Psi\right) + \frac{1}{Pe_r}\nabla_{\phi}^2\Psi, \tag{A.5}$$

knowing that $\nabla_{\phi}$ is the gradient operator in the direction of $\phi$. Elements with Lagrangian shape functions of order quadratic are used for $\Psi$.

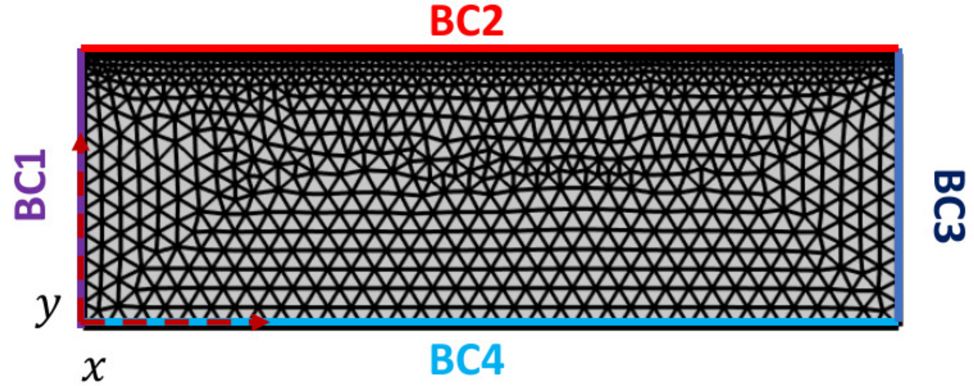

(a) Component 1

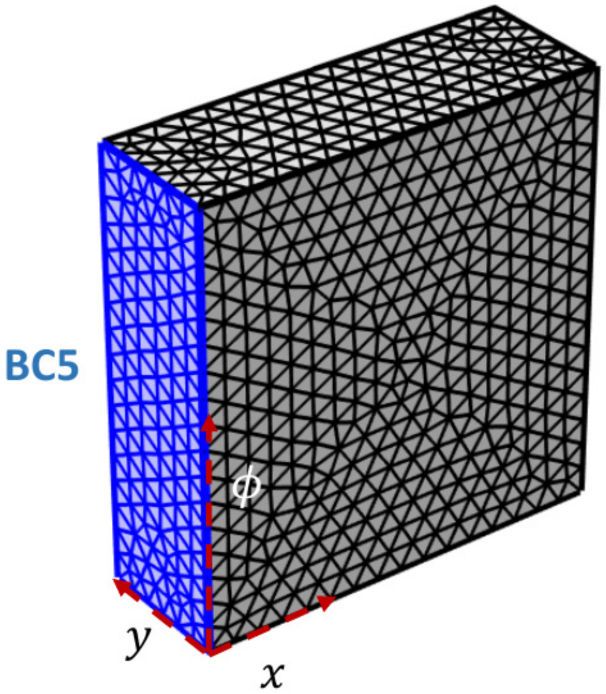

(b) Component 2

Figure A.1 – FE mesh for components 1 and 2 in method 1. BC1: creeping inflow, BC2: No slip condition, BC3: pressure outlet, BC4: symmetry condition, BC5: Dirichlet condition for $\Psi$.

All the computations were carried out on a workstation Dell PowerEdge R930 with Intel Xeon E7-8860 v4 @ 2.20 GHz CPU with 72 threads and 1TB RAM. The computation was around 3 h and 36 minutes in each case for the three Peclet regimes. The used mesh for component 1 is COMSOL's predefined free triangular mesh of fine resolution of 3852 elements. While for component 2, it is free tetrahedral of coarser size, with scale geometry of 9 in the $x$, $y$, and $\phi$ direction of 552663and 17064 tetrahedral and triangular elements, respectively.

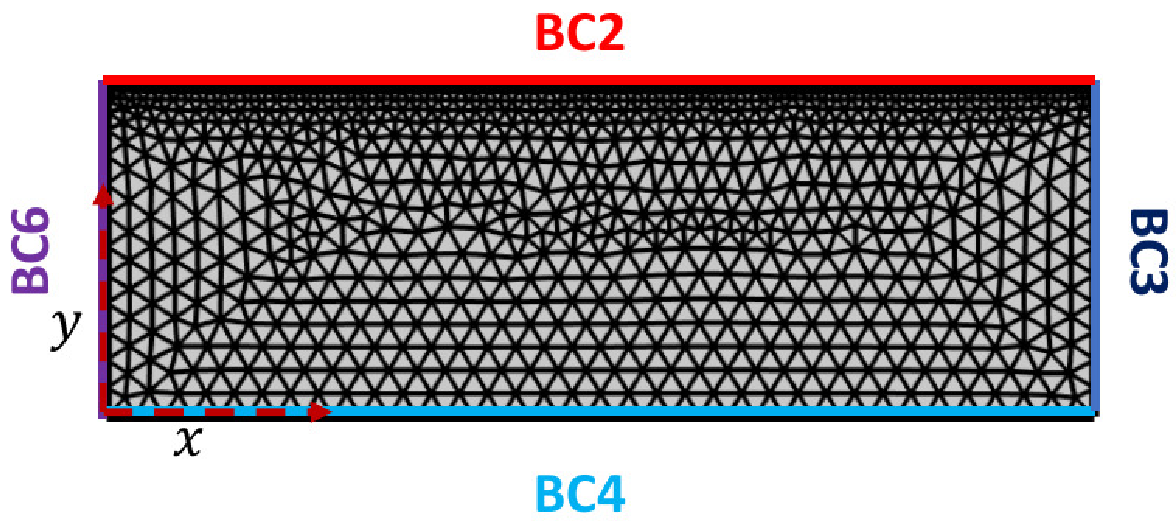

Figure A.2 – FE mesh for model 2 BC2: No slip condition, BC3: pressure outlet, BC4: symmetry condition, BC6: creeping inflow + Dirichlet BC for $\mathbf{A}_2$.

### A.2.2 Method 2

The second model is composed of a 2D rectangular channel, with the given boundary conditions BC2, BC3, and BC4, while BC6 is the inlet flow velocity in addition to the Dirichlet boundary conditions for $\mathbf{A}_2$. The model is composed of two physics, one for solving the creeping flow, and the other is a coefficient partial differential equations, for solving the evolution of $\mathbf{A}_2$ ($A_{11}$, $A_{12}$ and $A_{22}$ ). In this model, Eqs. (2.18), (2.19) and (2.20) are solved using quadratic and IBOF closures [46, 156]. All the computations were carried out on a laptop HP EliteBook 8570p with Intel core i7 and 8GB RAM. The computation was around 16 min in each case for the three Peclet regimes. The used mesh is the COMSOL's predefined free triangular mesh of fine resolution of 3852 elements.

### A.2.3 Numerical precision

The dimensionless Fokker-Planck equation can be written as

$$Pe_{\perp}\mathbf{u}\cdot\nabla_{\mathbf{x}}\Psi - Pe_{\perp}\nabla_{\mathbf{x}}\cdot(\mathbf{D}_t\cdot\nabla_{\mathbf{x}}\Psi) + Pe_{\perp}\nabla_{\mathbf{p}}\cdot(\dot{\mathbf{p}}_j\Psi) - \frac{Pe_{\perp}}{Pe_r}\nabla^2_{\mathbf{p}}\Psi = 0. \tag{A.6}$$

It is important to study the precision of a new numerical simulation. After each computation, the normalization of the probability distribution function and the bulk concentration at the outlet is obtained, and the error is calculated. Figure A.3 shows the error calculated from the numerical normalization of $\Psi$ with the exact one. It is found that at high and low translational diffusions, the error is between 1% and 2%, which is acceptable. The highest error is at $Pe_{\perp} = 1$. Numerical instabilities in COMSOL Multiphysics occur when the element Peclet number exceeds 1. Element Peclet number relates the convective term, element mesh size and the diffusion term. An element Peclet number greater than one is caused by either large convective or small diffusive activity for an acceptable mesh element size. In this work, two element Peclet numbers are found, spatial (relating the spatial diffusion with spatial convection) [299] and configurational (relating the rotary diffusion with rotary convection).

For low $Pe_{\perp}$, diffusion is dominant in this case, the model is stable, and element Peclet numbers are less than 1. For high $Pe_{\perp}$, spatial convection is dominant, in this case, stabilization in the spatial domain is considered by COMSOL (streamline and crosswind diffusion). For $Pe_{\perp} = 1$, the spatial element Peclet number is less than 1, while the configurational 1 equals the rotary Peclet number, which is greater than 1. In this case, the COMSOL's stabilization is not implemented.

## A.3 Closure errors

The scale axis for the error using IBOF closure is from $0 - 5\%$, while using quadratic closure is $0 - 10\%$

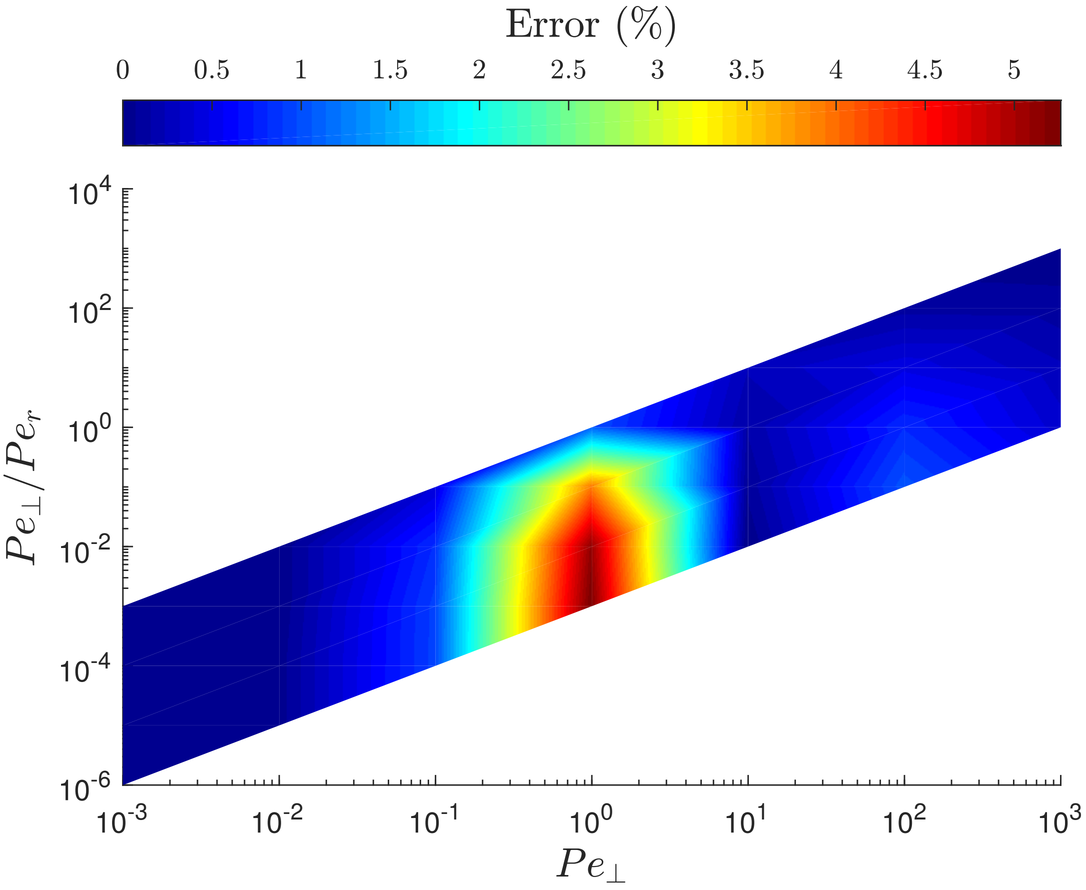

Figure A.3 – Percentage of the numerical errors calculated from the normalization of $\Psi$, for the case of planar channel with homogeneous concentration and planar random orientation at the inlet as a function of Peclet numbers.

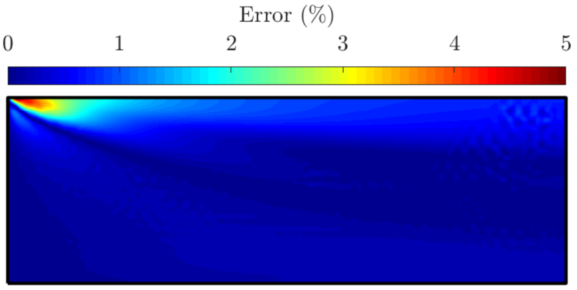

(a) $Pe_r = 10, Pe_\perp = 10^3$

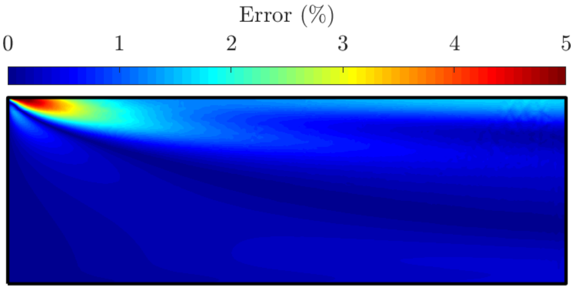

(b) $Pe_r = 10^3, Pe_\perp = 10^3$

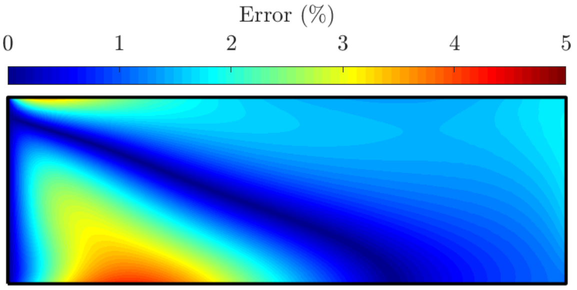

(c) $Pe_r = 10, Pe_\perp = 10$

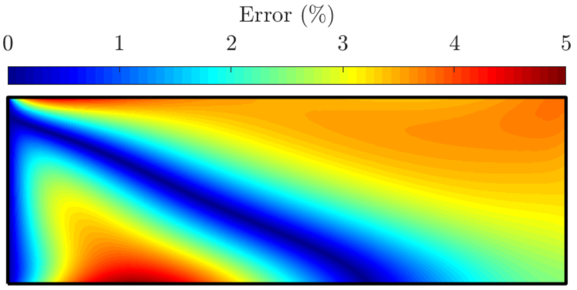

(d) $Pe_r = 10^3, Pe_\perp = 10$

Figure A.4 – Percentage error of concentration $c$ for IBOF closure with respect to method 1.

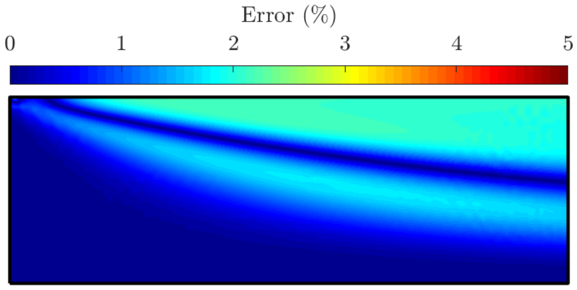

(a) $Pe_r = 10, Pe_\perp = 10^3$

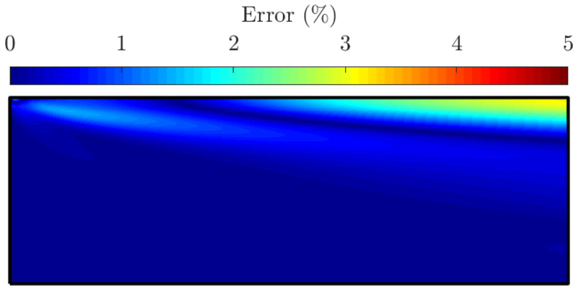

(b) $Pe_r = 10^3, Pe_\perp = 10^3$

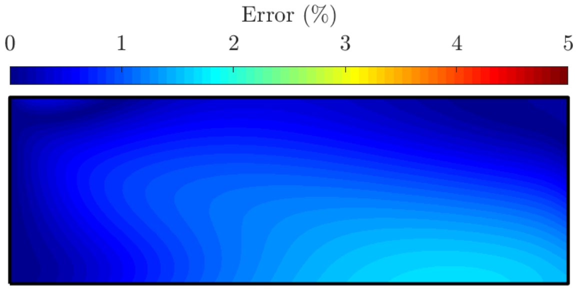

(c) $Pe_r = 10, Pe_\perp = 10$

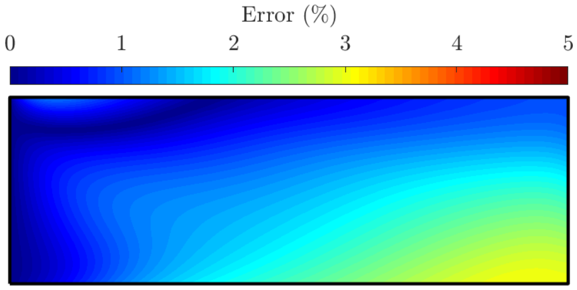

(d) $Pe_r = 10^3, Pe_\perp = 10$

Figure A.5 – Percentage error of orientation component $A_{11}/c$ for IBOF closure with respect to method 1.

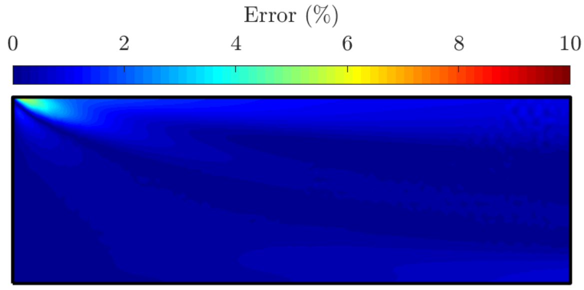

(a) $Pe_r = 10, Pe_\perp = 10^3$

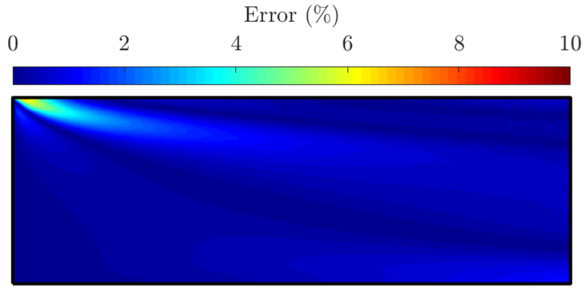

(b) $Pe_r = 10^3, Pe_\perp = 10^3$

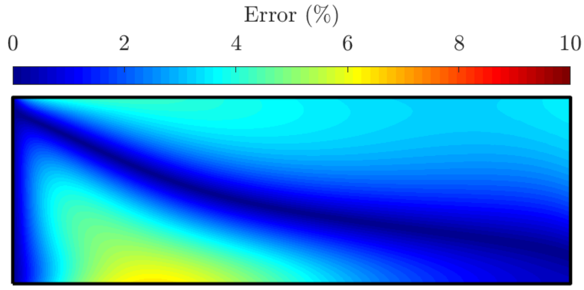

(c) $Pe_r = 10, Pe_\perp = 10$

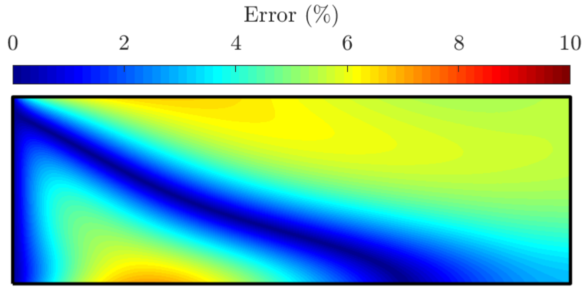

(d) $Pe_r = 10^3, Pe_\perp = 10$

Figure A.6 – Percentage error of concentration $c$ for quadratic closure with respect to method 1.

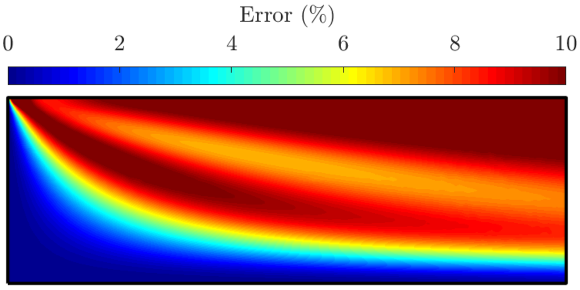

(a) $Pe_r = 10, Pe_\perp = 10^3$

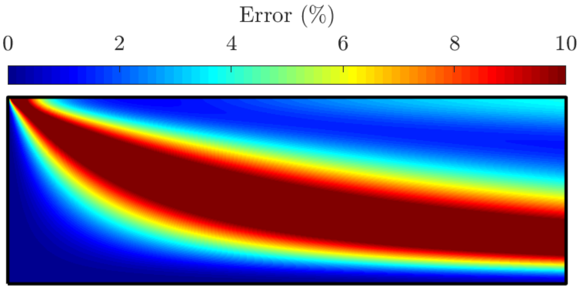

(b) $Pe_r = 10^3, Pe_\perp = 10^3$

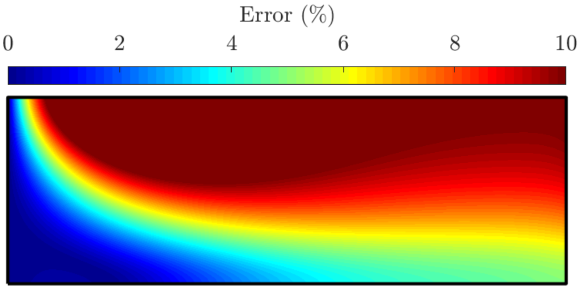

(c) $Pe_r = 10, Pe_\perp = 10$

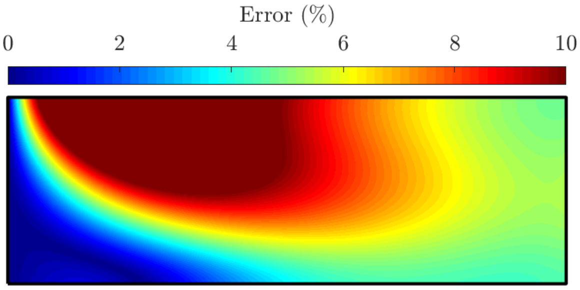

(d) $Pe_r = 10^3, Pe_\perp = 10$

Figure A.7 – Percentage error of orientation component $A_{11}/c$ for quadratic closure with respect to method 1.

Appendix B

# APPENDICES: BROWNIAN ROD-LIKE PARTICLES SUSPENSION IN NON-HOMOGENEOUS SYSTEM: THE EFFECT OF FLOW/ROD COUPLING

## B.1 Model validation

A single particle Smoluchowski equation can be obtained in the dilute regime as follows [22, 26, 27, 40]

$$\frac{\partial \Psi}{\partial t} = -\nabla_{\mathbf{x}} \cdot (\dot{\mathbf{r}}_c \Psi) - \nabla_{\mathbf{p}} \cdot (\dot{\mathbf{p}} \Psi) \, . \tag{B.1}$$

Eq. B.1 can be written by taking into account the fluid incompressibility condition as

$$\frac{D\Psi}{Dt} = \nabla_{\mathbf{x}} \cdot (\mathbf{D}_t \cdot \nabla_{\mathbf{x}} \Psi) - \nabla_{\mathbf{p}} \cdot (\dot{\mathbf{p}}_j \Psi) + D_r \nabla^2_{\mathbf{p}} \Psi. \tag{B.2}$$

The dimensionless form of FP equation (Eq. B.2) is

$$\frac{D\Psi}{Dt} = \nabla^*_{\mathbf{x}} \cdot \left\{ \left[ \frac{1}{Pe_{\|}} \mathbf{pp} + \frac{1}{Pe_{\perp}} (\boldsymbol{\delta} - \mathbf{pp}) \right] \cdot \nabla^*_{\mathbf{x}} \Psi \right\} - \nabla_{\mathbf{p}} \cdot (\dot{\mathbf{p}}_j \Psi) + \frac{1}{Pe_r} \nabla^2_{\mathbf{p}} \Psi. \tag{B.3}$$

To solve the FP equation for the probability distribution function of the particle orientation and concentration in 3D ($\Psi$), a Finite Volume Method (FVM) is employed in the configurational space to discretize the partial differential equation. Following the works of [96] and [98], the numerical method is updated to deal with the 3D representation of Brownian particles in non-homogeneous systems, Eqs. 3.1, 3.2 and B.3 are solved. This numerical solution is based on discretizing the Fokker-Planck equation in FVM for $N$x$N$ number of equations [96, 98]. The model is implemented using COMSOL Multiphysics 6.1 livelinked with MATLAB R2022B. The particles/flow two ways coupling is modeled as a weak contribution in the flow physics. The study of the numerical solution of the model is performed to verify the used model in a simple shear flow. We compare the results with published data in the case of a homogeneous system by performing steady single-point calculations (SPC) using FVM. SPC calculation is performed by discretizing the half sphere of the unit radius into $N = 120$x$120$ area elements, while for the FE scheme where only $N = 20$x$20$ element areas are considered. Starting from the initially homogeneous concentration $c_0 = 1$ and the initially isotropic orientation of the particles, the orientation state is expressed as a function of total strain in Fig. B.1. $A_{11}/c$ and $A_{22}/c$ are proportional to the magnitude of the alignment in the flow direction and velocity gradient direction, respectively, while $A_{12}/c$ indicates the direction of alignment. The model is simulated for $Pe_r = 10$, $Pe_{\perp} = 10^9$ (which has no physical effect on translational diffusion except for stabilizing the numerical scheme) in a transient study for $\gamma = 30$ without considering the hydrodynamic and Brownian coupling effects. The concentration remains homogeneous ($c = 1$) during the study. Fig. B.1 illustrates a comparison between SPC, FE and IBOF results. The FE results and the macromodel provide accurate dynamics and the appropriate steady-state values. This analysis confirms the well-implementation of the FE code and the IBOF accuracy in these studies.

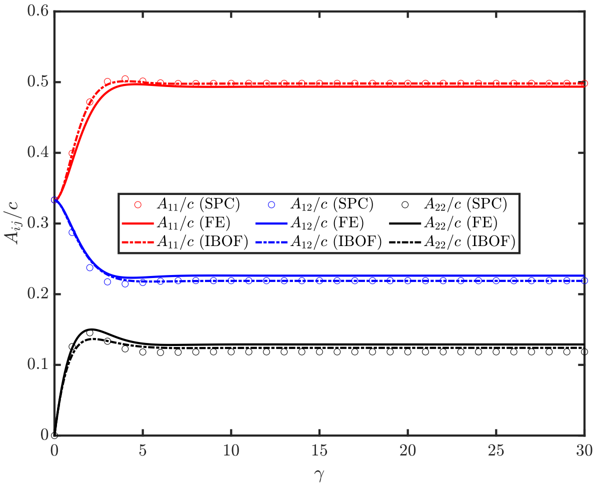

Figure B.1 – Comparison of the IBOF closure approximation [46] with the FE and single-point calculations (SPC) of the conformation tensor components in simple shear flow ($\dot{\gamma} = 1$) with respect to strain $|\gamma|$.

## B.2 Effect of translational diffusion on the rheological transient behaviors in Poiseuille flow

Fig. B.2 shows the evolution of the shear stress profile along the $y$-direction for the mentioned time steps at various $Pe_\perp$ numbers. The results indicate that the shear stress $\Sigma_{xy}$ of the suspension is highest near the walls, where the shear stress and the alignment of the particles are highest, and lowest at the center of the channel, where the shear stress and the alignment of the particles are lowest. As $Pe_\perp$ increases, $\Sigma_{xy}$ increases.

Figs. B.3 and B.4 present the normal stress differences for the mentioned translational Peclet numbers at the same time steps. Due to the higher rod alignment at higher translational Peclet numbers, first normal stress differences increase with the increase of $Pe_\perp$. For $Pe_\perp = 10^{-1}$ and $10^{-2}$, $N_1$ values are around zero. Second normal stress differences have negative values, they have higher values around the center of the channel than near the walls. As time increases, $N_2$ decreases till they reach the steady state. Increasing $Pe_\perp$ leads to lower values of $N_2$, at low $Pe_\perp$, $N_2$ remains around zeros. Due to the anisotropic nature of the suspension, normal stress differences develop. The particles initially take some time to align and arrange themselves in the flow direction after the flow is initiated.

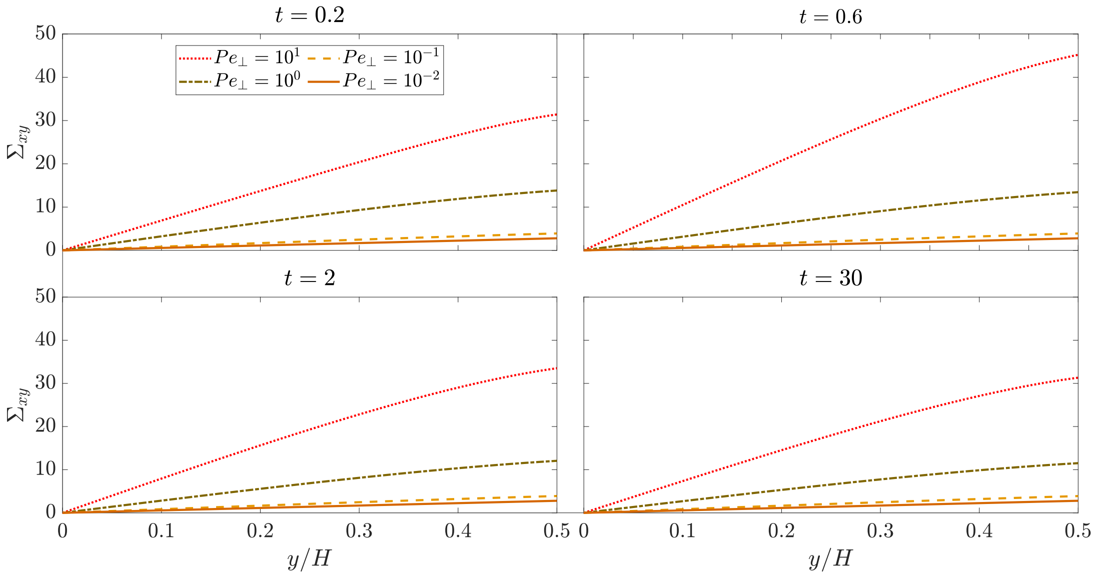

Figure B.2 – Effect of the translational Peclet number on the shear stress $\Sigma_{xy}$ along the $y$-direction for various $Pe_\perp$ numbers at different time $t$.

## B.3 Effect of translational diffusion in Couette flow: Transient plots

The dimensionless form of Cauchy equation in polar coordinates can be expressed as

$$\begin{bmatrix} \frac{1}{r}\frac{\partial}{\partial r}\left(r\frac{\partial u}{\partial r}\right)+\left(\frac{1}{r^2}\right)\frac{\partial^2 u}{\partial \theta^2} \\ \\ \frac{1}{r}\frac{\partial}{\partial r}\left(r\frac{\partial v}{\partial r}\right)+\left(\frac{1}{r^2}\right)\frac{\partial^2 v}{\partial \theta^2} \\ \\ 0 \end{bmatrix} + \begin{bmatrix} \frac{\partial P}{\partial r} \\ \\ \frac{1}{r}\frac{\partial P}{\partial \theta} \\ \\ 0 \end{bmatrix} = \begin{bmatrix} \frac{3N_b}{r}\left(\frac{\partial crA_{rr}}{\partial r}-\frac{1}{3}\frac{\partial rc}{\partial r}\right)+\frac{3N_b}{r}\frac{\partial cA_{r\theta}}{\partial \theta} \\ \\ \frac{3N_b}{r}\left(\frac{\partial rcA_{r\theta}}{\partial r}\right)+\frac{3N_b}{r}(\frac{\partial A_{\theta\theta}}{\partial \theta}-\frac{1}{3}\frac{\partial c}{\partial \theta}) \\ \\ \frac{3N_b}{r}\left(\frac{\partial rA_{rz}}{\partial r}\right)+\frac{3N_b}{r}\frac{\partial A_{\theta z}}{\partial \theta} \end{bmatrix} \tag{B.4}$$

By removing the zero terms, Eq. B.4 becomes

$$\begin{bmatrix} 0 \\ \\ \frac{1}{r}\frac{\partial}{\partial r}\left(r\frac{\partial v}{\partial r}\right) \\ \\ 0 \end{bmatrix} + \begin{bmatrix} \frac{\partial P}{\partial r} \\ \\ 0 \\ \\ 0 \end{bmatrix} = \begin{bmatrix} \frac{3N_b}{r}\left(\frac{\partial crA_{rr}}{\partial r}-\frac{1}{3}\frac{\partial rc}{\partial r}\right)+\frac{3N_b}{r}\frac{\partial cA_{r\theta}}{\partial \theta} \\ \\ \frac{3N_b}{r}\left(\frac{\partial rcA_{r\theta}}{\partial r}\right) \\ \\ 0 \end{bmatrix} \tag{B.5}$$

By taking a look on the second line of Eq. B.5, it shows that the extra stress term $\frac{3N_b}{r}\left(\frac{\partial rcA_{r\theta}}{\partial r}\right)$, affects velocity component in the $\theta$. It is impossible to solve this term analyt-

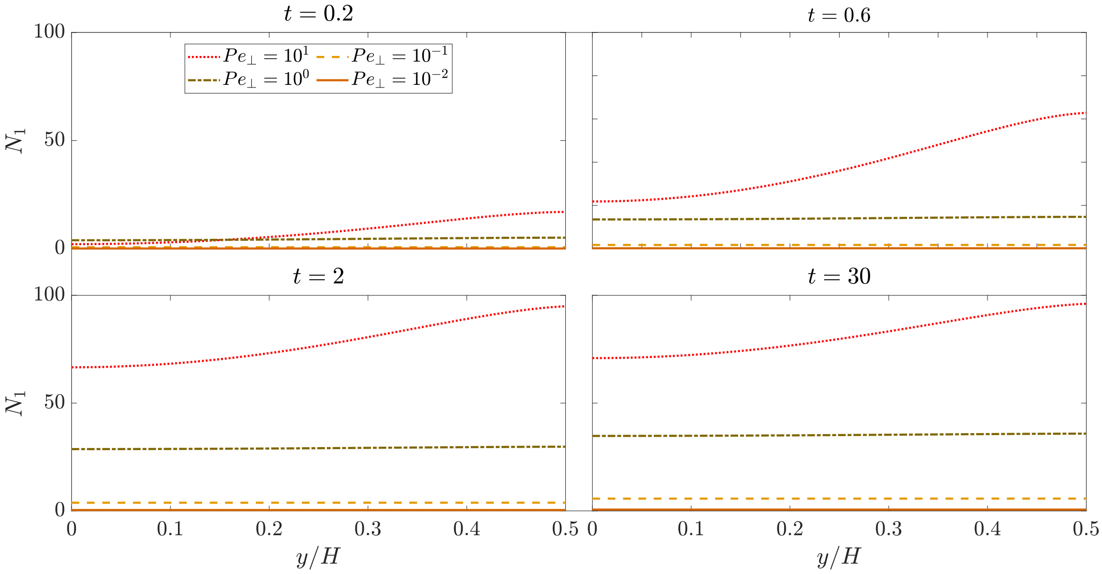

Figure B.3 – Effect of the translational Peclet number on the first normal stress difference $N_1$ along the $y$-direction for various $Pe_\perp$ numbers at different time $t$.

ically. But it can be shown that this term is responsible for the reverse flow in couette fow after a critical value of $N_b$.

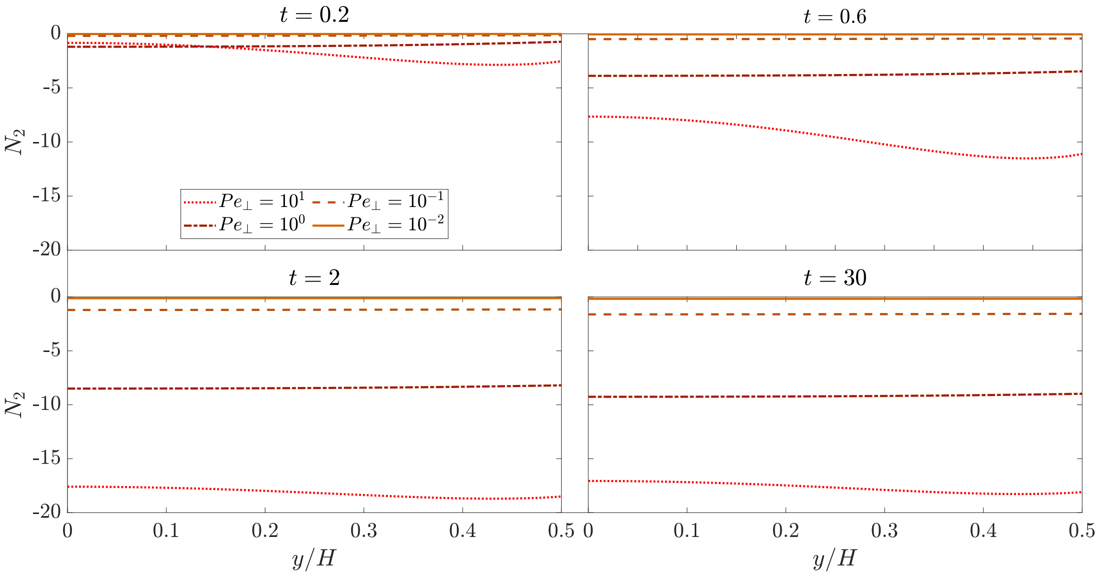

Figure B.4 – Effect of the translational Peclet number on the second normal stress difference $N_2$ along the $y$-direction for various $Pe_\perp$ numbers at different time $t$.

### Appendix C

# APPENDICES: SUSPENSION OF ACTIVE ROD-LIKE PARTICLES IN COMPLEX FLOWS

## C.1 Second-order moment of $\Psi$

The second-order moment of $\Psi$, $\mathbf{A}_2$, contains information on the local concentration and orientation of particles and is defined as

$$\mathbf{A}_2 = \int_{\mathbf{p}} \mathbf{pp}\Psi d\mathbf{p}, \tag{C.1}$$

The trace of $\mathbf{A}_2$ is the concentration field $c$, which represents the mean number density in the suspension, it is the zeroth-order moment of $\Psi$

$$c = \mathbf{A}_2 : \boldsymbol{\delta} = \int_{\mathbf{p}} \Psi d\mathbf{p}, \tag{C.2}$$

The first order moment of $\Psi$, $\mathbf{n}$, represents the nematic order of the particles and it is defined as

$$\mathbf{n} = \int_{\mathbf{p}} \mathbf{p}\Psi d\mathbf{p}, \tag{C.3}$$

The third-order moment of $\Psi$, $\mathbf{A}_3$, is defined as

$$\mathbf{A}_3 = \int_{\mathbf{p}} \mathbf{ppp}\Psi d\mathbf{p}, \tag{C.4}$$

while the fourth-order moment of $\Psi$, $\mathbf{A}_4$, is defined as

$$\mathbf{A}_4 = \int_{\mathbf{p}} \mathbf{pppp}\Psi d\mathbf{p}, \tag{C.5}$$

The evolution equation of the concentration of the active particles in a suspending fluid is

$$\frac{Dc}{Dt} = D_{\perp}\nabla^2_{\mathbf{x}} c + (D_{\parallel} - D_{\perp})\nabla_{\mathbf{x}}\nabla_{\mathbf{x}}\mathbf{A}_2 + V_s\nabla_{\mathbf{x}} \cdot (c\mathbf{n}) \tag{C.6}$$

$V$ represents the volume, which is large enough to contain a statistically significant number of particles but smaller than the characteristic length scale of the macroscopic properties of the system under consideration. In the case of active particles, the odd-order tensors do not equal zeros due to the non-symmetric shapes of the particles. Since the active particles are not symmetric, unlike the passive particles, the orientation component $A_{12}/c$ is not enough to give information about the polarisation of the particle. Fig. C.1 shows the different polarisation of the particle depending on the signs of $A_{12}$ and $n_2$.

The evolution of $\mathbf{A}_2$ is obtained by premultiplying Eq. 4.5 with the tensor $\mathbf{pp}/V$ and integrating it over the spatial and configurational spaces.

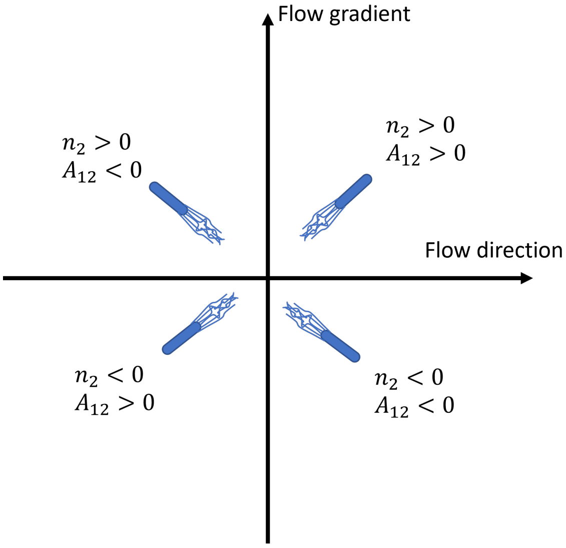

Figure C.1 – Representation shows the meaning of the nematic order of a asymmetric particle.

$$\begin{aligned}\frac{D\mathbf{A}_2}{Dt} =& -\frac{1}{2}\left(\boldsymbol{\omega}\cdot\mathbf{A}_2 - \mathbf{A}_2\cdot\boldsymbol{\omega}\right) + \frac{\lambda}{2}\left(\dot{\boldsymbol{\gamma}}\cdot\mathbf{A}_2 + \mathbf{A}_2\cdot\dot{\boldsymbol{\gamma}} - 2\mathbf{A}_4 : \dot{\boldsymbol{\gamma}}\right) \\ &+ 2D_r\left(c\boldsymbol{\delta} - \alpha\mathbf{A}_2\right) + D_\perp\nabla^2_{\mathbf{x}}\mathbf{A}_2 + \left(D_\parallel - D_\perp\right)\nabla_{\mathbf{x}}\nabla_{\mathbf{x}} : \mathbf{A}_4 + V_s\nabla_{\mathbf{x}}\cdot\mathbf{A}_3.\end{aligned} \tag{C.7}$$

$\alpha$ equals 2 in 2D and 3 in 3D. It can be noticed that the time evolution of the tensor $\mathbf{A}_2$ depends on higher-order moments of $\Psi$. Hence, the problem requires a closure approximation. The last term in Eq. C.7 is the Hessian operator and the last two terms of Eq. C.7 implicitly show the coupling between the local concentration and the local orientation of Brownian particles. Unfortunately, unlike the case of passive particles, the closure approximations found in the literature do not work for non-symmetric particles. So the problem here requires closure approximations for solving $\mathbf{A}_4$ and $\mathbf{A}_3$ as a function of $\mathbf{A}_2$.

DOCTORAT
BRETAGNE SCIENCES
LOIRE POUR L'INGENIEUR

**Titre :** Diffusion translationnelle anisotrope dans les suspensions colloïdales passives et actives : rhéologie et écoulements complexes.

**Mot clés :** Suspensions, particules actives, particules browniennes, orientation, concentration, diffusion translationnelle anisotrope, modélisation numérique.

**Résumé :** Ce travail de recherche s'intéresse aux écoulements de suspensions de particules cylindriques browniennes et actives dans des géométries plus ou moins complexes. Pour mieux comprendre la relation entre la concentration et l'orientation de ces bâtonnets, ainsi que leur dynamique complexe, un macro-modèle basé sur l'équation cinétique de Fokker-Planck est développé en introduisant une diffusion translationnelle anisotrope. Pour les suspensions de particules browniennes, les simulations numériques, en considérant un couplage faible, mettent en avant la relation entre l'orientation des particules et leur concentration. Le couplage fort montre quant à lui l'influence des particules sur les vitesses d'écoulement et les propriétés rhéologiques du système. Ce travail de recherche est ensuite étendu aux particules actives en introduisant une vitesse d'autopropulsion propre à ces systèmes mobiles. Les solutions numériques sont obtenues en résolvant l'équation de Fokker-Planck associée. Le couplage faible montre une accumulation de particules actives près des parois tandis que la prise en compte du couplage fort prédit une bande de cisaillement.

**Title:** Anisotropic Translational Diffusion in Passive and Active Colloidal Suspensions: rheology and complex flows.

**Keywords:** Suspensions, Active particles, Brownian particles, Orientation, Concentration, Anisotropic translational diffusion , Numerical modeling.

**Abstract:** This research work focuses on the flow of Brownian and active rod-like particles suspensions in more or less complex geometries. To further understand the relationship between rod concentration and orientation, as well as their complex dynamics, a macro-model based on the kinetic Fokker-Planck equation is developed by introducing an anisotropic translational diffusion. For Brownian rod suspensions, the numerical simulations reveal this relation by considering the one-way coupling. The two-way coupling shows the influence of the rods on the flow velocity and the rheological properties. The research work is then extended to active particles by incorporating the self-propulsion velocity encountered in these motile systems. The solutions are obtained by solving the associated Fokker-Planck equation. The one-way coupling show the wall accumulation of active particles while two-way coupling predicted a shear banding.